Numerical study of instability patterns of film-substrate systems

Fan Xu

Université de Lorraine **École doctorale EMMA**
UFR MIM

Étude numérique des modes d'instabilités des systèmes film-substrat

Numerical study of instability patterns of film-substrate systems

THÈSE

présentée et soutenue publiquement le 02 décembre 2014

pour l'obtention du

Doctorat de l'Université de Lorraine

Spécialité : **Mécanique des Matériaux**

par

Fan XU

Composition du jury

Rapporteurs :	Pr. Basile Audoly	Université Pierre et Marie Curie (Paris 6), France
	Pr. Yibin Fu	Keele University, UK
Examinateurs :	Pr. Martine Ben Amar	École Normale Supérieure, France
	Pr. Hachmi Ben Dhia	École Centrale Paris, France
Directeur :	Pr. Michel Potier-Ferry	Université de Lorraine, France
Co-directeur :	Dr. Salim Belouettar	CRP Henri Tudor, Luxembourg

Laboratoire d'Étude des Microstructures et de Mécanique des Matériaux — UMR CNRS 7239
Centre de Recherche Public Henri Tudor

Mis en page avec la classe thloria.

Acknowledgments

After all the confusion or epiphany, depression or inspiration, sadness or happiness, finally it comes to the stage when we are modest and grateful, as the last thing that I learned from my doctoral studies.

I would like to begin by expressing my most sincere gratitude to my Ph.D. advisor, Professor Michel Potier-Ferry, an inspiring and extraordinary person to work with during the entire span of this thesis. In addition to introducing me to the subject of instability and guiding me to grow in computational mechanics, his patient guidance and relentless pursuit of excellence have helped shape me into not only a good researcher with rigorous attitude but also a responsible and considerate person than I otherwise would have been. Plainly put, he has been a great mentor. It has been an honor and a privilege working with him over the last three years.

Sincere appreciation is extended to my co-advisor, Dr. Salim Belouettar, for his kind supports and helps as well as deep trusts for giving me full autonomy in research activity.

I would like to express my gratitude to the other thesis committee members, Professor Basile Audoly, Professor Yibin Fu, Professor Martine Ben Amar and Professor Hachmi Ben Dhia, for taking the time to read this thesis and for offering helpful comments and suggestions. Professor Basile Audoly and Professor Yibin Fu deserve a special thank for their inspiring and encouraging reports on this thesis.

Many thanks go in particular to Professor Yanping Cao at Tsinghua University for his expert advice and valuable scientific discussions, which enlightened me and eliminated my confusions on some technical points.

I would also like to record my gratitude to my colleagues and my friends, Dr. Yu Cong and Dr. Yao Koutsawa, for our scientific (and not-so-scientific) discussions. It has been a pleasure working with them.

Special thanks go to Professor Hamid Zahrouni for allowing me to use his powerful workstation to perform heavy simulations.

My thanks also go to my friends, Kodjo Attipou, Cai Chen, Yajun Zhao, Junliang Dong, Qi Wang, Dr. Wei Ye, Dr. Jingfei Liu, Dr. Kui Wang, Alex Gansen, Qian Shao, Sandra Hoffmann, Dr. Duc Tue Nguyen, *etc.* for sharing my joy and sadness, and offering helps and supports whenever needed. I treasure every minute that I have spent with them.

Lastly, I would like to give my most special thanks to my parents and my fiancée for their unconditional love, 24/7 support, share of happiness and for always believing in me. Without their encouragement I would never have made it this far.

Financial support for this research was provided by AFR Ph.D. Grants from Fonds National de la Recherche of Luxembourg (Grant No. FNR/C10/MS/784868).

To my parents
To my fiancée

Table of contents

List of Figures

General introduction

Surface wrinkles of stiff thin layers bound to soft materials have been widely observed in nature, such as wrinkles of hornbeam leaf and human skin, which has raised considerable research interests for several decades. When depositing a stiff thin film on a polymeric soft substrate, the developed residual compressive stresses in the film during the cooling process due to the large mismatch of thermal expansion coefficient between the film and the substrate, are relieved by buckling with wrinkle patterns, which was pioneered by Bowden *et al.* [29] in 1998. These surface wrinkles are a nuisance in some applications, but can be widely applied in modern industry ranging from micro/nano-fabrication of flexible electronic devices with controlled morphological patterns [30, 151] to the mechanical property measurement of material characteristics [79].

Over the last decade, several theoretical, numerical and experimental works have been devoted to stability analyses in order to determine the critical conditions of instability and the corresponding wrinkling patterns [36, 37, 43, 89, 85, 151, 143, 9, 10, 11]. Although linear perturbation analyses can predict the wavelength at the initial stage of instability threshold, determination of the following post-buckling morphological evolution really requires nonlinear buckling analyses. During post-buckling, the wavelength and amplitude of wrinkles may vary with respect to externally applied compressive load. However, instability problems are complex and often involve strong effects of geometrical nonlinearities, large rotations, large displacements, large deformations, loading path dependence and multiple symmetry-breakings. That is why most nonlinear buckling analyses have resorted to numerical approaches since only a limited number of exact analytical solutions can be obtained.

In most of previous works, the 2D or 3D film/substrate system is often discretized by spectral method or Fast Fourier Transform (FFT) algorithm, which is fairly computationally inexpensive but prescribes periodic boundary conditions and simple geometries. Moreover, within the spectral or FFT framework, it is rather difficult to describe localized behavior that often occurs in soft matters. By contrast, such systems can be modeled by using finite element methods, which is more computationally expensive but more flexible to describe complex geometries and general boundary conditions, and allows using com-

mercial computer codes. In addition, there is a shortage of study concerning the effect of boundary conditions on instability patterns, which is important in practice. Localizations are often caused by stress concentration near the boundary or by symmetry-breakings, and finite element method is a good way to capture the localized behavior such as folding, creasing or ridging, while the spectral or FFT technique has difficulties to achieve it.

Overall, pattern formation modeling and post-buckling analysis deserve new numerical investigations, especially through finite element method that can provide the whole view and insight into the formation and evolution of wrinkle patterns in any condition. Therefore, the main objective of the present thesis is to apply advanced numerical methods for multiple-bifurcation analyses of film/substrate systems. These advanced numerical approaches include path-following techniques, bifurcation indicators, bridging techniques, multi-scale analyses, *etc.* The point of this thesis lies in, but is not limited to, the application of the following numerical methods to the instability pattern formation of film/substrate systems:

- Finite element method to be able to deal with all the geometries, behaviors and boundary conditions;
- Path-following technique for nonlinear problem resolution;
- Bifurcation indicator to detect bifurcation points and the associated instability modes;
- Reduction techniques of models by multi-scale approaches;
- Bridging techniques to couple full models and reduced-order models concurrently.

The thesis is outlined as follows.

In Chapter 1, literature review revisits previous contributions and reports cutting-edge works as well as research trends in the relative fields. Challenges and problems that need to be overcome and solved are positioned and discussed. Besides, the main methods and techniques that will be applied and developed in the following chapters are introduced. This includes firstly an advanced numerical continuation technique to solve nonlinear differential equations, namely Asymptotic Numerical Method (ANM) [52, 46, 45, 47]; secondly a Fourier-related multi-scale modeling technique for instability pattern formation; and lastly the well-known Arlequin method [20, 24] for model coupling between different scales or different meshes.

In Chapter 2, we apply advanced numerical methods for bifurcation analyses to typical film/substrate systems, and focus on the post-bifurcation evolution involving secondary bifurcations and the associated instability modes. A finite element model based on the

ANM is developed for nonlinear analysis of pattern formation, with a particular attention on the effect of boundary conditions. Up to four successive bifurcation points have been detected. The evolution of wrinkling patterns and post-bifurcation modes including period-doubling has been observed beyond the first bifurcation.

Next in Chapter 3, following the same strategy, we extend the 2D work to 3D cases. Spatial pattern formation in stiff thin films on compliant substrates is investigated based on a 3D finite element model by coupling shell elements representing the film and block elements describing the substrate. Typical post-bifurcation patterns include sinusoidal, checkerboard and herringbone shapes, with possible spatial modulations, boundary effects and localizations. Up to four successive bifurcation points have been found on nonlinear response curves.

Chapter 4 presents a very original nonlocal bridging technique between microscopic and macroscopic models for the wrinkling analysis. We discuss how to connect a fine and a coarse model within the Arlequin framework. We propose a nonlocal reduction-based coupling operator that allows us to accurately describe the response of the system near the boundary and to avoid locking phenomena in the coupling zone. The proposed method can be viewed as a guide for coupling techniques involving other reduced-order models and it shows a flexible way to analyze cellular instability problems involving thin boundary layers, *e.g.* membrane wrinkling, buckling of thin metal sheets, *etc.*

In the last Chapter 5, a macroscopic modeling framework for film/substrate systems is developed based on the technique of slowly variable Fourier coefficients [54, 56]. More specifically, a 2D macroscopic film/substrate model is derived from the 2D model presented in Chapter 2, with all the mechanical fields being represented by Fourier coefficients. In this way, the computational cost can be reduced significantly, since only a few number of elements are sufficient to describe nearly periodic wrinkles. In the same spirit, a 3D macroscopic film/substrate model that couples a nonlinear envelope membrane-wrinkling model and a linear elastic macroscopic model is then established.

Unless particularly mentioned, computations performed throughout the thesis have been based on self-developed computer codes in MATLAB.

Introduction générale

Le plissement dans les films minces sur un substrat plus mou a été largement observé dans la nature, par exemple dans les feuilles d'arbres et la peau humaine. Ces phénomènes ont suscité un intérêt considérable depuis plusieurs décennies. Lors du dépôt d'un film sur un substrat polymère souple, des contraintes résiduelles de compression se développent dans le film pendant la phase de refroidissement en raison du grand décalage de coefficient thermique entre le film et le substrat, puis elles se relaxent par flambage: on se reportera par exemple à l'article pionnier de Bowden *et al.* [29] en 1998. Ces plis de surface sont une nuisance dans certaines applications, mais peuvent être largement utilisés dans l'industrie moderne pour des applications allant de la micro/nano-fabrication de dispositifs électroniques flexibles avec motifs morphologiques contrôlés [30, 151] à la mesure des propriétés mécaniques des matériaux [79].

Au cours de la dernière décennie, des recherches théoriques, numériques et experimentales ont été consacrées aux analyses de stabilité afin de déterminer les conditions critiques d'instabilité et les modes correspondants [36, 37, 43, 89, 85, 151, 143, 9, 10, 11]. Bien que les analyses linéaires de perturbation puissent prévoir la longueur d'onde à l'initiation de l'instabilité, la détermination de l'évolution morphologique ultérieure nécessite vraiment des analyses non-linéaires. Au cours du post-flambage, la longueur d'onde et l'amplitude peuvent varier. Mais, les problèmes d'instabilité sont complexes et impliquent souvent de forts effets de non-linéarité géométrique, de grandes rotations, de grands déplacements, de grandes déformations, une dépendance par rapport au chemin de chargement et de multiples brisures de symétrie. C'est pourquoi la plupart des analyses non-linéaires de flambement ont recouru à des approches numériques parce qu'on ne peut obtenir qu'un nombre limité de solutions exactes de manière analytique.

Dans la plupart des travaux antérieurs, le système film/substrat en 2D ou 3D est souvent discretisé par la méthode spectrale ou la transformée de Fourier rapide (FFT), qui coûtent peu cher en termes de temps calcul mais imposent des conditions aux limites périodiques et des géométries simples. En outre, dans le cadre spectral ou FFT, il est assez difficile de décrire un comportement localisé qui apparait souvent avec la matière molle. En revanche, ces systèmes peuvent être modélisés par la méthode des éléments

finis, ce qui est plus coûteux en temps calcul mais plus flexible pour décrire des géométries complexes et des conditions aux limites génériques, et permet d'utiliser des codes de calculs commerciaux. En plus, il y a peu d'études concernant les effets de conditions aux limites sur les modes d'instabilité, ce qui est important dans la pratique. Les localisations sont souvent causées par la concentration des contraintes près des bords ou par les multiples brisures de symétrie, et la méthode des éléments finis est une bonne façon de capturer des comportements localisés tels que le pliage, le plissement ou la formation de crêtes, ce qui est plus difficile avec la technique spectrale ou FFT.

Globalement, la modélisation de la formation de plis et l'analyse de post-flambage méritent de nouvelles investigations numériques, en particulier par la méthode des éléments finis qui peut founir une vue complète de la formation et de l'évolution des modes de plissement dans toutes les conditions. L'objectif principal de cette thèse est donc d'appliquer aux systèmes film/substrat des méthodes numériques avancées pour des analyses de bifurcations multiples. Ces approches numériques avancées incluent des techniques de cheminement, des indicateurs de bifurcation, des méthodes de couplage de modèle, des analyses multi-échelle, *etc.* Le point fort de cette thèse est l'application des méthodes numériques suivantes aux instabilités dans les systèmes film/substrat:

- Méthode des éléments finis pour pouvoir traiter toutes les géométries, tous les comportements et conditions aux limites;
- Technique de cheminement pour la résolution de problèmes non-linéaires;
- Indicateur de bifurcation pour détecter les points de bifurcations et les modes d'instabilité associés;
- Techniques de réduction de modèles par des approches multi-échelles;
- Méthodes de couplage pour coupler les modèles complets et les modèles réduits.

Le contenu détaillé de la thèse est décrite ci-dessous.

Dans le Chapitre 1, une revue de la littérature présente les travaux récents et les tendances de la recherche dans le domaine. Les défis et les problèmes à surmonter sont positionnés et discutés. Par ailleurs, les méthodes et techniques principales qui seront appliquées et développées dans les chapitres suivants sont introduits: tout d'abord une technique numérique de pilotage pour résoudre les équations différentielles non-linéaires, à savoir la Méthode Asymptotique Numérique (MAN) [52, 46, 45, 47]; deuxièmement une technique de modélisation multi-échelle de type Fourier pour la formation de modes d'instabilité; et enfin la méthode Arlequin [20, 24] bien connue pour le couplage des modèles entre différentes échelles ou différents maillages.

Dans le Chapitre 2, nous appliquons des méthodes numériques avancées pour des analyses de bifurcations aux modèles typiques de systèmes film/substrat, et il se concentre sur l'évolution post-bifurcation impliquant bifurcations secondaires et modes d'instabilité associés. Un modèle éléments finis basés sur la MAN est développé pour l'analyse non-linéaire, avec une attention particulière sur l'effet des conditions aux limites. Jusqu'à quatre points de bifurcation successifs ont été détectés. L'évolution des modes de plissement et des modes de post-bifurcation, y compris le doublement de la période, a été observée au-delà de la première bifurcation.

Dans le Chapitre 3, suivant la même stratégie, nous étendons le travail 2D au 3D. La formation de modes spatiaux dans les films minces sur des substrats mous est étudiée à partir d'un modèle éléments finis 3D par le couplage d'éléments de coque et d'éléments volumiques. Les modes typiques de post-bifurcation incluent des formes sinusoïdaux, de damiers et de chevrons, avec des modulations spatiales possibles, des effets des conditions aux limites et des localisations. Jusqu'à quatre points de bifurcation successifs ont été trouvés sur des courbes de réponse non-linéaires.

Le Chapitre 4 présente une technique très originale de couplage non-local entre les modèles microscopiques et macroscopiques pour l'analyse de plissement. Nous discutons comment connecter un modèle fin et un modèle grossier dans le cadre Arlequin. Nous proposons un opérateur de réduction non-local qui nous permet de décrire avec précision la réponse du système à proximité de la frontière et d'éviter des phénomènes de verrouillage dans la zone de couplage. La méthode proposée peut être considérée comme un guide pour les techniques de couplage impliquant d'autres modèles réduits et il montre la manière flexible pour analyser les problèmes d'instabilité cellulaire impliquant des couches minces, par exemple, le plissement des membrane, le flambage de tôles minces métalliques, *etc.*

Dans le dernier Chapitre 5, un cadre de modélisation macroscopique pour les systèmes film/substrat est développé sur la base de la technique de Fourier à coefficients lentement variables [54, 56]. Plus précisément, un modèle 2D macroscopique de film/substrat est dérivé du modèle 2D présenté dans le Chapitre 2, tous les champs mécaniques étant représentés par des coefficients de Fourier. De cette manière, le coût de calcul peut être considérablement réduit, car seul un petit nombre d'éléments suffit pour décrire les plis périodiques. Dans le même esprit, un modèle 3D macroscopique de film/substrat est établi, qui couple un modèle de membrane-plissement enveloppe non-linéaire et un modèle macroscopique élastique linéaire.

Sauf mention particulière, les calculs effectués tout au long de la thèse ont été basés sur les codes informatiques de notre cru écrits dans MATLAB.

Chapter 1

Bibliographic review

Contents

1.1 Surface morphological instabilities of film/substrate systems

1.1.1 Literature review

Wrinkles of a stiff thin layer attached on a soft substrate have been widely observed in nature (see Fig. 1.1) and these phenomena have raised considerable research interests

over the last decade [29, 120, 64, 59, 128, 133, 31, 100]. The underlying mechanism of wrinkling is generally understood as a stress-driven instability, analogous to Euler buckling of an elastic column under compressive stress. By depositing a stiff film on an elastomeric soft substrate, the developed residual compressive stresses in the film during the cooling process due to the large thermal expansion coefficient mismatch between the film and the substrate are relieved by buckling with a pattern of wrinkles, while the film remains bonded to the substrate, which was pioneered by Bowden *et al.* [29, 30] in 1998. These surface wrinkles are a nuisance in some applications, but can be widely applied ranging from micro/nano-fabricating surfaces with ordered patterns with unique wetting [29, 30], buckled single crystal silicon ribbons [151], optical property of electronic eye camera, mechanical property measurement of surface characteristics of the materials [79], biomedical engineering [70] as well as biomechanics [19, 60, 115], to the design of flexible semiconductor devices and stretchable electronics [133], conformable skin sensors, smart surgical gloves, and structural health monitoring devices [151].

(a) (b) (c)

Figure 1.1: Wrinkles in nature: (a) hornbeam leaf wrinkles, (b) finger wrinkles, (c) wrinkles in landform. [pictures from internet]

When subjected to sufficiently large in-plane compressive stresses, in order to minimize the total potential elastic energy, a film/substrate system may buckle into different intricate patterns depending on loading and boundary conditions, *e.g.* sinusoidal, checkerboard, herringbone, hexagonal and triangular patterns, as shown in Figs. 1.2 and 1.3. One of the mathematical expressions of those pattern shapes is the combinations of

trigonometric functions [35], which can be written as

$$\begin{aligned}
\text{1D sinusoidal mode:} \quad & z = \sin(kx), \\
\text{Checkerboard mode:} \quad & z = \cos(kx)\cos(ky), \\
\text{Herringbone mode:} \quad & z = \cos(kx) + \sin(kx)\cos(ky), \\
\text{Hexagonal mode:} \quad & z = \cos(kx) + 2\cos\left(\frac{1}{2}kx\right)\cos\left(\frac{\sqrt{3}}{2}ky\right), \\
\text{Triangular mode:} \quad & z = -\sin(kx) + 2\sin\left(\frac{1}{2}kx\right)\cos\left(\frac{\sqrt{3}}{2}ky\right).
\end{aligned} \tag{1.1}$$

First, let us distinguish three typical phenotypes in morphological instability of soft materials: wrinkling, folding and creasing (see Fig. 1.4). Wrinkling is related to periodic or aperiodic surface undulations appearing on a flat surface. It often occurs during the buckling of thin structures with lateral foundations. For example in 2D cases, a stiff film bonded to a compliant substrate may buckle into sinusoidal waves. Folding usually refers to a buckling induced surface structure with a localized surface valley. Folds are often observable during the post-buckling evolution of surface wrinkles in a hard layer lying on a gel substrate or floating on a liquid. The term folding has been extensively adopted in some fields like biomedicine and tectonophysics to represent traditional wrinkling. By contrast, creasing usually appears at the surface of soft materials without hard skins, when an initially smooth surface forms a sharp self-contacting sulci [116].

The broad interest on surface morphological instabilities of stiff thin layers attached on soft substrates has motivated recent studies, especially focusing on stability analysis. Several theoretical, numerical and experimental works have been devoted to linear perturbation analyses and nonlinear buckling analyses in order to determine the critical conditions of instability and the corresponding wrinkling patterns [87, 43, 88, 89, 85, 120, 151, 143, 9, 10, 11, 109, 93]. In particular, there are many analytical solutions of models linearized from homogeneous finite deformation, in the case of half-spaces [76, 62] as well as film/substrate systems [144, 36, 37]. Cai and Fu [37] analytically studied the buckling of a pre-stressed coated elastic half-space with the aid of the exact theory of nonlinear elasticity, treating the coating as an elastic layer and using its thickness as a small parameter. Besides, they also determined the imperfection sensitivity of a neo-Hookean surface layer bonded to a neo-Hookean half-space [36]. Although linear perturbation analyses can predict the wavelength at the initial stage of instability threshold, determination of the post-buckling morphological evolution and the mode transition of surface wrinkles really requires nonlinear buckling analyses. During post-buckling, the wrinkle wavelength and amplitude will vary with respect to externally applied compressive load. Due to its well-

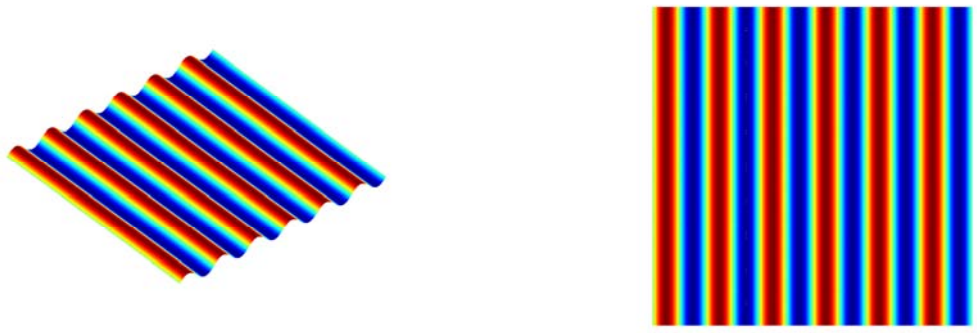

(a)

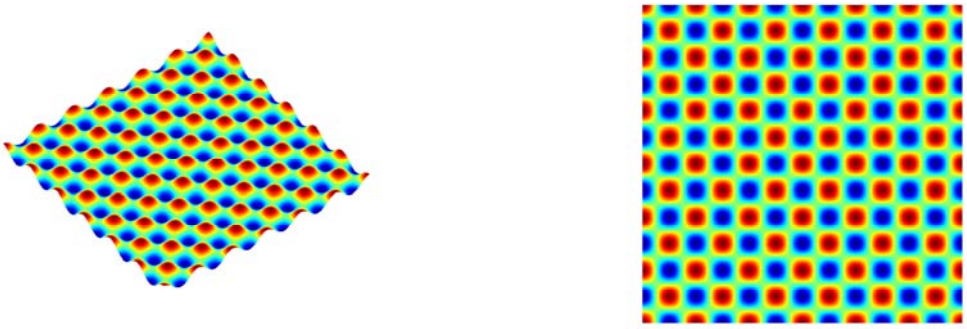

(b)

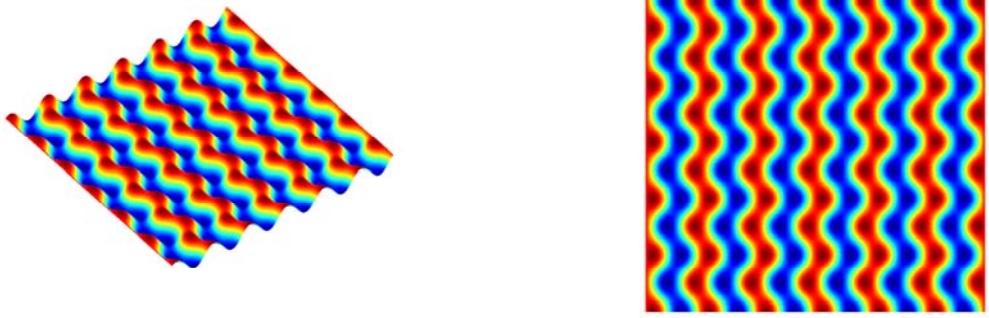

(c)

Figure 1.2: Schematics of mode shapes: (a) sinusoidal mode, (b) checkerboard mode, (c) herringbone mode.

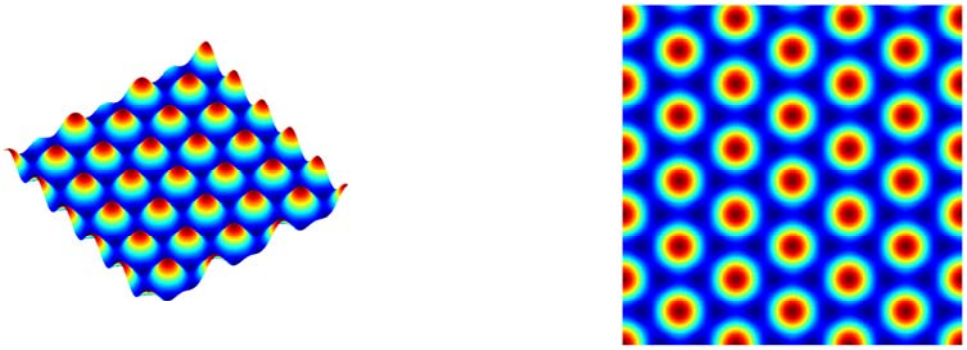

(a)

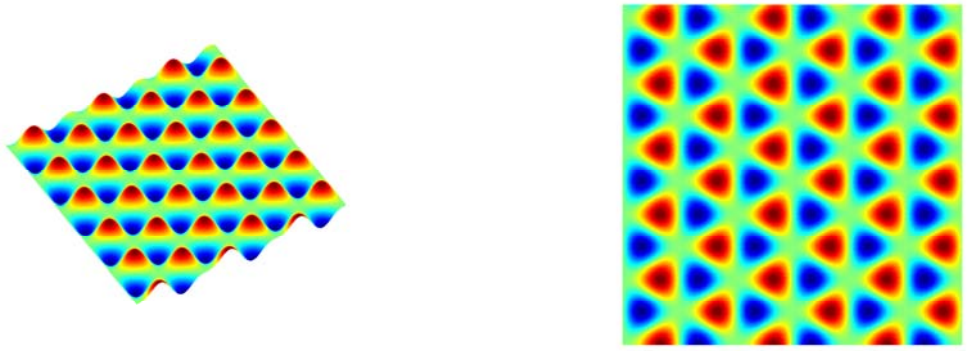

(b)

Figure 1.3: Schematics of mode shapes: (a) hexagonal mode, (b) triangular mode.

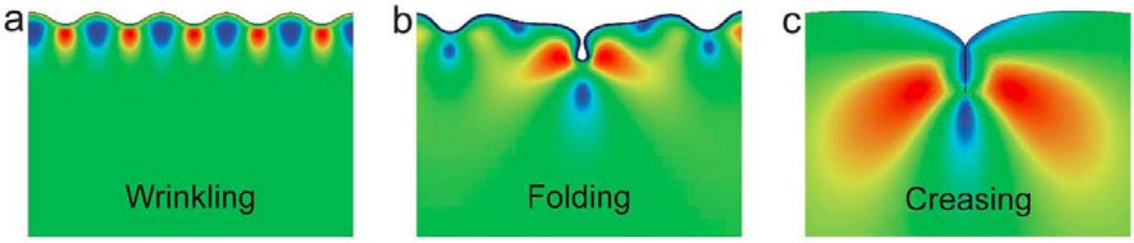

Figure 1.4: Schematic of three types of morphological instability: (a) wrinkling, (b) folding, and (c) creasing [116].

known difficulty, most post-buckling analyses have resorted to numerical and experimental approaches, since only a limited number of exact analytical solutions can be obtained in very simple or simplified cases.

Some researchers considered the wrinkling of thin film by using Föppl-von Kármán nonlinear elastic plate theory and applied linear elasticity theory for the substrate, and then carried out the minimization of the potential energy to characterize the effective instability parameters, which is quite a classical and simple way to model the film/substrate systems. Chen and Hutchinson [43] have elucidated nonlinear aspects on the buckling behavior of some periodic modes and developed a closed-form solution. They calculated the wavelength and amplitude of sinusoidal wrinkles through considering an infinitely thick substrate. Through numerical way by using finite element method and simulating a single elementary cell, a square or a parallelogram with periodic boundary conditions, Chen and Hutchinson [43] found that the herringbone pattern has the minimum energy among several patterns including sinusoidal and checkerboard, which is the reason why it was frequently observed in experiments. Huang *et al.* [89] extended the work of Chen and Hutchinson [43] to the case of a film bound to a substrate of finite thickness. Instead of modeling the substrate as a Winkler foundation (a foundation made of an array of springs and dashpots) [88], they developed a spectral method to evolve two-dimensional patterns of wrinkles in separate spaces and represented the three-dimensional elastic field of the substrate in the Fourier space. The calculation of wrinkle patterns was performed in a square cell in the plane with periodic boundary conditions replicating the cell to the entire plane. They observed stripe wrinkles, checkerboard, labyrinths or herringbone patterns depending on the loading conditions and showed that the wavelength of the wrinkles remains constant as the amplitude of the wrinkles increases. Independently, Mahadevan and Rica [120] proposed an analysis of herringbone patterns based on amplitude equations, which is suitable for the analysis of large wavelength perturbations on top of the straight wrinkles, but with an assumption that does not apply to the geometry of herringbones. Audoly and Boudaoud [9] proposed a simplified buckling model by considering a film attached on an isotropic half-infinite substrate and then solved it in the Fourier space. They found that the undulating stripes evolve smoothly towards a pattern similar to herringbone one under increasing loads. In their companion papers [10, 11], they conducted asymptotic methods and Fast Fourier Transform (FFT) algorithm to explore aspects of behavior expected in the range of very large overstress with emphasis on the herringbone mode.

Most previous studies consider a homogeneous substrate, while systems consisting of a stiff thin layer resting on an elastic graded substrate are often encountered both in nature and industry. In nature, many living soft tissues including skins, brains, mucosa

of esophagus and pulmonary airway can be modeled as a soft substrate covered by a stiff thin surface layer [115]. It is noted that the sub-surface layer (*i.e.* substrate) usually has gradient mechanical properties because of the spatial variation in the microstructure or composition. Besides, many practical systems in industry have a functionally graded substrate [109, 79, 40, 160]. For instance, the deposition process of a stiff thin film on a soft substrate may lead to a variation of the mechanical properties of the substrate along the thickness direction (functionally graded), which would affect the wrinkling of film/substrate system [79]. Lee *et al.* [109] performed a stability and bifurcation analysis for the surface wrinkling of an elastic half space under in-plane compression, with Young's modulus arbitrarily varying along the depth. They developed a finite element method to solve this problem. Cao *et al.* [40] carried out theoretical analyses and finite element simulations for a hard film wrinkling on an elastic graded substrate subjected to in-plane compression. In particular, they investigated two typical variations in the substrate modulus along the depth direction, expressed by a power function and an exponential function, respectively. Nevertheless, up to now, there is a shortage of theoretical or numerical investigation on the instability of a stiff layer lying on an elastic graded substrate.

On the other hand, when the substrate is made of viscous or viscoelastic materials, wrinkling patterns may evolve with time due to their time-dependent mechanical properties [87, 93]. In such systems, the instability characteristics can be determined by integrating the methods of energetics and kinetics [85]. A spectral method was developed by Huang and Im [86] for numerical simulations of wrinkle growth and coarsening in stressed thin films on a viscoelastic layer. A random perturbation distribution of lateral deflection is imposed to trigger disordered labyrinth patterns. Later, a Fourier transform method was employed by Im and Huang [93] for wrinkling analysis of an anisotropic crystal film on a viscoelastic substrate layer. Even so, investigations in terms of the effects of viscosity on wrinkling pattern evolution are still very limited and still deserve much further effort.

Notwithstanding much effort have been made on the modeling of morphological wrinkling in film/substrate systems, most of those previous studies are mainly constrained to determine the critical conditions of instability and corresponding wrinkling patterns near the instability threshold. The post-buckling evolution and mode transition of surface wrinkles are only recently being pursued [128, 129, 31, 100, 115, 39, 38, 40, 163, 146, 160].

Experimentally through thin elastic membranes being supported on a much softer elastic solid or a fluid, Pocivavsek *et al.* [128] found a transition from periodic surface wrinkling to symmetry-broken folding when the compression is beyond a critical value. When the fluid substrate is replaced by a polydimethylsiloxane (PDMS) foundation, the film/substrate system shows distinctly different pattern evolution with increasing com-

pression. Brau *et al.* [31] experimentally discovered that further compressions above the onset of buckling triggers multiple bifurcations: one wrinkle grows in amplitude at the expense of its neighbors. These bifurcations create a period-doubling or even a period-quadrupling surface topography under progressive compressions. Li *et al.* [115] numerically reproduced these interesting phenomena in volumetric growth and surface wrinkling of a mucosa and submucosa by using a pseudo dynamic solution method. Through numerical simulations, Cao and Hutchinson [39] uncovered advanced post-bifurcation modes including period-doubling, folding and a newly identified mountain ridge mode, in the post-buckling of a bilayer system wherein an unstretched film is bonded to a prestretched compliant neo-Hookean substrate with buckling arising as the stretch in the substrate is relaxed. Then, Zang *et al.* explored this localized mountain ridge mode in greater depth by finite element simulation and an analytical film/substrate model. Meanwhile, Cao and Hutchinson [38] provided another further insight into the connection between wrinkling and an alternative surface mode, the finite amplitude crease or sulcus. Additionally, hierarchical folding of an elastic membrane on a viscoelastic substrate can be observed under a continuous biaxial compressive stress: the folds delineate individual domains and each domain subdivides into smaller ones over multiple generations [100]. By experimentally modifying the boundary conditions and geometry, Kim *et al.* [100] demonstrated control over the final network morphology.

1.1.2 Challenges and discussion

Although considerable progresses have been made over the last decade on the modeling of morphological wrinkling in film/substrate systems, there remain lots of significant and interesting problems that deserve further investigations. Advances in theoretical and numerical modeling in this field are impeded by a number of mechanical, mathematical and numerical complexities. For instance, the surface instability of stiff layers on soft materials usually involves strong geometrical nonlinearities, large rotations, large displacements, large deformations, loading path dependence, multiple symmetry-breakings, nonlinear constitutive relations, localizations, and other complexities, which makes the theoretical and numerical analyses quite difficult. The morphological post-buckling evolution and mode shape transition beyond the critical load are incredibly complicated, especially in 3D cases, and the conventional numerical methods of post-buckling have difficulties in predicting and detecting all the bifurcations and the associated wrinkling modes on their complex response curves. Reliable and robust path-following techniques are in strong demand for post-buckling analyses of film/substrate system, especially for predicting and tracing surface mode transitions, while it was rarely explored in the literature. Moreover, in conventional finite element analysis, the post-buckling simulation may suffer from the

convergence issue if the film is much stiffer than the substrate.

In most of previous works, the 2D or 3D spatial problem is often discretized by spectral method or FFT algorithm, which is fairly computationally inexpensive but prescribes periodic boundary conditions and simple geometries. Furthermore, within the spectral or FFT framework, it is quite difficult to capture localized behavior that often occurs in soft matters in complex geometries and boundary conditions. It has been early recognized by Chen and Hutchinson [43] that such systems can also be studied by using finite element methods, which is more computationally expensive but more flexible to describe complex geometries and general boundary conditions, and allows using commercial computer codes. However, only few following contributed works can be found in literatures and 3D finite element simulations of film/substrate buckling were studied only in few papers [35]. Besides, the post-buckling evolution and mode transition of surface wrinkles in 3D film/substrate systems are merely studied in the case of periodic cells [35]. In particular, Cai *et al.* [35] employed an analytical upper-bound method through a 3D model considering a nonlinear Föppl-von Kármán plate bonded to a linear elastic foundation. Through performing 3D finite element simulations on a specific unit cell with periodic boundary conditions, a new equilateral triangular mode was identified and the mode transition from a triangular mode to an asymmetric three lobed mode under increasing overstress was analyzed.

Still, there is a shortage of study concerning the effect of boundary conditions on instability patterns, which is important in practice. Localizations are often caused by stress concentration due to the real boundary and loading conditions or by symmetry-breakings, and finite element method is a good way to capture the localized behavior such as folding or ridging, while the spectral or FFT technique has difficulties to achieve it.

Overall, pattern formation and evolution deserve further numerical investigations, especially through finite element method that can provide the overall view and insight into the formation and evolution of wrinkle patterns in any condition. Can one obtain the variety of wrinkling patterns reported in the literature by using classical finite element models? Can one predict and trace the whole evolution path of buckling and post-buckling of this system? Can one capture the exact post-buckling modes on strong nonlinear response curves? Under what kind of loading and boundary conditions can each type of patterns be observed at what value of bifurcation loads? What are the effects of boundary conditions and material properties on pattern formation and evolution? What are the critical parameters influencing their wavelengths and amplitudes?

These questions will be addressed in this thesis, from 2D to 3D cases, from analytical to numerical methods, from classical to multi-scale perspectives. We will start from developing 2D and 3D classical finite element film/substrate models that consider nonlinear

geometry for the film and linear elasticity for the substrate, as often employed in the literature [43, 89, 9, 10, 11], by taking into account the boundary effects and localizations, by following the post-buckling evolution path, by predicting the bifurcation points, then move to the multi-scale standpoint. The introduction on main advanced numerical methods that we need to solve the problems and to develop the subjects will be briefed in the following sections, which includes firstly an advanced nonlinear resolution perturbation technique, namely Asymptotic Numerical Method (ANM) as a path-following approach to predict bifurcations, and secondly a recent Fourier series based multi-scale modeling technique for cellular instability pattern formation, and then lastly the well-known Arlequin method for multiple models/domains coupling between different scales or levels.

1.2 Asymptotic Numerical Method for nonlinear resolution

As mentioned in the last section, post-buckling evolution of film/substrate systems beyond the critical load are usually complicated, while the conventional numerical resolution approaches have difficulties in getting a reliable convergent solution and predicting all the bifurcations as well as the associated instability patterns on their evolution paths. These challenges pose a need for developing an effective nonlinear resolution technique that can follow the post-buckling evolution path on film/substrate instability problem. In this thesis, Asymptotic Numerical Method (ANM) [52, 46, 45, 47] will be incorporated with 2D and 3D models of film/substrate systems to resolve extremely strong geometrical nonlinearities. It offers considerable advantages in terms of efficiency and reliability to get a robust path-following technique compared with classic iterative algorithms. For some cases involving multiple bifurcations, probably, it would be rather difficult to achieve a convergent solution on very strong nonlinear response curves by using conventional numerical methods.

The solution to many physical problems can be achieved through the resolution of nonlinear problems depending on a real parameter λ. The corresponding nonlinear system of equations can be written as

$$\mathbf{R}(\mathbf{U}, \lambda) = 0, \tag{1.2}$$

where $\mathbf{U} \in \mathbb{R}^n$ is the unknown vector and $\mathbf{R} \in \mathbb{R}^n$ is a vector of "n" equations that are supposed to be sufficiently smooth with respect to $\mathbf{U}$ and λ.

The main idea of the ANM is to compute a solution path $(\mathbf{U}, \lambda)$ of the nonlinear system (1.2) using a step-by-step method, with each step corresponding to a truncated Taylor series. The standing point $(\mathbf{U}^{j+1}, \lambda^{j+1})$ of the step $(j+1)$ is determined using the

last point solution $(\mathbf{U}^j, \lambda^j)$ of the previous step j (see Fig. 1.5).

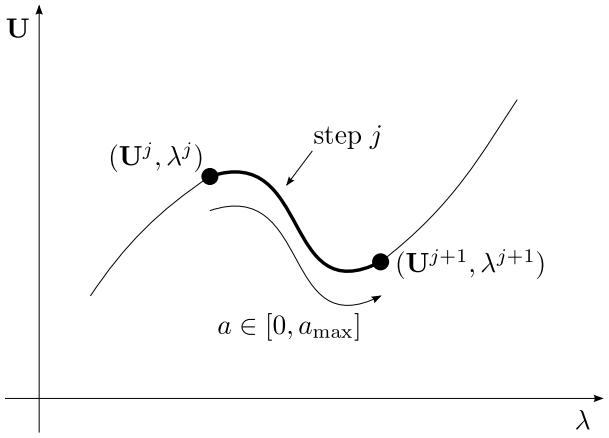

Figure 1.5: Descriptive scheme of the ANM.

The ANM has been proven to be an efficient path-following technique to deal with various nonlinear problems both in solid and fluid mechanics [162, 34, 4, 121, 125, 126, 106, 112, 49]. The idea of the ANM application is to associate a perturbation technique with an appropriate numerical resolution scheme, such as finite element method. This allows transforming a given nonlinear problem into a set of linear problems to be solved successively, leading to a numerical representation of the solution in the form of power series truncated at relatively high orders. Once the series are fully computed, an accurate approximation of the solution path is provided inside a determined radius of convergence. Unlike classical incremental-iterative algorithm, this method does not require iterative corrections thanks to the high order predictor [104, 5]. For efficiency concerns, all governing equations need to be set into quadratic form before applying the series expansion. Details of these procedures can be found in [52, 46, 45, 47].

1.2.1 Perturbation technique

Starting from a known point solution $(\mathbf{U}^j, \lambda^j)$, the solution path is represented by truncated power series using a path parameter a:

$$\begin{cases} \mathbf{U}(a) = \mathbf{U}^j + \sum_{p=1}^{\infty} a^p \mathbf{U}_p = \mathbf{U}^j + a\mathbf{U}_1 + a^2\mathbf{U}_2 + \dots \\ \lambda(a) = \lambda^j + \sum_{p=1}^{\infty} a^p \lambda_p = \lambda^j + a\lambda_1 + a^2\lambda_2 + \dots \end{cases} \tag{1.3}$$

This solution path is a solution of Eq. (1.2), which can be written as

$$\begin{aligned} 0 =& \mathbf{R}(\mathbf{U}^j + a\mathbf{U}_1 + a^2\mathbf{U}_2 + \ldots, \lambda^j + a\lambda_1 + a^2\lambda_2 + \ldots) \\ =& \mathbf{R}(\mathbf{U}^j, \lambda^j) + \frac{\partial \mathbf{R}}{\partial \mathbf{U}}\rfloor_j(a\mathbf{U}_1 + a^2\mathbf{U}_2 + \ldots) + \frac{\partial \mathbf{R}}{\partial \lambda}\rfloor_j(a\lambda_1 + a^2\lambda_2 + \ldots) \\ &+ \frac{1}{2}\frac{\partial^2 \mathbf{R}}{\partial \mathbf{U}^2}\rfloor_j(a\mathbf{U}_1 + a^2\mathbf{U}_2 + \ldots)(a\mathbf{U}_1 + a^2\mathbf{U}_2 + \ldots) + \ldots \end{aligned} \tag{1.4}$$

Considering the fact that $\mathbf{R}(\mathbf{U}^j, \lambda^j) = 0$, and after rearranging the terms as increasing power of a, the above equation becomes

$$\begin{aligned} 0 =& a\left\{\frac{\partial \mathbf{R}}{\partial \mathbf{U}}\rfloor_j \mathbf{U}_1 + \frac{\partial \mathbf{R}}{\partial \lambda}\rfloor_j \lambda_1\right\} \\ &+ a^2\left\{\frac{\partial \mathbf{R}}{\partial \mathbf{U}}\rfloor_j \mathbf{U}_2 + \frac{\partial \mathbf{R}}{\partial \lambda}\rfloor_j \lambda_2 + \frac{1}{2}\frac{\partial^2 \mathbf{R}}{\partial \mathbf{U}^2}\rfloor_j \mathbf{U}_1\mathbf{U}_1 + \frac{1}{2}\frac{\partial^2 \mathbf{R}}{\partial \lambda^2}\rfloor_j \lambda_1^2 + \frac{\partial^2 \mathbf{R}}{\partial \mathbf{U}\partial \lambda}\rfloor_j \lambda_1 U_1\right\} \\ &+ a^3\left\{\frac{\partial \mathbf{R}}{\partial \mathbf{U}}\rfloor_j \mathbf{U}_3 + \frac{\partial \mathbf{R}}{\partial \lambda}\rfloor_j \lambda_3 + \text{terms depending on } \mathbf{U}_1, \mathbf{U}_2, \lambda_1, \lambda_2\right\} \\ &\vdots \\ &+ a^p\left\{\frac{\partial \mathbf{R}}{\partial \mathbf{U}}\rfloor_j \mathbf{U}_p + \frac{\partial \mathbf{R}}{\partial \lambda}\rfloor_j \lambda_p + \underbrace{\text{terms depending on } \mathbf{U}_1 \ldots \mathbf{U}_{p-1}, \lambda_1 \ldots \lambda_{p-1}}_{-\mathbf{F}_p^{nl}}\right\} \\ &\vdots \end{aligned} \tag{1.5}$$

Or in a condensed form:

$$\mathbf{R}(\mathbf{U}(a), \lambda(a)) = a\mathbf{R}_1 + a^2\mathbf{R}_2 + a^3\mathbf{R}_3 + \ldots = 0. \tag{1.6}$$

Eq. (1.6) should be verified for each value of a. Therefore, the resolution of the nonlinear system (1.2) leads to the resolution of a recurrent system of linear equations in the following form:

$$\mathbf{R}_p = 0 \quad \textit{for} \quad p \geqslant 1. \tag{1.7}$$

At each order p, the vector of equations $\mathbf{R}_p = 0$ is a linear system with respect to $\mathbf{U}_p$ and λ_p:

$$\frac{\partial \mathbf{R}}{\partial \mathbf{U}}\rfloor_j \mathbf{U}_p + \frac{\partial \mathbf{R}}{\partial \lambda}\rfloor_j \lambda_p = \mathbf{F}_p^{nl}, \tag{1.8}$$

where the right-hand sides member $\mathbf{F}_p^{nl}$ only depends on the terms of previous orders.

1.2.2 Path parameter

Eq. (1.8) represents a system of n linear equations and $(n+1)$ unknowns. Therefore, a complementary condition is needed as also required in predictor−corrector methods. This complementary condition can be found by defining the path parameter a using the quasi-arc-length parameter (by projection of the increment on the tangent direction $(\mathbf{U}_1, \lambda_1)$) as follows:

$$a = (\mathbf{U} - \mathbf{U}^j)\mathbf{U}_1 + (\lambda - \lambda^j)\lambda_1. \tag{1.9}$$

After substituting Eq. (1.3) into Eq. (1.9), one can obtain the supplementary condition at each order:

$$\begin{cases} \|\mathbf{U}_1\|^2 + \lambda_1^2 = 1, \\ \mathbf{U}_p\mathbf{U}_1 + \lambda_p\lambda_1 = 0. \end{cases} \tag{1.10}$$

The calculation of the step j is achieved by the calculation of N_{order} right-hand sides $\mathbf{F}_p^{nl}$ and the resolution of N_{order} linear problems in Eqs. (1.8) and (1.10). In contrast to the other predictor−corrector methods, only one matrix $\frac{\partial \mathbf{R}}{\partial \mathbf{U}}\rfloor_j$ needs to be calculated and inversed, which can save an important amount of calculation time.

1.2.3 Continuation approach

To achieve an efficient algorithm, the analysis of validity range and the definition of a new starting point should be adaptive, *i.e.* the value of path parameter a has to be automatically determined by satisfying a given accuracy tolerance. A simple way to define the value of a_{max} follows the remark: polynomial solutions are very similar inside the radius of convergence of the series, but they tend to rapidly separate when this radius is reached. Thus, a simple criterion is to require that the difference of displacements between two successive orders should be smaller than a given precision parameter δ:

$$\text{Validity range: } a_{max} = \left(\delta \frac{\|\mathbf{u}_1\|}{\|\mathbf{u}_n\|}\right)^{1/(n-1)}, \tag{1.11}$$

where the notation $\|\cdot\|$ stands for the Euclidean norm. The method for determining a_{max} consists in imposing an accuracy parameter δ, and that the relative difference between solutions of two successive orders be small in comparison with δ [45]. Note that a_{max} is computed in *a posteriori* manner based on the available series coefficients. So the step length determination in the ANM framework can be considered as fully adaptive and completely automatic as opposed to classical iterative algorithms.

When there is a bifurcation point on the solution path, the radius of convergence is defined by the distance to the bifurcation. Thus, the step length becomes smaller and

smaller, which looks as if the continuation process "knocks" against the bifurcation [13]. This accumulation of small steps is a very good indicator of the presence of a bifurcation point on the path. All the bifurcations can be easily identified in this way by the user without any special tool.

1.2.4 Bifurcation indicator

As mentioned in Section 1.1.1, complex systems such as stiff thin layers bound to soft materials often involves strong geometrical nonlinearities and multiple bifurcations, which makes the numerical resolution quite difficult. The detection of bifurcation points is really a challenge. In literatures, test functions are widely introduced to compute critical points. They are scalar functions vanishing at a singular point. Once a critical point is detected between two states, its accurate position can be determined through using a bisection or secant iteration scheme. Two classes of methods, *i.e.* direct methods and indirect methods, can be distinguished. In direct methods, the existence condition of critical points is embedded in the system of equations to be solved [152, 156, 155] and the solution of system is exactly the critical point. The indirect methods consist in computing a solution branch and evaluating test functions. The most popular test functions are the determinant or the smallest eigenvalue of tangent stiffness matrix. To distinguish bifurcation point from limit point, the current stiffness parameter is used [150]. Once the bifurcation points are obtained, the associated eigenmodes can be captured. The resulting nonlinear problems are usually solved by the Newton−Raphson method with a choice of piloting strategy [14].

Despite a lot of progresses have been made using the Newton−Raphson method, an efficient and reliable algorithm is quite difficult to be established. Indeed, it would cost considerable computing time in the bisection sequence and corrector iteration because of very small step lengths close to the bifurcation. In the framework of the ANM, a bifurcation indicator has been proposed to detect bifurcation points [27, 148, 96, 28]. It is a scalar function obtained through introducing a fictitious perturbation force in the problem, which becomes zero exactly at the bifurcation point. Indeed, this indicator measures the intensity of the system response to perturbation forces, which can be computed explicitly along the equilibrium branch through perturbation technique. Next, the roots of this function characterize singular points easily and exactly, since the function is known in a closed form. By evaluating it through an equilibrium branch, all the critical points existing on this branch and the associated bifurcation modes can be determined.

In this thesis, these generic bifurcation schemes will be explicitly incorporated with 2D and 3D models of film/substrate systems in order to carry out multiple-bifurcation analyses that involve capturing exact bifurcation points and the corresponding instability

modes.

1.3 Multi-scale modeling for instability pattern formation

Instability pattern formation is a very common phenomenon in nature [120] and in scientific fields [50, 7, 80]. In these cases, the spatial shape of system responses looks like a slowly modulated oscillation. Direct calculation of such cellular instabilities in a big sample often requires numerous degrees of freedom, such as membrane wrinkling [134], Rayleigh−Bénard convection in large boxes [124, 139, 121], buckling of long structures [51, 114, 3], microbuckling of carbon nanotubes [135, 77] or fiber microbuckling of composites [103, 149, 63], surface morphological instabilities of stiff thin films attached on compliant substrates [29, 43, 9], flatness defects in sheets induced by industrial processes [66, 95, 2]. Therefore, from the computational point of view, it is better to apply reduced-order models not only to satisfy the desired accuracy but also to dramatically cut down the computational time and cost.

Classically, such cellular instabilities can be modeled by bifurcation analysis according to the famous Ginzburg−Landau theory [153, 94]. The Ginzburg−Landau equation follows an asymptotic double scale analysis. At the local level, one accounts for the periodic nature of buckles, while the slow variations of envelopes are described at the macroscopic scale. Nevertheless, the macroscopic evolutions governed by the Ginzburg−Landau equation have some drawbacks. First, this bifurcation equation is valid only close to the critical state. Second, it cannot account for the coupling between global nonlinear behavior and appearance of patterns, for instance, for structures undergoing both local and global buckling. Third, within the Ginzburg−Landau double scale approach, it is not easy to deduce consistent boundary conditions.

A new approach based on the concept of Fourier series with slowly varying coefficients has been presented recently, which is developed to study the instabilities with nearly periodic patterns [54, 55, 56]. It has been consecutively applied in buckling of a long beam lying on a nonlinear elastic foundation [122], global and local instability interaction of sandwich structures [119], and membrane wrinkling [57, 58]. This multi-scale approach is based on the Ginzburg−Landau theory [153, 94]. In the proposed theory, the envelope equation is derived from an asymptotic double scale analysis and the nearly periodic fields (reduced model) are represented by Fourier series with slowly varying coefficients. This mathematical representation yields macroscopic models in the form of generalized continua. In this technique, the macroscopic field is defined by Fourier coefficients of

the microscopic field. It has been established that the models obtained in this way are consistent with the Ginzburg−Landau technique, but they can remain valid away from the bifurcation [56]. Besides, the coupling between global and local buckling can be taken into account in a computationally efficient manner [119]. Moreover, this approach could be very useful to analyze instability problems like Rayleigh−Bénard convection whose discretization requires a huge number of degrees of freedom.

As in paper [56], the multi-scale approach, based on the concept of Fourier series with slowly varying coefficients, will be adopted in this thesis. Let us consider a physical phenomenon described by the field $U(x)(x \in \mathbb{R})$. The instability wave number q is supposed to be known. All the unknowns of model $U = \{u(x), v(x), n(x)...\}$ are described as Fourier series, whose coefficients vary more slowly than the harmonics:

$$U(x) = \sum_{j=-\infty}^{+\infty} U_j(x) e^{jiqx}, \tag{1.12}$$

where the Fourier coefficient $U_j(x)$ denotes the envelope for the j^{th} order harmonic and $U_{-j}(x)$ denotes its conjugate value. The macroscopic unknown fields $U_j(x)$ slowly vary

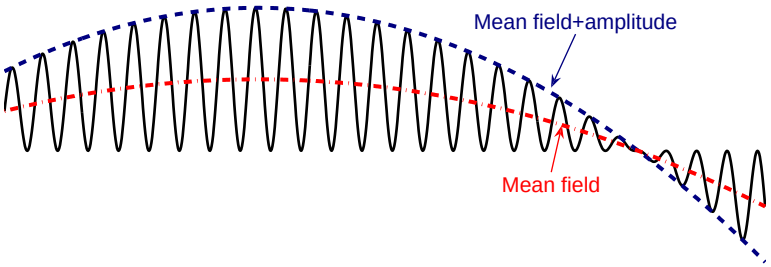

Figure 1.6: At least two macroscopic fields (the mean field and the amplitude of the fluctuation) are necessary to describe a nearly periodic response.

over a period $\left[x, x + \frac{2\pi}{q}\right]$ of the oscillation. It is worth mentioning that at least two functions, $U_0(x)$ and $U_1(x)$, are necessary to describe the nearly periodic patterns as depicted in Fig. 1.6. The zero order variable $U_0(x)$ is identified as the mean value and $U_1(x)$ represents the envelope or amplitude of the spatial oscillations. Notice that $U_0(x)$ is real valued and $U_1(x)$ can be expressed as $U_1(x) = r(x)e^{i\varphi(x)}$. The latter mathematical expression represents the first harmonic where $r(x)$ is the amplitude modulation and $\varphi(x)$ is the phase modulation. The main idea of macroscopic modelling is to deduce differential equations satisfied by the amplitude $U_j(x)$.

In the present thesis, this Fourier-related multi-scale modeling methodology will be applied in buckling of an elastic beam subjected to a nonlinear Winkler foundation firstly. Then, a generalized framework for macroscopic modeling of film/substrate will be pro-

posed. Lastly, it goes to specific 2D and 3D cases with simplifications and assumptions to save computational cost when studying nearly periodic morphological instabilities in film/substrate systems.

1.4 Arlequin method for model coupling

In this thesis, the Arlequin method [20, 24] will be used to analyze the influence of boundary conditions on multi-scale modeling of instability pattern formation. More specifically, the coarse model, obtained from a suitable Fourier-related technique [56] presented in the last section, is inaccurate in the boundary region. Hence, near the boundary, the full model is employed, which is then coupled to the coarse model in the remainder of the domain within the Arlequin framework. This multiple-domain coupling strategy offers a flexible way to design multi-scale models so as to balance the desired accuracy and the computational cost.

Despite of considerable advances in computational techniques and computing power, direct simulation of those cellular instability problems is still not a viable option. For instance, the discretization of Rayleigh−Bénard convection problems in large boxes [124, 139] requires a huge number of degrees of freedom [121], which is a challenge for direct computations. Therefore, there is a need for reliable and efficient techniques in a consistent manner that can take into account the most important scales involved in the goal of the simulation, while allowing ones to flexibly choose the desired level of accuracy and detail of description.

Generally, direct finite element modeling of structures involving local defects such as cracks, holes and inclusions, is very cumbersome when the local refinement needs to be considered. To overcome these difficulties, important innovations and efficient numerical methods have been developed during several decades to improve the flexibility of finite element method. Let us list a few in particular the meshless method [18], the sequential adaptation method (*i.e.* h-adaptation, p-adaptation and hp-adaptation), the multigrid (MG) method, the partition of unity finite element method (PUFEM) [12], the generalized finite element method (GFEM) [145], the extended finite element method (XFEM) [17, 123].

All these approaches are essentially monomodel and may either lack flexibility or relevance to address the above issues. Later, hierarchical global-local strategies, including s-version method by Fish [67, 69, 68] and Arlequin method by Ben Dhia *et al.* [20, 24, 21, 22], allow the superposition of different mechanical models and different meshes. The s-version method is a multilevel solution scheme where each level is discretized using finite element mesh of arbitrary element size and polynomial order. It superimposes additional

local refined meshes to an existing global one, thus allowing different modeling in the superimposed meshes. Like the s-method, the Arlequin method aims at creating a multi-model framework. Opposed to s-method, the models are not added but overlapped and glued to each others in the Arlequin framework. In addition, since not only displacement fields but also complete mechanical states (*e.g.* stress and strain) are potentially allowed to concurrently exist in the superposition zone, the Arlequin method has no redundancy problem. Besides, the iteration of the superposition process (by taking care of gluing zones) can potentially lead to relevant multi-scale models.

Over the last decade, the Arlequin method or the bridging domain method [157] have been successfully applied to couple heterogeneous models in various cases. One can couple classical continuum and shell models [24], particle and continuum models [157, 15, 130, 16, 41, 131], heterogeneous meshes [24, 81] or more generally heterogeneous discretizations [23, 25]. By superposing and gluing models, the Arlequin method offers an extended modeling framework for the design of various mechanical models for engineering materials and structures in a rather flexible way.

In this thesis, within the Arlequin framework, discussion on the transition between a fine and a coarse model will be provided, which is almost a generic but hard topic in applying bridging techniques to reduced-order models or multi-scale models. Especially, a new bridging technique based on a nonlocal reduction operator defined by Fourier series will be presented and highlighted.

1.4.1 Energy distribution

In the Arlequin framework, the domain of the whole mechanical system is partitioned into two overlapping sub-zones Ω_1 and Ω_2. Let S_g denote the gluing zone supposed to be a non-zero measured polyhedral subset of $S = \Omega_1 \cap \Omega_2$.

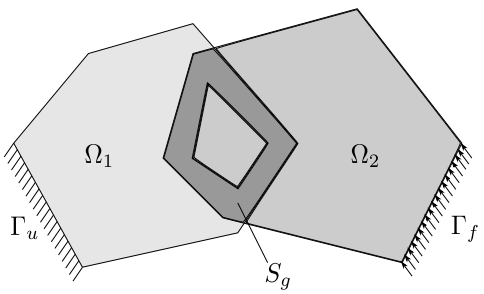

Figure 1.7: Arlequin method in a general mechanical problem.

The potential energy contribution of the whole system and external load can be re-

spectively expressed as

$$\mathcal{P}_i^{int}(\boldsymbol{u}_i) = \frac{1}{2}\int_{\Omega_i} \alpha_i \boldsymbol{\sigma}(\boldsymbol{u}_i) : \boldsymbol{\varepsilon}(\boldsymbol{u}_i) \mathrm{d}\Omega, \tag{1.13}$$

$$\mathcal{P}_i^{ext}(\boldsymbol{u}_i) = \int_{\Omega_i} \beta_i \boldsymbol{f} \cdot \boldsymbol{u}_i \mathrm{d}\Omega. \tag{1.14}$$

In order to have consistent modeling and not to count the energy in the overlapping domain twice, the energy associated to each domain is balanced by weight functions which are represented by α_i for the internal work and β_i for the external work. These weight functions are assumed to be positive piecewise continuous in Ω_i and satisfy the following equations:

$$\begin{cases} \alpha_1 = \beta_1 = 1, & \text{in } \Omega_1 \backslash S, \\ \alpha_2 = \beta_2 = 1, & \text{in } \Omega_2 \backslash S, \\ \alpha_1 + \alpha_2 = \beta_1 + \beta_2 = 1, & \text{in } S. \end{cases} \tag{1.15}$$

One can choose constant, linear, cubic, or higher-order polynomial functions for energy distribution (see Fig. 1.8). More details on selection of these functions can be found in [24, 15, 41, 131].

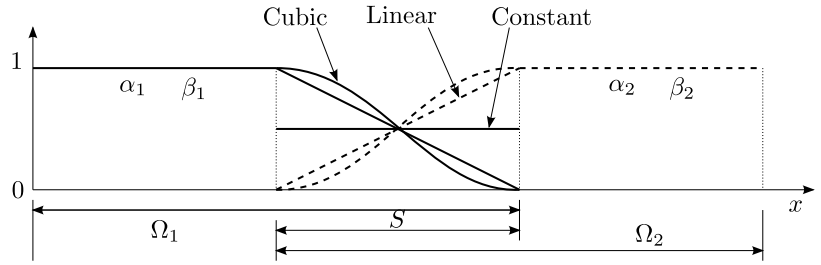

Figure 1.8: Different weight functions for energy distribution.

1.4.2 Coupling choices

The Arlequin method aims at connecting two spatial approximations of an unknown field, generally a fine approximation U_f and a coarse approximation U_r. The idea is to require that these two approximations are neighbor in a weak and discrete sense and to introduce Lagrange multipliers in the corresponding differential problems.

A major concern in the Arlequin framework is to define an appropriate coupling operator. At the continuous level, a bilinear form must be chosen, which can be L^2-type, H^1-type or energy type [24, 22, 15]. The H^1-type coupling operator $\mathscr{C}$ can be defined as

$$\mathscr{C}(\boldsymbol{\lambda}, \boldsymbol{u}) = \int_{S_g} \left(\boldsymbol{\lambda} \cdot \boldsymbol{u} + \ell^2 \boldsymbol{\varepsilon}(\boldsymbol{\lambda}) : \boldsymbol{\varepsilon}(\boldsymbol{u})\right) \mathrm{d}\Omega. \tag{1.16}$$

When $\ell = 0$, it becomes an L^2-type coupling operator. The choice of the length ℓ and the comparisons between H^1 and L^2 couplings have been well discussed in the literature [24, 75, 15, 81].

The first and important application of the Arlequin method is the coupling between two different meshes discretizing the same continuous problem: in this case, the mediator problem should be discretized by a coarse mesh to avoid locking phenomena [24] and spurious stress peaks [81]. In a recent paper [41], the origin of these so-called "ghost forces" was carefully analyzed, and some corrections were proposed with an appropriate choice of weights and especially by introducing interaction forces between coarse and fine model. Now we present a very representative example [24] to explicitly show the differences of displacement field caused by choices of mediator space. This example has been previously studied by Ben Dhia and Rateau [24] to illustrate the relationship between the coupling operator and the deterioration of the condition number. Let us consider a 1D small strain linear elastic mechanical problem, which consists in evaluating the vertical displacement field, u, in a vertical column with uniform cross section, clamped at both ends and loaded by its own weight. For convenience, the Young's modulus E, the section S, the density ρ and the gravity factor g are chosen to satisfy $\rho g = ES$. Continuous 1D linear elements are conducted to approximate displacement fields as well as Lagrange multiplier fields. Different refinements of the superimposed models are considered. Precisely, we define the coarse domain as $\Omega_c = [0, 2]$ and the fine domain as $\Omega_f = [1, 3]$. The weight functions α_f and β_f are associated to the fine model. The analytical solution of displacement field is denoted as reference. Figs. 1.9 and 1.10 illustrate the influence of mediator space used to discretize the Lagrange multiplier field on the mechanical states solution. It can be seen that depending on whether the gluing forces space is chosen based on the glue zone of the fine or the coarse finite element model, the fine mechanical state is either tightly locked to the coarse one (see Fig. 1.9), or linked to an average value in a weak sense (see Fig. 1.10).

However, the two connected problems are not always in the same space, as for example when dealing with particle and continuous problems. In this case, a prolongation operator has to be introduced to convert the discrete displacement into a continuous one, and then a connection between continuous fields is performed [15]: this is consistent because the continuous model can be seen as the coarsest one. A similar approach has been applied in the coupling between shell and 3D models. A prolongation operator has been introduced (*i.e.* from the coarse to the fine level) and the integration is done in the 3D domain but the discretization of the Lagrange multiplier corresponds to a projection on the coarsest problem: thus, in this sense, this coupling of shell/3D is also achieved at the coarse level. In the same spirit, for the coupling between a fine model and a macroscopic envelope model

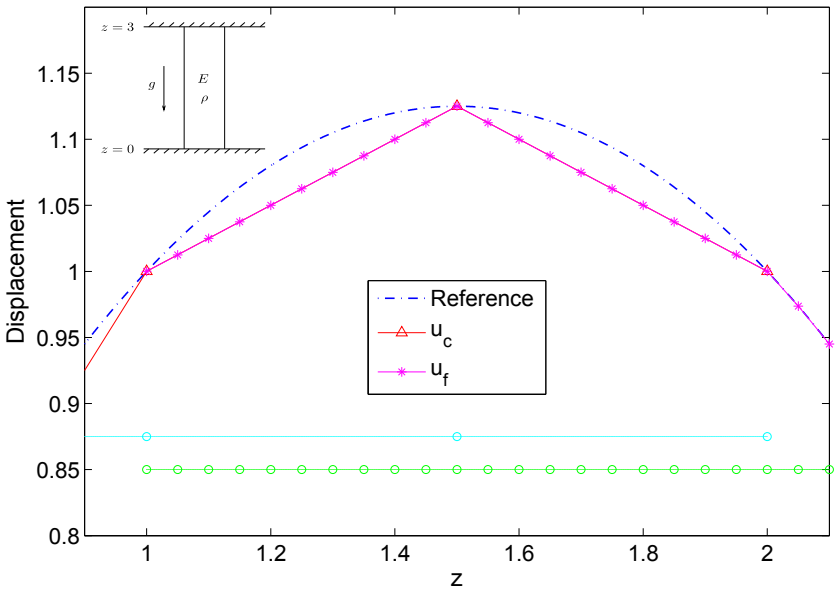

Figure 1.9: Mediator space is based on the fine mesh. Arlequin parameters: $\alpha_f = 0.99, \beta_f = 0.5$.

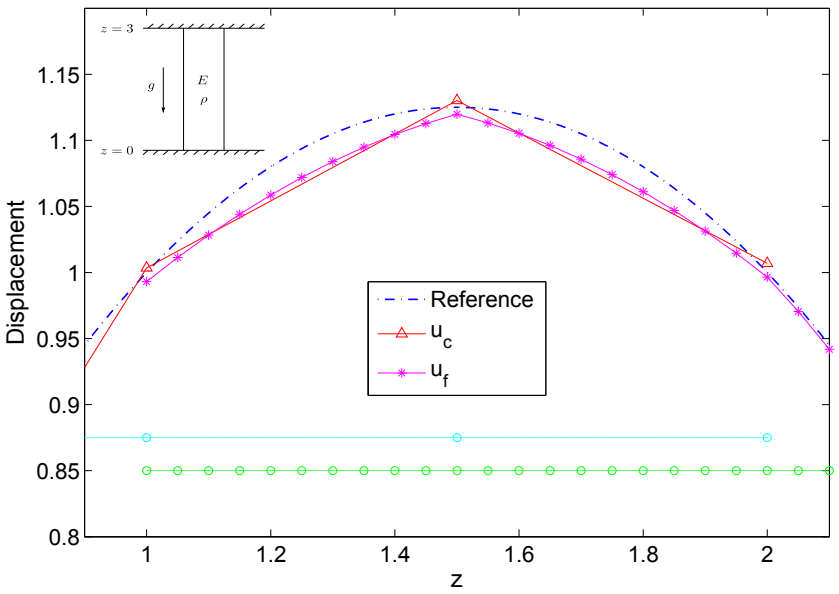

Figure 1.10: Mediator space is based on the coarse mesh. Arlequin parameters: $\alpha_f = 0.99, \beta_f = 0.5$.

that is discussed in this thesis, the connection should also be done at the coarse level, *i.e.* between Fourier coefficients. On the contrary, a prolongation operator from the coarse to the fine model had been introduced in the previous paper [84] and the connection had been done at this level. Therefore, one can wonder if the imperfect connection observed in [84] could be improved by introducing a coupling at the relevant level. This thesis tries to answer this question by studying again the Swift−Hohenberg equation [147] that is a simple and representative example of quasi-periodic instabilities. Very probably, the same ideas can be applied to 2D macroscopic membrane models that were recently introduced in [57, 58]. Note that the presented new technique can be considered as a nonlocal coupling since it connects Fourier coefficients involving integrals on a period. A similar nonlocal coupling has been introduced in [131] in the case of an atomic-to-continuum coupling, where the atomic model is reduced by averaging over a representative volume.

1.5 Chapter conclusion

This chapter aims at positioning the context and focus of the present thesis with consideration of research trends in fields of instability pattern formation modeling of film/substrate systems. The challenges in modeling and post-buckling resolution, especially from numerical standpoint, were discussed as well. We presented the main technical ingredients that we need to solve the problems and to develop the subjects in the following chapters. This includes firstly an advanced numerical nonlinear resolution technique, namely Asymptotic Numerical Method (ANM) that is a robust path-following technique; then secondly a Fourier-related multi-scale modeling technique for cellular instability pattern formation; and thirdly the well-known Arlequin method for multiple models/domains coupling between different scales or different meshes. A simple benchmark case is presented to demonstrate the effect of different choices of mediator space when using the Arlequin method. In the following chapters, we will present how to model surface wrinkling of film/substrate system, from 2D to 3D cases, from classical to multi-scale perspectives, and how the ANM framework is adapted and incorporated in various finite element models for nonlinear problem resolution and bifurcation analysis, and how to extend and improve the Arlequin framework for instability pattern formation from a multi-scale standpoint.

Chapter 2

Multiple bifurcations in wrinkling analysis of film/substrate systems

Contents

2.1 Introduction

Wrinkles of a stiff thin layer attached on a soft substrate have been widely observed in nature and these phenomena have raised considerable interests over the last decade. The underlying mechanism of wrinkling is generally understood as a stress-driven instability, analogous to Euler buckling of an elastic column under compressive stress. The pioneering work of Bowden *et al.* [29] implied that surface wrinkling of film/substrate system can widely apply ranging from micro/nano-fabricating surfaces with ordered patterns with unique wetting, buckled single crystal silicon ribbons, optical property of electronic eye camera, mechanical property measurement of surface characteristics of the materials, to the design of flexible semiconductor devices and stretchable electronics. This leads to several theoretical and experimental works in terms of stability study devoted to linear perturbation analysis and nonlinear buckling analysis [87, 43, 88, 89, 85, 120, 151, 143, 9, 10, 11, 93]. In particular, there are many analytical solutions of models linearized from homogeneous finite deformation, in the case of half-spaces [76, 62, 141] as well as film/substrate systems [144, 36, 37]. It has been also recognized that wrinkling can be the precursor of delamination and failure of the film [141]. However, most previous studies have been mainly constrained to determine the critical conditions of instability and corresponding wrinkling patterns near the instability threshold. The post-buckling evolution and mode transition of surface wrinkles are only recently being pursued [31, 39, 38, 163, 146]. To our best knowledge, the effect of boundary conditions on wrinkling has not yet been investigated.

This study aims at applying advanced numerical methods for bifurcation analysis to typical models of film/substrate system and focuses on the post-bifurcation evolution involving secondary bifurcations and advanced wrinkling modes like period-doubling mode. For this purpose, a finite element (FE) model based on Asymptotic Numerical Method (ANM) [52, 46, 45, 47] is developed for the nonlinear analysis of wrinkle formation. In this model, the film undergoing moderate deflections is described by Föppl-von Kármán nonlinear elastic plate theory, while the substrate is considered to be a linear elastic solid. This idea is analogous to the modeling of sandwich structures considering each layer described by its own kinematic formulation and the displacement continuity is satisfied at each interface [114, 113, 83].

Instead of solving the resulting nonlinear equations using classical predictor−corrector algorithms such as the Newton−Raphson procedure, we adopted the ANM which appears as a significantly efficient continuation technique [61, 6] without any corrector iteration. It has been proven to be an efficient path-following technique to deal with various nonlinear problems both in solid mechanics [162, 4, 121, 8, 126, 106, 112] and in fluid mechanics

[32, 71, 97, 74]. The underlying principle of the ANM is to build up the nonlinear solution branch in the form of relatively high order truncated power series. The resulting series are then introduced into the nonlinear problem, which helps to transform it into a sequence of linear problems that can be solved numerically. In this way, one gets approximations of the solution path that are very accurate inside the radius of convergence. Moreover, by taking the advantage of the local polynomial approximations of the branch within each step, the algorithm is remarkably robust and fully automatic. Furthermore, unlike incremental-iterative methods, the arc-length step size in the ANM is fully adaptive since it is determined *a posteriori* by the algorithm. A small radius of convergence and step accumulation appear around the bifurcation and imply its presence.

Detection of bifurcation points is really a challenge. Direct computation of eigenvalues of the Jacobian matrix is possible, but it costs considerable computing time in bisection sequences. Such methods are expensive and difficult to manage, with the only advantage to be available in libraries like ARPACK [110]. A more efficient approach is to iteratively solve the nonlinear system characterizing the bifurcation points. This technique was initiated in [140] for ordinary bifurcations and in [98] for Hopf bifurcation, but the convergence of the process depends strongly on the initial guess. There is another class of methods, named "indirect methods", where one computes a "bifurcation indicator" vanishing at singular points. So the determinant of the Jacobian matrix is a bifurcation indicator that is not easy to compute for large scale problems. That is why we prefer another bifurcation indicator that is a sort of measure of the tangent stiffness, is easily implemented and applied in the ANM framework and yields the bifurcation mode. Its reliability has been assessed by many applications in solid mechanics [28, 96, 148] as well as for stationary and instationary bifurcations in fluid flows [32, 71, 74]. Alternative techniques are also available from the ANM framework like the method of Padé approximants [28] or an attractive method of series re-analysis introduced recently in [48], but we limited ourselves to the most secure and validated technique. Note that it is also possible to combine several methods to get a very reliable detection technique [32, 71, 74].

This chapter explores the occurrence and post-bifurcation evolution of aperiodic mode beyond the onset of the primary sinusoidal wrinkling mode in greater depth. The work presented in this chapter, *i.e.* multiple bifurcations in wrinkling analysis of thin films on compliant substrates, is viewed as an interesting, original and the first work that addresses the post-bifurcation response of film/substrate systems from the quantitative standpoint, which has been published in *International Journal of Non-Linear Mechanics* [160].

2.2 Mechanical model and dimensional analysis

We consider an elastic stiff film of thickness h_f bound to an elastic compliant substrate of thickness h_s that can vary by orders of magnitude in applications, whose surface can buckle under in-plane compression (see Fig. 2.1). Upon wrinkling, the film elastically buckles to relax the compressive stress and the substrate concurrently deforms to maintain perfect bonding at the interface. In the following, the elastic potential energy of the system, is considered in the framework of Hookean elasticity. The film/substrate system is considered to be two-dimensional. Let x and z be the longitudinal and the transverse coordinates. The top surface of the film is traction free. The deformation of the system is described by a deflection w along the z direction and a displacement u along the x direction.

In the literature, most of the authors model the film by Föppl-von Kármán nonlinear elastic plate theory [43, 85, 9], which implies moderate rotations and small strains. When the film wrinkles, the wavelength is much larger than the film thickness, so that Föppl-von Kármán nonlinear elastic plate theory can adequately model the thin film [105]. Moreover, the substrate is generally considered to be a linear elastic solid with 2D plane strain deformation. These assumptions make sense in the case of a large stiffness ratio E_f/E_s, E_f and E_s being Young's modulus of the film and the substrate, respectively. Typically, we will consider a ratio E_f/E_s in the range $\mathcal{O}(10^4)$. In this range, critical strains are very small and thus the linear elastic framework is relevant. Other studies consider much softer films or stiffer substrates, typically with a stiffness ratio E_f/E_s in the range $\mathcal{O}(10)$, where the critical strain is relatively large and the small strain framework is no longer appropriate. Therefore, large strain constitutive laws such as neo-Hookean hyperelasticity have to be chosen for $E_f/E_s \approx \mathcal{O}(10)$ [39, 92]. In this chapter, we limit ourselves to large stiffness ratio $E_f/E_s \approx \mathcal{O}(10^4)$ so that we can choose the most common framework:

1. The film is represented as a geometrically nonlinear beam with Föppl-von Kármán approximation.

2. The constitutive law of the substrate is 2D linear elasticity.

The same framework and especially the beam model were chosen in the most of previous mentioned papers, but obviously a careful application of 2D finite elements should be possible as for instance in [92], with the drawback of leading to very large scale problems due to the film thinness.

Such limitations are not necessary when analytically solving incremental systems and 2D/3D models can be considered for the film. Nevertheless, beam/plate models are better

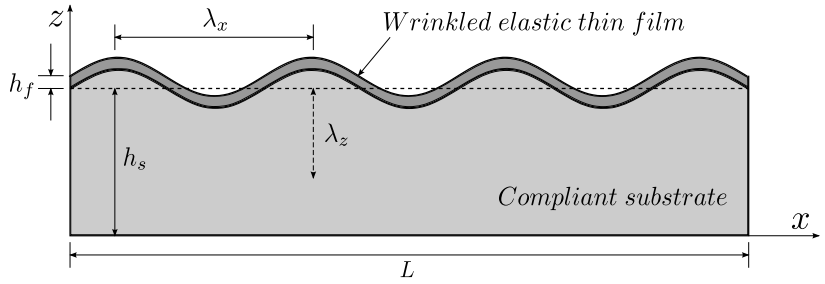

Figure 2.1: An elastic stiff film resting on a compliant substrate under in-plane compression. The wrinkle wavelength λ_x is much larger than the film thickness h_f. The ratio of the substrate thickness h_s to the wavelength, h_s/λ_x, can vary from a small fraction to a large number.

for numerical studies of very thin films. Their consistency with 3D approaches are well established for film/substrate systems, see for instance [44, 37].

Based on the above assumptions, the internal potential energy $\mathcal{P}_{int}$ of the film/substrate system on a cellular wavelength can be given by a sum of two parts:

$$\mathcal{P}_{int} = \frac{1}{2}\int_0^{\lambda_x}\left(E_f h_f \varepsilon_x^2 + \frac{E_f h_f^3 K^2}{12}\right)\mathrm{d}x + \frac{1}{2}\int_0^{\lambda_x}\int_0^{\lambda_z} {}^t\varepsilon_s \mathbf{L}_s \varepsilon_s \mathrm{d}z\mathrm{d}x, \tag{2.1}$$

in which

$$\begin{cases} \varepsilon_x = \dfrac{du_f}{dx} + \dfrac{1}{2}\left(\dfrac{dw_f}{dx}\right)^2, \\ K = \dfrac{d^2 w_f}{dx^2}, \\ {}^t\varepsilon_s = \left\{\dfrac{\partial u_s}{\partial x}, \dfrac{\partial w_s}{\partial z}, \dfrac{\partial u_s}{\partial z} + \dfrac{\partial w_s}{\partial x}\right\}, \end{cases} \tag{2.2}$$

where E_f and $\mathbf{L}_s$ are Young's modulus of the film and elastic matrix of the substrate, respectively. Let u_f and w_f be the longitudinal and transverse displacement of the film, while u_s and w_s denote the longitudinal and transverse displacement of the substrate, respectively.

The response of the film can be considered periodic or nearly periodic, but the wavelength λ_x is not given *a priori*. The surface instability does not necessarily affect the entire substrate, but only an influence zone whose depth is of the order of λ_z. In Appendix A, it is explained why the ratio $\alpha = \lambda_x/\lambda_z$ is of the order of unity. In order to carry out

dimensional analysis, firstly, we introduce some dimensionless variables as follows:

$$\begin{cases} x = \lambda_x \overline{x}, \\ z = \lambda_z \overline{z}, \\ u = \dfrac{h_f^2}{\lambda_x} \overline{u}, \\ w = h_f \overline{w}, \\ \mathbf{L}_s = E_s \overline{\mathbf{L}}_s, \end{cases} \tag{2.3}$$

where the notation $\overline{\cdot}$ stands for dimensionless variables. By introducing Eq. (2.3) into Eq. (2.2), one can obtain

$$\begin{cases} \varepsilon_x = \dfrac{h_f^2}{\lambda_x^2} \overline{\varepsilon}_x, \\ K = \dfrac{h_f}{\lambda_x^2} \overline{K}, \\ {}^t\varepsilon_s = \dfrac{h_f}{\lambda_x} \left\{ 0, \dfrac{1}{\alpha} \dfrac{\partial \overline{w}_s}{\partial \overline{z}}, \dfrac{\partial \overline{w}_s}{\partial \overline{x}} \right\} + \left(\dfrac{h_f}{\lambda_x} \right)^2 \left\{ \dfrac{\partial \overline{u}_s}{\partial \overline{x}}, 0, \dfrac{1}{\alpha} \dfrac{\partial \overline{u}_s}{\partial \overline{z}} \right\}. \end{cases} \tag{2.4}$$

Since the surface wrinkling wavelength λ_x is much larger than the film thickness h_f, the term $(h_f/\lambda_x)^2$ is much smaller than the term h_f/λ_x and it can be reasonably neglected. Then substituting Eq. (2.4) into Eq. (2.1), consequently,

$$\overline{\mathcal{P}}_{int} = \frac{E_f h_f^5}{2\lambda_x^3} \int_0^1 \left(\overline{\varepsilon}_x^2 + \frac{\overline{K}^2}{12} \right) \mathrm{d}\overline{x} + \frac{E_s h_f^2 \alpha}{2} \int_0^1 \int_0^1 {}^t\overline{\varepsilon}_s \overline{\mathbf{L}}_s \overline{\varepsilon}_s \mathrm{d}\overline{z} \mathrm{d}\overline{x}. \tag{2.5}$$

The critical wavelength can be obtained when the two coefficients $E_f h_f^5/(2\lambda_x^3)$ and $E_s h_f^2 \alpha/2$ have the same order, consequently,

$$\frac{E_f h_f^5/(2\lambda_x^3)}{E_s h_f^2 \alpha/2} = \mathcal{O}(1). \tag{2.6}$$

Then the critical wavelength λ_x^c reads

$$\lambda_x^c = \mathcal{O}\left[h_f \left(\frac{E_f}{\alpha E_s} \right)^{1/3} \right], \tag{2.7}$$

which is consistent with the analytical solution provided based on linearized stability analysis in [85]. Therefore, only the dimensionless stiffness matrix $\overline{\mathbf{L}}_s$ appears in the energy (2.5). For an isotropic substrate, the only significant parameter is Poisson's ratio ν_s and one can suspect that its influence is relatively weak. In other words, for a very large

system ($L \gg \lambda_x, h_s \gg \lambda_x$) and a given ν_s, the film/substrate system is generic and all these systems are equivalent according to the change of variables in Eq. (2.3). In more general situations, some parameters can affect the response of film/substrate system, especially the wave number (L/λ_x), the relative thickness of the substrate (h_s/λ_x), the anisotropy of the substrate ($\overline{\mathbf{L}}_s$) and the heterogeneity of the substrate. In what follows, we will discuss the effect of boundary conditions, graded material properties and anisotropy of the substrate in the case of a not too large wave number.

2.3 1D reduced model

The film/substrate system will be studied numerically within the previously described framework: a linear elastic substrate and a film modeled with Föppl-von Kármán approximation. In the literature, this system is generally discretized by Fast Fourier Transform (FFT) [85, 9, 10, 11], which disregards boundary effects. Standard finite element model would be a good candidate for this problem. For convenience, we will adapt a finite element procedure [114, 113, 83] used for sandwich beams. First, the substrate is divided into layers, which leads to a 1D multilayer model. Then this 1D model will be discretized by standard 1D elements. The advantages of this approach are to ensure a perfect continuity between the film and substrate and also to preserve basic symmetries of the continuous system as well as bifurcation points arising from these symmetries.

The film/substrate system is considered to be two-dimensional and the geometry is as shown in Fig. 2.2. Let x and z be the longitudinal and the transverse coordinates. The length of the system is denoted as L. The parameters h_f, h_s and h_t are, respectively, the thickness of the film, the substrate and the total thickness of the system. Since the analytical kinematics of substrate is unknown, a finite element methodology has to be applied to discretize the substrate into some sublayers along the z direction first, then discretize it along the x direction. Consequently, h_i denotes the thickness of each sublayer in the substrate. Since the film is bound to the substrate, the displacement must be continuous at the interface, which is a restrictive assumption to derive general governing equations.

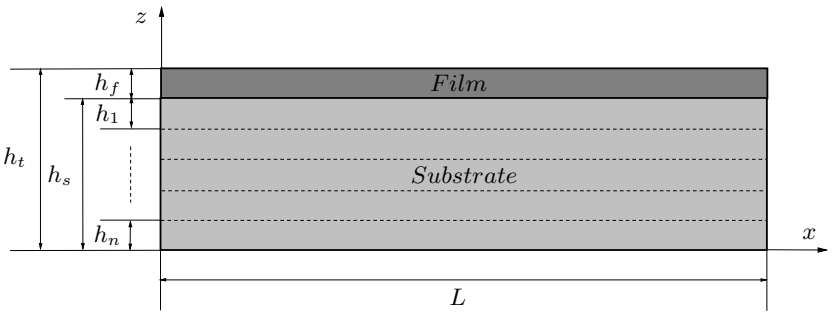

Figure 2.2: Geometry of the film/substrate system.

2.3.1 Kinematics

The kinematics of the film/substrate system by considering the first discretization along the z direction is given in Eq. (2.8)−(2.10).

$$\text{Film}\begin{cases} \mathscr{U}^f(x,z) = u^f(x) - \left(z - \dfrac{h_f}{2} - h_s\right)\dfrac{\partial \mathscr{W}^f(x,z)}{\partial x}, \\ \\ \mathscr{W}^f(x,z) = w^f(x). \end{cases} \qquad h_s \le z \le h_t \tag{2.8}$$

$$1^{st}\text{ sublayer}\begin{cases} \mathscr{U}^{s1}(x,\eta) = \dfrac{1-\eta}{2}u_0(x) + \dfrac{1+\eta}{2}u_1(x), \\ \\ \mathscr{W}^{s1}(x,\eta) = \dfrac{1-\eta}{2}w_0(x) + \dfrac{1+\eta}{2}w_1(x). \end{cases} \qquad -1 \le \eta \le 1,\ (h_s - h_1) \le z \le h_s \tag{2.9}$$

$$n^{th}\text{ sublayer}\begin{cases} \mathscr{U}^{sn}(x,\eta) = \dfrac{1-\eta}{2}u_{n-1}(x) + \dfrac{1+\eta}{2}u_n(x), \\ \\ \mathscr{W}^{sn}(x,\eta) = \dfrac{1-\eta}{2}w_{n-1}(x) + \dfrac{1+\eta}{2}w_n(x). \end{cases} \qquad -1 \le \eta \le 1,\ 0 \le z \le h_n \tag{2.10}$$

Here, the longitudinal and transverse displacement fields are represented by $\mathscr{U}$ and $\mathscr{W}$, respectively. Let u^f and w^f denote the longitudinal and transverse displacement fields of the neutral fiber of the film, while u_n and w_n are the longitudinal and transverse displacement fields at the interfaces between each sublayer of the substrate, respectively. The superscript f and sn stand for the film and the n^{th} sublayer of the substrate, respectively. The local coordinate along the z direction is described by η. Note that in above kinematic model, the displacement continuity is automatically satisfied at the interfaces

between different sublayers.

2.3.2 Finite element formulation

The expression of the internal virtual work of film/substrate system can be simplified by neglecting stresses whose energetic contribution are quite low, *i.e.* σ^f_{zz} and σ^f_{xz}. Consequently, the following constitutive and geometric equations are taken into account:

$$\begin{cases} \sigma^f_{xx} = E_f \epsilon^f_{xx}, \\ \sigma^{sn}_{xx} = (\lambda_s + 2G_s)\,\epsilon^{sn}_{xx} + \lambda_s \epsilon^{sn}_{zz}, \\ \sigma^{sn}_{zz} = (\lambda_s + 2G_s)\,\epsilon^{sn}_{zz} + \lambda_s \epsilon^{sn}_{xx}, \\ \sigma^{sn}_{xz} = G_s \gamma^{sn}_{xz}, \end{cases} \tag{2.11}$$

$$\begin{cases} \epsilon^f_{xx} = \mathscr{U}^f_{,x} + \dfrac{1}{2}(\mathscr{W}^f_{,x})^2, \\ \epsilon^{sn}_{xx} = \mathscr{U}^{sn}_{,x}, \\ \epsilon^{sn}_{zz} = \mathscr{W}^{sn}_{,z}, \\ \gamma^{sn}_{xz} = \mathscr{U}^{sn}_{,z} + \mathscr{W}^{sn}_{,x}, \end{cases} \tag{2.12}$$

where E_f, E_s and ν_s are Young's modulus of the film, substrate, and Poisson's ratio of the substrate, respectively. Lamé's first parameter λ_s is expressed as $\lambda_s = E_s\nu_s/\left[(1+\nu_s)(1-2\nu_s)\right]$, while G_s is the shear modulus of the substrate expressed as $G_s = E_s/\left[2(1+\nu_s)\right]$. The notation $,_x$ stands for the partial derivative $\frac{\partial}{\partial x}$.

The principle of virtual work reads

$$\mathcal{P}_{int}\left(\delta\mathbf{u}\right) + \mathcal{P}_{ext}\left(\delta\mathbf{u}\right) = 0, \quad \forall \delta\mathbf{u} \in K.A. \tag{2.13}$$

where $\delta\mathbf{u}$ is the virtual displacement and $K.A.$ represents the space of kinematically admissible displacements, while $\mathcal{P}_{int}\left(\delta\mathbf{u}\right)$ and $\mathcal{P}_{ext}\left(\delta\mathbf{u}\right)$ are the internal and external virtual work, respectively. The internal virtual work of system is given as

$$\mathcal{P}_{int}\left(\delta\mathbf{u}\right) = -\int_{\Omega^f} \sigma^f_{xx}\delta\epsilon^f_{xx}\mathrm{d}\Omega - \sum_{sn}\int_{\Omega^{sn}} \left(\sigma^{sn}_{xx}\delta\epsilon^{sn}_{xx} + \sigma^{sn}_{zz}\delta\epsilon^{sn}_{zz} + \sigma^{sn}_{xz}\delta\gamma^{sn}_{xz}\right)\mathrm{d}\Omega, \tag{2.14}$$

where Ω^f and Ω^{sn} stand for the domain of the film and the n^{th} sublayer in the substrate, respectively. Considering the load proportional to a scalar parameter λ, the external virtual work is defined as

$$\mathcal{P}_{ext}(\delta\mathbf{u}) = \lambda \int_{\Omega} \mathbf{F}\delta\mathbf{u}\mathrm{d}\Omega, \tag{2.15}$$

where $\mathbf{F}$ denotes the external load. Through substituting Eq. (2.8)−(2.12) into Eq. (2.13), the film/substrate model can be developed in the following parts.

Internal virtual work of the substrate

First, let us define the unknown variables in each sublayer

$$\langle \mathbf{q}_1^{sn} \rangle = \langle u_{n-1} \quad w_{n-1} \quad u_n \quad w_n \rangle \,, \tag{2.16}$$

$$\langle \mathbf{q}_2^{sn} \rangle = \langle u_{n-1,x} \quad w_{n-1,x} \quad u_{n,x} \quad w_{n,x} \rangle \,. \tag{2.17}$$

According to the kinematics (2.10), the displacement field reads

$$\left\{ \begin{array}{c} \mathscr{U}^{sn} \\ \mathscr{W}^{sn} \end{array} \right\} = [\mathbf{N}^z] \left\{ \mathbf{q}_1^{sn} \right\} , \tag{2.18}$$

where

$$[\mathbf{N}^z] = \left[\begin{array}{cccc} \dfrac{1-\eta}{2} & 0 & \dfrac{1+\eta}{2} & 0 \\ 0 & \dfrac{1-\eta}{2} & 0 & \dfrac{1+\eta}{2} \end{array} \right] . \tag{2.19}$$

The strain vector $\{\varepsilon^{sn}\}$ and stress vector $\{\mathbf{s}^{sn}\}$ can be respectively expressed as

$$\{\varepsilon^{sn}\} = \left\{ \begin{array}{c} \epsilon_{xx}^{sn} \\ \epsilon_{zz}^{sn} \\ \gamma_{xz}^{sn} \end{array} \right\} = [\mathbf{B}_1] \left\{ \mathbf{q}_1^{sn} \right\} + [\mathbf{B}_2] \left\{ \mathbf{q}_2^{sn} \right\} , \tag{2.20}$$

$$\{\mathbf{s}^{sn}\} = [\mathbf{C}^{sn}] \{\varepsilon^{sn}\} , \tag{2.21}$$

in which

$$[\mathbf{B}_1] = \left[\begin{array}{cccc} \dfrac{1-\eta}{2} & 0 & \dfrac{1+\eta}{2} & 0 \\ 0 & -\dfrac{1}{h_n} & 0 & \dfrac{1}{h_n} \\ -\dfrac{1}{h_n} & 0 & \dfrac{1}{h_n} & 0 \end{array} \right] , \tag{2.22}$$

$$[\mathbf{B}_2] = \left[\begin{array}{cccc} 0 & 0 & 0 & 0 \\ 0 & 0 & 0 & 0 \\ 0 & \dfrac{1-\eta}{2} & 0 & \dfrac{1+\eta}{2} \end{array} \right] , \tag{2.23}$$

$$[\mathbf{C}^{sn}] = \left[\begin{array}{ccc} \lambda_s + 2G_s & \lambda_s & 0 \\ \lambda_s & \lambda_s + 2G_s & 0 \\ 0 & 0 & G_s \end{array} \right] . \tag{2.24}$$

The internal virtual work of the substrate can be represented as the sum of all the

sublayers:

$$\begin{aligned}\mathcal{P}_{int}^{s}\left(\delta\mathbf{u}\right) &= -\int_0^L\int_0^{h_s}\langle\delta\varepsilon^s\rangle\left\{\mathbf{s}^s\right\}\mathrm{d}z\mathrm{d}x \\ &= -\int_0^L\left(\sum_{sn}\langle\delta\mathbf{q}_1^{sn}\rangle\underbrace{\int_0^{h_n}{}^T[\mathbf{B}_1]\left\{\mathbf{s}^{sn}\right\}\mathrm{d}z}_{\Phi}+\sum_{sn}\langle\delta\mathbf{q}_2^{sn}\rangle\underbrace{\int_0^{h_n}{}^T[\mathbf{B}_2]\left\{\mathbf{s}^{sn}\right\}\mathrm{d}z}_{\Psi}\right)\mathrm{d}x.\end{aligned} \tag{2.25}$$

Through considering Eqs. (2.20) and (2.21), one can obtain

$$\Phi=\sum_{sn}\left(\int_0^{h_n}{}^T[\mathbf{B}_1]\left[\mathbf{C}^{sn}\right]\left[\mathbf{B}_1\right]\mathrm{d}z\left\{\mathbf{q}_1^{sn}\right\}+\int_0^{h_n}{}^T[\mathbf{B}_1]\left[\mathbf{C}^{sn}\right]\left[\mathbf{B}_2\right]\mathrm{d}z\left\{\mathbf{q}_2^{sn}\right\}\right), \tag{2.26}$$

$$\Psi=\sum_{sn}\left(\int_0^{h_n}{}^T[\mathbf{B}_2]\left[\mathbf{C}^{sn}\right]\left[\mathbf{B}_1\right]\mathrm{d}z\left\{\mathbf{q}_1^{sn}\right\}+\int_0^{h_n}{}^T[\mathbf{B}_2]\left[\mathbf{C}^{sn}\right]\left[\mathbf{B}_2\right]\mathrm{d}z\left\{\mathbf{q}_2^{sn}\right\}\right). \tag{2.27}$$

One can also combine the above two equations in the following form:

$$\left\{\begin{array}{c}\Phi\\ \Psi\end{array}\right\}=\left[\mathbf{C}^s\right]\left\{\begin{array}{c}\mathbf{q}_1^{sn}\\ \mathbf{q}_2^{sn}\end{array}\right\}. \tag{2.28}$$

Now we consider the discretization of substrate along the x direction. The unknown vectors can be given as

$$\left\{\mathbf{q}_1^{sn}\right\}=\left[\mathbf{N}^s\right]\left\{\mathbf{v}^s\right\}, \tag{2.29}$$

$$\left\{\mathbf{q}_2^{sn}\right\}=\left[\mathbf{N}_{,x}^s\right]\left\{\mathbf{v}^s\right\}, \tag{2.30}$$

where $\{\mathbf{v}^s\}$ is the elementary unknown vector of the substrate and $[\mathbf{N}^s]$ is the shape function. Note that the longitudinal displacement u is discretized by linear Lagrange functions, while the transverse displacement w is discretized by Hermite functions. Consequently, the internal virtual work of the substrate can be written as

$$\begin{aligned}\mathcal{P}_{int}^{s}\left(\delta\mathbf{u}\right) &= -\sum_e\langle\delta\mathbf{v}^s\rangle\int_0^{l_e}\left({}^T[\mathbf{N}^s]\Phi+{}^T[\mathbf{N}_{,x}^s]\Psi\right)\mathrm{d}x \\ &= -\sum_e\langle\delta\mathbf{v}^s\rangle\int_0^{l_e}\left(\left[{}^T\mathbf{N}^s,\ {}^T\mathbf{N}_{,x}^s\right]\left[\mathbf{C}^s\right]\left[\begin{array}{c}\mathbf{N}^s\\ \mathbf{N}_{,x}^s\end{array}\right]\right)\mathrm{d}x\{\mathbf{v}^s\},\end{aligned} \tag{2.31}$$

where l_e is the length of 1D element.

Internal virtual work of the film

As for the thin film, the strain energy is mainly generated by normal strain ϵ^f_{xx}, the other two terms ϵ^f_{zz} and γ^f_{xz} being neglected. Consequently, the internal virtual work of the film is expressed as

$$\begin{aligned}\mathcal{P}^f_{int}(\delta\mathbf{u}) &= -\int_{\Omega^f} \sigma^f_{xx}\delta\epsilon^f_{xx}\mathrm{d}\Omega \\ &= -\int_0^L \left[N^f\left(\delta u^f_{,x} + w^f_{,x}\delta w^f_{,x}\right) + M^f\delta w^f_{,xx}\right]\mathrm{d}x,\end{aligned} \tag{2.32}$$

where

$$\begin{cases} N^f = E_f h_f\left(u^f_{,x} + \dfrac{1}{2}(w^f_{,x})^2\right), \\ M^f = \dfrac{1}{12}E_f h_f^3 w^f_{,xx}. \end{cases} \tag{2.33}$$

The generalized strain vector $\{\varepsilon^f\}$ of the film is defined as

$$\left\{\varepsilon^f\right\} = \left([\mathbf{H}] + \frac{1}{2}[\mathbf{A}(\mathbf{q}^f)]\right)\left\{\mathbf{q}^f\right\}, \tag{2.34}$$

in which

$$[\mathbf{H}] = \begin{bmatrix} 1 & 0 & 0 \\ 0 & 0 & 1 \end{bmatrix}, \qquad [\mathbf{A}(\mathbf{q}^f)] = \begin{bmatrix} 0 & w^f_{,x} & 0 \\ 0 & 0 & 0 \end{bmatrix}, \qquad \left\{\mathbf{q}^f\right\} = \begin{Bmatrix} u^f_{,x} \\ w^f_{,x} \\ w^f_{,xx} \end{Bmatrix}. \tag{2.35}$$

Since $[\mathbf{A}(\mathbf{q}^f)]$ and $\left\{\mathbf{q}^f\right\}$ are linear functions of u^f and w^f, the internal virtual work of the film in Eq. (2.32) is a quadratic form with respect to the displacement and the stress:

$$\mathcal{P}^f_{int}(\delta\mathbf{u}) = -\int_0^L \left\langle\delta\mathbf{q}^f\right\rangle\left({}^T[\mathbf{H}] + {}^T[\mathbf{A}(\mathbf{q}^f)]\right)\left\{\mathbf{s}^f\right\}\mathrm{d}x, \tag{2.36}$$

where the generalized stress of the film reads

$$\left\{\mathbf{s}^f\right\} = \begin{Bmatrix} N^f \\ M^f \end{Bmatrix} = [\mathbf{D}]\left([\mathbf{H}] + \frac{1}{2}[\mathbf{A}(\mathbf{q}^f)]\right)\left\{\mathbf{q}^f\right\}, \tag{2.37}$$

in which

$$[\mathbf{D}] = \begin{bmatrix} E_f h_f & 0 \\ 0 & \frac{1}{12}E_f h_f^3 \end{bmatrix}. \tag{2.38}$$

Note that the discretization of unknown variables $\{\mathbf{q}^f\}$ takes the same shape function as for the substrate, *i.e.* Lagrange functions for the longitudinal displacement and Hermite functions for the transverse displacement.

Connection between the film and the substrate

In the kinematics (2.8)−(2.10), there are $2(n+2)$ unknown functions depending on the number of sublayers in the substrate. As the film is bonded to the substrate, the displacement should be continuous at the interface. Therefore, the connection between the film and the substrate reads

$$\begin{cases} \mathscr{U}^f(x, h_s) = \mathscr{U}^{s1}(x, -1), \\ \mathscr{W}^f(x, h_s) = \mathscr{W}^{s1}(x, -1). \end{cases} \tag{2.39}$$

From Eqs. (2.8)−(2.9) and (2.39), the following relations can be obtained:

$$\begin{cases} u^f = u_0 - \dfrac{h_f}{2} w_{0,x}, \\ w^f = w_0. \end{cases} \tag{2.40}$$

Consequently, the above conditions reduce the unknown functions to $2(n+1)$ independent unknown variables $\{u_0, w_0, u_1, w_1, \ldots, u_n, w_n\}$.

2.4 Resolution technique and bifurcation analysis

Asymptotic Numerical Method (ANM) [52, 46, 45, 47] is used to solve the resulting nonlinear equations. The ANM is a path-following technique that is based on the succession of high order power series expansions (perturbation technique) with respect to a well chosen path parameter, which appears as an efficient continuation predictor without any corrector iteration. Besides, one can get approximations of the solution path that are very accurate inside the radius of convergence. In this chapter, the main interest of the ANM is its ability to detect bifurcation points. First, small steps are often associated with the occurrence of a bifurcation. Then, a bifurcation indicator will be defined, which permits to exactly detect the bifurcation load and the corresponding nonlinear mode.

2.4.1 Path-following technique

Let us write a generalized nonlinear problem as

$$\mathbf{R}(\mathbf{U}, \lambda) = \mathbf{L}(\mathbf{U}) + \mathbf{Q}(\mathbf{U}, \mathbf{U}) - \lambda \mathbf{F} = 0, \tag{2.41}$$

where $\mathbf{U}$ is a mixed vector of unknowns including displacement and stress, $\mathbf{L}(\cdot)$ a linear operator, $\mathbf{Q}(\cdot,\cdot)$ a quadratic one, $\mathbf{F}$ the external load vector and $\mathbf{R}$ the residual vector. The external load parameter is denoted as a scalar λ. The principle of the ANM continuation consists in describing the solution path by computing a succession of truncated power series expansions. From a known solution point $(\mathbf{U}_0, \lambda_0)$, the solution $(\mathbf{U}, \lambda)$ is expanded into truncated power series of a perturbation parameter a:

$$\mathbf{U}(a) = \mathbf{U}_0 + \sum_{p=1}^{n} a^p \mathbf{U}_p = \mathbf{U}_0 + a\mathbf{U}_1 + a^2\mathbf{U}_2 + \ldots + a^n\mathbf{U}_n, \tag{2.42}$$

$$\lambda(a) = \lambda_0 + \sum_{p=1}^{n} a^p \lambda_p = \lambda_0 + a\lambda_1 + a^2\lambda_2 + \ldots + a^n\lambda_n, \tag{2.43}$$

$$a = \langle \mathbf{u} - \mathbf{u}_0, \mathbf{u}_1 \rangle + (\lambda - \lambda_0)\,\lambda_1, \tag{2.44}$$

where n is the truncation order of the series. Eq. (2.44) defines the path parameter a that can be identified to an arc-length parameter. By introducing Eqs. (2.42) and (2.43) into Eqs. (2.41) and (2.44), then equating the terms at the same power of a, one can obtain a set of linear problems:

Order 1 :

$$\mathbf{L}_t^0\left(\mathbf{U}_1\right) = \lambda_1 \mathbf{F}, \tag{2.45}$$

$$\langle \mathbf{u}_1, \mathbf{u}_1 \rangle + \lambda_1^2 = 1. \tag{2.46}$$

Order $p \geqslant 2$:

$$\mathbf{L}_t^0\left(\mathbf{U}_p\right) = \lambda_p \mathbf{F} - \sum_{r=1}^{p-1} \mathbf{Q}\left(\mathbf{U}_r, \mathbf{U}_{p-r}\right), \tag{2.47}$$

$$\langle \mathbf{u}_p, \mathbf{u}_1 \rangle + \lambda_p \lambda_1 = 0, \tag{2.48}$$

where $\mathbf{L}_t^0(\cdot) = \mathbf{L}(\cdot) + 2\mathbf{Q}(\mathbf{U}_0, \cdot)$ is the linear tangent operator. Note that this operator depends only on the initial solution and takes the same value for every order p, which leads to only one matrix inversion at each step. These linear problems are solved by FE method. Once the value of $\mathbf{U}_p$ is calculated, the path solution at the step $(j+1)$ can be obtained through Eq. (2.42).

The maximum value of the path parameter a should be automatically defined by analyzing the convergence of the power series at each step. The a_{max} can be based on the difference of displacements at two successive orders that must be smaller than a given

precision parameter δ:

$$\text{Validity range: } a_{max} = \left(\delta \frac{\|\mathbf{u}_1\|}{\|\mathbf{u}_n\|} \right)^{1/(n-1)}, \tag{2.49}$$

where the notation $\|\cdot\|$ stands for the Euclidean norm. Unlike incremental-iterative methods, the arc-length step size a_{max} is adaptive since it is determined *a posteriori* by the algorithm. When there is a bifurcation point on the solution path, the radius of convergence is defined by the distance to the bifurcation. Thus, the step length defined in Eq. (2.49) becomes smaller and smaller, which looks as if the continuation process "knocks" against the bifurcation [13]. This accumulation of small steps is a very good indicator of the presence of a singularity on the path. All the bifurcations can be easily identified in this way by the user without any special tool.

It is worth mentioning that there are only two parameters controlling the algorithm. The first one is the truncation order n of the series. It was previously discussed that the optimal truncation order should be large enough between 15 and 20, but bigger values (*e.g.* $n = 50$) lead to good results for large scale problems as well [121]. Another important parameter is the chosen tolerance δ that affects the residual. For instance, very small values of tolerance (*e.g.* $\delta = 10^{-6}$) ensure quite a high accuracy and a pretty robust path-following process.

In this chapter, the ANM has been chosen for its ability for branch-switching and to detect bifurcation points, but not necessarily to reduce the computation time. Nevertheless, let us underline that this computation time may remain moderate even with many terms of the series. For instance in [121], very large scale problems have been solved and 50 terms of Taylor series have been computed for a cost smaller than the one of two linear problems. Complementary results can be found in [47].

The implementation of the recurrence formulae as (2.47) is relatively simple for Föppl-von Kármán nonlinear plate or Navier-Stokes equations, but it can be tedious in a more general constitutive framework. That is why some tools have been proposed to compute high order derivatives of constitutive laws [112] that are based on techniques of Automatic Differentiation [72]. Very efficient software is available for small systems [99].

In this chapter, the simplest ANM algorithm is considered. A variant with possible correction phases [104] should lead to somewhat smaller computation time. Here, the priority is the reliability of path-following and it is simpler to choose very small values of the accuracy parameter δ in (2.49) to ensure a secure method for bifurcation analysis.

The presented algorithm belongs to the family of continuation methods and not to local bifurcation analyses that are generally associated with the names of [118, 138, 101]. It is certainly possible to numerically compute a branch issued from a bifurcation point

in the form of high order Taylor series, while historical papers used only few terms computed analytically. From such numerical results, see for instance [28], it appears that the radius of convergence can be large, but finite, so that the standard ANM algorithm remains necessary for the next steps. Note that a recent study [117] attempts to deduce a computational method from Koiter's ideas.

2.4.2 Detection of bifurcation points

There are many methods to detect bifurcation points, the most important ones being briefly mentioned in the introduction. None of these methods is perfect, the main difficulty being their reliability. That is why we have chosen the bifurcation indicator method that has been proven to be very secure in many cases of solid and fluid mechanics, see for instance [28, 32, 71, 74, 96, 148]. At each step, one defines a scalar parameter that vanishes only when the tangent stiffness matrix is singular. This indicator is a scalar measure of the tangent stiffness, while it is not an eigenvalue except at the singular point.

Definition of a bifurcation indicator

Let $\Delta\mu\mathbf{f}$ be a fictitious perturbation force applied to the structure at a given deformed state $(\mathbf{U}, \lambda)$, where $\Delta\mu$ is the intensity of the force $\mathbf{f}$ and $\Delta\mathbf{U}$ is the associated response. Through superposing the applied load and perturbation, the fictitious perturbed equilibrium can be described by

$$\mathbf{L}\left(\mathbf{U}+\Delta\mathbf{U}\right)+\mathbf{Q}\left(\mathbf{U}+\Delta\mathbf{U},\mathbf{U}+\Delta\mathbf{U}\right)=\lambda\mathbf{F}+\Delta\mu\mathbf{f}. \tag{2.50}$$

Considering the equilibrium state and neglecting the quadratic terms, one can obtain the following auxiliary problem:

$$\mathbf{L}_t\left(\Delta\mathbf{U}\right)=\Delta\mu\mathbf{f}, \tag{2.51}$$

where $\mathbf{L}_t(\cdot)=\mathbf{L}(\cdot)+2\mathbf{Q}(\mathbf{U},\cdot)$ is the tangent operator at the equilibrium point $(\mathbf{U},\lambda)$. If $\Delta\mu$ is imposed, this leads to a displacement tending to infinity in the vicinity of the critical points. To avoid this problem, the following displacement based condition is imposed:

$$\left\langle \mathbf{L}_t^0\left(\Delta\mathbf{U}-\Delta\mathbf{U}_0\right),\Delta\mathbf{U}_0\right\rangle=0, \tag{2.52}$$

where $\mathbf{L}_t^0(\cdot)$ is the tangent operator at the starting point $(\mathbf{U}_0,\lambda_0)$ and the direction $\Delta\mathbf{U}_0$ is the solution of $\mathbf{L}_t^0(\Delta\mathbf{U}_0)=\mathbf{f}$. Consequently, $\Delta\mu$ is deduced from the linear system (2.51) and (2.52):

$$\Delta\mu=\frac{\langle\Delta\mathbf{U}_0,\mathbf{f}\rangle}{\langle\mathbf{L}_t^{-1}(\mathbf{f}),\mathbf{f}\rangle}. \tag{2.53}$$

Since the scalar function $\Delta\mu$ represents a measure of the stiffness of structure and becomes zero at the singular points, it can define a bifurcation indicator. It can be directly computed from Eq. (2.53) but it requires to decompose the tangent operator at each point throughout the solution path. For this reason, the system (2.51) and (2.52) can be more efficiently resolved by the ANM.

Goal: find a_b such that: $\mathbf{L}_t\left(\mathbf{U}(a_b)\right)\Delta\mathbf{U}=0$
Method: $\mathbf{L}_t\left(\mathbf{U}(a)\right)\Delta\mathbf{U}=\Delta\mu\mathbf{f}$, $\langle\mathbf{L}_t^0\left(\Delta\mathbf{U}-\Delta\mathbf{U}_0\right),\Delta\mathbf{U}_0\rangle=0$
Output: when $\Delta\mu(a_b)=0$, $\Delta\mathbf{U}(a_b)$ is the bifurcation mode

Thus, the bifurcation indicator $\Delta\mu(a)$ is easily computed from the auxiliary problems (2.51) and (2.52). This function $\Delta\mu(a)$ depends on the fictitious perturbation force $\mathbf{f}$, but the numerical solutions of the initial problem (2.41), the bifurcation points and the bifurcation modes are quite independent on it. Exceptionally, the bifurcation indicator could miss a bifurcation if the fictitious force vector $\mathbf{f}$ is orthogonal to the instability mode. The choice of a random perturbation force avoids this problem. In what follows, each field $\Delta\mathbf{U}(a_b)$ is called instability mode.

Computation of the bifurcation indicator by the ANM

The perturbation $(\Delta\mathbf{U},\Delta\mu)$ is searched by the following asymptotic series expansions:

$$\Delta\mathbf{U}(a)=\Delta\mathbf{U}_0+\sum_{p=1}^{n}a^p\Delta\mathbf{U}_p=\Delta\mathbf{U}_0+a\Delta\mathbf{U}_1+a^2\Delta\mathbf{U}_2+\ldots+a^n\Delta\mathbf{U}_n, \tag{2.54}$$

$$\Delta\mu(a)=\Delta\mu_0+\sum_{p=1}^{n}a^p\Delta\mu_p=\Delta\mu_0+a\Delta\mu_1+a^2\Delta\mu_2+\ldots+a^n\Delta\mu_n. \tag{2.55}$$

By substituting Eqs. (2.54) and (2.55) into Eqs. (2.51) and (2.52), one can obtain the following sequence of linear problems:

Order 0 :

$$\mathbf{L}_t^0\left(\Delta\mathbf{U}_0\right)=\Delta\mu_0\mathbf{f}, \tag{2.56}$$

where the condition $\Delta\mu_0=1$ is prescribed *a priori* at each step.

Order $p\geqslant 1$:

$$\mathbf{L}_t^0\left(\Delta\mathbf{U}_p\right)=\Delta\mu_p\mathbf{f}-2\sum_{j=1}^{p}\mathbf{Q}\left(\mathbf{U}_j,\Delta\mathbf{U}_{p-j}\right), \tag{2.57}$$

$$\langle\Delta\mathbf{U}_p,\mathbf{f}\rangle=0, \tag{2.58}$$

where the vectors $\mathbf{U}_j$ are determined during the computation of the equilibrium branch and $\mathbf{L}_t^0$ is exactly the same tangent operator obtained from the equilibrium branch. Even

though this procedure requires computing the order p series at each step, the corresponding computing speed is fast since the same tangent stiffness matrix is used at every order.

The discretization of the problem at the order p in Eqs. (2.57) and (2.58) gives

$$\left[\mathbf{K}_t^0\right]\{\Delta\mathbf{u}_p\} = \Delta\mu_p\{\mathbf{f}\} + \{\Delta\mathbf{F}_p\}, \tag{2.59}$$

$$^T\{\Delta\mathbf{u}_p\}\left[\mathbf{K}_t^0\right]\{\Delta\mathbf{u}_0\} = 0, \tag{2.60}$$

where $[\mathbf{K}_t^0]$ denotes the tangent stiffness matrix computed at the starting point $(\mathbf{U}_0, \lambda_0)$. The vectors $\{\Delta\mathbf{u}_p\}$ and $\{\Delta\mathbf{u}_0\}$, respectively represent nodal displacements at the order p and order 0 associated to the fictitious perturbation $\{\mathbf{f}\}$. The vector $\{\Delta\mathbf{F}_p\}$ depends only on the solutions at the previous $(p-1)$ orders. From Eqs. (2.59) and (2.60), one can obtain

$$\Delta\mu_p = -\frac{\langle\Delta\mathbf{F}_p, \Delta\mathbf{u}_0\rangle}{\langle\mathbf{f}, \Delta\mathbf{u}_0\rangle}. \tag{2.61}$$

Since $\Delta\mu_p$ is computed and then substitute it into Eq. (2.59), one can get $\Delta\mathbf{u}_p$. In this way, all the asymptotic expansion terms of the bifurcation indicator can be determined.

2.5 Results and discussion

The path-following technique described in Section 2.4.1 will be used in any case, near bifurcation points or away. Specific procedures to compute branches emanating from bifurcation are available [28, 73, 148], but for simplicity we limited ourselves to the basic continuation algorithm in Section 2.4.1. That is why we introduce a small perturbation force to trigger a continuous transition from the fundamental branch to the bifurcated one: this transverse perturbation $f_z = 10^{-6}$ is imposed in the middle of the film. The introduction of such small perturbation forces is quite a common technique in the solution of bifurcation problems by continuation techniques [61, 6], even when using commercial finite element codes. This artifice could be avoided by applying a specific procedure to compute the bifurcation branch as in [28, 148]. In this chapter, the perturbation force f_z allows us to compute the whole bifurcated branch with a single continuation algorithm. Note that these forces differ from the fictitious perturbation force in Section 2.4.2 that acts only on the bifurcation indicator. To check if the global tangent stiffness matrix $\mathbf{K}_t$ is positive definite, Crout decomposition is applied at each step during the nonlinear resolution to evaluate the stability of the solution. The cost of this stability test is negligible since Crout decomposition has also to be done to solve the problems (2.45) and (2.47).

The sketch of the film/substrate system under compression forces is illustrated in Fig.

2.3. On the bottom surface of the substrate, the vertical displacement w_n, and the tangential traction are taken to be zero. On both left and right sides, simply supported and clamped boundary conditions will be considered, respectively. Precisely, the transverse displacement w_i, is locked to be zero in the case of simply supported boundary conditions and its derivative $w_{i,x}$ is also zero in the case of clamped boundary conditions. The material and geometric parameters of film/substrate system are similar to those in [151, 143, 29], which is shown in Table 2.1. The huge ratio of Young's modulus, E_f/E_s, determines the critical wavelength λ_x^c that remains practically unchanged as the amplitude of the wrinkles increases [85]. Poisson's ratio is a dimensionless measure of the degree of compressibility. Compliant materials in the substrate, such as elastomers, are nearly incompressible with $\nu_s = 0.48$. A relative thin film has been chosen so that an isotropic and homogeneous system is not parameter dependent, as established in Section 2.2.

In what follows, we will investigate the effect of boundary conditions and material properties of the substrate on instability patterns in the whole buckling and post-buckling evolution. The dimensional analysis in Section 2.2 demonstrated that the 2D response of film/substrate systems is not parameter dependent within the chosen framework. More precisely, for isotropic materials, a thick and soft substrate (sufficiently large h_s/λ_x and E_f/E_s) and a response with many waves (large L/λ_x), the only influencing parameter is Poisson's ratio of the substrate. Therefore, all the responses of such systems should be similar. Nevertheless, the literature reports a variety of nonlinear responses of these systems, including period-doubling, localized creasing, folding and ridging [39, 146, 163]. Some of these responses cannot be obtained here since this study is limited to 2D systems with small strains in the substrate. In this part, we will discuss the influence of the substrate anisotropy and two cases of elastic graded materials [40]. Besides, two cases of boundary conditions for the film/substrate will be studied: simply supported and clamped, respectively. To our best knowledge, previous studies in the literature did not consider the effect of boundary conditions and anisotropy of the substrate. Thus, we will detail most of the possible bifurcation sequences in the basic case of 2D systems with a very soft substrate.

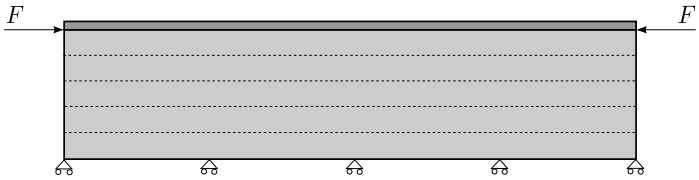

Figure 2.3: Sketch of the film/substrate system under a compression test.

Table 2.1: Material and geometric parameters of the film/substrate system.

$E_f(MPa)$	$E_s(MPa)$	ν_f	ν_s	$L(mm)$	$h_t(mm)$	$h_f(mm)$
1.3×10^5	1.8	0.3	0.48	1.5	0.1	10^{-3}

2.5.1 Film/substrate with simply supported boundary conditions

Very fine meshes, at least ten elements within one wavelength, are adopted to discretize the film/substrate system along the x direction. As for the z direction, convergence analysis is examined through the test with different number of sublayers. Fig. 2.4 shows the applied load versus transverse displacement with respectively 5, 10, 15, 20 or 25 sublayers in the substrate. It can be observed that fifteen sublayers are sufficient to obtain a convergent solution and well agree with the critical load of full 2D model (CPE8R elements in [1]). Besides, the critical load of sinusoidal wrinkles based on classical linearized stability analysis was presented in [43, 85], with Föppl-von Kármán nonlinear elastic plate assumption for the film. For a finite thick substrate, the critical load is expressed as $F_c = 1/4 h_f \overline{E}_f \left(3\overline{E}_s/\overline{E}_f\right)^{2/3}$, where $\overline{E}_f = E_f/\left(1-{v_f}^2\right)$ and $\overline{E}_s = E_s/\left(1-{v_s}^2\right)$. By introducing the material and geometric parameters in Table 2.1, one can obtain the analytical solution for periodic boundary conditions $F_c = 0.048 N/mm$, which is very close to our FE results with real boundary conditions (about $0.049 N/mm$ in Fig. 2.4).

The established 1D FE model based on the ANM gives a very fast computing speed with small number of steps to reach the secondary or higher bifurcations (see Fig. 2.5). Four bifurcations have been detected from the small step accumulation in the ANM framework. Besides, it is found that the transverse displacement along the z direction follows an exponential distribution as shown in Fig. 2.6. This result is analytically justified in Appendix A.

Although the small step accumulation is a good indicator of the occurrence of bifurcation, the exact bifurcation points may locate between two neighbouring steps, which cannot be captured directly. Therefore, bifurcation indicators are computed to detect the exact position of bifurcation points. By evaluating this indicator through an equilibrium branch, all the critical points (see Fig. 2.7) existing on this branch and the associated bifurcation modes (see Fig. 2.8) can be determined. Overall, four bifurcation points have been found. Fig. 2.8 shows a sequence of wrinkling patterns corresponding to the critical loads and their associated instability modes. The first instability mode is localized near the boundary and starts at $\lambda = 0.04893$. Then the pattern tends to be a uniform sinusoidal mode at the second bifurcation point when $\lambda = 0.055681$. A period-doubling mode occurs at the third bifurcation point when $\lambda = 0.086029$. Besides, a localized ridge mode can be evident in the middle. At the fourth bifurcation point when $\lambda = 0.11595$,

an aperiodic mode (period-trebling and period-quadrupling) emerges. The stability of all these solutions has been checked by using Crout decomposition of tangent stiffness matrices. Lastly, it is noted that the strain is less than 1% at the bifurcation and lower than 4% at the end of the loading process. Likely, more accurate results at the end of loading could be obtained in a finite strain hyperelasticity framework. The same remark holds for the following examples.

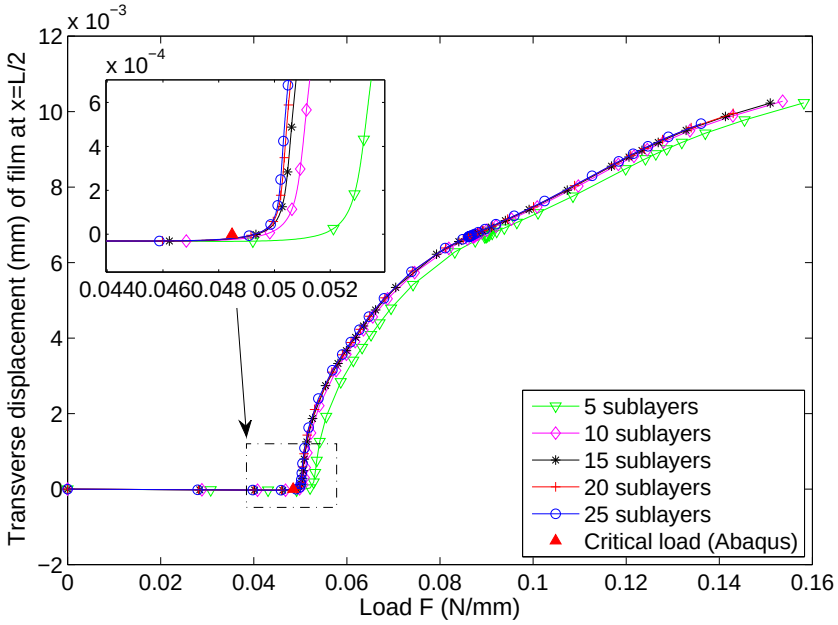

Figure 2.4: Convergence test of film/substrate system with simply supported boundary conditions. The substrate is respectively divided into 5, 10, 15, 20 or 25 sublayers. ANM parameters: $n = 15$, $\delta = 10^{-5}$, 45 steps. Each point corresponds to one ANM step.

2.5.2 Film/substrate with clamped boundary conditions

Following the same strategy, we study the pattern formation in the case of clamped boundary conditions. Very fine meshes are adopted to discretize the film/substrate system along the x direction. Convergence of the computational results is carefully examined. In Figs. 2.9 and 2.10, two bifurcation points have also been captured through evaluating the bifurcation indicators along the equilibrium branch. The same method will also be used in the following examples, but the corresponding indicator curves will no longer be presented. The sequence of wrinkling patterns corresponding to the bifurcation loads and their associated instability modes are illustrated in Fig. 2.11. The two modes correspond to modulated oscillations, the first one with a sinusoidal envelope and the second one with a hyperbolic tangent shape. These modes are quite common [122] and can be predicted

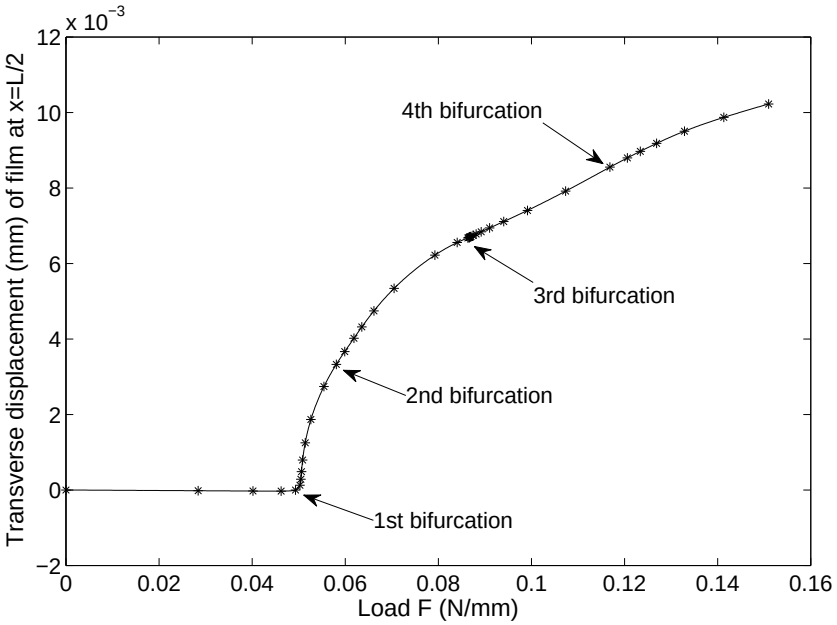

Figure 2.5: Bifurcation curve of film/substrate system with simply supported boundary conditions. Four bifurcations are observed. ANM parameters: $n = 15$, $\delta = 10^{-5}$, 45 steps. Each point corresponds to one ANM step.

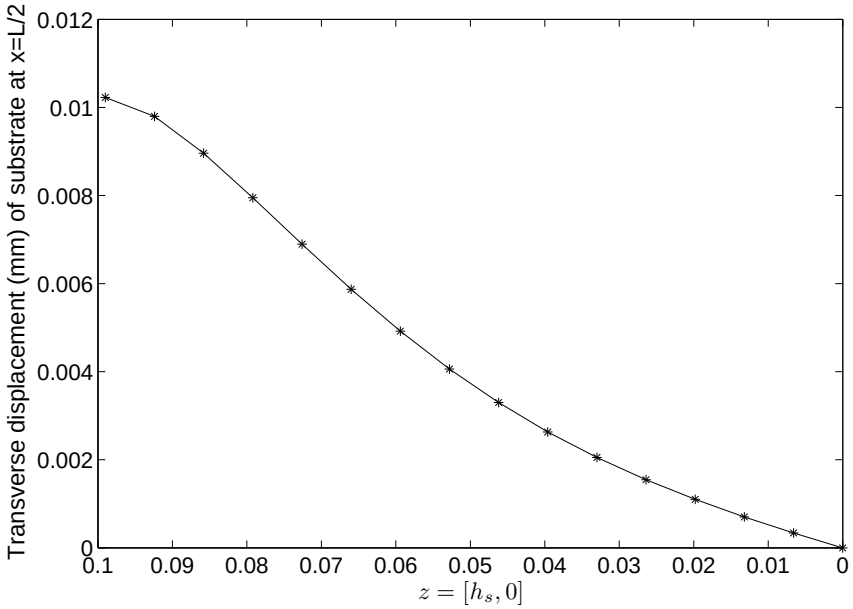

Figure 2.6: Transverse displacement along the z direction. Results follow an exponential distribution.

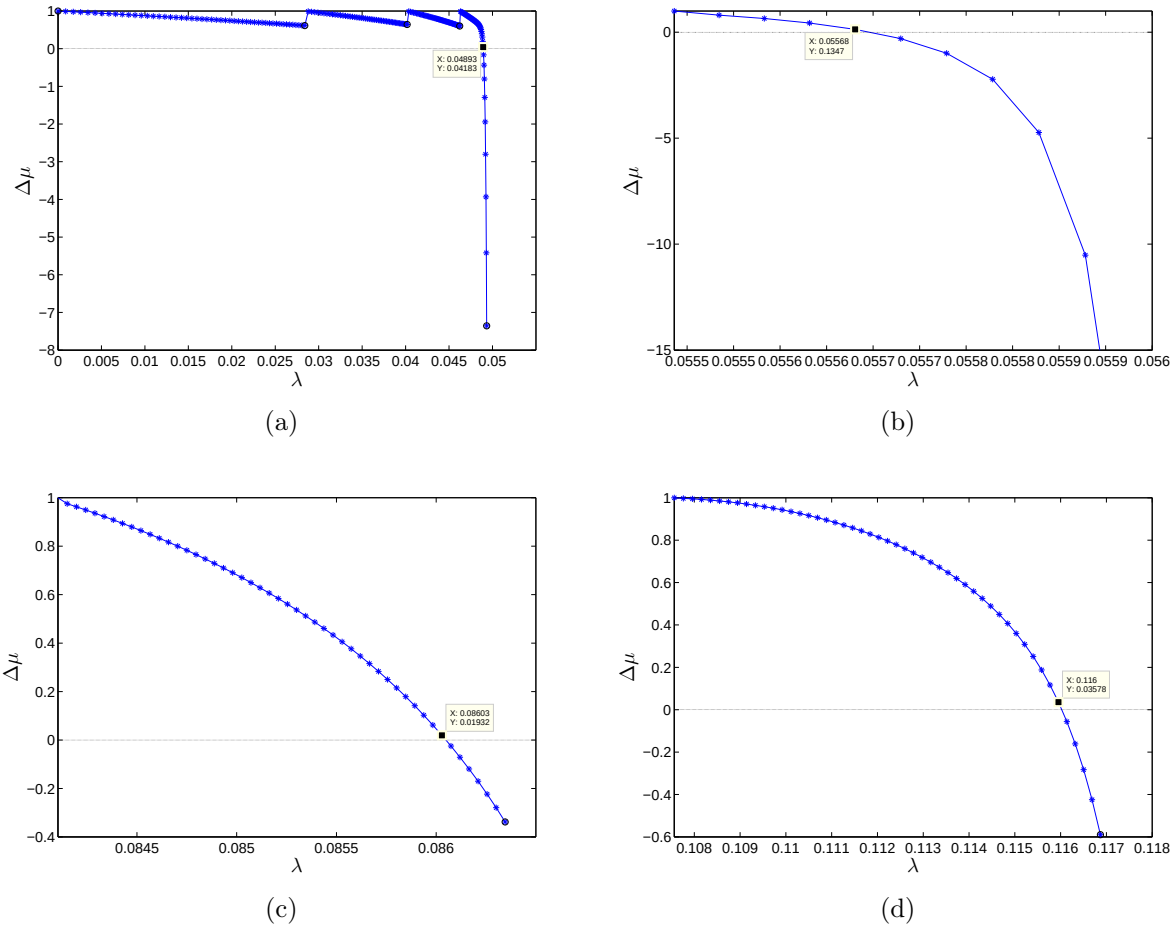

Figure 2.7: Bifurcation indicators as a function of load parameter for film/substrate system with simply supported boundary conditions. (a) The 1st bifurcation point when $\lambda = 0.04893$. (b) The 2nd bifurcation point when $\lambda = 0.05568$. (c) The 3rd bifurcation point when $\lambda = 0.08603$. (d) The 4th bifurcation point when $\lambda = 0.116$. The condition $\Delta\mu_0 = 1$ is prescribed *a priori* at each ANM step.

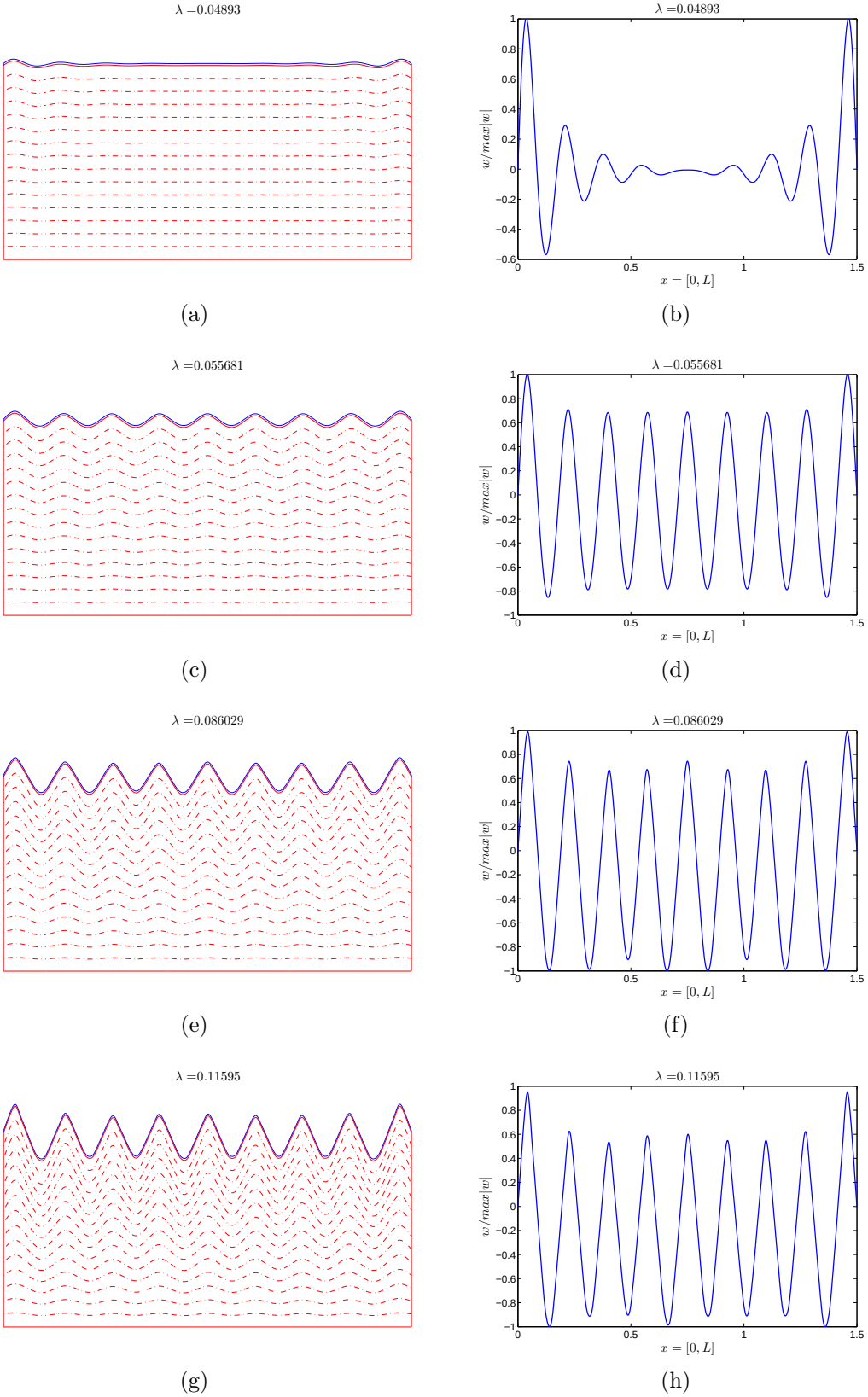

Figure 2.8: The left column shows a sequence of wrinkling patterns corresponding to its critical load determined by bifurcation indicators in Fig. 2.7. The right column presents the associated instability modes. Simply supported boundary conditions are imposed. (b) The 1st mode. (d) The 2nd mode. (f) The 3rd mode. (h) The 4th mode.

by the asymptotic Ginzburg−Landau equation [56]. The first bifurcation mode in Fig. 2.8b has been inhibited by the clamped boundary conditions and it does not appear in this case. The period-doubling was not observed in the range of load-displacement curve in Fig. 2.9 either. Nevertheless, the observed patterns are quite similar except near the boundary: compare for instance Fig. 2.8c and Fig. 2.11c, Fig. 2.8d and Fig. 2.11d.

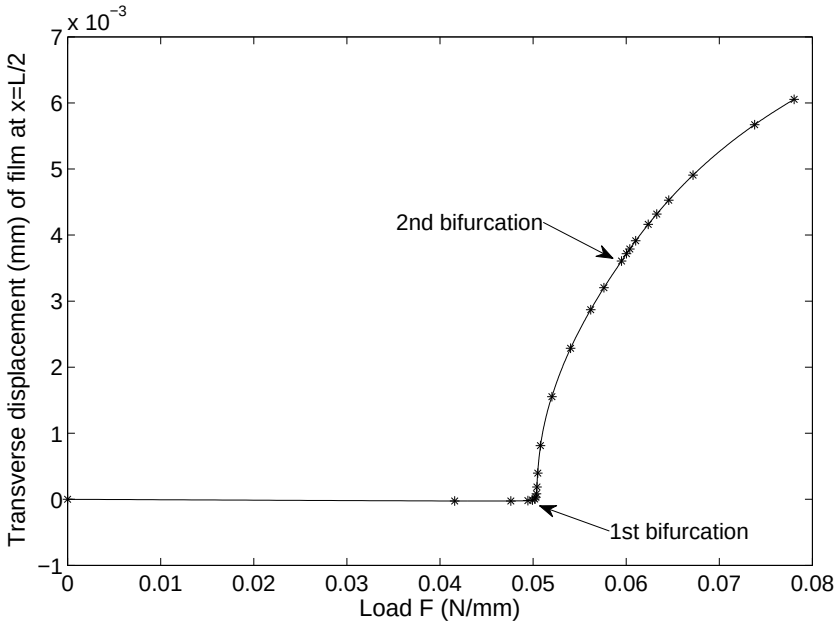

Figure 2.9: Bifurcation curve of film/substrate system with clamped boundary conditions. Two bifurcations are observed. ANM parameters: $n = 15$, $\delta = 10^{-3}$, 25 steps. Each point corresponds to one ANM step.

2.5.3 Functionally Graded Material (FGM) substrate with simply supported boundary conditions

In Section 2.2, it has been shown that the elastic matrix $\mathbf{L}_s$ contributes to the potential energy, which would affect wrinkling patterns to some extent. In what follows, we will extend the 1D FE model to consider the substrate as elastic graded materials to study the influence of variable Young's modulus on the pattern formation. Systems consisting of a stiff thin layer resting on an elastic graded substrate are often encountered both in nature and industry. In nature, many living soft tissues including skins, brains, mucosa of esophagus and pulmonary airway can be modeled as a soft substrate covered by a stiff thin surface layer [115]. It is noted that the sub-surface layer (*i.e.* substrate) usually has graded mechanical properties because of the spatial variation in the microstructure or composition. Besides, many practical systems in industry have a functionally grad-

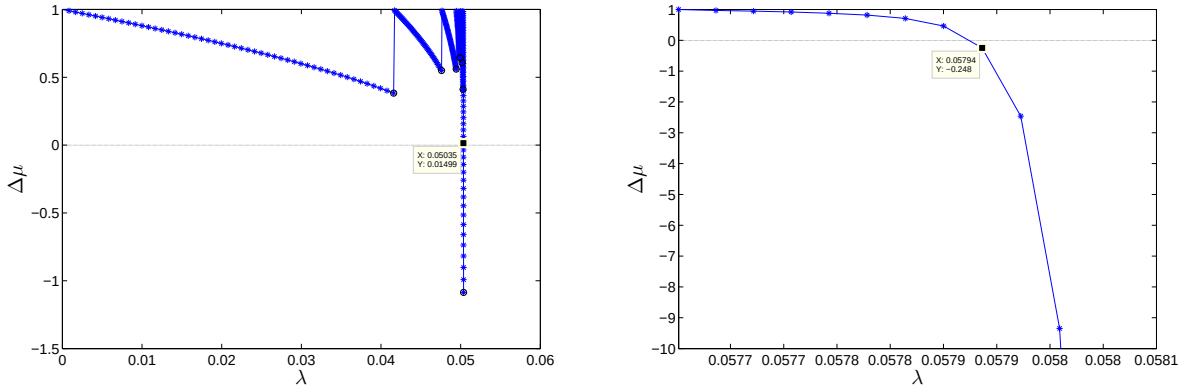

(a) (b)

Figure 2.10: Bifurcation indicators as a function of load parameter for film/substrate system with clamped boundary conditions. (a) The 1st bifurcation point when $\lambda = 0.05035$. (b) The 2nd bifurcation point when $\lambda = 0.05794$. The condition $\Delta\mu_0 = 1$ is prescribed *a priori* at each ANM step.

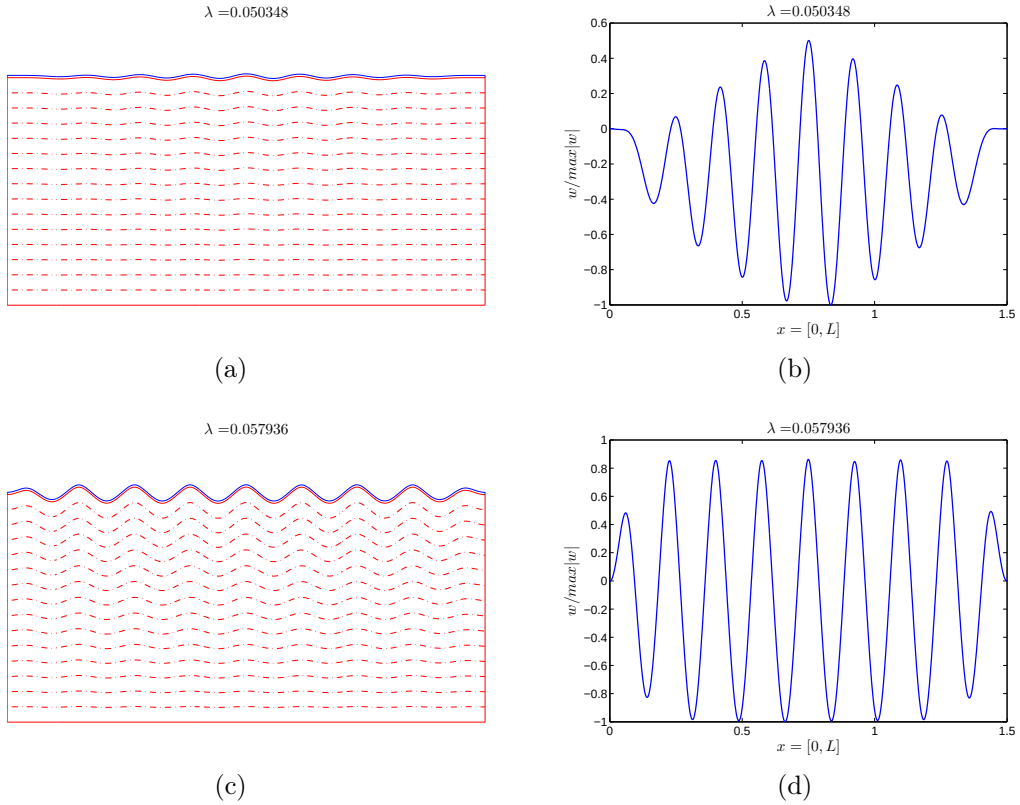

(a) (b)

(c) (d)

Figure 2.11: The left column shows a sequence of wrinkling patterns corresponding to its critical load determined by bifurcation indicators in Fig. 2.10. The right column presents the associated instability modes. Clamped boundary conditions are imposed. (b) The 1st mode. (d) The 2nd mode.

ed substrate [109, 79, 40]. For instance, the deposition process of a stiff thin film on a soft substrate may lead to a variation of the mechanical properties of the substrate along the thickness direction (functionally graded), which would affect the wrinkling of film/substrate system [79]. In particular, we explore typical exponential variations of Young's modulus of the substrate along the thickness direction (softening $\overline{E}_{s1}$ and stiffening $\overline{E}_{s2}$) (see Fig. 2.12), while Poisson's ratio is constant as before. In fact, these two typical kinds of exponential variations (softening and stiffening) were also assumed in [40, 109] for studying the effect of graded material property on pattern formation.

First, we investigate the pattern formation with simply supported boundary conditions and softening Young's modulus $\overline{E}_{s1}$. The first bifurcation occurs at $\lambda = 0.024935$, which happens much earlier than the homogeneous case since the stiffness of the system reduces under the exponential grading Young's modulus situation (see Fig. 2.13 and Fig. 2.5). Instability modes are also captured by computing bifurcation indicators. The first mode is localized near the boundary (see Fig. 2.14). Hence, it seems typically related to the simply supported boundary conditions. The second mode is periodic with little boundary effect. The wavelength is larger than in the homogeneous case due to the softening of the substrate, which is consistent with Eq. (2.7). The third mode corresponds to a period-doubling.

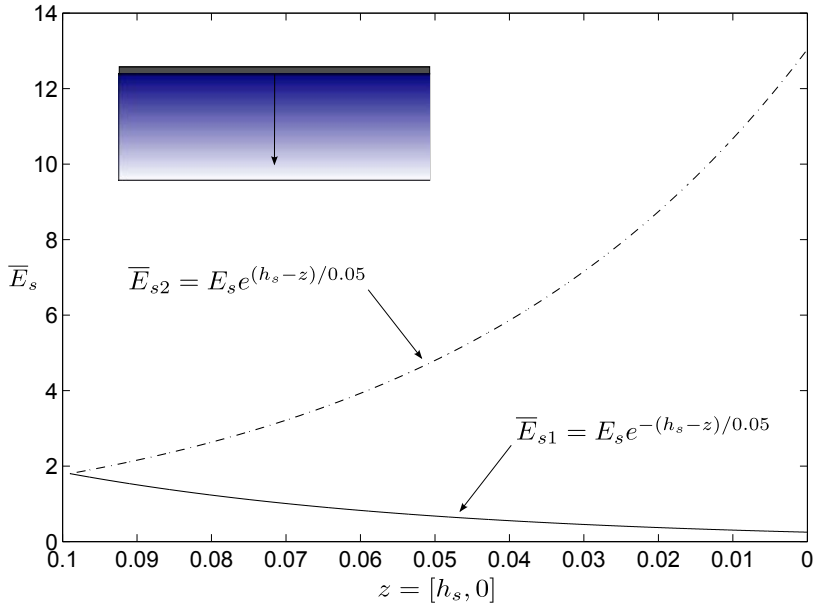

Figure 2.12: Exponential variations of Young's modulus of the substrate along the thickness.

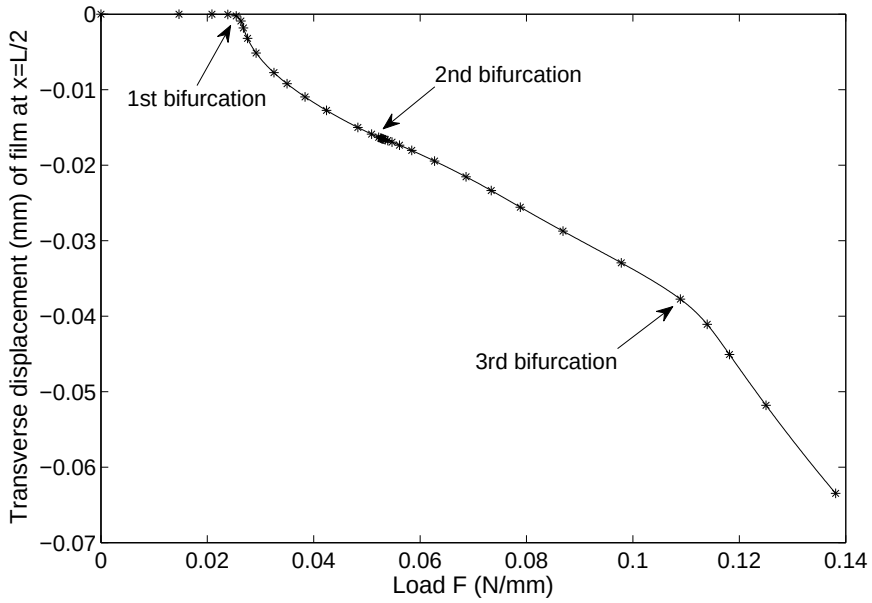

Figure 2.13: Bifurcation curve of FGM substrate with simply supported boundary conditions and softening Young's modulus $\overline{E}_{s1}$. Three bifurcations are observed. ANM parameters: $n = 15$, $\delta = 10^{-5}$, 37 steps. Each point corresponds to one ANM step.

2.5.4 FGM substrate with clamped boundary conditions

We study the pattern formation of FGM substrate with clamped boundary conditions and softening Young's modulus $\overline{E}_{s1}$. Three bifurcations have been observed (see Fig. 2.15). The first bifurcation appears at $\lambda = 0.026732$, which occurs earlier than in the homogeneous case as expected (see Fig. 2.15 and Fig. 2.9). The sequence of wrinkling patterns corresponding to the bifurcation loads and the associated instability modes are shown in Fig. 2.16. The first bifurcation mode corresponds to a sinusoidal envelope while the second one looks like a hyperbolic tangent, as in the case of a homogeneous substrate. The period-doubling mode occurs at the third bifurcation point when $\lambda = 0.099932$.

2.5.5 FGM substrate with stiffening Young's modulus

We explore the wrinkle formation in the case of a stiffening Young's modulus $\overline{E}_{s2}$. Up to now at each bifurcation point, only one branch has been computed, which is proven to be stable because of the positivity of Jacobian matrix. This stability after bifurcation is classical for supercritical bifurcation. In the present case of a stiffening Young's modulus, we try to compute both the fundamental branch and the bifurcated one. The bifurcated branch has been always observed in the previous cases and it naturally results from the path-following algorithm. Bifurcation theory provides theoretical means to define all the

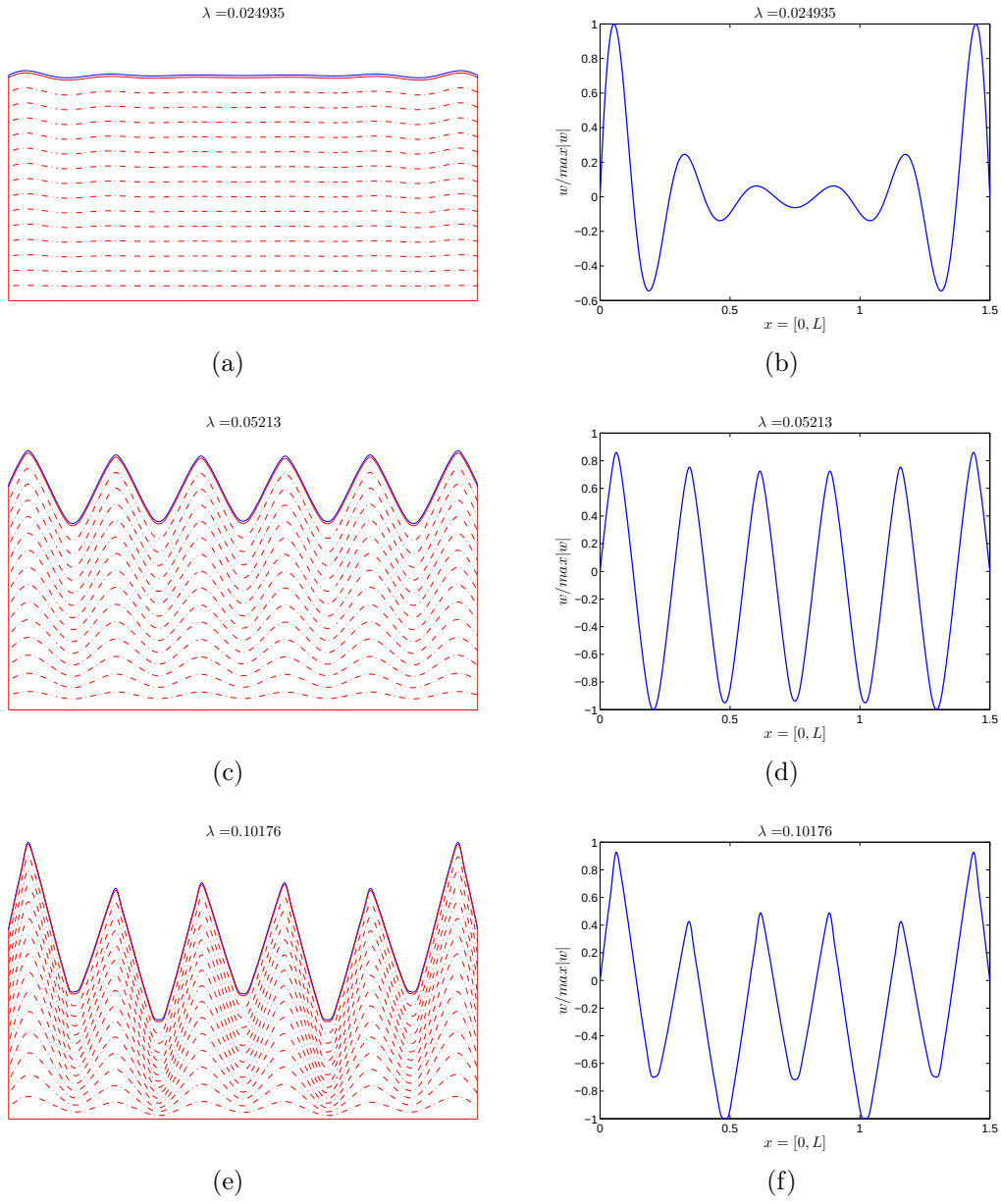

Figure 2.14: The left side shows a sequence of wrinkling patterns corresponding to its critical load determined by bifurcation indicators. The right side presents the associated instability modes. Simply supported boundary conditions and softening Young's modulus $\overline{E}_{s1}$ are applied in the FGM case. (b) The 1st mode. (d) The 2nd mode. (f) The 3rd mode.

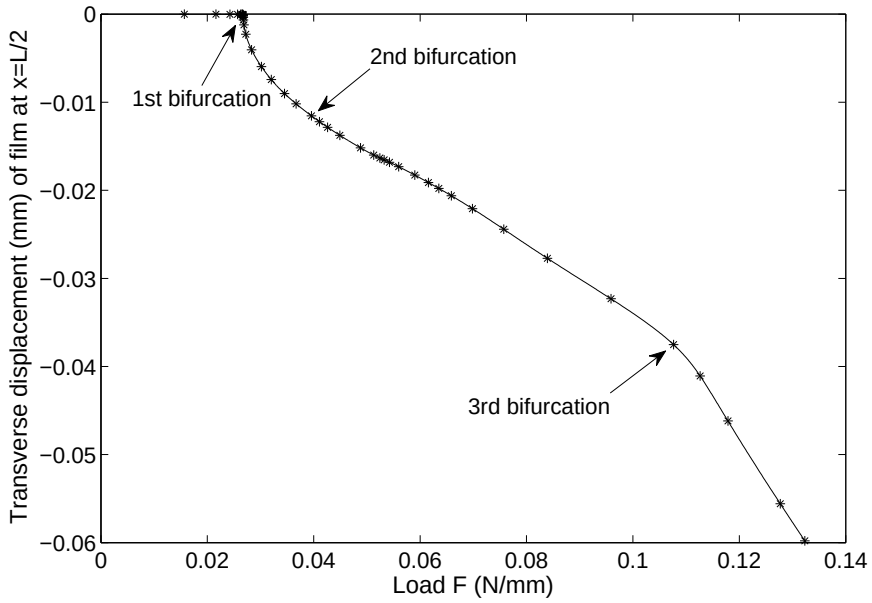

Figure 2.15: Bifurcation curve of FGM substrate with clamped boundary conditions and softening Young's modulus $\overline{E}_{s1}$. Three bifurcations are observed. ANM parameters: $n = 15$, $\delta = 10^{-5}$, 45 steps. Each point corresponds to one ANM step.

branches emanating from a bifurcation point and this can lead to practical algorithms [28, 148]. Nevertheless, the fundamental branch can also be found without changes in the path-following algorithm in Section 2.4.1. The idea is to relax the tolerance δ just before the bifurcation. Practically, as recommended in [13, 47], we keep the same precision parameter $\delta = 10^{-5}$ up to the neighbourhood of the third bifurcation. Then we increase this parameter to $\delta = 10^{-2}$. Consequently, two solution branches clearly distinguish in Fig. 2.17. We checked that the post-bifurcation branch remains accurate despite of the greater value of tolerance δ (residual lower than 10^{-3}) and that the Jacobian matrix is no longer positive along the fundamental solution, as expected theoretically. Similar bifurcation portraits could be found in all the other cases, but the practical interest of computing unstable branches is rather limited.

In Figs. 2.18 and 2.19, the response shows four bifurcation points, the first two ones being very similar to those obtained in the previous cases, but with a shorter wavelength: the first mode is strongly influenced by boundary conditions and the second one corresponds to a uniform amplitude in the bulk. The third and the fourth bifurcation modes are slightly different from those in Fig. 2.8 (homogeneous substrate) and Fig. 2.14 (softening Young's modulus $\overline{E}_{s1}$). Indeed, period-doubling is not observed here, but only a slow modulation of the wrinkle envelopes. Hence, period-doubling mode appears as a possible event that does not happen in any case.

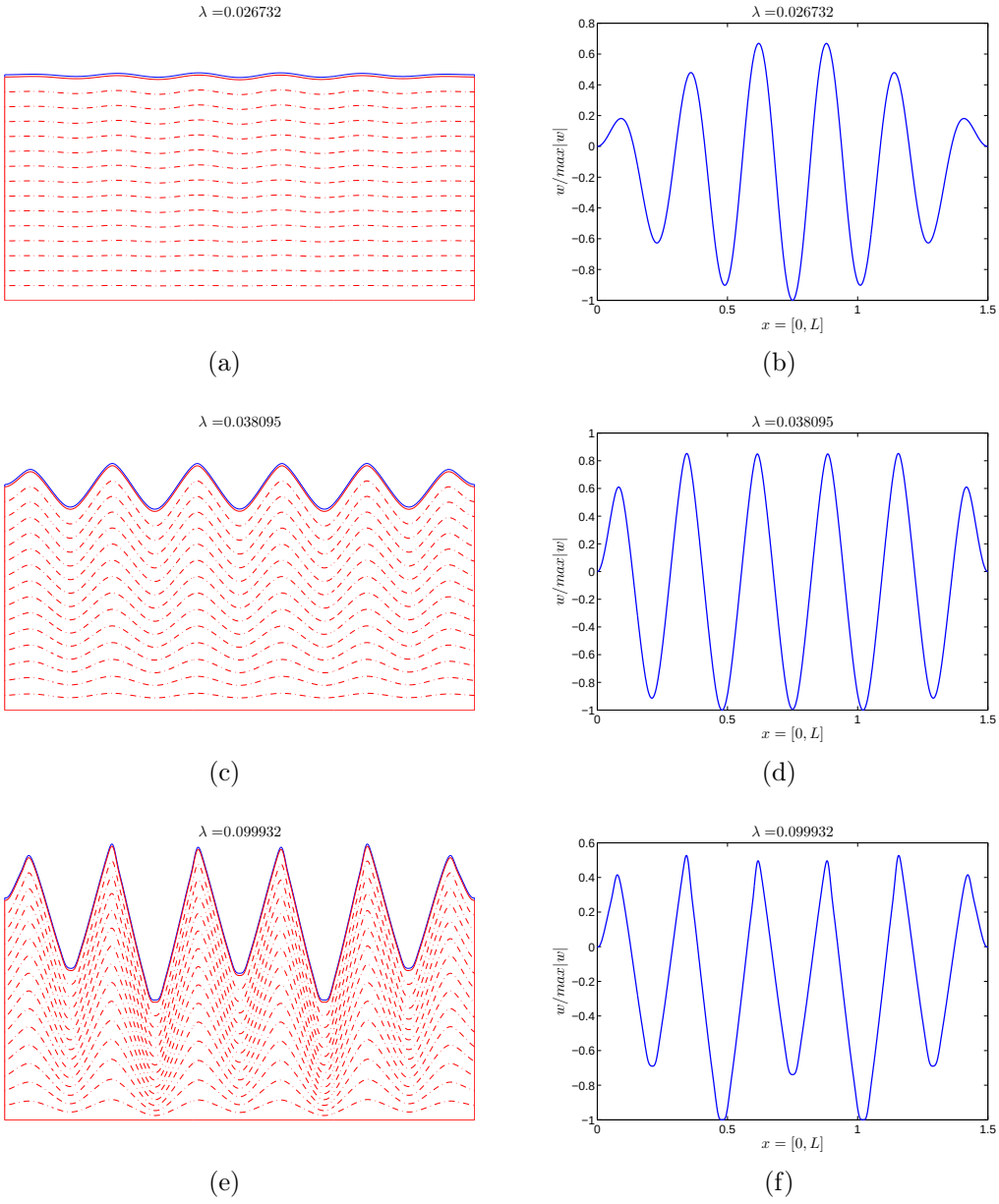

Figure 2.16: The left side shows a sequence of wrinkling patterns corresponding to its critical load determined by bifurcation indicators. The right side presents the associated instability modes. Clamped boundary conditions and softening Young's modulus $\overline{E}_{s1}$ are applied in the FGM case. (b) The 1st mode. (d) The 2nd mode. (f) The 3rd mode.

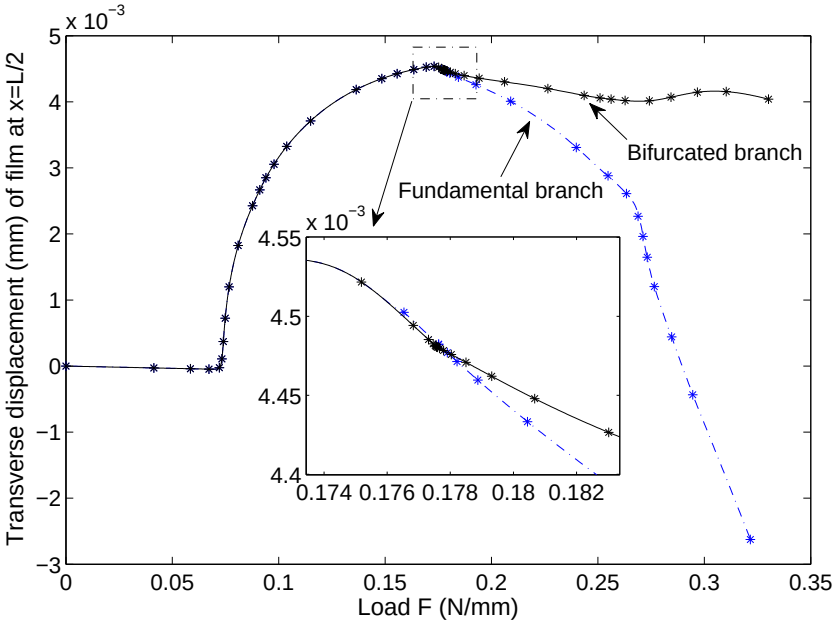

Figure 2.17: Bifurcation curve of FGM substrate with stiffening Young's modulus $\overline{E}_{s2}$ and simply supported boundary conditions. Bifurcated branch and fundamental branch are distinguished. Each point corresponds to one ANM step. ANM parameters: (1) $n = 15$, $\delta = 10^{-5}$, 50 steps for the bifurcated branch; (2) $n = 15$, $\delta = 10^{-5}$, $\delta = 10^{-2}$ after 22 steps for the fundamental branch.

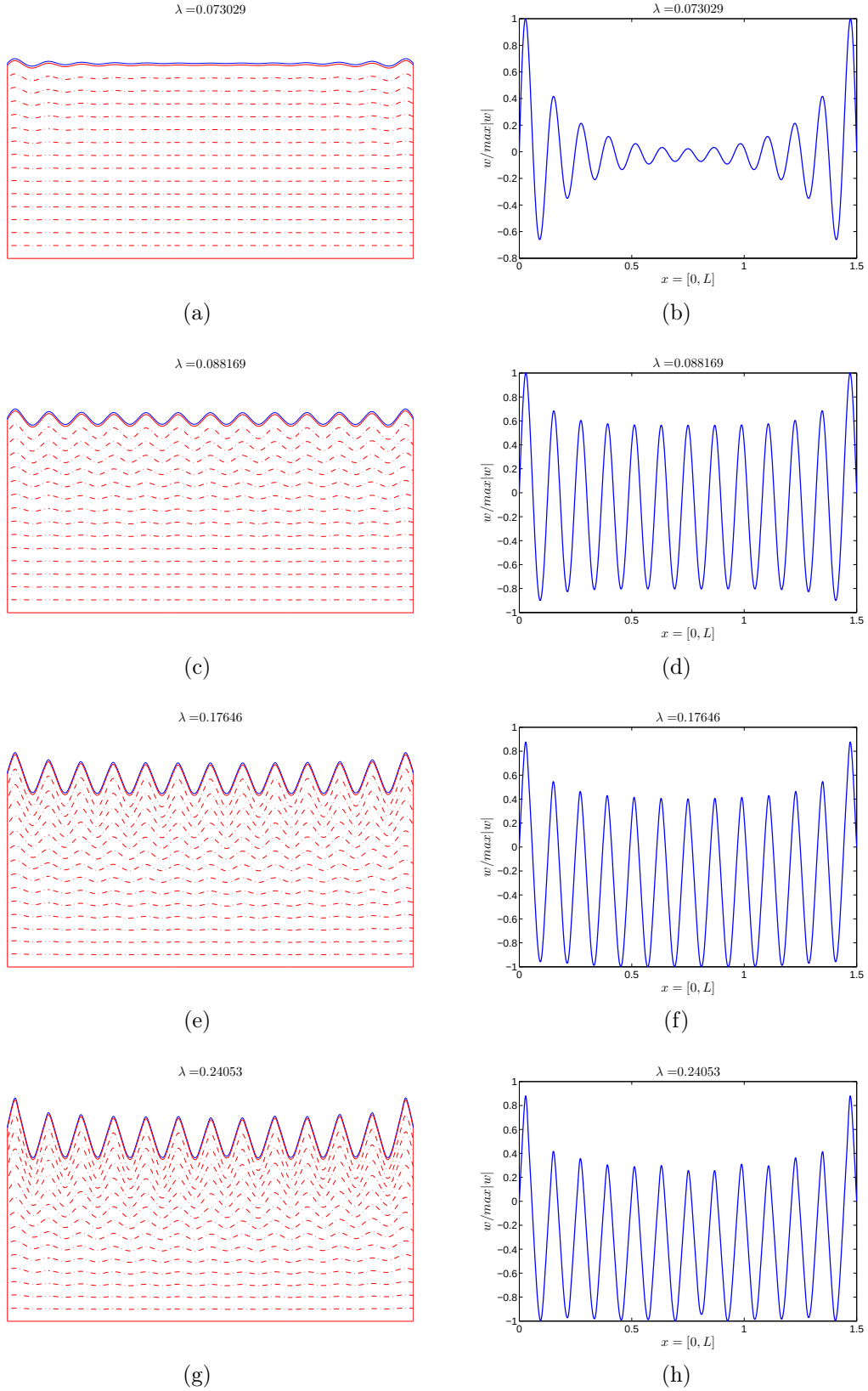

Figure 2.18: The left side shows a sequence of wrinkling patterns corresponding to the bifurcated branch. The right side presents the associated instability modes. Stiffening Young's modulus $\overline{E}_{s2}$ and simply supported boundary conditions are applied in the FGM case. (b) The 1st mode. (d) The 2nd mode. (f) The 3rd mode. (h) The 4th mode.

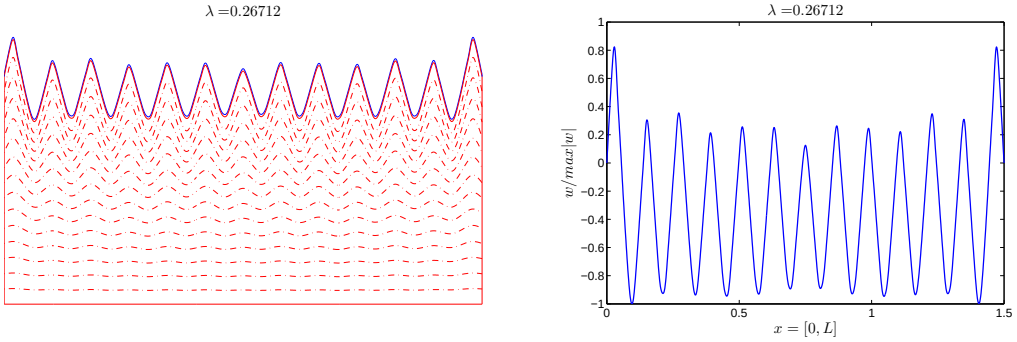

(a) (b)

Figure 2.19: The left side shows the wrinkling pattern corresponding to the fundamental branch. The right side presents the associated 4th instability mode.

2.5.6 Anisotropic substrate

We study the effect of an orthotropic substrate on pattern formation. Simply supported boundary conditions are applied. The elastic matrix of the substrate in Eq. (2.24) becomes

$$[\mathbf{C}^{sn}] = \begin{bmatrix} \dfrac{E_1(1-\nu_{23})}{1-2\nu_{12}\nu_{21}-\nu_{23}} & -\dfrac{E_1\nu_{21}}{\nu_{23}+2\nu_{12}\nu_{21}-1} & 0 \\ -\dfrac{E_2\nu_{12}}{\nu_{23}+2\nu_{12}\nu_{21}-1} & \dfrac{E_2(\nu_{12}\nu_{21}-1)}{(1+\nu_{23})(\nu_{23}+2\nu_{12}\nu_{21}-1)} & 0 \\ 0 & 0 & \dfrac{E_s}{2(1+\nu_{12})} \end{bmatrix}. \tag{2.62}$$

Precisely, here we choose $E_1 = 10E_s$, $E_2 = E_s$, $\nu_{12} = \nu_s$, $\nu_{21} = \nu_s/10$ and $\nu_{23} = \nu_s$.

From Fig. 2.20, one can see that the anisotropic system is slightly stiffer than the isotropic one, but the post-buckling path follows the similar trend as the isotropic case. Furthermore, small step accumulations appear almost in the same loading region in both curves, which implies the bifurcation loads are comparable. Three instability modes are detected by computing bifurcation indicators in the anisotropic case (see Fig. 2.21). The comparison between these three modes in Fig. 2.21 and the final shape in Fig. 2.22 is a little disturbing since a period-doubling appears clearly in the final shape, but not in the modes. Likely this period-doubling grows continuously along the response curve.

2.5.7 Comments

Three types of bifurcation modes have been encountered in the four studied cases. First, a mode localized near the boundary can primarily appear in the case of simply supported boundary conditions. Then the instability pattern tends to be periodic except

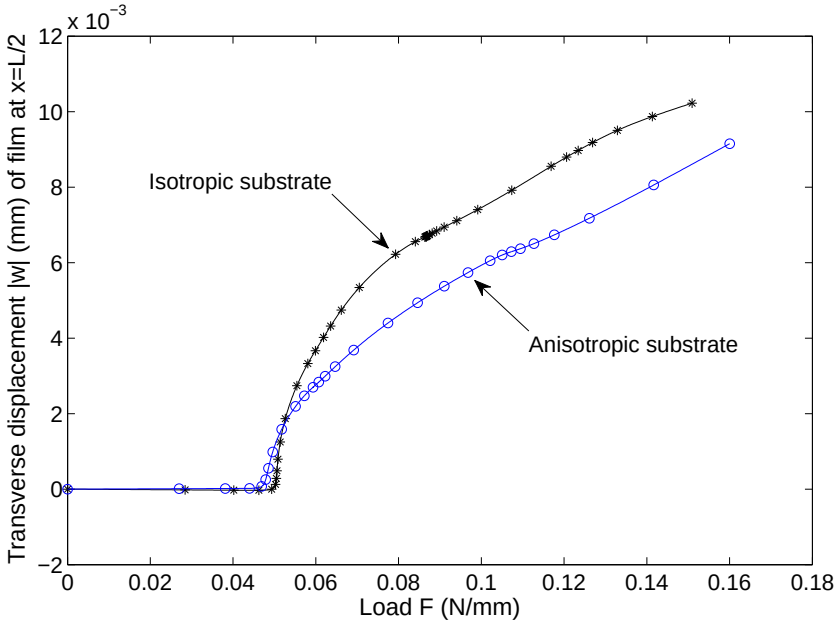

Figure 2.20: Comparison of bifurcation curves between anisotropic substrate and isotropic one. Each point corresponds to one ANM step. ANM parameters: (1) $n = 15$, $\delta = 10^{-5}$, 29 steps for the anisotropic case; (2) $n = 15$, $\delta = 10^{-5}$, 45 steps for the isotropic case.

in the boundary region where the response is influenced by the boundary conditions. Last, this perfect periodicity can be broken by another bifurcation, leading to period-doubling, period-trebling or even period-quadrupling modes. Such a loss of periodicity had been previously discussed, for instance in [39, 163, 146]. Curiously, all the computed bifurcations are supercritical so that the post-bifurcation solutions remain stable.

The responses of the system as well as the third bifurcation mode are represented in Fig. 2.23 as a function of the substrate properties: isotropic homogeneous, orthotropic homogeneous, inhomogeneous softening and stiffening, respectively. The bifurcation portrait seems generic at the beginning: a boundary mode is followed by a second mode that is almost periodic except in the boundary region. The third and eventually fourth bifurcations are no longer periodic, but several forms can be encountered: a clear period-doubling in the FGM softening case, a more confused situation for homogeneous isotropic substrates (see Fig. 2.8) or modulated modes without period-doubling in the FGM stiffening and orthotropic cases.

The multiple bifurcations can be seen as markers of the evolution of instability patterns, but sometimes the pattern can change continuously without obvious bifurcation: such an evolution has been found in the anisotropic case in Section 2.5.6 where period-doubling mode appears in the final shape (see Fig. 2.22), but not in the observed bifurcation modes (see Fig. 2.21). This is not surprising because bifurcation is not a generic singularity and

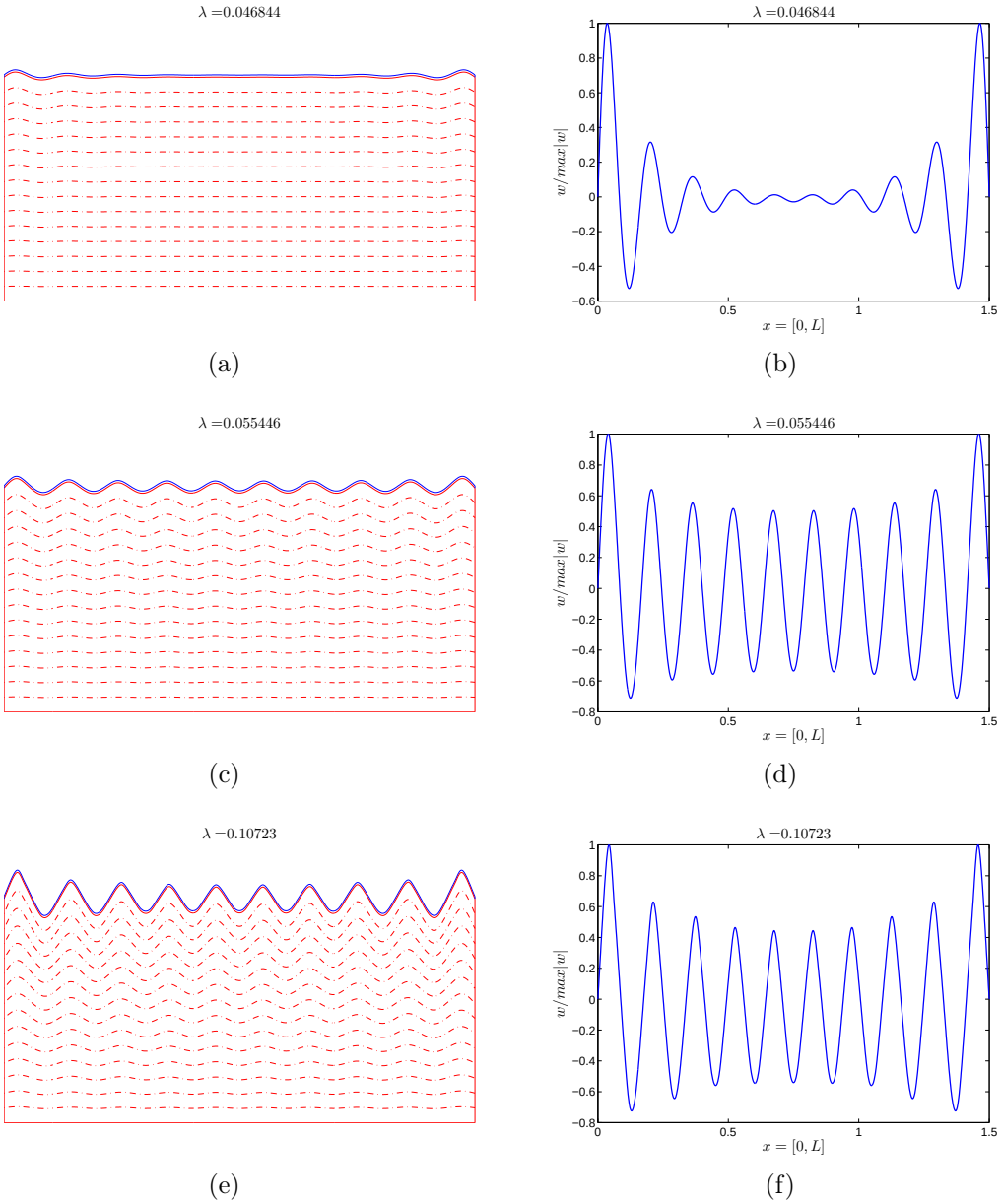

Figure 2.21: The left column shows a sequence of wrinkling patterns corresponding to its critical load determined by bifurcation indicators. The right column presents the associated instability modes. Simply supported boundary conditions are imposed in the anisotropic case. (b) The 1st mode. (d) The 2nd mode. (f) The 3rd mode.

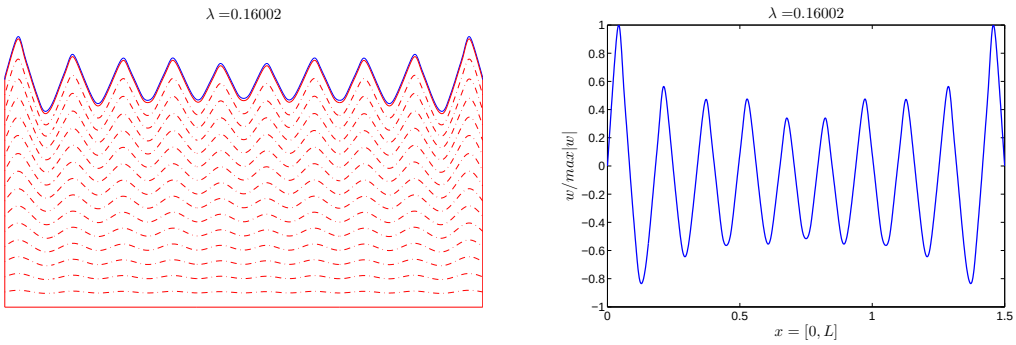

(a) (b)

Figure 2.22: Anisotropic substrate with simply supported boundary conditions under compression: (a) wrinkling pattern in the final step, (b) final shape of the film.

can be destroyed by a small perturbation of the system.

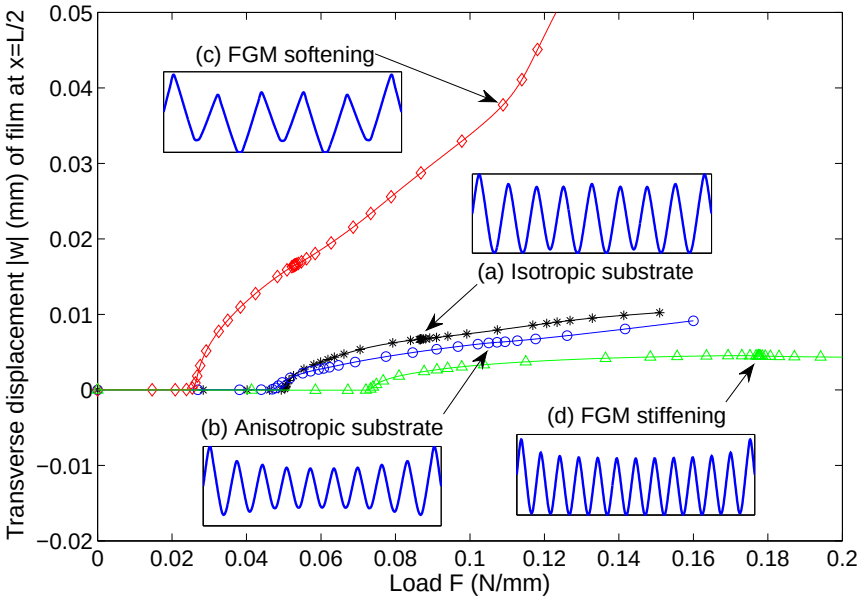

Figure 2.23: Comparison of bifurcation curves among four different cases with simply supported boundary conditions: (a) isotropic substrate, (b) anisotropic substrate, (c) FGM substrate with softening Young's modulus, (d) FGM substrate with stiffening Young's modulus.

2.6 Chapter conclusion

Wrinkling phenomena of stiff films bound to compliant substrates were investigated from the quantitative standpoint, with a particular attention on the effect of boundary

conditions, which was rarely studied previously. A classical model was used associating geometrically nonlinear beam for the film and linear elasticity for the substrate. The presented results rely heavily on robust solution techniques based on the ANM that is able to detect secondary bifurcations and to compute bifurcation modes on a nonlinear response curve. Probably, it would be rather difficult to detect all the bifurcations found in this chapter by conventional numerical methods. Six cases have been studied that are characterized by the boundary conditions and by the material properties of the substrate (homogeneous, graded material and orthotropic). Up to four successive bifurcation points have been found and the bifurcation portrait seems more or less generic. In the case of a simply supported film/substrate system, the first mode is a boundary mode. Then the pattern tends to be periodic in the bulk and the response near the ends is locally influenced by boundary conditions. When the amplitude increases, the periodicity is broken and one can observe period-doubling bifurcations or appearance of modulated patterns.

The present study is limited to moderate rotations and 2D domains. It would be an interesting challenge to extend this analysis in 3D cases [43, 35], without too restrictive assumptions, but the computation time could increase dramatically. In this respect, an idea is to introduce reduced-order models, for instance via the technique of slowly variable Fourier coefficients [54, 56, 122, 58]. Nevertheless, 3D film/substrate models are essential because the periodicity can be broken by 3D bifurcations before the occurrence of period-doubling mode [35, 159].

Chapter 3

Pattern formation modeling of 3D film/substrate systems

Contents

3.1 Introduction

Surface morphological instabilities of stiff thin layers attached on soft substrates are of growing interest in a number of academic domains including micro/nano-fabrication and metrology [29], flexible electronics [133], mechanical and physical measurement of

material properties [79], and biomedical engineering [70] as well as biomechanics [115]. The pioneering work of Bowden *et al.* [29] leads to several theoretical and numerical works in terms of stability study devoted to linear perturbation analysis and nonlinear buckling analysis [87, 43, 88, 89, 85, 86, 93, 120, 151, 143, 9, 10, 11, 109]. In most of these papers, the 2D or 3D spatial problem is discretized by either spectral method or Fast Fourier Transform (FFT) algorithm, which is fairly inexpensive but prescribes periodic boundary conditions. In this framework, several types of wrinkling modes have been observed, including sinusoidal, checkerboard, herringbone (see Fig. 3.1) and disordered labyrinth patterns. It has been early recognized by Chen and Hutchinson [43] that such systems can also be studied by finite element methods, which is more computationally expensive but more flexible to describe complex geometries and more general boundary conditions, and allows using commercial computer codes. In addition, 3D finite element simulations of film/substrate instability were studied only in few papers [43, 35]. Furthermore, the post-buckling evolution and mode transition of surface wrinkles in 3D film/substrate systems are rarely studied and only in the case of periodic cells [35], which still deserves further investigation, especially through finite element method that can provide the overall view and insight into the formation and evolution of wrinkle patterns in more general conditions. Can one obtain the variety of 3D wrinkling modes reported in the literature by using classical finite element models? Can one describe the whole evolution path of buckling and post-buckling of this system? Under what kind of loading and boundary conditions can each type of patterns be observed at what value of bifurcation loads? These questions will be addressed in this chapter.

This study aims at applying advanced numerical methods for bifurcation analysis to typical cases of film/substrate system and focuses on the post-buckling evolution involving multiple bifurcations and symmetry-breakings, for the first time with a particular attention on the effect of boundary conditions. For this purpose, a 2D finite element (FE) model was previously developed for multiperiodic bifurcation analysis of wrinkle formation [160]. In this model, the film undergoing moderate deflections is described by Föppl-von Kármán nonlinear elastic theory, while the substrate is considered to be a linear elastic solid. Following the same strategy, we extend the work to 3D cases by coupling shell elements to represent the film and block elements to describe the substrate. Therefore, large displacements and rotations in the film can be considered and the spatial distribution of wrinkling modes like sinusoidal, checkerboard and herringbone (see Fig. 3.1) could be investigated.

Surface instability of stiff layers on soft materials usually involves strong geometrical nonlinearities, large rotations, large deformations, loading path dependence, multiple symmetry-breakings and other complexities, which makes the numerical resolution quite

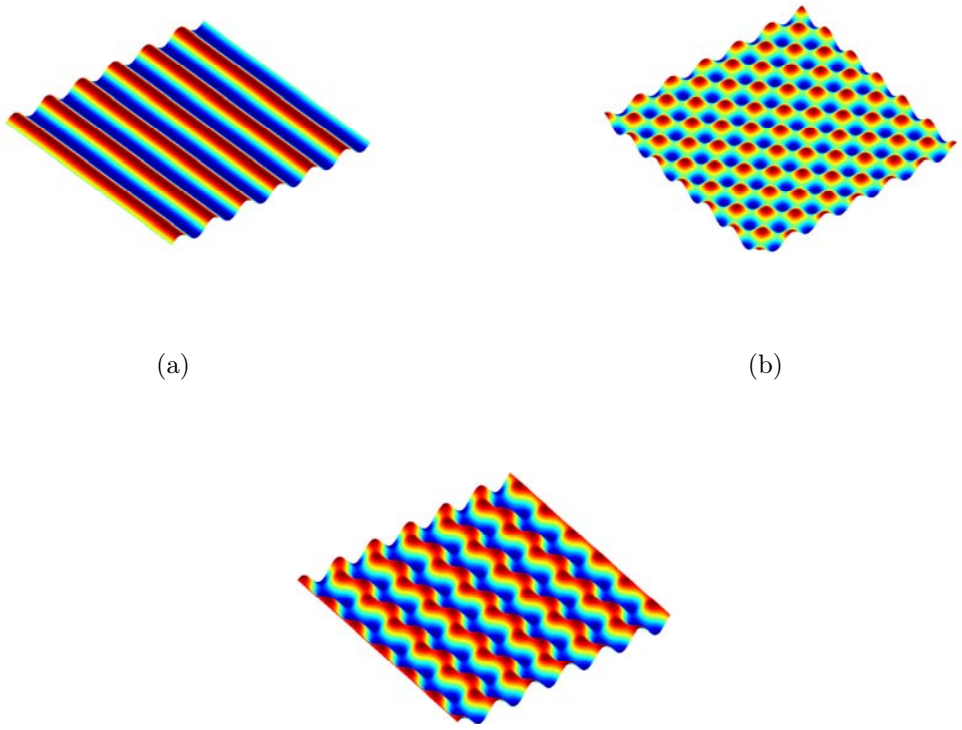

(a) (b)

(c)

Figure 3.1: Schematics of wrinkling patterns: (a) sinusoidal mode, (b) checkerboard mode, (c) herringbone mode (a periodic array of zigzag wrinkles).

difficult. The morphological post-buckling evolution and mode shape transition beyond the critical load are incredibly complicated, especially in 3D cases, and the conventional numerical methods have difficulties in detecting all the bifurcation points and associated instability modes on their evolution paths. To solve the resulting nonlinear equations, continuation techniques give efficient numerical tools to compute these nonlinear response curves [61, 6]. In this chapter, we adopted Asymptotic Numerical Method (ANM) [52, 46, 45, 47] which appears as a significantly efficient continuation technique without any corrector iteration. The underlying principle of the ANM is to build up the nonlinear solution branch in the form of relatively high order truncated power series. The resulting series are then introduced into the nonlinear problem, which helps to transform it into a sequence of linear problems that can be solved numerically. In this way, one gets approximations of the solution path that are very accurate inside the radius of convergence. Since few global stiffness matrix inversions are required (only one per step), the performance in terms of computing time is quite attractive. Moreover, as a result of the local polynomial approximations of the branch within each step, the algorithm is remarkably robust and fully automatic. Furthermore, unlike incremental-iterative methods, the arc-length step size in the ANM is fully adaptive since it is determined *a posteriori* by the algorithm. A small radius of convergence and step accumulation appear around the bifurcation and imply its presence.

Detection of bifurcation points is really a challenge. Despite a lot of progresses have been made using the Newton−Raphson method, an efficient and reliable algorithm is quite difficult to be established. Indeed, it would cost considerable computing time in the bisection sequence and corrector iteration because of very small step lengths close to the bifurcation. In the ANM framework, a bifurcation indicator has been proposed to detect bifurcation points [27, 148, 96, 28]. It is a scalar function obtained through introducing a fictitious perturbation force in the problem, which becomes zero exactly at the bifurcation point. Indeed, this indicator measures the intensity of the system response to perturbation forces. By evaluating it through an equilibrium branch, all the critical points existing on this branch and the associated bifurcation modes can be determined.

This chapter explores the occurrence and post-bifurcation evolution of sinusoidal, checkerboard and herringbone mode in greater depth. The work presented in this chapter, *i.e.* 3D finite element modeling for instabilities in thin films on soft substrates, is considered as an interesting study and a valuable contribution to film/substrate instability problems, which has been published in *International Journal of Solids and Structures* [159].

3.2 3D mechanical model

We consider an elastic thin film bonded to an elastic substrate, which can buckle under compression. Upon wrinkling, the film elastically buckles to relax the compressive stress and the substrate concurrently deforms to maintain perfect bonding at the interface. In the following, the elastic potential energy of the system, is considered in the framework of Hookean elasticity. The film/substrate system is considered to be three-dimensional and the geometry is as shown in Fig. 3.2. Let x and y be in-plane coordinates, while z is the direction perpendicular to the mean plane of the film/substrate. The width and length of the system are denoted by L_x and L_y, respectively. The parameters h_f, h_s and h_t represent, respectively, the thickness of the film, the substrate and the total thickness of the system. Young's modulus and Poisson's ratio of the film are denoted by E_f and ν_f, while E_s and ν_s are the corresponding material properties for the substrate.

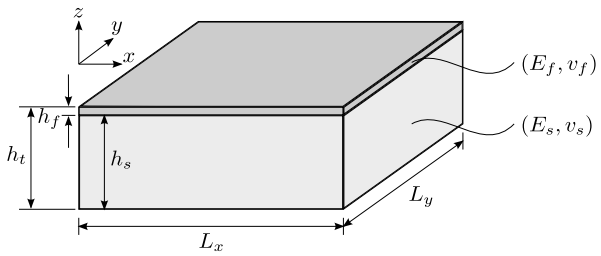

Figure 3.2: Geometry of film/substrate system.

The 3D film/substrate system will be modeled in a rather classical way, the film being represented by a thin shell model to allow large rotations while the substrate being modeled by small strain elasticity. Indeed, the considered instabilities are governed by nonlinear geometric effects in the stiff material, while these effects are much smaller in the soft material. Since the originality of this chapter lies in the numerical treatment of multiple bifurcations, we limit ourselves to this classical framework for the sake of consistency with previous literatures. The large rotation framework for the film has been chosen because of the efficiency of the associated finite element. Note that the same choice of a shell with finite rotations coupled with small strain elasticity in the substrate had been presented for numerical reasons in [43]. The application range of this model is limited by two small parameters: the aspect ratio of the film h_f/L_x, h_f/L_y and the stiffness ratio E_s/E_f. In the case of a larger ratio E_s/E_f, a finite strain model should be considered in the substrate as in [92] and this would be not too difficult to be implemented in our framework [126].

3.2.1 Nonlinear shell formulation for the film

Challenges in the numerical modeling of such film/substrate systems come from the extremely large ratio of Young's modulus ($E_f/E_s \approx \mathcal{O}(10^5)$) as well as the big thickness difference ($h_s/h_f \geqslant \mathcal{O}(10^2)$), which requires very fine mesh if using 3D block elements both for the film and for the substrate. Since finite rotations of middle surface and small strains are considered in the thin film, nonlinear shell formulations are quite suitable and efficient for modeling. Hereby, a three-dimensional shell formulation proposed by Bücheter *et al.* [33] is applied. It is based on a 7-parameter theory including a linear varying thickness stretch as extra variable, which allows applying a complete 3D constitutive law without condensation. It is distinguished from classical shell models that are usually based on degenerated constitutive relations (*e.g.* Kirchhoff−Love, Reissner−Mindlin theories). It is also incorporated via the Enhanced Assumed Strain (EAS) concept proposed by Simo and Rifai [142] to improve the element performance and to avoid locking phenomena such as Poisson thickness locking, shear locking or volume locking. This hybrid shell formulation can describe large deformation problems with hyperelasticity and has been successively applied to nonlinear elastic thin-walled structures such as cantilever beam, square plate, cylindrical roof and circular deep arch [137, 162, 28].

Geometry and kinematics of shell element are illustrated in Fig. 3.3, where the position vectors are functions of curvilinear coordinates $(\theta^1, \theta^2, \theta^3)$. The geometry description relies on the middle surface θ^1 and θ^2 of the shell, while θ^3 represents the coordinate in the thickness direction. The current configuration is defined by the middle surface displacement and the relative displacement between the middle and the upper surfaces. The large rotations are taken into account without any rotation matrix since the current direction vector is obtained by adding a vector to one of the initial configurations.

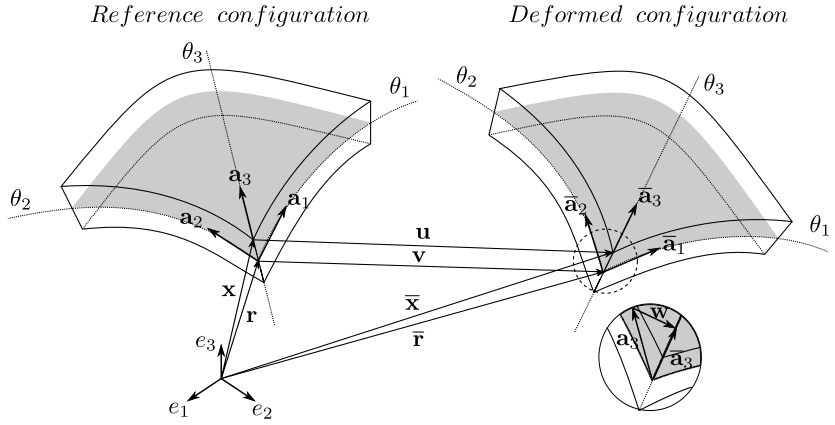

Figure 3.3: Geometry and kinematics of shell.

In the initial undeformed configuration, the position vector $\mathbf{x}$ representing any point

in the shell can be defined as

$$\mathbf{x}(\theta^\alpha, \theta^3) = \mathbf{r}(\theta^\alpha) + \theta^3 \mathbf{a}_3(\theta^\alpha), \tag{3.1}$$

where $\mathbf{r}(\theta^\alpha)(\alpha = 1, 2)$ denotes the projection of $\mathbf{x}$ in the middle surface and θ^3 describes its perpendicular direction with $\theta^3 \in [-h_f/2, h_f/2]$ in which h_f is the reference thickness of shell. The normal vector of middle surface is represented by $\mathbf{a}_3 = \mathbf{a}_1 \times \mathbf{a}_2$.

Similarly, in the current deformed configuration, we define the position of point $\mathbf{x}$ by the vector $\overline{\mathbf{x}}$:

$$\overline{\mathbf{x}}(\theta^\alpha, \theta^3) = \overline{\mathbf{r}}(\theta^\alpha) + \theta^3 \overline{\mathbf{a}}_3(\theta^\alpha), \tag{3.2}$$

where

$$\begin{cases} \overline{\mathbf{r}} = \mathbf{r} + \mathbf{v}, \\ \overline{\mathbf{a}}_3 = \mathbf{a}_3 + \mathbf{w}. \end{cases} \tag{3.3}$$

Therefore, the displacement vector associated with an arbitrary material point in the shell, linearly varies along the thickness direction reads

$$\mathbf{u}(\theta^\alpha, \theta^3) = \overline{\mathbf{x}} - \mathbf{x} = \mathbf{v}(\theta^\alpha) + \theta^3 \mathbf{w}(\theta^\alpha). \tag{3.4}$$

Totally, six degrees of freedom can be distinguished in Eq. (3.4) to describe the shell kinematics: three vector components related to the translation of the middle surface (v_1, v_2, v_3) and other three components updating the direction vector (w_1, w_2, w_3).

The Green−Lagrange strain tensor is used to describe geometrical nonlinearity, which can be expressed in the covariant base:

$$\gamma = \frac{1}{2}\left(\overline{g}_{ij} - g_{ij}\right) \mathbf{g}^i \otimes \mathbf{g}^j \quad with \quad i, j = 1, 2, 3, \tag{3.5}$$

where $\mathbf{g}^i$ are the contravariant base vectors, while $g_{ij} = \mathbf{g}^i \cdot \mathbf{g}^j$ and $\overline{g}_{ij} = \overline{\mathbf{g}}^i \cdot \overline{\mathbf{g}}^j$ respectively represent the components of covariant metric tensor in the initial configuration and the deformed one [33].

The hybrid shell formulation is derived from a three-field variational principle based on the Hu−Washizu functional [33, 162]. The stationary condition can be written as

$$\mathbf{\Pi}_{EAS}\left(\mathbf{u}, \widetilde{\gamma}, \mathbf{S}\right) = \int_\Omega \left\{ {}^t\mathbf{S} : \left(\gamma_u + \widetilde{\gamma}\right) - \frac{1}{2} {}^t\mathbf{S} : \mathbf{D}^{-1} : \mathbf{S} \right\} \mathrm{d}\Omega - \lambda \mathbf{P}_e(\mathbf{u}), \tag{3.6}$$

where $\mathbf{D}$ is the elastic stiffness tensor. The unknowns are, respectively, the displacement field $\mathbf{u}$, the second Piola−Kirchhoff stress tensor $\mathbf{S}$ and the compatible Green−Lagrange strain γ_u. The enhanced assumed strain $\widetilde{\gamma}$, satisfies the condition of orthogonality with

respect to the stress field. The work of external load is denoted by $\mathbf{P}_e(\mathbf{u})$, while λ is a scalar load parameter.

Concerning the enhanced assumed strain $\widetilde{\gamma}$, classical shell kinematics requires the transversal strain field to be zero ($\gamma_{33} = 0$). In reality, since 3D constitutive relations are concerned, this condition is hardly satisfied due to Poisson effect, especially for bending dominated cases. This phenomenon is commonly referred to as "Poisson thickness locking". To remedy this issue, an enhanced assumed strain $\widetilde{\gamma}$ contribution has been introduced in the shell formulation [33], acting across the shell thickness direction and supplementing the compatible strain field γ_u. It describes the linear variation of the the thickness stretch or compression, and is expressed with respect to the local curvilinear coordinates θ^3:

$$\widetilde{\gamma} = \theta^3 \widetilde{\gamma}_{33} \mathbf{g}^3 \otimes \mathbf{g}^3 \quad with \quad \widetilde{\gamma}_{33} = \widetilde{\gamma}_{33}(\theta^\alpha), \tag{3.7}$$

and satisfies the condition of orthogonality with respect to the stress field $\mathbf{S}$:

$$\int_\Omega {}^t\mathbf{S} : \widetilde{\gamma} \, \mathrm{d}\Omega = 0. \tag{3.8}$$

In this way, "spurious" transversal strains induced by Poisson effect for bending dominated kinematics are balanced by the assumed strain $\widetilde{\gamma}$, which clears the "thickness locking" problem. This approach is applied in this chapter, since the associated finite element is very efficient, especially for very thin shells [162, 28].

A 8-node quadrilateral element with reduced integration is utilized for the 7-parameter shell formulation. The enhanced assumed strain $\widetilde{\gamma}$ does not require inter element continuity, neither contribute to the total number of nodal degrees of freedom. Therefore, it can be eliminated by condensation at the element level, which preserves the formal structure of a 6-parameter shell theory with totally 48 degrees of freedom per element.

3.2.2 Linear elasticity for the substrate

Since the displacement, rotation and strain remain relatively small in the substrate, the linear isotropic elasticity theory with updated geometry can accurately describe the substrate. The nonlinear strain-displacement behavior has essentially no influence on the results of interest [43].

The potential energy of the substrate can be expressed as

$$\mathbf{\Pi}_s(\mathbf{u}_s) = \frac{1}{2} \int_\Omega {}^t\varepsilon : \mathbf{L}_s : \varepsilon \mathrm{d}\Omega - \lambda \mathbf{P}_e(\mathbf{u}_s), \tag{3.9}$$

where $\mathbf{L}_s$ is the elastic matrix of the substrate. In this chapter, 8-node linear block

elements with reduced integration are applied to discretize the substrate, with totally 24 degrees of freedom on each block element.

3.2.3 Connection between the film and the substrate

As the film is bonded to the substrate, the displacement should be continuous at the interface. However, the shell elements for the film and 3D block elements for the substrate cannot be simply joined directly since they belong to dissimilar elements. Therefore, additional incorporating constraint equations have to be employed. Hereby, Lagrange multipliers are applied to couple the corresponding node displacements in compatible meshes between the film and the substrate (see Fig. 3.4). Note that using 8-node linear block element here is only for coupling convenience, 20-node quadratic block element would be another good candidate, while both of them follow the same coupling strategy. Consequently, the stationary function of film/substrate system is given in a Lagrangian form:

$$\mathscr{L}(\mathbf{u}_f, \mathbf{u}_s, \ell) = \mathbf{\Pi}_{EAS} + \mathbf{\Pi}_s + \sum_{node\ i} \ell_i \left[\mathbf{u}_f^-(i) - \mathbf{u}_s(i)\right], \tag{3.10}$$

in which

$$\mathbf{u}_f^-(i) = \mathbf{v}(i) - \frac{h_f}{2}\mathbf{w}(i). \tag{3.11}$$

where the displacements of the film and the substrate are respectively denoted as $\mathbf{u}_f$ and $\mathbf{u}_s$, while the Lagrange multipliers are represented by ℓ. At the interface, the displacement continuity is satisfied at the same nodes and connects the bottom surface of the film ($\mathbf{u}_f^-$) and the top surface of the substrate. From Eq. (3.10), three equations are obtained according to $\delta\mathbf{u}_f$, $\delta\mathbf{u}_s$ and $\delta\ell$:

$$\begin{cases} \delta\mathbf{\Pi}_{EAS} + \sum\limits_{node\ i} \ell_i \delta\mathbf{u}_f^-(i) = 0, \\ \delta\mathbf{\Pi}_s - \sum\limits_{node\ i} \ell_i \delta\mathbf{u}_s(i) = 0, \\ \sum\limits_{node\ i} \delta\ell_i \mathbf{u}_f^-(i) - \sum\limits_{node\ i} \delta\ell_i \mathbf{u}_s(i) = 0. \end{cases} \tag{3.12}$$

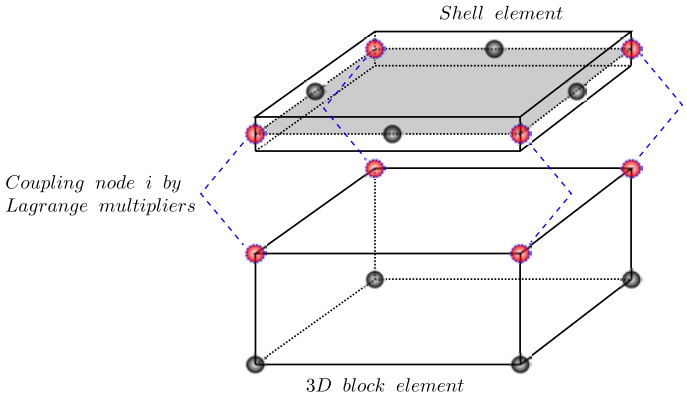

Figure 3.4: Sketch of coupling at the interface.

3.3 Resolution technique and bifurcation analysis

Asymptotic Numerical Method (ANM) [52, 46, 45, 47] is used to solve the resulting nonlinear equations. The ANM is a path-following technique that is based on a succession of high order power series expansions (perturbation technique) with respect to a well chosen path parameter. It appears as an efficient continuation predictor without any corrector iteration. Moreover, one can get approximations of the solution path that are very accurate inside the radius of convergence. In this chapter, the main interest of the ANM is its ability to detect bifurcation points. First, small steps are often associated with the occurrence of a bifurcation. Then, a bifurcation indicator will be defined, which allows exactly detecting the bifurcation load and the corresponding nonlinear mode.

3.3.1 Path-following technique

The resulting nonlinear problem (3.12) can be rewritten as

$$\delta\mathscr{L}(\mathbf{u}_f, \mathbf{u}_s, \ell) = \langle \mathbf{R}(\mathbf{U}, \lambda), \delta\mathbf{U} \rangle = 0, \tag{3.13}$$

in which

$$\mathbf{R}(\mathbf{U}, \lambda) = \mathbf{L}(\mathbf{U}) + \mathbf{Q}(\mathbf{U}, \mathbf{U}) - \lambda\mathbf{F} = 0, \tag{3.14}$$

where $\mathbf{U} = (\mathbf{u}_f, \mathbf{u}_s, \ell)$ is a mixed vector of unknowns, $\mathbf{R}$ the residual vector, $\mathbf{L}(\cdot)$ a linear operator, $\mathbf{Q}(\cdot, \cdot)$ a quadratic one and $\mathbf{F}$ the external load vector. The external load parameter is denoted as a scalar λ. The principle of the ANM continuation consists in describing the solution path by computing a succession of truncated power series expansions. From a known solution point $(\mathbf{U}_0, \lambda_0)$, the solution $(\mathbf{U}, \lambda)$ is expanded into truncated power

series of a perturbation parameter a:

$$\mathbf{U}(a) = \mathbf{U}_0 + \sum_{p=1}^{n} a^p \mathbf{U}_p = \mathbf{U}_0 + a\mathbf{U}_1 + a^2\mathbf{U}_2 + \ldots + a^n\mathbf{U}_n, \tag{3.15}$$

$$\lambda(a) = \lambda_0 + \sum_{p=1}^{n} a^p \lambda_p = \lambda_0 + a\lambda_1 + a^2\lambda_2 + \ldots + a^n\lambda_n, \tag{3.16}$$

$$a = \langle \mathbf{u} - \mathbf{u}_0, \mathbf{u}_1 \rangle + (\lambda - \lambda_0)\,\lambda_1, \tag{3.17}$$

where n is the truncation order of the series. Eq. (3.17) defines the path parameter a that can be identified to an arc-length parameter. By introducing Eqs. (3.15) and (3.16) into Eqs. (3.13) and (3.17), then equating the terms at the same power of a, one can obtain a set of linear problems.

The maximum value of the path parameter a should be automatically defined by analyzing the convergence of the power series at each step. The a_{max} can be based on the difference of displacements at two successive orders that must be smaller than a given precision parameter δ:

$$\text{Validity range: } a_{max} = \left(\delta \frac{\|\mathbf{u}_1\|}{\|\mathbf{u}_n\|} \right)^{1/(n-1)}, \tag{3.18}$$

where the notation $\|\cdot\|$ stands for the Euclidean norm. Unlike incremental-iterative methods, the arc-length step size a_{max} is adaptive since it is determined *a posteriori* by the algorithm. When there is a bifurcation point on the solution path, the radius of convergence is defined by the distance to the bifurcation. Thus, the step length defined in Eq. (3.18) becomes smaller and smaller, which looks as if the continuation process "knocks" against the bifurcation [13]. This accumulation of small steps is a very good indicator of the presence of a singularity on the path. All the bifurcations can be easily identified in this way by the user without any special tool.

It is worth mentioning that there are only two parameters controlling the algorithm. The first one is the truncation order n of the series. It was previously discussed that the optimal truncation order should be large enough between 15 and 20, but bigger values (*e.g.* $n = 50$) lead to good results for large scale problems as well [121]. Another important parameter is the chosen tolerance δ that affects the residual. For instance, very small values of tolerance (*e.g.* $\delta = 10^{-6}$) ensure quite a high accuracy and a pretty robust path-following process.

3.3.2 Detection of bifurcation points

Detection of exact bifurcation points is a challenge. It takes much computation time in the bisection sequence and in many Newton−Raphson iterations because of small steps close to the bifurcation. In the framework of the ANM, a bifurcation indicator has been proposed to capture exact bifurcation points in an efficient and reliable algorithm [27, 148, 96, 28].

Let $\Delta\mu\mathbf{f}$ be a fictitious perturbation force applied to the structure at a given deformed state $(\mathbf{U}, \lambda)$, where $\Delta\mu$ is the intensity of the force $\mathbf{f}$ and $\Delta\mathbf{U}$ is the associated response. Through superposing the applied load and perturbation, the fictitious perturbed equilibrium can be described by

$$\mathbf{L}\left(\mathbf{U}+\Delta\mathbf{U}\right)+\mathbf{Q}\left(\mathbf{U}+\Delta\mathbf{U},\mathbf{U}+\Delta\mathbf{U}\right)=\lambda\mathbf{F}+\Delta\mu\mathbf{f}. \tag{3.19}$$

Considering the equilibrium state and neglecting the quadratic terms, one can obtain the following auxiliary problem:

$$\mathbf{L}_t\left(\Delta\mathbf{U}\right)=\Delta\mu\mathbf{f}, \tag{3.20}$$

where $\mathbf{L}_t(\cdot)=\mathbf{L}(\cdot)+2\mathbf{Q}(\mathbf{U},\cdot)$ is the tangent operator at the equilibrium point $(\mathbf{U},\lambda)$. If $\Delta\mu$ is imposed, this leads to a displacement tending to infinity in the vicinity of the critical points. To avoid this problem, the following displacement based condition is imposed:

$$\left\langle\mathbf{L}_t^0\left(\Delta\mathbf{U}-\Delta\mathbf{U}_0\right),\Delta\mathbf{U}_0\right\rangle=0, \tag{3.21}$$

where $\mathbf{L}_t^0(\cdot)$ is the tangent operator at the starting point $(\mathbf{U}_0,\lambda_0)$ and the direction $\Delta\mathbf{U}_0$ is the solution of $\mathbf{L}_t^0(\Delta\mathbf{U}_0)=\mathbf{f}$. Consequently, $\Delta\mu$ is deduced from the linear system (3.20) and (3.21):

$$\Delta\mu=\frac{\langle\Delta\mathbf{U}_0,\mathbf{f}\rangle}{\langle\mathbf{L}_t^{-1}(\mathbf{f}),\mathbf{f}\rangle}. \tag{3.22}$$

Since the scalar function $\Delta\mu$ represents a measure of the stiffness of structure and becomes zero at the singular points, it can define a bifurcation indicator. It can be directly computed from Eq. (3.22), but it requires to decompose the tangent operator at each point throughout the solution path. For this reason, the system (3.20) and (3.21) can be more efficiently resolved by the ANM.

Goal: find a_b such that: $\mathbf{L}_t\left(\mathbf{U}(a_b)\right)\Delta\mathbf{U}=0$
Method: $\mathbf{L}_t\left(\mathbf{U}(a)\right)\Delta\mathbf{U}=\Delta\mu\mathbf{f}$, $\left\langle\mathbf{L}_t^0\left(\Delta\mathbf{U}-\Delta\mathbf{U}_0\right),\Delta\mathbf{U}_0\right\rangle=0$
Output: when $\Delta\mu(a_b)=0$, $\Delta\mathbf{U}(a_b)$ is the bifurcation mode

In what follows, each field $\Delta\mathbf{U}(a_b)$ is called instability mode or wrinkling mode. Note that it is recommended to use a random perturbation force vector $\mathbf{f}$ [27, 28]. The bifur-

cation indicator in Eq. (3.22) vanishes at singular points only if the fictitious force vector $\mathbf{f}$ is not orthogonal to the instability mode. The choice of a random perturbation force can avoid this problem. It is worth mentioning that the fictitious perturbation force $\mathbf{f}$ influences neither the numerical solutions of the initial problem (3.13) nor the detection of bifurcation points via (3.20) and (3.21), but only the auxiliary unknown $\Delta\mathbf{U}(a)$.

3.4 Results and discussion

Three types of wrinkling patterns, sinusoidal, checkerboard and herringbone, will be investigated under different loading and boundary conditions. On the bottom surface of the substrate, the deflection u_z and the tangential traction are taken to be zero. The material and geometric properties of film/substrate system are similar to those in [151, 143, 29, 160], which is shown in Table 3.1. The different dimensional parameters and loading conditions for each case are presented in Table 3.2 and Fig. 3.5, respectively. The huge ratio of Young's modulus, E_f/E_s, determines the critical wavelength λ_c that remains practically unchanged as the amplitude of the wrinkles increases [89, 160]. Poisson's ratio is a dimensionless measure of the degree of compressibility. Compliant materials in the substrate, such as elastomers, are nearly incompressible with $\nu_s = 0.48$. A relative thin film has been chosen so that an isotropic and homogeneous system is not parameter dependent [160]. In order to trigger a transition from the fundamental branch to the bifurcated one, small perturbation forces, $f_z = 10^{-8}$, are imposed in the film. The introduction of such small perturbation forces is quite a common technique in the solution of bifurcation problems by continuation techniques [61, 6], even when using commercial finite element codes. This artifice could be avoided by applying a specific procedure to compute the bifurcation branch as in [28, 148]. In this chapter, the perturbation forces f_z allow us to compute the whole bifurcated branch with a single continuation algorithm. Note that these forces differ from the fictitious perturbation force in Section 3.3.2 that acts only on the bifurcation indicator. The number of elements required for a convergent solution was carefully examined. Critical loads can be detected by bifurcation points in the load-displacement curve. Although the small step accumulation is a good indicator of the occurrence of bifurcation, the exact bifurcation points may locate between two neighbouring steps, which cannot be captured directly. Therefore, bifurcation indicators are computed to detect the exact position of bifurcation points. By evaluating this indicator through an equilibrium branch, all the critical points existing on this branch and the associated bifurcation modes can be determined. In what follows, we will explore in greater depth the formation and evolution of three kinds of patterns (sinusoidal, checkerboard and herringbone) in the case of a not too large wave number. In experiments, one often

observes more disordered wrinkles, like a frustrated labyrinth [29, 161]. These more intricate patterns can be predicted by generic finite element procedure as the one presented in this chapter, provided that sufficient computer resources are available.

Table 3.1: Common characteristics of material and geometric properties.

$E_f(MPa)$	$E_s(MPa)$	ν_f	ν_s	$h_f(mm)$	$h_s(mm)$
1.3×10^5	1.8	0.3	0.48	10^{-3}	0.1

Table 3.2: Different parameters of film/substrate systems.

	$L_x(mm)$	$L_y(mm)$	Loading
Film/Sub I	1.5	1.5	Uniaxial
Film/Sub II	1	1	Equi-biaxial
Film/Sub III	0.75	1.5	Biaxial step

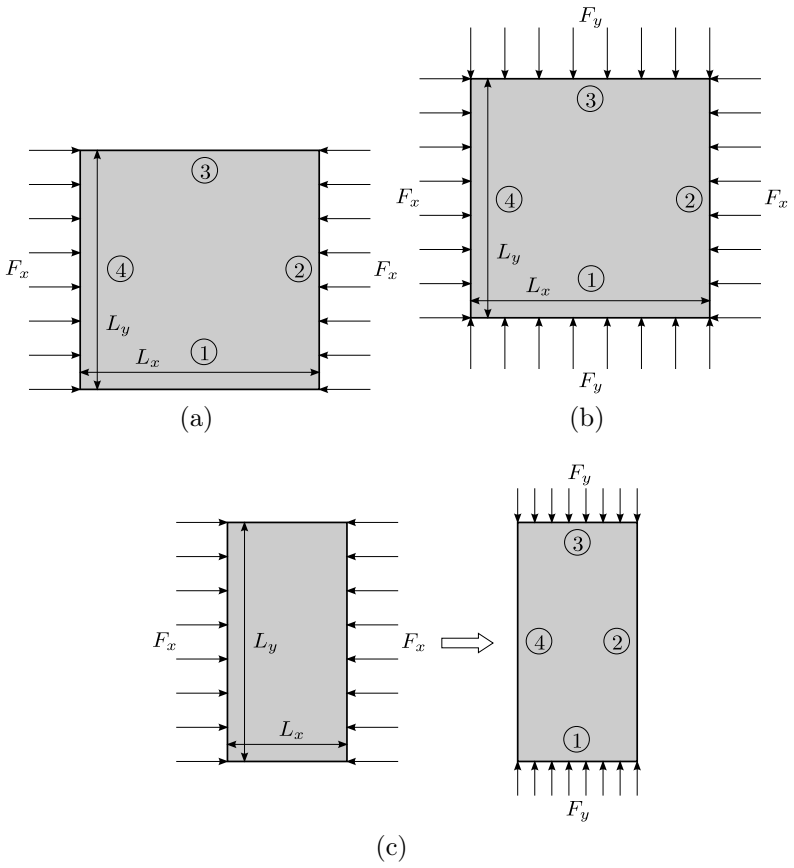

Figure 3.5: Loading conditions: (a) Film/Sub I under uniaxial compression, (b) Film/Sub II under equi-biaxial compression, (c) Film/Sub III under biaxial step loading.

3.4.1 Sinusoidal patterns

First, we study the sinusoidal pattern formation and evolution via Film/Sub I. The film is uniaxially compressed along the x direction as shown in Fig. 3.5a. The displacements v_2, v_3, w_2 and w_3 are taken to be zero on loading sides ② and ④ (see Fig. 3.5a) that are parallel to O_y. This means that these sides are simply supported because the rotation w_1 around O_y is not locked. The other two sides ① and ③ are set to be free. To avoid rigid body motions, the displacement v_1 in the film center is locked as well. The film is meshed with 50×50 shell elements to ensure at least five elements within one wavelength. The substrate is compatibly discretized by 12500 block elements with five layers. Totally, the film/substrate system contains 100827 degrees of freedom (DOF) including the Lagrange multipliers.

The critical load of sinusoidal wrinkles based on classical linearized stability analysis was presented in [43, 89], with Föppl-von Kármán nonlinear elastic plate assumption for the film. For a finite thick substrate, the critical load is expressed as $F_c = 1/4 h_f \overline{E}_f \left(3\overline{E}_s/\overline{E}_f\right)^{2/3}$, where $\overline{E}_f = E_f/\left(1-{v_f}^2\right)$ and $\overline{E}_s = E_s/\left(1-{v_s}^2\right)$. By introducing the material and geometric parameters in Table 3.1, one can obtain the analytical solution for periodic boundary conditions $F_c = 0.048 N/mm$, which is close to our 3D finite element results with real boundary conditions (about $0.052 N/mm$ in Fig. 3.6).

The established 3D model based on the ANM offers a very fast computing speed to reach secondary bifurcations with few steps (see Fig. 3.6). These steps are very large except in the very small region where the load is between 0.052 and 0.056 N/mm. In this region, one can observe two packets of small steps corresponding to two bifurcation points. Their exact locations have been captured through evaluating the bifurcation indicators along the equilibrium branch (see Fig. 3.7). The same method will also be used in the following examples, but the corresponding curves will no longer be presented. The sequence of wrinkling modes Δv corresponding to the bifurcation loads and their associated instability modes Δv_3 are illustrated in Fig. 3.8. These two instability modes are similar to classical patterns obtained for instance in membrane wrinkling. Their shapes are sinusoidal with fast oscillations in the compressive direction and with spatial modulation. These oscillations are located in the center of the film for the first mode and near the sides ② and ④ for the second one, which corresponds to zones where the compressive stresses are larger. When the load increases, the pattern tends to a more or less uniform sinusoidal shape (see Fig. 3.9) with small boundary effects close to the loading sides. In other words, boundary effects are important at the first appearance of wrinkles, then the amplitudes of the oscillations tend to be uniform. Similar evolutions have been obtained in similar problems where one converges to an oscillation whose envelope looks like a hyperbolic tangent, for instance for a clamped beam [122] or a clamped membrane [58].

The tendency to a uniform oscillation is in agreement with predictions of the asymptotic Ginzburg−Landau equation [56].

Following the same strategy, we investigate the surface morphological instability via Film/Sub I in the case of clamped boundary conditions. More specifically, the displacements w_1 is also taken to be zero on loading sides ② and ④ (see Fig. 3.5a) that are parallel to O_y. This means that these sides are clamped because the rotation w_1 around O_y is locked. The other boundary conditions and loadings are the same as before. The same mesh as in simply supported case is carried out.

Two bifurcation points have been found as shown in Fig. 3.10. The two instability modes correspond to modulated oscillations (see Fig. 3.11). The first one is similar to simply supported case except the vanishing rotations on the boundary. The second one takes a hyperbolic tangent envelope except a small localization in the middle. Then the pattern tends to be a uniform hyperbolic tangent shape when the load reaches the final step (see Fig. 3.12).

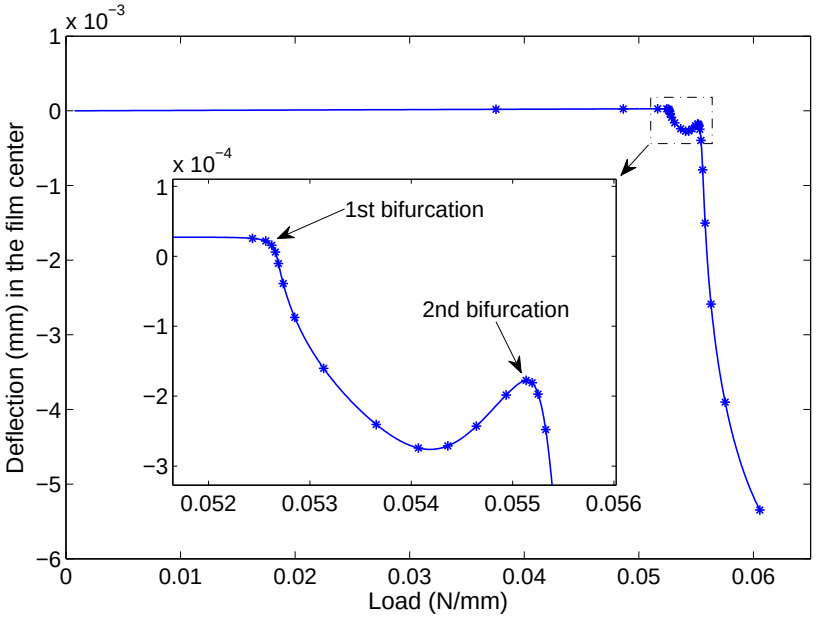

Figure 3.6: Bifurcation curve of Film/Sub I with simply supported boundary conditions under uniaxial compression. Two bifurcations are observed. ANM parameters: $n = 15$, $\delta = 10^{-4}$, 26 steps. Each point corresponds to one ANM step.

3.4.2 Checkerboard patterns

Checkerboard modes are explored via Film/Sub II. The square film is under equibiaxial compression both in x and y direction (see Fig. 3.5b). The deflections v_3 on four

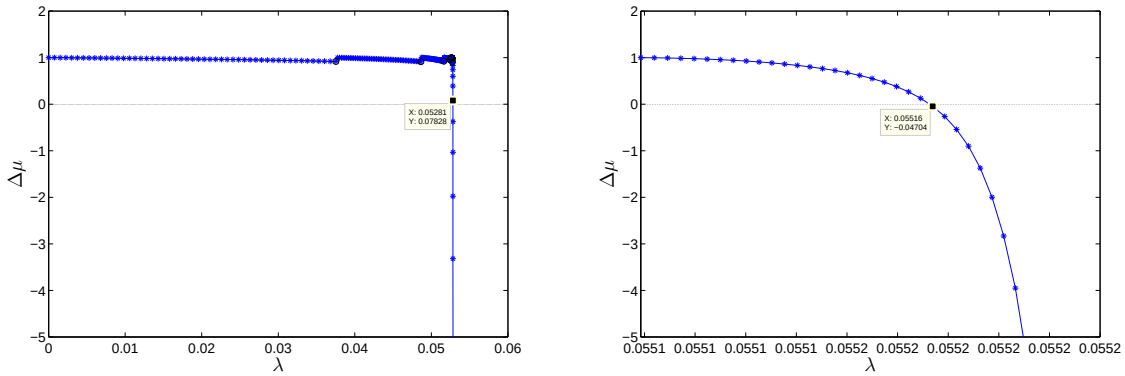

(a) (b)

Figure 3.7: Bifurcation indicators as a function of load parameter of Film/Sub I with simply supported boundary conditions: (a) the first bifurcation point when $\lambda = 0.05281$, (b) the 2nd bifurcation point when $\lambda = 0.05516$. The indicators vanish at bifurcation points.

edges ①, ②, ③ and ④, are locked to be zero, which means the film is simply supported on the whole boundary. The displacements v_1 and v_2 in the film center are also set to be zero to avoid rigid body movements. The same mesh as in the sinusoidal case with totally 100827 DOF is performed.

Four bifurcations have been captured through computing bifurcation indicators (see Fig. 3.13). In any case, the main symmetries with respect to the medians have been preserved. The first wrinkling load is slightly lower than in the uniaxial loading case ($\lambda = 0.048361$ instead of 0.052812). Fig. 3.14 presents a sequence of wrinkling modes Δv corresponding to the critical loads and their associated instability modes Δv_3. In the first mode, the pattern is not uniform and one observes a corner effect due to stress concentration in this area. As in the two previous cases, this first bifurcation is due to local effects that should not appear under periodic boundary conditions. The uniform checkerboard mode matures in the bulk at the second bifurcation, but this growth in the center seems to occur gradually since the first bifurcation. Boundary and corner effects are significantly growing when the load reaches the third bifurcation (see Fig. 3.14e). Nevertheless, it still maintains the checkerboard shape in the middle bulk. The fourth mode is very similar to the third mode due to their proximate critical loads, which cannot be obviously distinguished and is not shown here. The wrinkling pattern in the final step is depicted in Fig. 3.15, which appears strong boundary and corner effects. The growth of checkerboard patterns is not as stable as for the previously observed sinusoidal patterns, since three bifurcations occur for rather small values of the deflection ($v_3/h_f \approx 0.375$) and there is a local maximum value of the deflection. Note that the checkerboard mode is

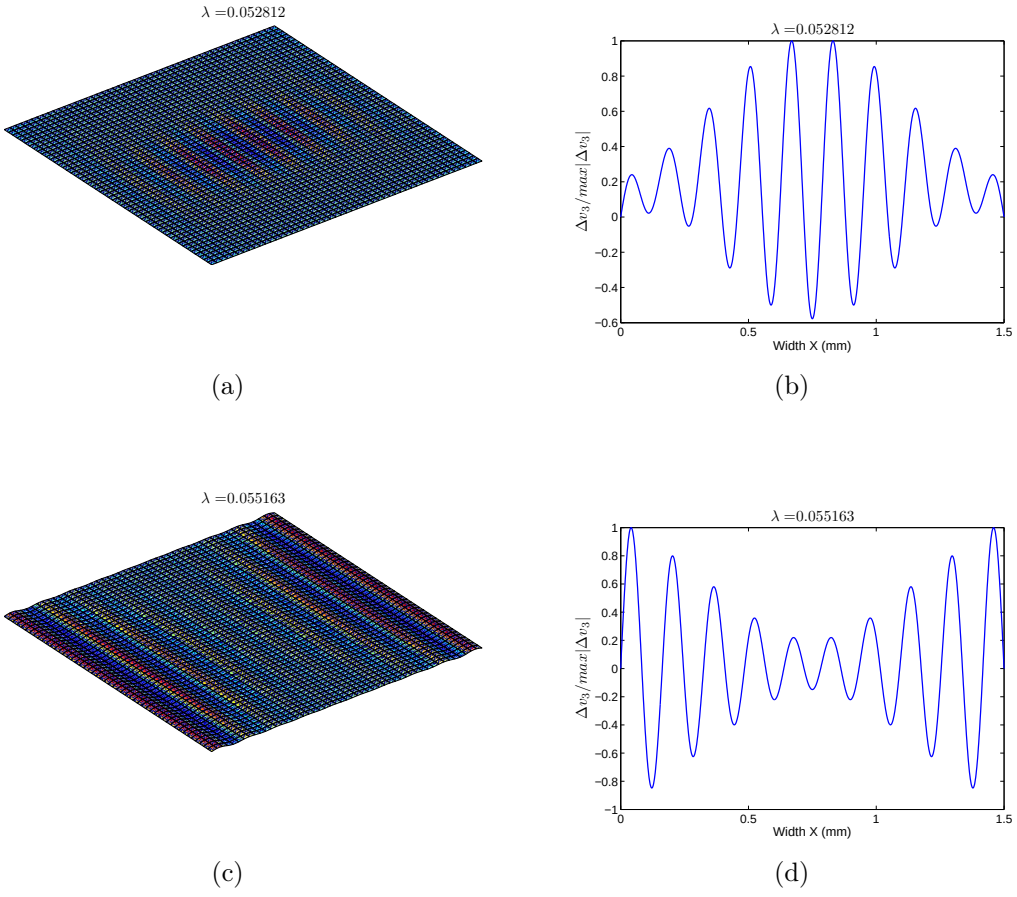

Figure 3.8: Film/Sub I with simply supported boundary conditions under uniaxial compression. The left column shows a sequence of wrinkling modes Δv corresponding to its critical load determined by bifurcation indicators in Fig. 3.7. The right column presents the associated instability modes Δv_3 at the line $Y = 0.5L_y$: (b) the 1st mode, (d) the 2nd mode.

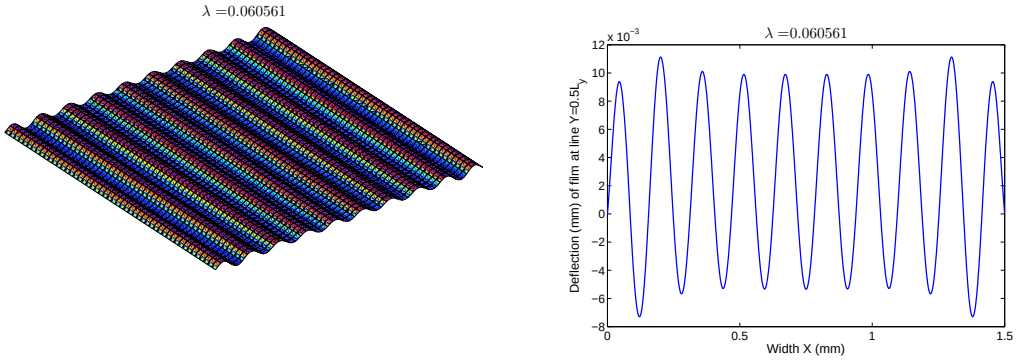

(a) (b)

Figure 3.9: Film/Sub I with simply supported boundary conditions under uniaxial compression: (a) sinusoidal pattern v in the final step, (b) the final shape v_3.

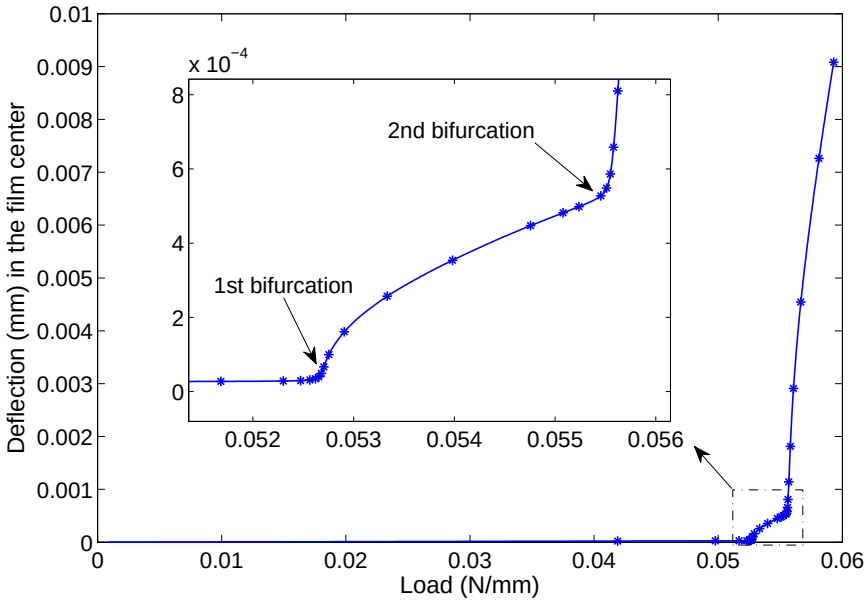

Figure 3.10: Bifurcation curve of Film/Sub I with clamped boundary conditions under uniaxial compression. Two bifurcations are observed. ANM parameters: $n = 15$, $\delta = 10^{-4}$, 28 steps. Each point corresponds to one ANM step.

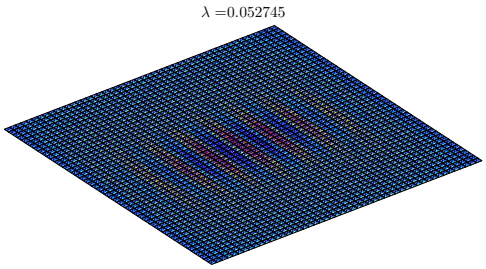

(a)

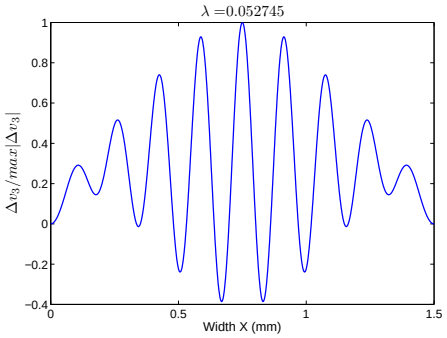

(b)

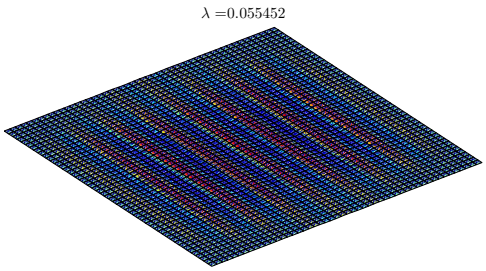

(c)

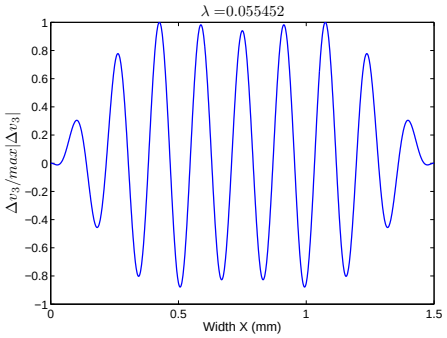

(d)

Figure 3.11: Film/Sub I with clamped boundary conditions under uniaxial compression. The left column shows a sequence of wrinkling modes Δv corresponding to its critical load determined by bifurcation indicators. The right column presents the associated instability modes Δv_3 at the line $Y = 0.5L_y$: (b) the 1st mode, (d) the 2nd mode.

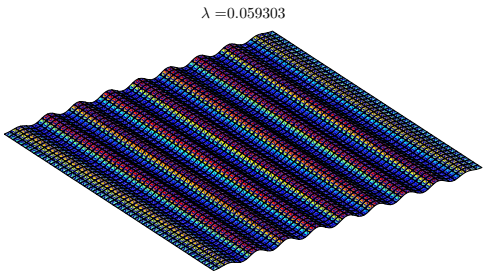

(a)

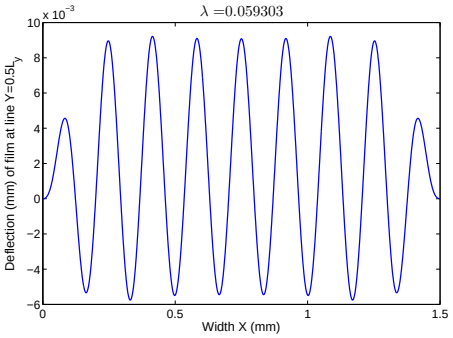

(b)

Figure 3.12: Film/Sub I with clamped boundary conditions under uniaxial compression: (a) sinusoidal pattern v in the final step, (b) the final shape v_3.

rarely observed in experiments because it is very sensitive to perturbation and it mainly appears under strictly symmetric loading, boundary and geometric conditions.

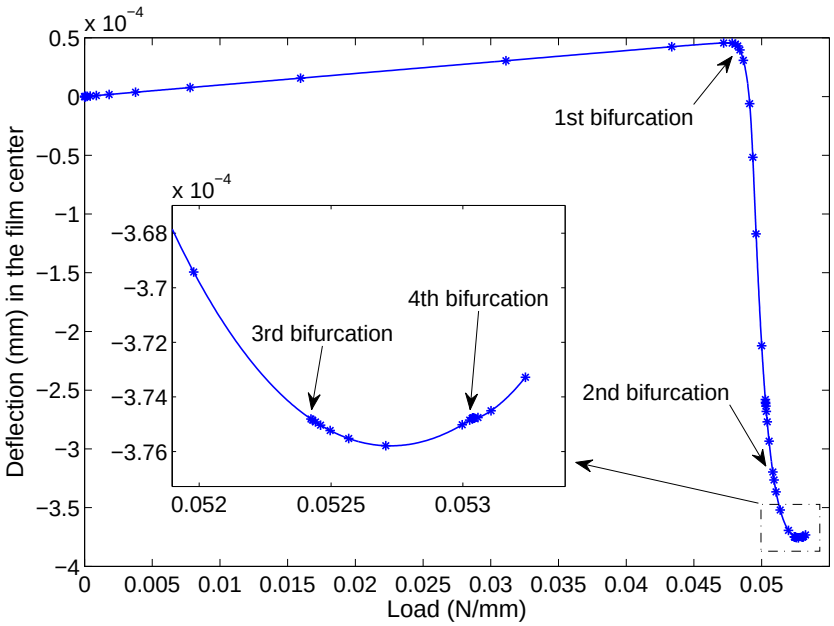

Figure 3.13: Bifurcation curve of Film/Sub II under equi-biaxial compression. Four bifurcations are observed. ANM parameters: $n = 15$, $\delta = 10^{-4}$, 80 steps. Each point corresponds to one ANM step.

3.4.3 Herringbone patterns

Herringbone modes are investigated via Film/Sub III with a rectangular surface ($L_x/L_y = 0.5$) so as to more clearly observe the patterns, since the wavelength λ_x and λ_y are not identical. The film is under biaxial step loading as shown in Fig. 3.5c. More precisely, the film is compressed along the x direction at the first step, where the loading and boundary conditions are the same as the sinusoidal case with simply supported boundary conditions in Section 3.4.1: simply supported on sides ② and ④, free on sides ① and ③. Then, the displacements v_1, v_3, w_1 and w_3 along four sides ①, ②, ③ and ④, are locked at the beginning of the second step of loading, which means that the sides ① and ③ are simply supported in this second step. Compressions on two edges ① and ③ are then imposed along the y direction. The film is meshed with 26×50 shell elements, while the substrate is compatibly discretized by 6500 block elements with five layers. Totally, the film/substrate system contains 53235 DOF including the Lagrange multipliers.

The uniaxial compression in the first step generates the same type of sinusoidal wrinkles as in Section 3.4.1. In Fig. 3.16a, two bifurcation points have been found. The

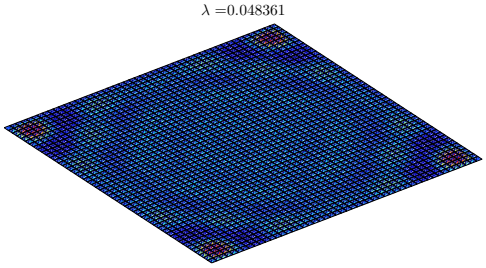

(a)

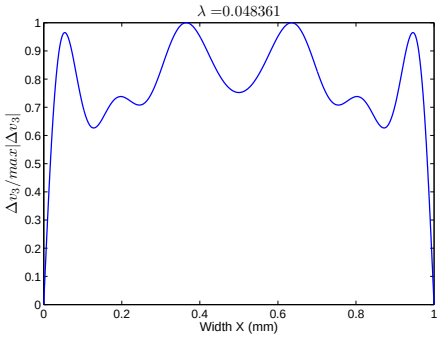

(b)

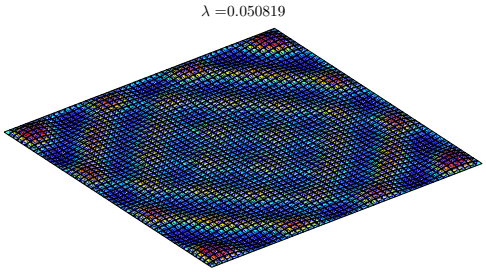

(c)

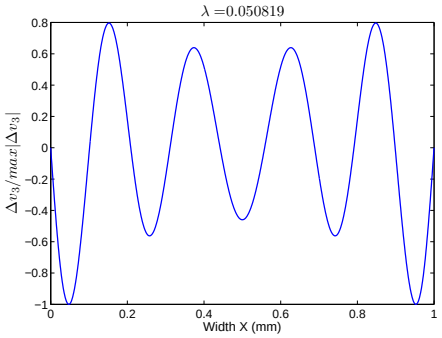

(d)

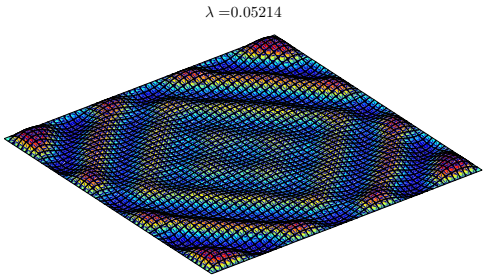

(e)

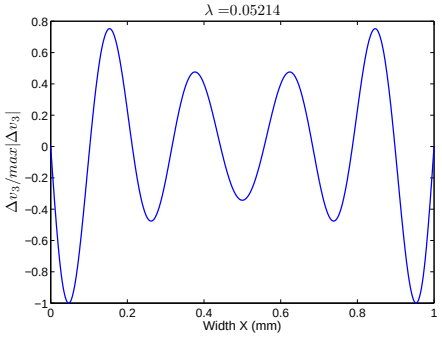

(f)

Figure 3.14: Film/Sub II under equi-biaxial compression. The left column shows a sequence of wrinkling modes Δv corresponding to its critical load determined by bifurcation indicators. The right column presents the associated instability modes Δv_3 at the line $Y = 0.5L_y$: (b) the 1st mode, (d) the 2nd mode, (f) the 3rd mode.

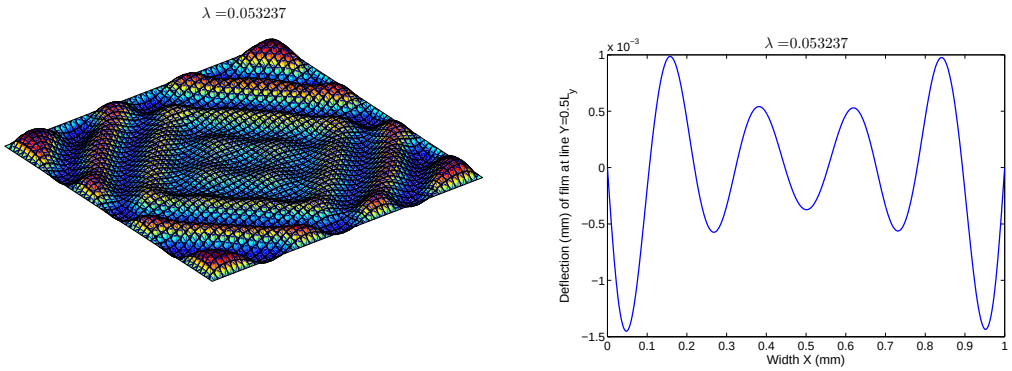

(a) (b)

Figure 3.15: Film/Sub II under equi-biaxial compression: (a) checkerboard pattern v in the final step, (b) the final shape v_3.

sequence of wrinkling modes Δv corresponding to the bifurcation loads and their associated instability modes Δv_3 are illustrated in Fig. 3.17. The first mode is modulated in a sinusoidal way while the second one corresponds to a quasi-uniformly distributed oscillation. During the second step of compression along the y direction, two bifurcations have been captured by computing bifurcation indicators (see Fig. 3.16b). The first mode shows aperiodic wrinkles (see Fig. 3.18a and Fig. 3.18b), where the perfect periodicity in Fig. 3.17d has been broken by the new bifurcation. Such a loss of periodicity had been previously discussed in [146, 39, 38, 40, 163, 160], where period-doubling or even period-quadrupling is observed. Here, the periodicity is broken by the appearance of 3D wrinkling patterns and one can wonder in which cases the sinusoidal modes lose their stabilities by the occurrence of period-doubling or 3D wrinkling modes. The herringbone mode (see Fig. 3.18c and Fig. 3.18d) appears around the second bifurcation with an in-plane wave occurring along the y direction in order to satisfy the minimum energy states [43, 10]. Apparently, the wavelength λ_y is larger than the sinusoidal wavelength λ_x, which is consistent with the experimental results in [161]. A symmetric phase shifting can be obviously seen in the final step (see Fig. 3.19), which justifies that the new in-plane wave spreads along the y direction while oscillates in the x direction. Nevertheless, the wave number in the x direction remains unchanged during the second step of loading.

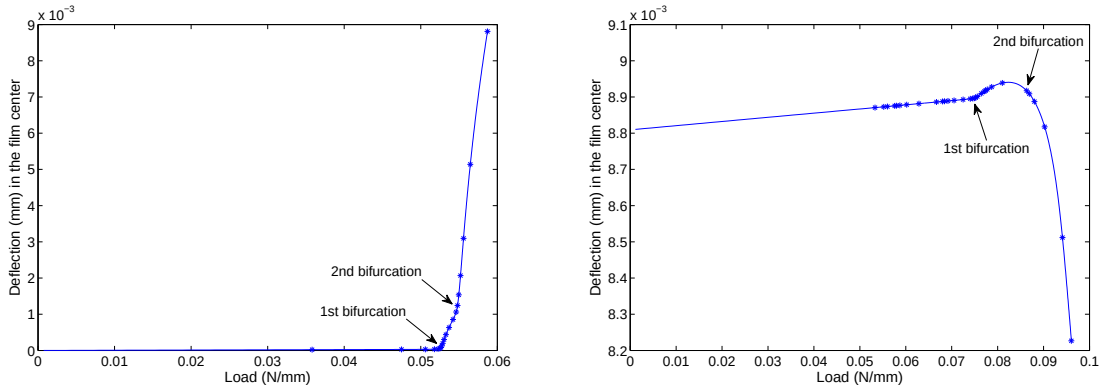

(a) (b)

Figure 3.16: Bifurcation curve of Film/Sub III: (a) the first step of compression along the x direction, ANM parameters: $n = 15$, $\delta = 10^{-4}$, 20 steps, (b) the second step of compression along the y direction, ANM parameters: $n = 15$, $\delta = 10^{-4}$, 31 steps. Each point corresponds to one ANM step.

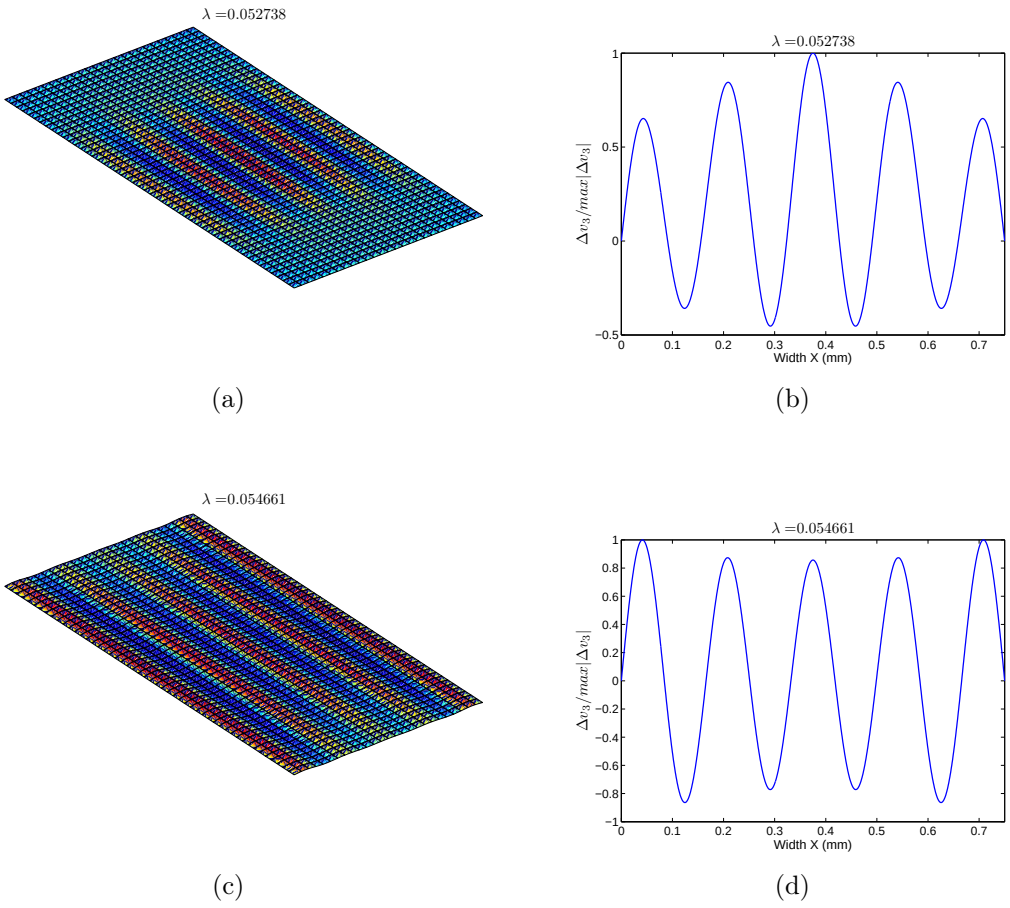

Figure 3.17: Film/Sub III under the first step of compression along the x direction. The left column shows a sequence of wrinkling modes Δv corresponding to its critical load determined by bifurcation indicators. The right column presents the associated instability modes Δv_3 at the line $Y = 0.5L_y$: (b) the 1st mode, (d) the 2nd mode.

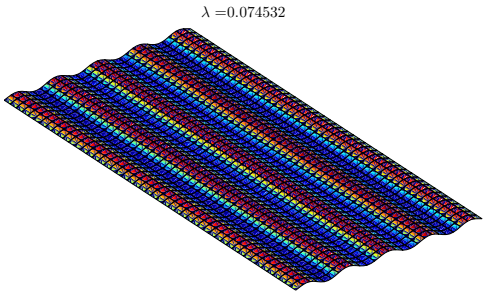

(a)

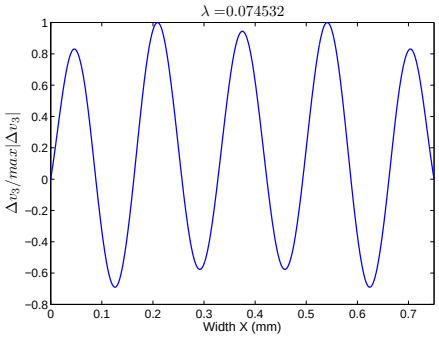

(b)

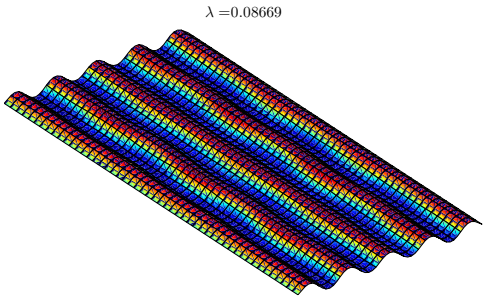

(c)

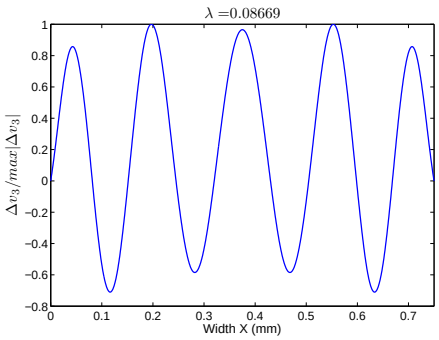

(d)

Figure 3.18: Film/Sub III under the second step of compression along the y direction. The left column shows a sequence of wrinkling modes Δv corresponding to its critical load determined by bifurcation indicators. The right column presents the associated instability modes Δv_3 at the line $Y = 0.5L_y$: (b) the 1st mode, (d) the 2nd mode.

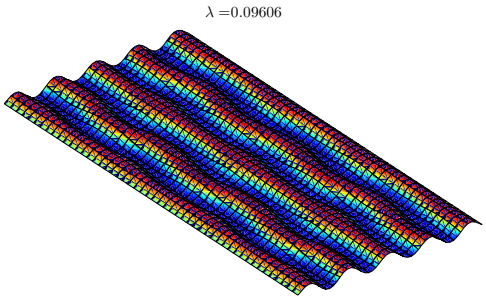

(a)

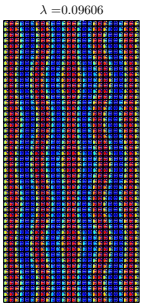

(b)

Figure 3.19: Film/Sub III under the second step of compression along the y direction: (a) herringbone pattern v in the final step, (b) top view of (a).

3.5 Chapter conclusion

Pattern formation and evolution of stiff films bound to compliant substrates were investigated, by accounting for boundary conditions in 3D cases, which was rarely studied previously. A classical model was applied associating geometrically nonlinear shell formulation for the film and linear elasticity for the substrate. Then the shell elements and block elements were coupled by introducing Lagrange multipliers. The presented results rely heavily on robust solution techniques based on the ANM that is able to detect secondary bifurcations and to compute bifurcation modes on a nonlinear response curve. Probably, it would be rather difficult to detect all the bifurcations found in this chapter by conventional numerical methods. Notably, the occurrence and evolution of sinusoidal, checkerboard and herringbone modes have been observed in the post-buckling range. The boundary conditions lead to non-uniformly distributed modes, but these boundary effects hold only at the onset of the instability and further bifurcation modes correspond to more or less uniform amplitudes of oscillations. In our simulations, the appearance of sinusoidal, checkerboard or herringbone patterns is mainly related to the loading conditions. The nonlinear behavior of moderately large wrinkles has been investigated and it seems that 1D patterns are more stable than 2D ones.

The presented nonlinear 3D model can describe moderately large displacements and rotations in the film, while the computation cost is dramatically increasing compared to the 2D model in [160] (100827 DOF in the 3D model instead of 1818 DOF in the 2D model). In this respect, an idea for simulating larger samples is to introduce reduced-order models, for example via the technique of slowly variable Fourier coefficients [54, 56, 122, 58].

Chapter 4

Bridging techniques for pattern formation modeling

Contents

4.1 Introduction

Wrinkling phenomenon is one of the major concerns for the analysis, design and optimization of structures [134] and material processing [2], self-organized surface morphology in biomechanics [64], pattern formation for micro/nano-fabrication [29], *etc.* To analyze such phenomena, we propose the use of macroscopic models based on envelope equations as in the field of cellular instability problems [153, 50, 80]. Such macroscopic descriptions are common for Rayleigh−Bénard convection [124, 139], buckling of long structures [51, 26, 3], surface wrinkling of stiff thin films resting on compliant substrates [29, 43, 88, 89, 9, 10, 11, 151, 31, 39, 163], fiber microbuckling and compressive failure of composites [63, 103, 149], wrinkling of membranes [134, 154, 132, 107, 108] and many other instabilities arising in various scientific fields [153, 50]. The responses of such systems are often nearly periodic spatial oscillations. Therefore, the evolution can be described by envelope models similar to the famous Ginzburg−Landau equation [139, 53, 91, 94].

A new approach has been recently adopted by Damil and Potier-Ferry [54, 55, 56] to model wrinkling phenomena. The approach is based on the Ginzburg−Landau theory [153, 94]. In the proposed theory, the envelope equation is derived from an asymptotic double scale analysis and the nearly periodic fields (reduced model) are represented by Fourier series with slowly varying coefficients. This mathematical representation yields macroscopic models in the form of generalized continua. In this case, the macroscopic field is defined by Fourier coefficients of the microscopic field. It has been shown recently that this approach is able to account for the coupling between local and global buckling in a computationally efficient manner [119] and it remains valid beyond the bifurcation point [56].

Nevertheless, a clear and secure account of boundary conditions cannot be obtained, which is a drawback intrinsically linked to the use of any model reduction. To solve this problem, a multi-scale modeling approach has been recently proposed in order to bypass the question of boundary conditions [84]: the full model is implemented near the boundary while the envelope model is considered elsewhere, and these two models are bridged by the Arlequin method [20, 24, 21, 22]. This idea makes it possible to clarify the question of boundary conditions, which keeps the advantages of the two approaches: the envelope model in the bulk makes it possible to simplify the response curves and limit the total number of degrees of freedom; the fine model avoids the cumbersome problem of the boundary conditions being applied to the envelope equation. In this chapter,

we revisit these coupling techniques between a reference model and a reduced model of Ginzburg−Landau type.

Over the last decade, various numerical techniques have been developed to couple heterogeneous models, *e.g.* the Arlequin method [20, 24, 21, 22] or the bridging domain method [157]. One can couple classical continuum and shell models [24], particle and continuum models [15, 130, 131, 16, 157], heterogeneous meshes [24, 81] or more generally heterogeneous discretizations [23, 25]. For instance, local stresses around the boundary have been computed by coupling 2D elasticity near the boundary and 1D beam model elsewhere [81, 82].

Basically, the Arlequin method aims at connecting two spatial approximations of an unknown field, generally a fine approximation U_f and a coarse approximation U_r. The idea is to require that these two approximations are neighbor in a weak and discrete sense and to introduce Lagrange multipliers in the corresponding differential problems. At the continuous level, a bilinear form must be chosen, which can be L^2-type, H^1-type or energy type [24, 22, 15]. The first and important application of the Arlequin method is the coupling between two different meshes discretizing the same continuous problem: in this case, the mediator problem should be discretized by a coarse mesh to avoid locking phenomena [24] and spurious stress peaks [81]. But the two connected problems are not always in the same space, as for instance when dealing with particle and continuous problems. In this case, a prolongation operator has to be introduced to convert the discrete displacement into a continuous one and next a connection between continuous fields is performed [15]: this is consistent because the continuous model can be seen as the coarsest one. A similar approach has been applied in the coupling between plate and 3D models. A prolongation operator has been introduced (*i.e.* from the coarse to the fine level) and the integration is done in the 3D domain but the discretization of the Lagrange multiplier corresponds to a projection on the coarsest problem: thus, in this sense, this coupling of plate/3D is also achieved at the coarse level. In the same spirit, for the coupling between a fine model and an envelope model that is discussed in this chapter, the connection should also be done at the coarse level, *i.e.* between Fourier coefficients. On the contrary, a prolongation operator from the coarse to the fine model had been introduced in the previous paper [84] and the connection had been done at this level. Therefore, one can wonder if the imperfect connection observed in [84] could be improved by introducing a coupling at the relevant level. This chapter tries to answer this question by studying again the Swift−Hohenberg equation [147] that is a simple and illustrative example of quasi-periodic bifurcation. Very probably, the same ideas can be applied to 2D macroscopic membrane models that were recently introduced in [57]. Note that the presented new technique can be considered as nonlocal since it connects

Fourier coefficients involving integrals on a period. A similar nonlocal coupling has been introduced in [131] in the case of an atomic-to-continuum coupling, where the atomic model is reduced by averaging over a representative volume.

The question addressed in this chapter is more or less generic in applying bridging techniques to reduced models or multi-scale models. The first papers about the Arlequin method focused on the choice of a bilinear form and its discretization. But in asymptotic multiple scale methods [136] or in computational homogenization [65], one clearly distinguishes two independent spatial domains: a macroscopic domain to account for slow variations and a microscopic domain for the rapid variations. Therefore, the connection operators between the two levels have to be clearly defined, as well as the level at which the coupling is achieved. This subject will be discussed in this chapter.

The work presented in this chapter, *i.e.* the new bridging technique based on a nonlocal reduction operator, is considered as an original, logical and relevant application of multi-scale modeling with good motivations, explanations and interesting numerical results, which has been published in *International Journal of Solids and Structures* [158].

4.2 Macroscopic modeling of instability pattern formation

The numerical test considered in this chapter is the famous Swift−Hohenberg equation [147] that corresponds to the problem of a compressed elastic beam coupled with a nonlinear foundation. It has been studied in many papers, for instance in [90, 91, 56, 122], because it is a very representative example in the study of cellular instabilities. From this microscopic model, a macroscopic envelope model will be presented and studied in the rest of the chapter. Among those discussed in [56], it is not the more accurate, but it is the simplest one and it is able to describe the amplitude modulation of the oscillation. Let us recall that the central point of this chapter is a bridging technique used to correct a reduced model near the boundary. This technique has to be robust and it has to play its part for several levels of reduced model.

4.2.1 Description of the microscopic model

We consider the example of an elastic beam subjected to a nonlinear elastic foundation as shown in Fig. 4.1. The unknowns are the components $u(x)$ and $v(x)$ of the displacement vector and the normal force $n(x)$, which represents $U(x) = \{u(x), v(x), n(x)\}$. We will

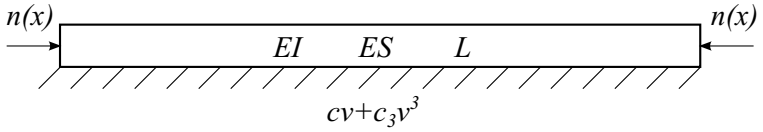

Figure 4.1: Sketch of an elastic beam on a nonlinear elastic foundation.

study the following set of differential equations:

$$\begin{cases} \dfrac{dn}{dx} + f = 0, & (a) \\ \dfrac{n}{ES} = \dfrac{du}{dx} + \dfrac{1}{2}\left(\dfrac{dv}{dx}\right)^2, & (b) \\ \dfrac{d^2}{dx^2}\left(EI\dfrac{d^2v}{dx^2}\right) - \dfrac{d}{dx}\left(n\dfrac{dv}{dx}\right) + cv + c_3v^3 = 0. & (c) \end{cases} \tag{4.1}$$

These equations will be referred to as the microscopic model that depends on four structural parameters EI, ES, c, c_3 and a given axial force $f(x)$. This system is able to describe periodic patterns. For instance, in the case without horizontal force ($f = 0$), with constant coefficients EI, c and a prescribed uniform compression stress μ ($n(x) = -\mu$), a relation between the critical load μ and the wave number q of periodic patterns can be deduced from the linearized version of (4.1−c):

$$\mu(q) = EIq^2 + \frac{c}{q^2}. \tag{4.2}$$

The critical wave number $q = \sqrt[4]{c/EI}$ can be defined as the minimum of the neutral stability curve $\mu(q)$.

Note that the solutions of the system (4.1) are stationary points of the following potential energy:

$$\mathcal{P}(u,v) = \int_0^L \left(\frac{ES}{2}\left(u' + \frac{v'^2}{2}\right)^2 + \frac{EI}{2}v''^2 + \frac{c}{2}v^2 + \frac{c_3}{4}v^4 - fu\right) \mathrm{d}x. \tag{4.3}$$

4.2.2 Reduction procedure by Fourier series

We will conduct a multi-scale approach based on the concept of Fourier series with slowly varying coefficients. Let us suppose that the instability wave number q is known. In this way, all the unknowns of model $U(x) = \{u(x), v(x), n(x)...\}$ can be written in the

form of Fourier series, whose coefficients vary more slowly than the harmonics:

$$U(x) = \sum_{j=-\infty}^{+\infty} U_j(x) e^{jiqx}, \tag{4.4}$$

where the Fourier coefficient $U_j(x)$ denotes the envelope for the j^{th} order harmonic, which is conjugated with $U_{-j}(x)$.

The macroscopic unknown fields $U_j(x)$ slowly vary over a period $\left[x, x + \frac{2\pi}{q}\right]$ of the oscillation. In practice, only a finite number of Fourier coefficients will be considered. As shown in Fig. 1.6, at least two functions $U_0(x)$ and $U_1(x)$ are necessary to describe nearly periodic patterns: $U_0(x)$ can be identified with the mean value while $U_1(x)$ represents the envelope or amplitude of the spatial oscillations. The mean value $U_0(x)$ is real valued, while the other envelopes are complex. Consequently, the envelope of the first harmonic $U_1(x)$ can be written as $U_1(x) = r(x)e^{i\varphi(x)}$, where $r(x)$ represents the amplitude modulation and $\varphi(x)$ is the phase modulation. If the phase varies linearly like $\varphi(x) = Qx + \varphi_0$, this type of approach is able to describe quasi-periodic responses whose wave number $q + Q$ slightly differs from the *a priori* chosen q. Hence, the method makes it possible to account for a change in wave number.

The main idea of macroscopic modeling is to deduce differential equations satisfied by the amplitude $U_j(x)$. Some calculation rules have been introduced in [54, 56] to manage these Fourier series with slowly varying coefficients.

4.2.3 A simple macroscopic model with two real envelopes

The previous reduction procedure has been applied to the microscopic model (4.1) and (4.3) (see [56]). Several reduced models have been established, depending on the number of harmonics and some additional assumptions. The general methodology to obtain the macroscopic models is detailed in Appendix B, as well as a very accurate reduced model with five harmonics and another with one real and one complex envelope in Appendix C. In this chapter, we only recall the simplest possible model that involves only three real functions: the mean values of the membrane unknowns $u_0(x)$, $n_0(x)$ and the first amplitude of the oscillation of deflection $v_1(x)$.

The potential energy of this simple macroscopic model is given by (see [56])

$$\mathcal{P}(u_0, v_1) = \int_0^L \left(\frac{ES}{2} \left(u_0' + v_1'^2 + q^2 v_1^2 \right)^2 + EI \left(6q^2 v_1'^2 + q^4 v_1^2 \right) + c v_1^2 + \frac{3c_3}{2} v_1^4 - f_0 u_0 \right) \mathrm{d}x. \tag{4.5}$$

The differential equations of the system follow from the stationarity of the potential energy

$\delta\mathcal{P} = 0$, which leads to

$$\begin{cases} \dfrac{dn_0}{dx} + f_0 = 0, & (a) \\ n_0 = ES\left(u_0' + v_1'^2 + q^2 v_1^2\right), & (b) \\ -\dfrac{d}{dx}\left[\left(6EIq^2 + n_0\right)\dfrac{dv_1}{dx}\right] + \left(EIq^4 + n_0 q^2 + c\right)v_1 + 3c_3 v_1^3 = 0. & (c) \end{cases} \tag{4.6}$$

The macroscopic model couples the 1D membrane Eqs. (4.6−a) and (4.6−b) with a second order differential equation (4.6−c) for the envelope $v_1(x)$, which is a sort of Ginzburg−Landau equation. In this chapter, we only consider the simplest case of a real $v_1(x)$, which has the drawback of fixing the phase in the bulk. A complete study of the model with a complex $v_1(x)$ can be found in [122], where better accuracy in the boundary layer has been established. One may wonder why the fourth order derivatives of v_1 have been dropped. It was theoretically and numerically established in [56], §5.1, that these high order derivatives can lead to spurious oscillations and lack of convergence for fine meshes. In fact, this is consistent with the basic assumption of a slowly varying envelope $d/dx \ll q$. On the contrary, one can consider removing all the derivatives in Eq. (4.6−c), but the discussion in previous papers showed that the resulting model is very poor and not consistent with the asymptotic Ginzburg−Landau approach.

4.2.4 Effective range of macroscopic models

The assumption of slowly varying amplitudes is the main restriction for application of envelope models. In other words, the length scales of the oscillations and of the envelope must be clearly distinguished. This limitation holds for the present Fourier approach as well as for the asymptotic one [56]. A known example is the localization of buckling patterns arising from long domains and softening nonlinearity ($c_3 < 0$). For instance, in [90], Fig. 8 demonstrates that the assumption is only valid very close to the bifurcation point. In other words, such localized behavior cannot be represented by slowly varying amplitude. In the same way, any envelope model is not able to perfectly account for boundary effects. That is the reason why we propose a double scale analysis, where the macroscopic model is considered in the bulk while the fine model is used near the boundary.

4.3 Transition operators in the framework of Fourier series with variable coefficients

The next problem studied in this chapter is the coupling between the macroscopic model (4.6) and the microscopic model (4.1). According to the Arlequin framework, a bilinear form has to be defined and this will be done in the following sections. In this part, we define and analyze transition operators between the full model and the reduced one.

4.3.1 Prolongation and reduction operators

Let us discuss the possible manners of connecting the fine and reduced models. Firstly, let us consider the transition from the envelopes $U_j(x)$ to the full model ($U_j(x) \to U(x)$). It has been previously introduced (see [84]):

$$\mathfrak{P}(U_j) = U(x) = \sum_{j=-\infty}^{+\infty} U_j(x) e^{jiqx}. \tag{4.7}$$

With the simplification in Section 4.2.3, the unknowns are reduced to the mean membrane displacement $u_0(x)$ and to the first envelope of the deflection $v_1(x)$. Consequently, the Eq. (4.7) can be simplified as

$$\mathfrak{P}(u_0, v_1) = \left\{ \begin{array}{c} u(x) \\ v(x) \end{array} \right\} = \left\{ \begin{array}{c} u_0(x) \\ 2v_1(x)\cos(qx+\varphi) \end{array} \right\}. \tag{4.8}$$

Conversely, according to the assumption of slowly varying envelope over a period $\left[x - \frac{\pi}{q}, x + \frac{\pi}{q}\right]$, the macroscopic unknowns can be deduced from microscopic ones by the classic formula of Fourier series:

$$U_j(x) = \frac{q}{2\pi} \int_{-\frac{\pi}{q}}^{\frac{\pi}{q}} U(x+y) e^{-jiq(x+y)} \mathrm{d}y. \tag{4.9}$$

Therefore, considering the simplified theory in Section 4.2.3, the reduction operator reads

$$\mathfrak{R}(u, v) = \left\{ \begin{array}{c} u_0(x) \\ v_1^R(x) \\ v_1^I(x) \end{array} \right\} = \frac{q}{2\pi} \int_{-\frac{\pi}{q}}^{\frac{\pi}{q}} \left\{ \begin{array}{c} u(x+y) \\ v(x+y)\cos[q(x+y)] \\ -v(x+y)\sin[q(x+y)] \end{array} \right\} \mathrm{d}y. \tag{4.10}$$

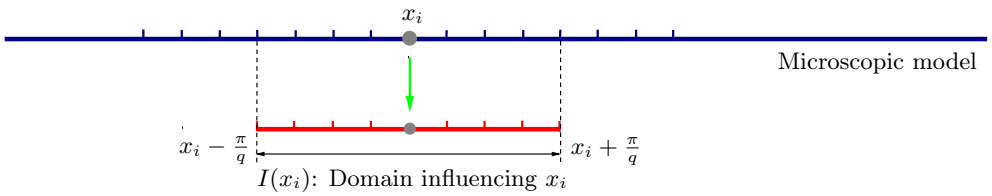

Figure 4.2: Schematic of the reduction from the microscopic model.

4.3.2 Numerical analysis of the reduction procedure

Theoretical remarks

Before presenting a bridging technique, we first examine the meaning of the reduction procedure in Eqs. (4.9) and (4.10). This is performed through the analysis of a numerical solution of the microscopic model (4.1). For a periodic function $U(x)$, the Fourier coefficients are given by Eq. (4.9). In what follows, we compute the real part U_j^R and imaginary part U_j^I as follows:

$$U_j^R(x) = \frac{q}{2\pi} \int_{-\frac{\pi}{q}}^{\frac{\pi}{q}} U(x+y) \cos\left[jq(x+y)\right] \mathrm{d}y, \tag{4.11}$$

$$U_j^I(x) = -\frac{q}{2\pi} \int_{-\frac{\pi}{q}}^{\frac{\pi}{q}} U(x+y) \sin\left[jq(x+y)\right] \mathrm{d}y. \tag{4.12}$$

From the mathematical standpoint, it is straightforward to obtain all the envelopes through Eq. (4.9). The reduction of transversal displacement and longitudinal displacement is conducted by considering five envelopes $j = 0$, $j = \pm 1$ and $j = \pm 2$, respectively.

We consider a beam with length $L = 30\pi$, $ES = 1$, $EI = 1$, $c = 1$ and $c_3 = 1/3$. We choose the instability wave number $q = 1$. The beam is subjected to an increasing global end shortening $u(L) = -\mu L$ and the body force is $f_0 = 0$. The whole beam is divided into 120 cubic elements, which means that the element length is $l_e = \pi/4$.

Theoretically, to implement this nonlocal reduction, we can choose any point x in Eqs. (4.11) and (4.12) as the center to carry out the integral over the period $\left[x - \frac{\pi}{q}, x + \frac{\pi}{q}\right]$ except the boundary regions $\left[0, \frac{\pi}{q}\right]$ and $\left[L - \frac{\pi}{q}, L\right]$. For simplicity, we choose each node of the microscopic mesh as the center of these integrals. Therefore, for each reduction point, the integral domain covers eight elements over the whole period as shown in Fig. 4.2. The discretization of this nonlocal reduction can be written as

$$U_j^R(x_i) = \frac{q}{2\pi} \int_{x_i - \frac{\pi}{q}}^{x_i + \frac{\pi}{q}} U(x) \cos\left(jqx\right) \mathrm{d}x \approx \frac{q}{2\pi} \frac{l_e}{2} \sum_{x_n \in gp} U(x_n) \cos(jqx_n), \tag{4.13}$$

$$U_j^I(x_i) = -\frac{q}{2\pi}\int_{x_i-\frac{\pi}{q}}^{x_i+\frac{\pi}{q}} U(x)\sin(jqx)\,\mathrm{d}x \approx -\frac{q}{2\pi}\frac{l_e}{2}\sum_{x_n\in gp} U(x_n)\sin(jqx_n), \tag{4.14}$$

where x_i are the nodes of the mesh and $x_n \in gp$ represent the corresponding Gauss points within the integration domain $I(x_i) = \left[x_i - \frac{\pi}{q}, x_i + \frac{\pi}{q}\right]$.

Note that the above equations should be limited to functions that are exactly periodic with a period $2\pi/q$. But in general, it is not possible to precisely predict the period of solutions of nonlinear equations that changes with their amplitudes. Let us consider for instance a harmonic function with a wave number Q that is close but a little different from the *a priori* given wave number q:

$$v(x) = e^{i(Qx+\varphi)} + e^{-i(Qx+\varphi)}, \quad Q \approx q, \quad Q \neq q. \tag{4.15}$$

From Eqs. (4.13) and (4.14), the first order Fourier coefficient can be written as

$$v_1(x) = \frac{q}{2\pi}\left(e^{i\varphi}\int_{-\frac{\pi}{q}}^{\frac{\pi}{q}} \underbrace{e^{i(Q-q)(x+y)}}_{Slowly\ variable}\,\mathrm{d}y + e^{-i\varphi}\int_{-\frac{\pi}{q}}^{\frac{\pi}{q}} \underbrace{e^{-i(Q+q)(x+y)}}_{Oscillating}\mathrm{d}y\right). \tag{4.16}$$

Therefore, the Fourier coefficients involve a slowly varying part and a rapidly varying one, this second part being disregarded by the macroscopic models in Section 4.2. The oscillating part is relatively small when the two wave numbers are close to each other.

Numerical tests for a simply supported beam

In order to analyze the practical accuracy of the reduction formulae (4.13) and (4.14), firstly, we have computed the response of the microscopic model (4.1) with simply supported boundary conditions: $v(0) = v''(0) = 0$, $v(L) = v''(L) = 0$. Then the reduction terms (4.13) and (4.14) are calculated when $\mu = 2.21$ for the orders $j = 0$, $j = 1$ and $j = 2$, respectively. Their spatial distribution is plotted in Fig. 4.3. It is found that only the imaginary part of the first order envelope v_1^I is not small, the ratios $|v_1^R/v_1^I|$ and $|v_0/v_1^I|$ being of the order of 10^{-3} or 10^{-4}. The second order amplitudes v_2^R and v_2^I even have a lower level than v_0. In other words, the response of $v(x)$ is approximately $0.3166\sin x$ and the complementary contributions are relatively small. This means that the effective wave number Q for $\mu = 2.21$ corresponds precisely to the predicted quantity $q = 1$. We have checked that the wave number is also $Q = 1$ for any μ in the interval $[2, 2.21]$.

Numerical tests for a clamped beam

With clamped boundary conditions: $v(0) = v'(0) = 0$, $v(L) = v'(L) = 0$, it is known that the effective wave number Q is not exactly the one predicted by the linear theory

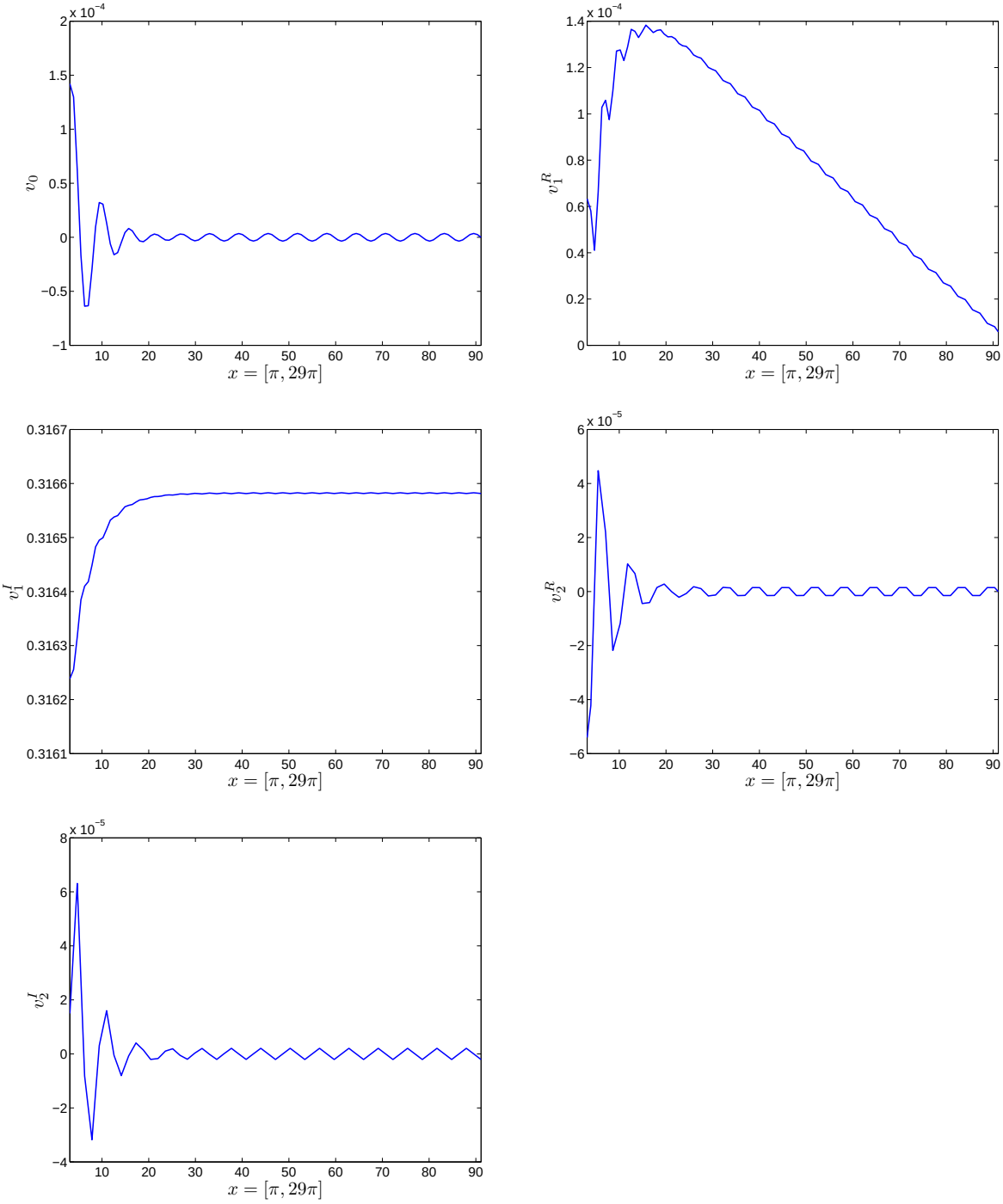

Figure 4.3: Buckling of a simply supported beam under uniform compression: one real envelope (v_0) and four complex envelopes (v_1^R, v_1^I, v_2^R, v_2^I). The reduction is performed over the domain $[\pi, 29\pi]$. The instability pattern for $\mu = 2.21$.

[122]. To verify this, we have computed the solution of the nonlinear problem (4.1) by the classic Newton−Raphson method and the corresponding macroscopic quantities v_0, v_1^R, v_1^I, v_2^R and v_2^I within the zone $[\pi, 29\pi]$. From Fig. 4.4, we can observe that the first envelope $|v_1|$ is bigger than the other three ones, but the ratio is larger than in the simply supported case and is approximately 10^{-1}. According to Eq. (4.16), this shows that the effective wave number is not exactly the expected value $q = 1$. Moreover, the envelopes obtained by Eqs. (4.13) and (4.14) are not precisely slowly variable and a rapidly varying part is observed as indicated in the oscillating part of Eq. (4.16).

The longitudinal displacements u_0, u_1^R, u_1^I, u_2^R and u_2^I are illustrated in Fig. 4.5. As expected, the zero order term u_0 is larger than the others and is almost linear, but there are also oscillating parts u_1^R and u_1^I with a ratio $|u_1^R/u_0| \approx \mathcal{O}(10^{-2})$ and $|u_1^I/u_0| \approx \mathcal{O}(10^{-2})$, u_2^R and u_2^I with a ratio $|u_2^R/u_0| \approx \mathcal{O}(10^{-2})$ and $|u_2^I/u_0| \approx \mathcal{O}(10^{-2})$, respectively.

Next, we have rebuilt the microscopic deflection $v(x) = \mathfrak{P}(v_i)$ from five envelopes ($j = 0$, $j = \pm 1$ and $j = \pm 2$) by Eq. (4.4) and we find that this reconstruction well describes the exact value as shown in Fig. 4.6. Furthermore, it can be noticed that only two envelopes v_1^I and v_1^R can sufficiently cover the microscopic model as shown in Fig. 4.7, which justifies the assumptions made in Section 4.2.3. The same reconstruction is demonstrated in Figs. 4.8 and 4.9 and this leads to the expected nearly linear response $u(x)$. However, $u(x)$ is not perfectly linear and its derivative $u'(x)$ fluctuates around -2.22 as shown in Fig. 4.10. This can be explained through the constitutive equation (4.1−b). Since there is no horizontal force $f = 0$, the normal force is constant $n(x) = -\mu$. The transversal displacement $v(x)$ being in a wave form, the deformation $u'(x)$ is in a wave form as well.

4.3.3 Comments

By considering the exact solution of the full problem, we have established that the macroscopic quantities defined by the reduction formulae (4.13) and (4.14) are not exactly slowly variable. They also account for an oscillating part that is small only if the effective wave number Q is very close to the *a priori* chosen wave number q. In the next sections, we will introduce a coupling between the two scales that is based on the reduction operator (4.10). A bridging technique based on the formulae (4.13) and (4.14) will be presented and evaluated. To smooth these oscillations, an L^2−type coupling operator will be used.

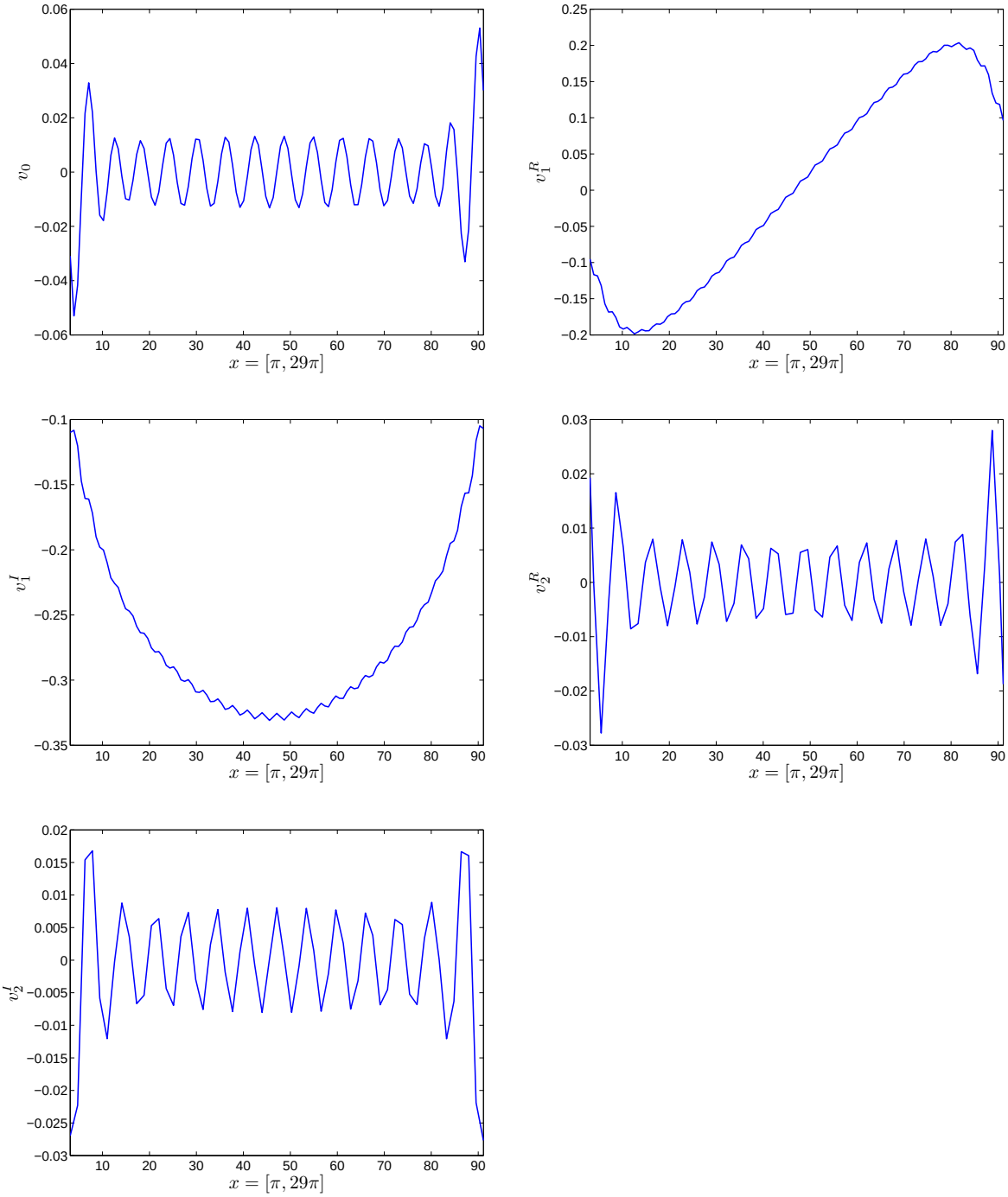

Figure 4.4: Buckling of a clamped beam under uniform compression: one real envelope (v_0) and four complex envelopes (v_1^R, v_1^I, v_2^R, v_2^I). The reduction is performed over the domain $[\pi, 29\pi]$. The instability pattern for $\mu = 2.21$.

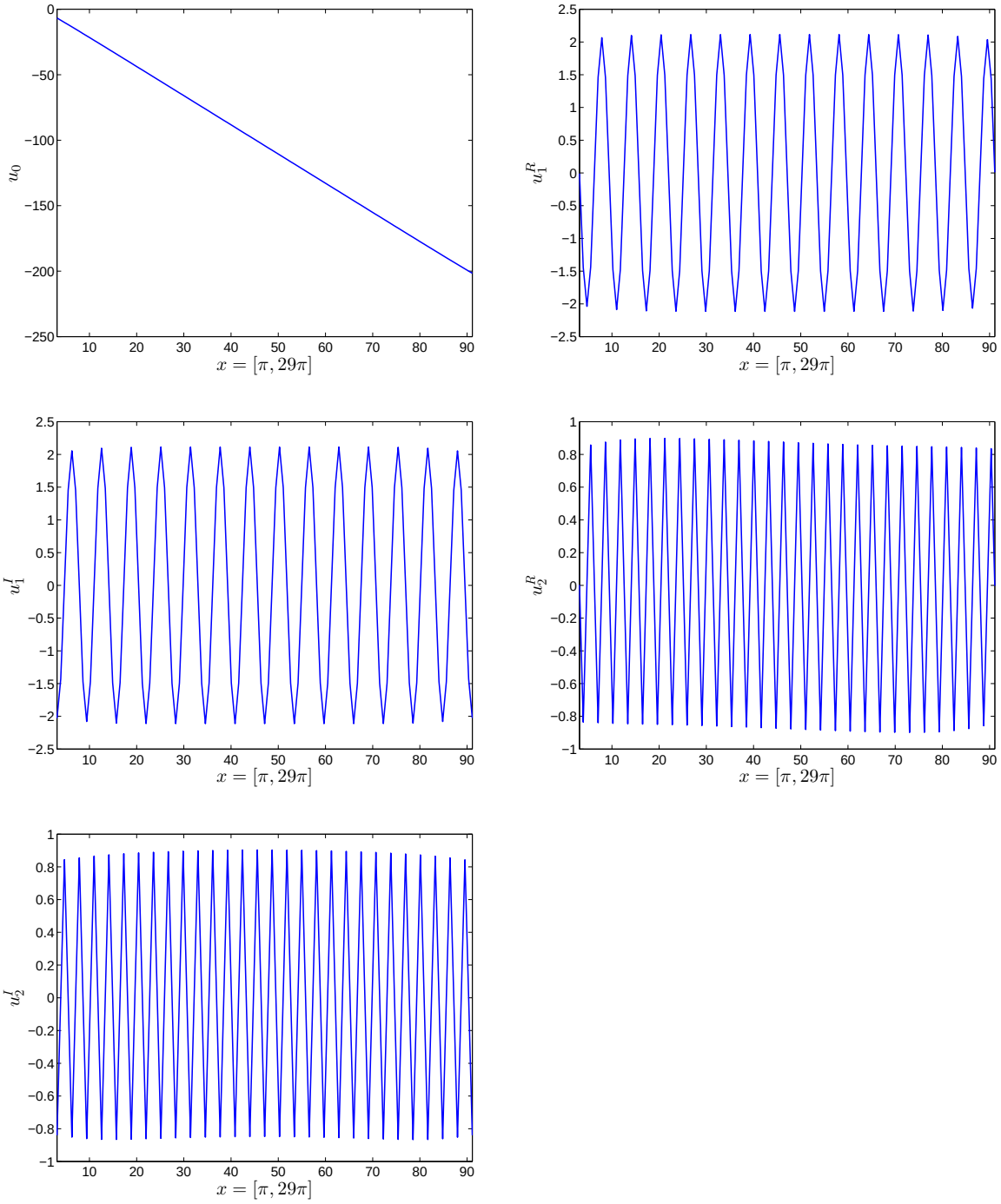

Figure 4.5: Buckling of a clamped beam under uniform compression: one real envelope (u_0) and four complex envelopes (u_1^R, u_1^I, u_2^R, u_2^I). The reduction is performed over the domain $[\pi, 29\pi]$. The instability pattern for $\mu = 2.21$.

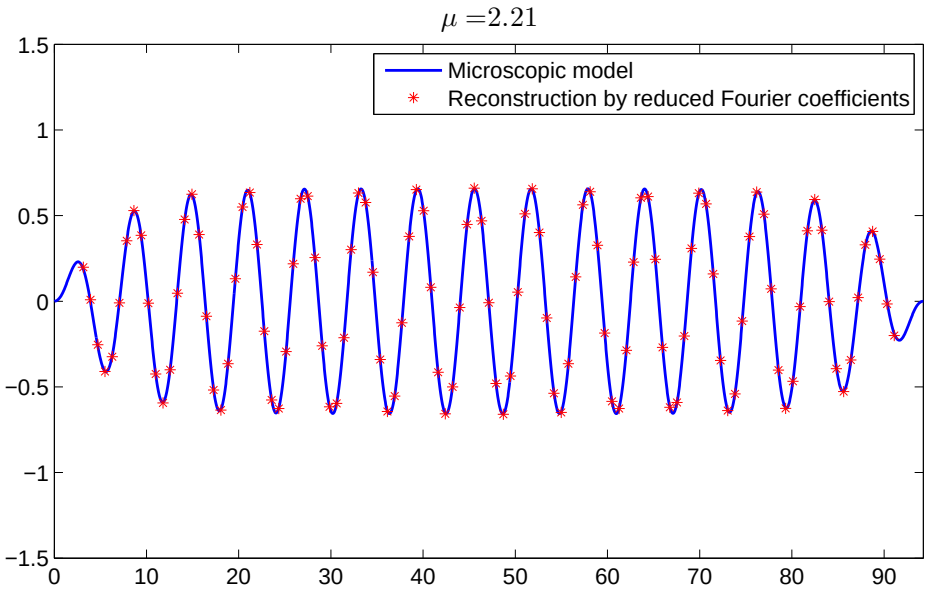

Figure 4.6: Buckling of a clamped beam under uniform compression. The instability pattern for $\mu = 2.21$. Reconstruction by all the reduced Fourier coefficients (v_0, v_1^R, v_1^I, v_2^R and v_2^I) is compared with the exact solution $v(x)$.

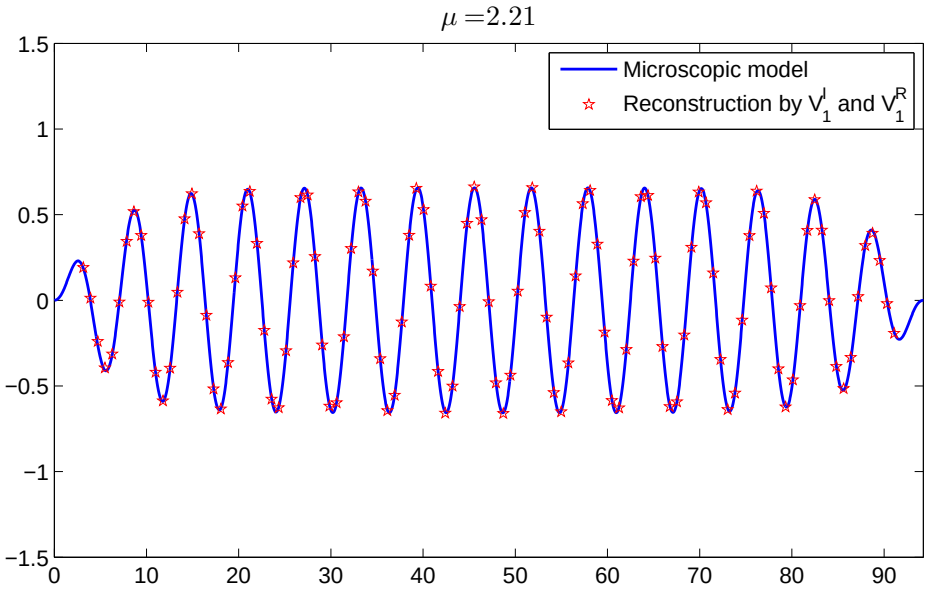

Figure 4.7: Buckling of a clamped beam under uniform compression. The instability pattern for $\mu = 2.21$. Reconstruction by two reduced Fourier coefficients v_1^I and v_1^R is compared with the exact solution $v(x)$.

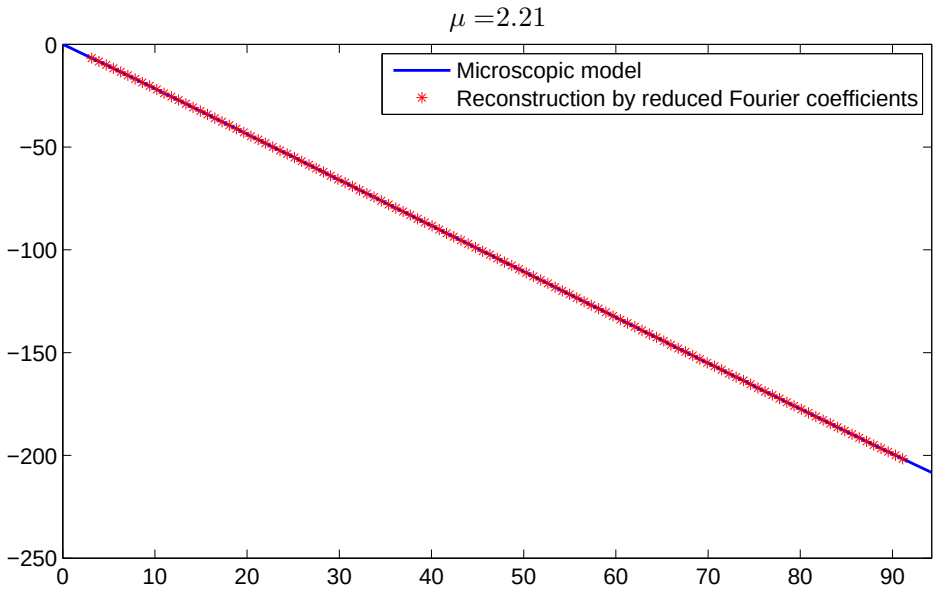

Figure 4.8: Buckling of a clamped beam under uniform compression. The instability pattern for $\mu = 2.21$. Reconstruction by all the reduced Fourier coefficients (u_0, u_1^R, u_1^I, u_2^R and u_2^I) is compared with the exact solution $u(x)$.

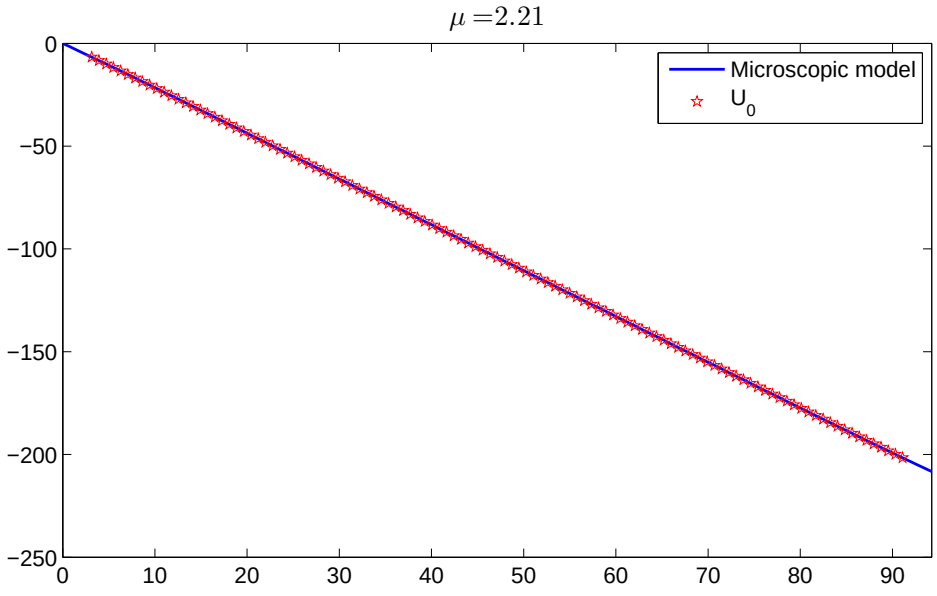

Figure 4.9: Buckling of a clamped beam under uniform compression. The instability pattern for $\mu = 2.21$. Reconstruction by only u_0 is compared with the exact solution $u(x)$.

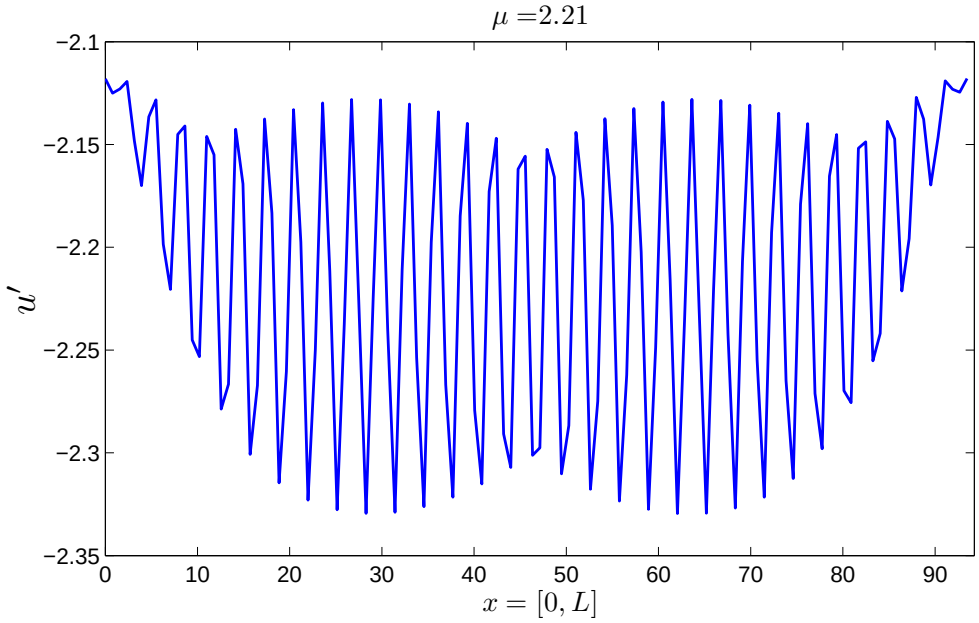

Figure 4.10: Buckling of a clamped beam under uniform compression: derivatives of the curve in Fig. 4.8. The instability pattern for $\mu = 2.21$.

4.4 Bridging technique and discretization

In this section, the microscopic model (4.1) and (4.3) is implemented in a small region close to the boundary, which allows for the introduction of "exact" boundary conditions into the system. The simplest envelope model (4.5) and (4.6) will be applied in the bulk. These two types of models can be bridged by the Arlequin method [20, 24, 21, 22]. According to the Arlequin framework, these two mechanical fields are matched in a weak sense inside the gluing zone and the potential energy is distributed between these two models.

4.4.1 Arlequin method in the context of prolongation or reduction coupling

The domain of the whole mechanical system is partitioned into two overlapping subzones: Ω_f (microscopic fine model domain) and Ω_r (macroscopic reduced model domain). The resulting superposition zone $S = \Omega_f \cap \Omega_r$ contains the gluing zone $S_g (S_g \subseteq S)$ (see Fig. 4.11). Here the two zones S and S_g cannot coincide because of the nonlocal character of the reduction operator.

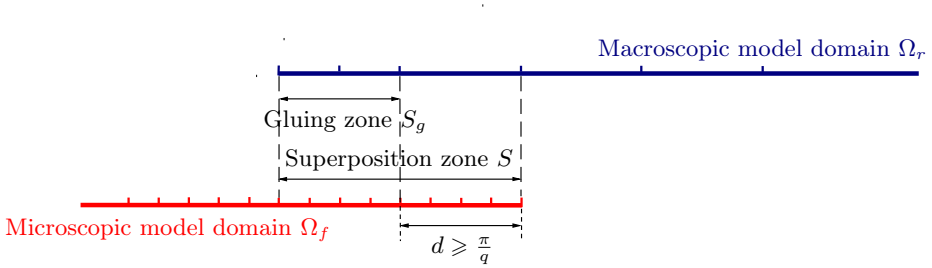

Figure 4.11: Definition of domains in the Arlequin framework.

Energy distribution

Setting $\boldsymbol{u}_f = \{u(x), v(x), x \in \Omega_f\}$ and $\boldsymbol{u}_r = \{u_0(x), v_1(x), x \in \Omega_r\}$, the energy contribution of the two models for the potential energy of the whole system defined in Eqs. (4.3) and (4.5) is as follows:

$$\begin{cases} \mathcal{P}_f(\boldsymbol{u}_f) = \displaystyle\int_{\Omega_f} [\alpha_f \mathcal{W}(\boldsymbol{u}_f) - \beta_f f u] \, \mathrm{d}\Omega, \\ \\ \mathcal{P}_r(\boldsymbol{u}_r) = \displaystyle\int_{\Omega_r} [\alpha_r \mathcal{W}(\boldsymbol{u}_r) - \beta_r f_0 u_0] \, \mathrm{d}\Omega, \end{cases} \tag{4.17}$$

where

$$\begin{cases} \mathcal{W}(\boldsymbol{u}_f) = \dfrac{ES}{2}(u' + \dfrac{v'^2}{2})^2 + \dfrac{EI}{2}v''^2 + \dfrac{c}{2}v^2 + \dfrac{c_3}{4}v^4, \\ \\ \mathcal{W}(\boldsymbol{u}_r) = \dfrac{ES}{2}(u_0' + v_1'^2 + q^2 v_1^2)^2 + EI(6q^2 v_1'^2 + q^4 v_1^2) + c v_1^2 + \dfrac{3c_3}{2}v_1^4. \end{cases} \tag{4.18}$$

In order to have consistent modeling of the energy in the overlapping domain, the energy associated to each domain is balanced by weight functions which are represented by α_i for the internal work and β_i for the external work. These weight functions are assumed to be positive piecewise continuous in Ω_i and satisfy the following equations:

$$\begin{cases} \alpha_f = \beta_f = 1, \quad \text{in } \Omega_f \backslash S, \\ \\ \alpha_r = \beta_r = 1, \quad \text{in } \Omega_r \backslash S, \\ \\ \alpha_f + \alpha_r = \beta_f + \beta_r = 1, \quad \text{in } S. \end{cases} \tag{4.19}$$

More details on selection of these functions can be found in [24, 15]. In this chapter, we choose piecewise linear continuous weight functions in the overlapping region S.

Coupling alternatives

The coupling technique implies a connection between the microscopic model and the envelope model. According to the Arlequin framework, generally, coupling based on the coarse model is preferred to avoid the locking phenomena. This requires defining a non-local reduction operator $\boldsymbol{u}_f \to \mathfrak{R}(\boldsymbol{u}_f)$ which involves the Fourier transform. Conversely, the other way is to perform the inverse connection by using a local prolongation operator $\boldsymbol{u}_r \to \mathfrak{P}(\boldsymbol{u}_r)$, which reproduces a compatible field from $\boldsymbol{u}_r$ to be coupled with $\boldsymbol{u}_f$ (see Section 4.3.1). Therefore, the coupling is conducted by requiring that one of the two following conditions could be satisfied in a mean sense:

$$\mathfrak{R}(\boldsymbol{u}_f) - \boldsymbol{u}_r = 0, \quad \forall x \in S_g; \tag{4.20}$$

$$\boldsymbol{u}_f - \mathfrak{P}(\boldsymbol{u}_r) = 0, \quad \forall x \in S_g. \tag{4.21}$$

The literature in terms of the Arlequin method recommends the first way (4.20) [24, 22, 15]. For simplicity, the prolongation method (4.21) was studied in [84]. Here, we will test the reduction approach (4.20) that should lead to a better coupling.

Prolongation coupling approach

The prolongation operator was defined in Eq. (4.8). The reduced model is based on strong simplifications and especially on the assumption of a constant arbitrary phase. As in [119], we choose $\varphi = -\pi/2$ in what follows, which leads to the following form of the prolongation operator:

$$\mathfrak{P}(\boldsymbol{u}_r) = \begin{bmatrix} 1 & 0 \\ 0 & 2\sin(qx) \end{bmatrix} \begin{Bmatrix} u_0 \\ v_1 \end{Bmatrix}, \quad \forall x \in S_g. \tag{4.22}$$

By introducing Lagrange multipliers $\boldsymbol{\lambda} = \{\lambda_u(x), \lambda_v(x), x \in S_g\}$ as a fictitious gluing force, the coupling equation (4.21) can be rewritten in a weak form as

$$\mathscr{C}\left(\boldsymbol{\lambda}, \boldsymbol{u}_f - \mathfrak{P}(\boldsymbol{u}_r)\right) = 0, \quad \forall \boldsymbol{\lambda} \in M, \tag{4.23}$$

where M is the mediator space. Eq. (4.23) could be considered as a constraint in an optimization problem. The corresponding stationary function is given in a Lagrangian form as

$$\mathscr{L}(\boldsymbol{u}_f, \boldsymbol{u}_r, \boldsymbol{\lambda}) = \mathcal{P}_f(\boldsymbol{u}_f) + \mathcal{P}_r(\boldsymbol{u}_r) + \mathscr{C}\left(\boldsymbol{\lambda}, \boldsymbol{u}_f - \mathfrak{P}(\boldsymbol{u}_r)\right). \tag{4.24}$$

From Eq. (4.24), three equations are obtained according to $\delta \boldsymbol{u}_f$, $\delta \boldsymbol{u}_r$ and $\delta \boldsymbol{\lambda}$:

$$\left\{ \begin{array}{l} \mathcal{P}_f(\delta \boldsymbol{u}_f) + \mathscr{C}(\boldsymbol{\lambda}, \delta \boldsymbol{u}_f) = 0, \quad \forall \delta \boldsymbol{u}_f \in K.A., \\ \\ \mathcal{P}_r(\delta \boldsymbol{u}_r) - \mathscr{C}\left(\boldsymbol{\lambda}, \mathfrak{P}(\delta \boldsymbol{u}_r)\right) = 0, \quad \forall \delta \boldsymbol{u}_r \in K.A., \\ \\ \mathscr{C}(\delta \boldsymbol{\lambda}, \boldsymbol{u}_f) - \mathscr{C}\left(\delta \boldsymbol{\lambda}, \mathfrak{P}(\boldsymbol{u}_r)\right) = 0, \quad \forall \delta \boldsymbol{\lambda} \in M, \end{array} \right. \tag{4.25}$$

where $K.A.$ stands for kinematically admissible. Finally, the coupling operator $\mathscr{C}$ is defined as follows:

$$\mathscr{C}(\boldsymbol{\lambda}, \boldsymbol{u}) = \int_{S_g} \left(\boldsymbol{\lambda} \cdot \boldsymbol{u} + \ell^2 \boldsymbol{\varepsilon}(\boldsymbol{\lambda}) : \boldsymbol{\varepsilon}(\boldsymbol{u}) \right) \mathrm{d}\Omega. \tag{4.26}$$

It is an H^1-type coupling operator. When $\ell = 0$, it becomes an L^2-type coupling operator. The choice of the length has been discussed in the literature [24, 75, 15, 81] and the difficulties of L^2 coupling have been pointed out. This point will be re-discussed in Section 4.5.3.

Reduction-based coupling approach

In Section 4.3.2, it was shown that the longitudinal displacement can be adequately described by a single envelope u_0 since it is almost linear. Moreover, the two longitudinal displacements coincide (see Eqs. (4.22) and (4.28) below) so that their bridging procedure (4.23) and (4.27) is identical.

In the transversal direction, the reduction operator is the first order Fourier coefficient that has a nonlocal character (see Eq. (4.10)). For simplicity, $\mathscr{C}(\boldsymbol{\lambda}, \boldsymbol{u})$ will be the L^2-type scalar product. The reduction operator has been defined in Eq. (4.10). With $\varphi = -\pi/2$, the weak form of coupling formula (4.20) reads

$$\mathscr{C}\left(\boldsymbol{\lambda}, \mathfrak{R}(\boldsymbol{u}_f) - \boldsymbol{u}_r\right) = 0, \quad \forall \boldsymbol{\lambda} \in M, \tag{4.27}$$

where

$$\mathfrak{R}(\boldsymbol{u}_f) = \left\{ \begin{array}{c} \mathfrak{R}_u(x) \\ \mathfrak{R}_v(x) \end{array} \right\} = \left\{ \begin{array}{c} u(x) \\ \dfrac{q}{2\pi} \displaystyle\int_{-\frac{\pi}{q}}^{\frac{\pi}{q}} v(x+y) \sin\left[q(x+y)\right] \mathrm{d}y \end{array} \right\}. \tag{4.28}$$

The corresponding stationary function is also in a Lagrangian form:

$$\mathscr{L}(\boldsymbol{u}_f, \boldsymbol{u}_r, \boldsymbol{\lambda}) = \mathcal{P}_f(\boldsymbol{u}_f) + \mathcal{P}_r(\boldsymbol{u}_r) + \mathscr{C}\left(\boldsymbol{\lambda}, \mathfrak{R}(\boldsymbol{u}_f) - \boldsymbol{u}_r\right). \tag{4.29}$$

From Eq. (4.29), one can obtain three equations according to $\delta \boldsymbol{u}_f$, $\delta \boldsymbol{u}_r$ and $\delta \boldsymbol{\lambda}$:

$$\begin{cases} \mathcal{P}_f(\delta \boldsymbol{u}_f) + \mathscr{C}(\boldsymbol{\lambda}, \mathfrak{R}(\delta \boldsymbol{u}_f)) = 0, \quad \forall \delta \boldsymbol{u}_f \in K.A., \\ \mathcal{P}_r(\delta \boldsymbol{u}_r) - \mathscr{C}\left(\boldsymbol{\lambda}, \delta \boldsymbol{u}_r\right) = 0, \quad \forall \delta \boldsymbol{u}_r \in K.A., \\ \mathscr{C}(\delta \boldsymbol{\lambda}, \mathfrak{R}(\boldsymbol{u}_f)) - \mathscr{C}\left(\delta \boldsymbol{\lambda}, \boldsymbol{u}_r\right) = 0, \quad \forall \delta \boldsymbol{\lambda} \in M. \end{cases} \tag{4.30}$$

Comments

In works of Ben Dhia and Rateau [24, 21, 22], it was established that it is better to discretize the coupling equation in a coarse manner (choice of the discrete mediator space M). In this chapter, we will further discuss whether the coupling equation has to be defined at a fine level (4.21) and (4.23) or at a coarse level (4.20) and (4.27).

4.4.2 Discretization

The chosen discretization of the microscopic model (4.1) is very classical with linear interpolation for the axial displacement and cubic Hermite interpolation for the deflection. C^0 elements can be chosen since the reduced energy (4.5) involves only the first derivatives. As in [56], we use 3-node quadratic elements. The discretization of the coupling operators is presented with more details.

Discretization of the prolongation coupling

The finite element method is applied to solve Eq. (4.25). The discretization of unknowns is as follows:

$$\boldsymbol{u}_f = \left\{ \begin{array}{c} u \\ v \end{array} \right\}^e = \left[\begin{array}{c} \boldsymbol{N}_u^f \\ \boldsymbol{N}_v^f \end{array} \right] \left\{ \begin{array}{c} \boldsymbol{Q}_f \end{array} \right\}^e, \tag{4.31}$$

$$\boldsymbol{u}_r = \left\{ \begin{array}{c} u_0 \\ v_1 \end{array} \right\}^e = \left[\begin{array}{c} \boldsymbol{N}_u^r \\ \boldsymbol{N}_v^r \end{array} \right] \left\{ \begin{array}{c} \boldsymbol{Q}_r \end{array} \right\}^e, \tag{4.32}$$

$$\boldsymbol{\lambda} = \left\{ \begin{array}{c} \lambda_u \\ \lambda_v \end{array} \right\}^e = \left[\begin{array}{c} \boldsymbol{N}_u^r \\ \boldsymbol{N}_v^r \end{array} \right] \left\{ \begin{array}{c} \boldsymbol{Q}_\lambda \end{array} \right\}^e, \tag{4.33}$$

where $\left\{\boldsymbol{Q}_f\right\}^e$, $\{\boldsymbol{Q}_r\}^e$ and $\{\boldsymbol{Q}_\lambda\}^e$ are the elementary nodal unknowns of $\boldsymbol{u}_f$, $\boldsymbol{u}_r$ and $\boldsymbol{\lambda}$, respectively. The shape functions $\boldsymbol{N}_u^f$ and $\boldsymbol{N}_v^f$ are, respectively, described by Lagrange and Hermite interpolating polynomials. To avoid locking the microscopic behavior to the macroscopic behavior in the coupling zone, the discretization of $\boldsymbol{\lambda}$ should be conducted as $\boldsymbol{u}_r$ (see more details in [24]).

Finally, one can obtain the global discrete system in the generic form of a mixed problem:

$$\begin{cases} \left[\mathcal{R}_f(\boldsymbol{Q}_f)\right] + \left[\boldsymbol{\mathcal{C}}_f\right]^t \{\boldsymbol{Q}_\lambda\} = 0, \\ \\ \left[\mathcal{R}_r(\boldsymbol{Q}_r)\right] - \left[\boldsymbol{\mathcal{C}}_r\right]^t \{\boldsymbol{Q}_\lambda\} = 0, \\ \\ \left[\boldsymbol{\mathcal{C}}_f\right] \left\{\boldsymbol{Q}_f\right\} - \left[\boldsymbol{\mathcal{C}}_r\right] \{\boldsymbol{Q}_r\} = 0, \end{cases} \tag{4.34}$$

where the residuals $\mathcal{R}_f(\boldsymbol{Q}_f)$ and $\mathcal{R}_r(\boldsymbol{Q}_r)$ are detailed in Appendix D. The coupling matrix $\boldsymbol{\mathcal{C}}_f$ and $\boldsymbol{\mathcal{C}}_r$ are assembled from the elementary matrices that have the following forms:

$$\boldsymbol{\mathcal{C}}_f^e = \int_{\Omega_e} \left(\begin{bmatrix} \boldsymbol{N}_u^r \\ \boldsymbol{N}_v^r \end{bmatrix} \begin{bmatrix} \boldsymbol{N}_u^f \\ \boldsymbol{N}_v^f \end{bmatrix}^t + \ell^2 \begin{bmatrix} \boldsymbol{N}_u^{r\prime} \\ \boldsymbol{N}_v^{r\prime} \end{bmatrix} \begin{bmatrix} \boldsymbol{N}_u^{f\prime} \\ \boldsymbol{N}_v^{f\prime} \end{bmatrix}^t \right) \mathrm{d}\Omega, \tag{4.35}$$

$$\boldsymbol{\mathcal{C}}_r^e = \int_{\Omega_e} \left(\begin{bmatrix} \boldsymbol{N}_u^r \\ \boldsymbol{N}_v^r \end{bmatrix} \begin{bmatrix} \boldsymbol{N}_u^r \\ 2\boldsymbol{N}_v^r \sin(qx) \end{bmatrix}^t + \ell^2 \begin{bmatrix} \boldsymbol{N}_u^{r\prime} \\ \boldsymbol{N}_v^{r\prime} \end{bmatrix} \begin{bmatrix} \boldsymbol{N}_u^{r\prime} \\ 2\boldsymbol{N}_v^{r\prime} \sin(qx) + 2q\boldsymbol{N}_v^r \cos(qx) \end{bmatrix}^t \right) \mathrm{d}\Omega, \tag{4.36}$$

in which Ω_e represents the elementary integration domain.

The resulting nonlinear system (4.34) is solved using the classic Newton−Raphson method.

Discretization of the reduction-based coupling

The discretization of unknowns $\boldsymbol{u}_f$, $\boldsymbol{u}_r$ and $\boldsymbol{\lambda}$ is the same as in Section 4.4.2. In addition, the global discrete system (4.34) has the same form as those in the prolongation coupling but with a completely different coupling matrix $\boldsymbol{\mathcal{C}}_f$ due to the nonlocal character of the coupling operator.

Now let us look at the discretization of the bilinear form $\mathscr{C}(\boldsymbol{\lambda}, \mathfrak{R}(\boldsymbol{u}_f))$ that follows from two integrations. The bilinear form $\mathscr{C}(\cdot,\cdot)$ is an integral in the macroscopic domain split into macroscopic elements E, each of them being associated with their Gauss points ($GP(E)$) in S_g. This first integral is quite classical with finite element method. The reduction operator $\mathfrak{R}(\cdot)$ is an integral in the interval $I(x_i) = \left[x_i - \frac{\pi}{q}, x_i + \frac{\pi}{q}\right]$ in the microscopic domain that is split into small elements e, each of them being associated with its Gauss points ($gp(e)$). Classically, these Gauss points are defined in a reference interval

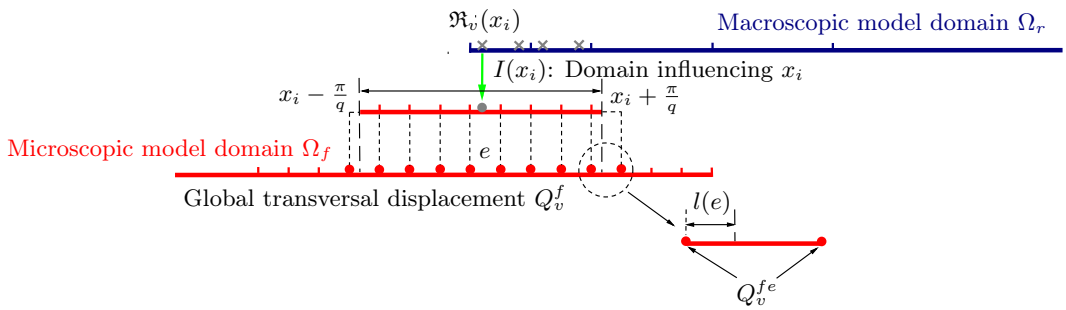

Figure 4.12: How the reduced Fourier coefficient $\mathfrak{R}_v(x_i)$ depends on the global microscopic transversal displacement Q_v^f.

$[-1, 1]$. The bilinear form is discretized in quite a classical way:

$$\mathscr{C}(\boldsymbol{\lambda}, \mathfrak{R}(\boldsymbol{u}_f)) = \sum_E \frac{L_E}{2} \sum_{x_i \in GP(E)} \left(\langle \boldsymbol{Q}_u^\lambda \rangle^E \{\boldsymbol{N}_u^r(x_i)\} \langle \boldsymbol{N}_u^f \rangle \left\{ \boldsymbol{Q}_u^f \right\}^e + \langle \boldsymbol{Q}_v^\lambda \rangle^E \{\boldsymbol{N}_v^r(x_i)\} \mathfrak{R}_v(x_i) \right), \tag{4.37}$$

where L_E is the length of the macroscopic elements. Note that two Gauss points on each macroscopic element can fully meet the accuracy requirements in this case (see Fig. 4.12). The reduction operator $\mathfrak{R}_v(x_i)$ in Eq. (4.28) is detailed from the following classical integration formula:

$$\begin{aligned} \mathfrak{R}_v(x_i) &= \frac{q}{2\pi} \int_{x_i - \frac{\pi}{q}}^{x_i + \frac{\pi}{q}} v(x) \sin(qx) \mathrm{d}x \approx \frac{q}{2\pi} \sum_e \frac{l(e)}{2} \sum_{x_j \in gp(e)} v(x_j) \sin(q x_j) \\ &= \frac{q}{2\pi} \sum_e \frac{l(e)}{2} \sum_{x_j \in gp(e)} \sin(q x_j) \langle \boldsymbol{N}_v^f(x_j) \rangle \left\{ \boldsymbol{Q}_v^f \right\}^e, \end{aligned} \tag{4.38}$$

where the length of the interval $l(e)$ is the intersection of the microscopic element with the integral region $I(x_i) = \left[x_i - \frac{\pi}{q}, x_i + \frac{\pi}{q} \right]$. It does not necessarily coincide with the interval of interpolation (see Fig. 4.12).

The coupling matrix $\boldsymbol{\mathcal{C}}_r$ can be assembled from the elementary matrices as

$$\boldsymbol{\mathcal{C}}_r^e = \int_{\Omega_e} \left(\begin{bmatrix} \boldsymbol{N}_u^r \\ \boldsymbol{N}_v^r \end{bmatrix} \begin{bmatrix} \boldsymbol{N}_u^r \\ \boldsymbol{N}_v^r \end{bmatrix}^t \right) \mathrm{d}\Omega. \tag{4.39}$$

The nonlinear system is solved using the classic Newton−Raphson method.

4.5 Numerical evaluation and assessment

4.5.1 Prolongation versus reduction-based coupling

Two coupling approaches are compared and evaluated. The numerical assessment is based on the results obtained on a beam resting on a nonlinear elastic foundation configuration. The clamped beam has the same parameters as reported in Section 4.3.2. The models are defined as

1. Microscopic model: 120 microscopic elements for the whole beam $[0, 30\pi]$.

2. Macroscopic model: 15 macroscopic elements for the whole beam $[0, 30\pi]$ with a wave number $q = 1$.

3. Prolongation coupling: 24 microscopic elements on the domain $[0, 6\pi]$, 12 macroscopic elements on the domain $[6\pi, 30\pi]$, the coupling zone is defined as the superposition zone ($S_g = S$) on the domain $[5\pi, 6\pi]$, where 2 macroscopic elements are bridged with 4 microscopic elements.

4. Reduction-based coupling: 32 microscopic elements on the domain $[0, 8\pi]$, 12 macroscopic elements on the domain $[6\pi, 30\pi]$, the superposition zone S is on the domain $[5\pi, 8\pi]$ while the coupling zone S_g is the domain $[5\pi, 6\pi]$ discretized by 2 macroscopic elements and 4 microscopic elements.

The boundary conditions for the microscopic model are those of a classical clamping: $v(0) = v'(0) = 0$, $v(L) = v'(L) = 0$, $u(0) = 0$, $u(L) = -\mu L$. The same boundary conditions have been applied for the bridging techniques (prolongation coupling and reduction-based coupling) at $x = 0$. As for the macroscopic model, it is known that at a clamped end, the envelope satisfies nearly $v_1(0) = v_1(L) = 0$. To be clear, only the left half part of the beam $[0, 15\pi]$ will be presented in the following figures, but the computations have been performed on the whole domain $[0, 30\pi]$.

The nonlinear problems have been solved by the Newton−Raphson procedure. Small step lengths have to be chosen in the region of the bifurcation $\mu \approx 2$. To ensure a transition from the fundamental branch to the bifurcated one, a transverse perturbation force g_{pert} is applied. The values of the perturbation force are given as $g_{pert} = 2 \times 10^{-3}$ for the microscopic model, $g_{pert} = 3 \times 10^{-5}$ for the macroscopic model and $g_{pert} = 2 \times 10^{-3}$ for the bridging models.

The numerical response of the structure is a spatial oscillation with a modulation near the end (see Fig. 4.13 and Fig. 4.14). Close to the bifurcation point $\mu = 2.01$, the envelope is nearly sinusoidal and it looks like a hyperbolic tangent away from the

bifurcation, which can be explained via the Ginzburg−Landau equation [153, 51]. In what follows, we distinguish the bulk behavior and the boundary behavior, respectively in the regions $[3\pi, 15\pi]$ and $[0, 3\pi]$. The post-buckling amplitude in the bulk is correctly captured by all the models, especially the macroscopic model (see Fig. 4.15). Indeed, the boundary conditions have little influence on the macroscopical amplitude in the bulk. In the same way, all the models correctly predict the bifurcation point $\mu \approx 2$. Near the boundary, the macroscopic model and prolongation coupling lead to divergent results. Only the reduction-based coupling is able to reproduce the prediction of the reference model (see Fig. 4.16). The details of the response near the boundary are illustrated in Fig. 4.19 for $\mu = 2.21$. One can observe the coincidence between the reduction-based coupling and the reference model. As for the macroscopic model and prolongation coupling, the post-buckling instability pattern is qualitatively similar to the reference model but with a significant phase shift.

It is well-known that the coupling matrices have to be defined on the coarse level to avoid locking phenomena. In [24], this coarse character is related to the discretization of the Lagrange multipliers $\boldsymbol{\lambda}$. In the present case, the coupling matrices $\boldsymbol{\mathcal{C}}_f^e$ and $\boldsymbol{\mathcal{C}}_r^e$ depend on the discretized mediator space, but there is also another alternative: to connect the Fourier coefficients (reduction-based coupling) or the functions of the fine model (prolongation coupling). Our results clearly establish that the coupling procedure has to be done in the coarse space, *i.e.* in the space of Fourier coefficients. Indeed, considering the values of the functions $v_f(x)$ and $v_r(x)$ in the gluing zone for the prolongation coupling (see Fig. 4.17), one can observe that the two functions coincide ($v_f(x) = v_r(x)$ in S_g) and this locking phenomenon causes undesirable behavior in the boundary region (see Fig. 4.19). On the contrary, as for the reduction-based coupling (see Fig. 4.18), $v_f(x)$ and $v_r(x)$ are not identical in the gluing zone, which leads to an accurate prediction in the boundary region (see Fig. 4.19).

4.5.2 About convergence

The definition of the numerical model depends on the three meshes (micro, macro and bridging), the reduced model and the location of gluing zone. The choice of meshes follows the same rules as with finite element technique and it is not re-discussed here. The definition of the reduced model induces some limits to the accuracy that can be expected in the macroscopic domain Ω_r. With the choice made in this chapter, one can get a good prediction of the amplitude of wrinkling patterns in this zone, but not their phase. This limitation clearly appears in Figs. 4.17 and 4.18 and cannot be improved within this reduced model. Thus, we focus on the influence of the gluing zone or, equivalently, on the size of the microscopic domain Ω_f. In Figs. 4.20 and 4.21, the Arlequin solution is

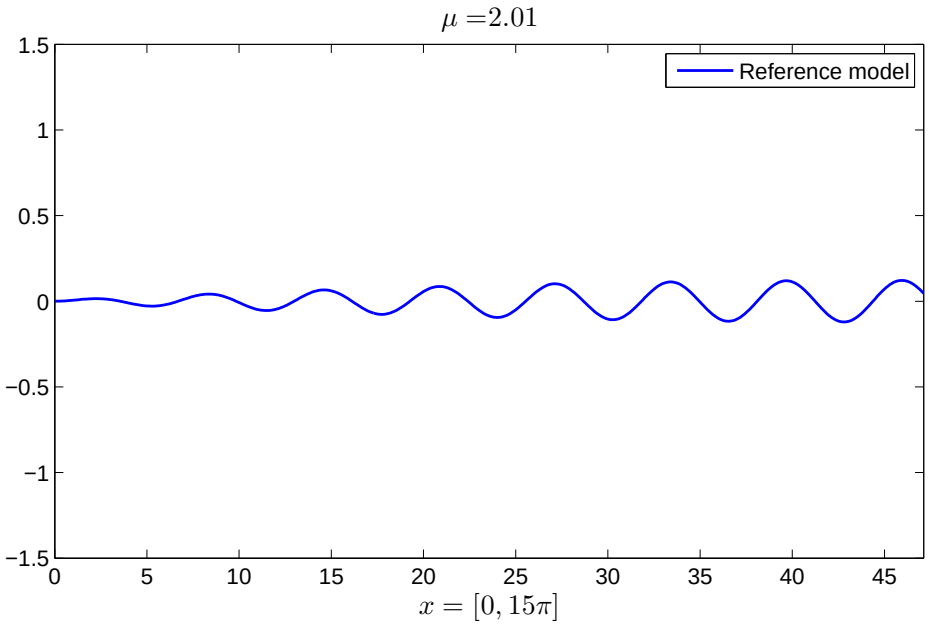

Figure 4.13: Buckling of a clamped beam under uniform compression: spatial distribution of the instability patterns for $\mu = 2.01$. Only the left half part of the beam is demonstrated.

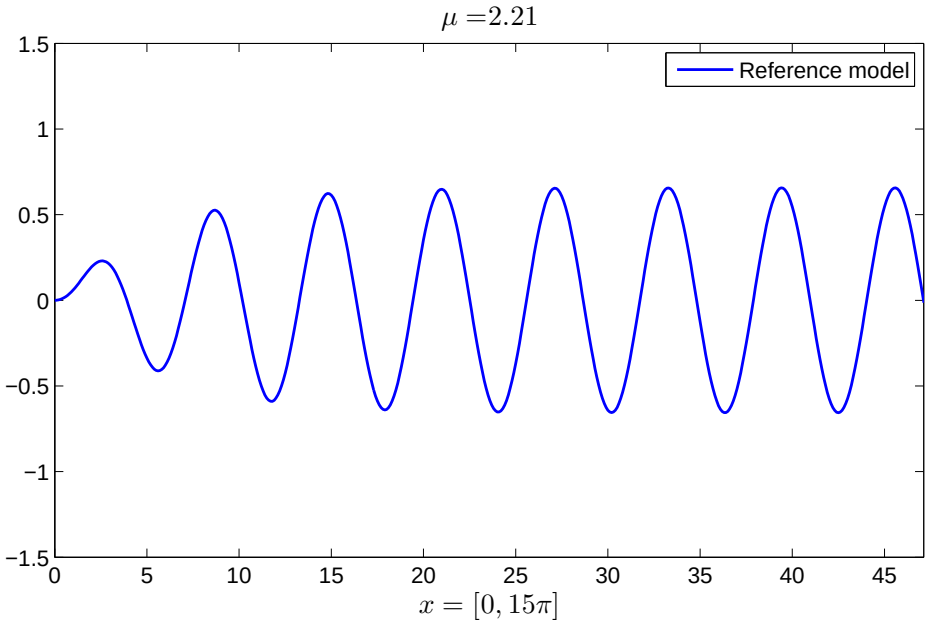

Figure 4.14: Buckling of a clamped beam under uniform compression: spatial distribution of the instability patterns for $\mu = 2.21$. Only the left half part of the beam is demonstrated.

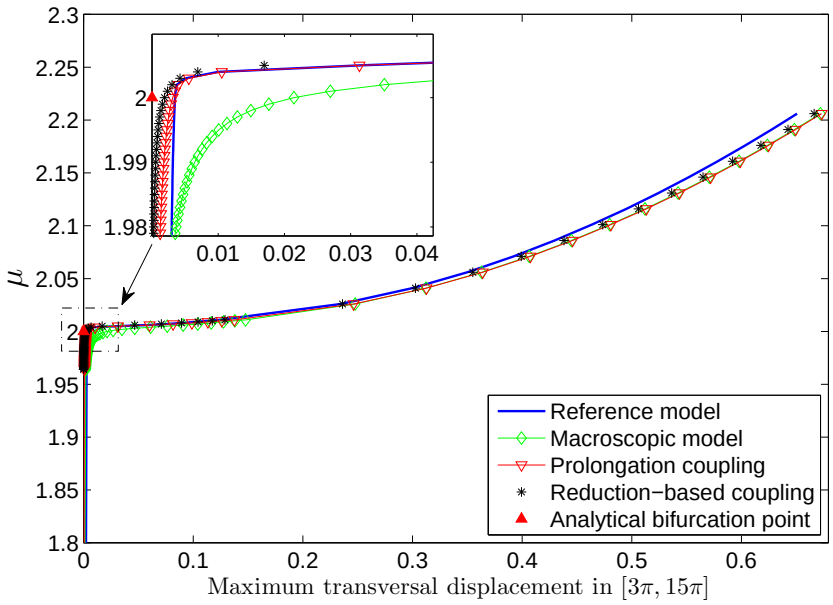

Figure 4.15: Buckling of a clamped beam under uniform compression: maximal deflection in $[3\pi, 15\pi]$ vs. applied shortening μ. The prolongation coupling and reduction-based coupling are depicted together.

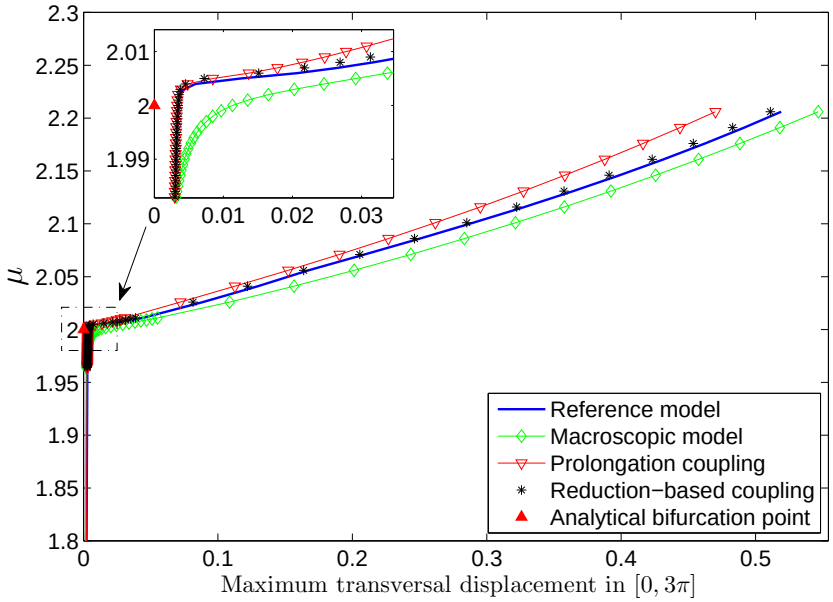

Figure 4.16: Buckling of a clamped beam under uniform compression: maximal deflection in $[0, 3\pi]$ vs. applied shortening μ. The prolongation coupling and reduction-based coupling are depicted together.

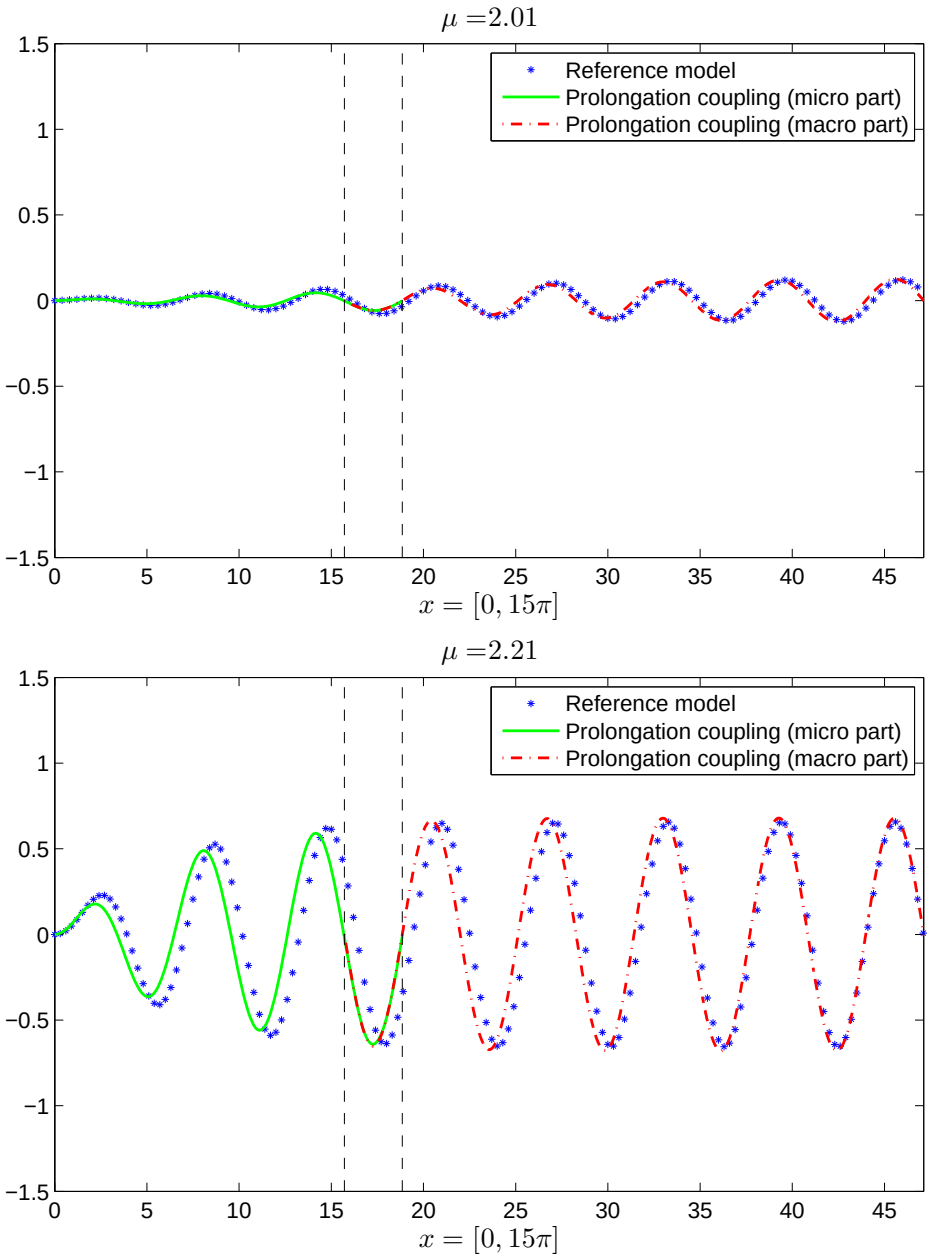

Figure 4.17: The prolongation coupling approach is implemented in the bridging technique. Buckling of a clamped beam under uniform compression: spatial distribution of the instability patterns for $\mu = 2.01$ and $\mu = 2.21$. Only the left half part of the beam is demonstrated.

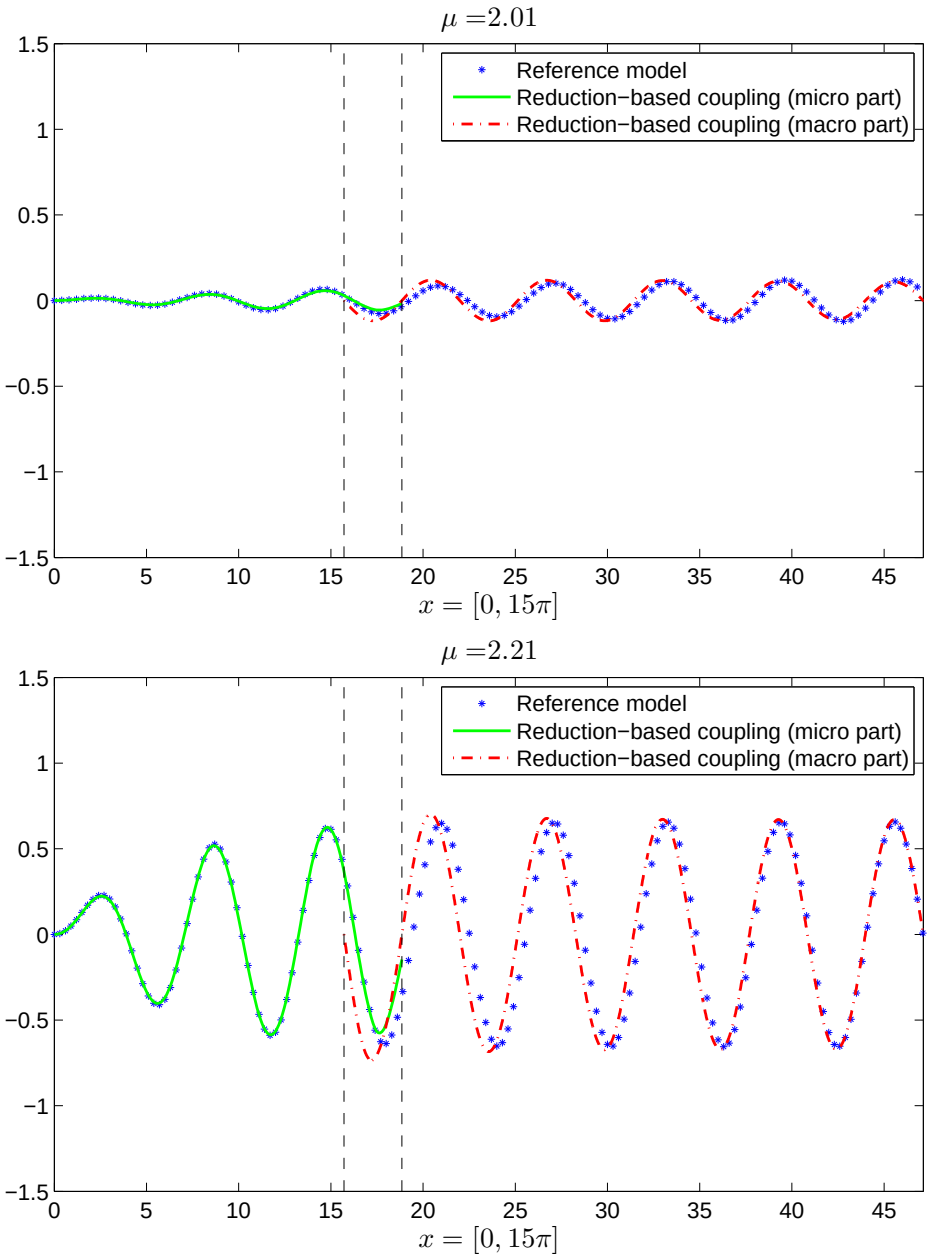

Figure 4.18: The reduction-based coupling approach is implemented in the bridging technique. Buckling of a clamped beam under uniform compression: spatial distribution of the instability patterns for $\mu = 2.01$ and $\mu = 2.21$. Only the left half part of the beam is demonstrated.

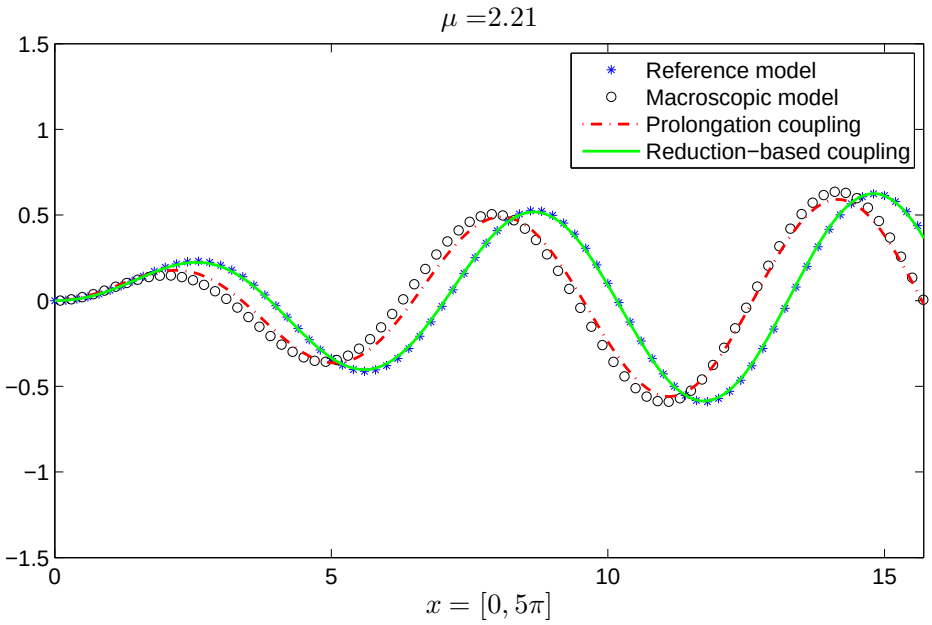

Figure 4.19: The left boundary region: spatial distribution of the instability patterns for $\mu = 2.21$. The prolongation coupling and reduction-based coupling are depicted together.

compared with the reference solution in the cases of gluing zones in $[3\pi, 4\pi]$ and $[8\pi, 9\pi]$, respectively. In the first case with a small Ω_f, the Arlequin solution is valid in almost all this interval $\Omega_f = [0, 3\pi]$. This is already a good result that was not found with the prolongation coupling, compared with Fig. 4.19. If one extends the microscopic domain Ω_f up to $[0, 8\pi]$, the Arlequin solution becomes accurate both in microscopic and gluing zones, which is the best accuracy to be expected with this reduced model.

4.5.3 H^1 versus L^2 coupling

The choice of the coupling bilinear form is a basic question within Arlequin method. The problems involved by L^2 coupling are known. It has been established that the Lagrange multiplier converges to a distribution and not to a function, for 1D elasticity with different meshes [24] and for atomistic-continuum coupling [15]. We come back to this discussion in the present case of a coupling between nonlinear beam and envelope model in the case of the prolongation coupling. The same clamped beam as in Section 4.5.1 is considered.

In Fig. 4.22, we have plotted the transversal displacement in the zone of the microscopic model on the left. It should be compared with Fig. 4.19 where the prolongation and reduction-based couplings were evaluated. The difference is rather weak, about few percents, while a significant difference was observed between the prolongation and reduction-based couplings. Nevertheless, this does not mean that H^1 and L^2 couplings

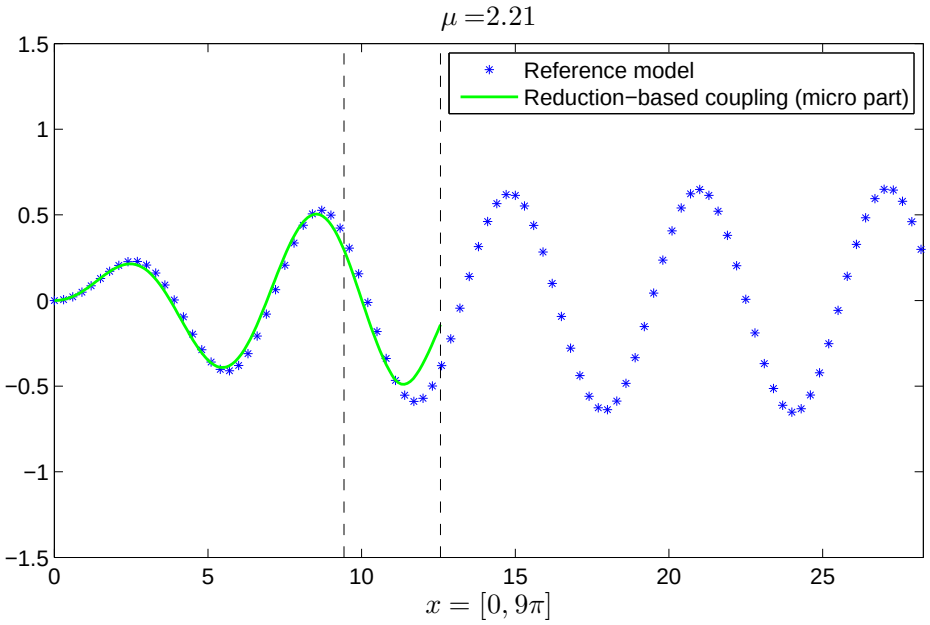

Figure 4.20: Spatial distribution of the instability patterns with the coupling zone in $[3\pi, 4\pi]$.

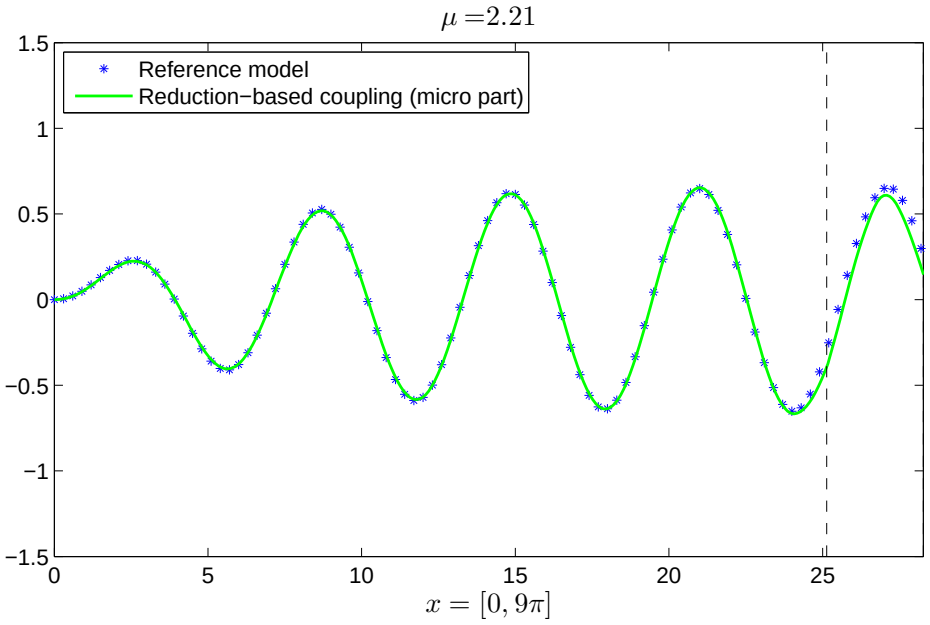

Figure 4.21: Spatial distribution of the instability patterns with the coupling zone in $[8\pi, 9\pi]$.

are equivalent. In Fig. 4.23, one evaluates the difference between the two displacements v_f and v_r in the cases of H^1 and L^2 couplings and one observes that this difference is much smaller with H^1 coupling. In the next Fig. 4.24, the spatial evolution of normal force $n(x)$ is depicted, as well as the macroscopic stress $n_0(x)$ that is the mean value of $n(x)$. In this case, these two quantities should be constant because of Eqs. (4.1−a) and (4.6−a). One observes rather strong oscillations in the coupling zone that are much severer in the L^2 case (about 4.2%) than in the H^1 case (about 1.6%). Nevertheless, these oscillations have little influence out of the gluing zone. Note that small oscillations existing in the microscopic zone on the left are due to membrane locking in finite element approximation. Finally, we present in Fig. 4.25 the variations of Lagrange multipliers in the two coupling cases. Localized forces are observed near the end of the gluing zone, which was expected by comparison with previous results; see for instance [24, 15, 41]. In the latter paper, the origin of these so-called "ghost forces" was carefully analyzed, and some corrections were proposed with an appropriate choice of weights and especially by introducing interaction forces between coarse and fine model.

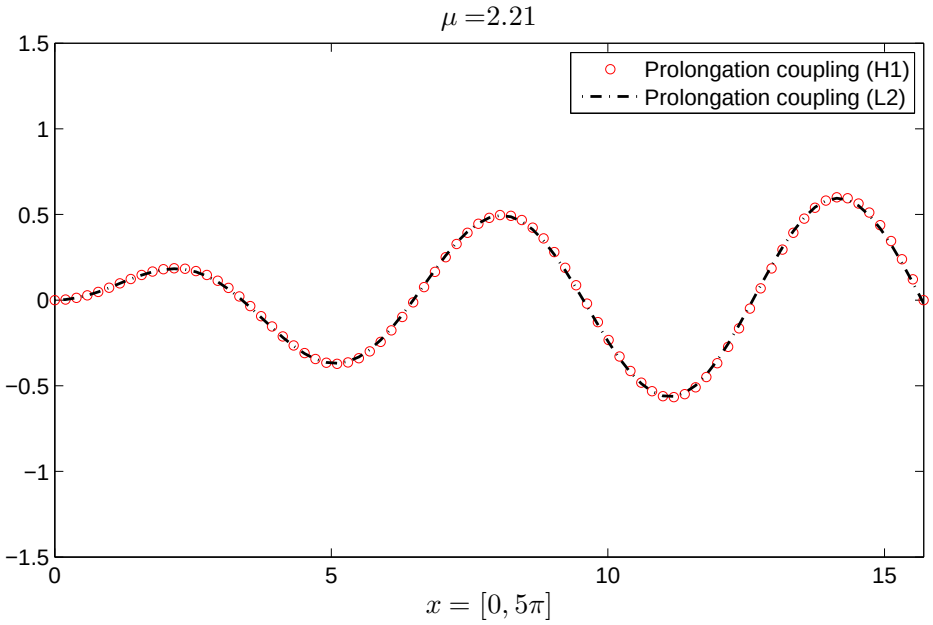

Figure 4.22: Deflection according to H^1 and L^2 couplings in the interval $[0, 5\pi]$ for $\mu = 2.21$.

Hence, there are differences between H^1 and L^2 couplings in the present case of bridging between a macroscopic and a microscopic model, which is very sensitive in the gluing zone. However, the coupling can be achieved at the micro or macro level. In the studied case, the best way is to couple in the macroscopic domain and this point is at least as important as the choice of the bilinear form, which is clearly shown in Figs. 4.19 and

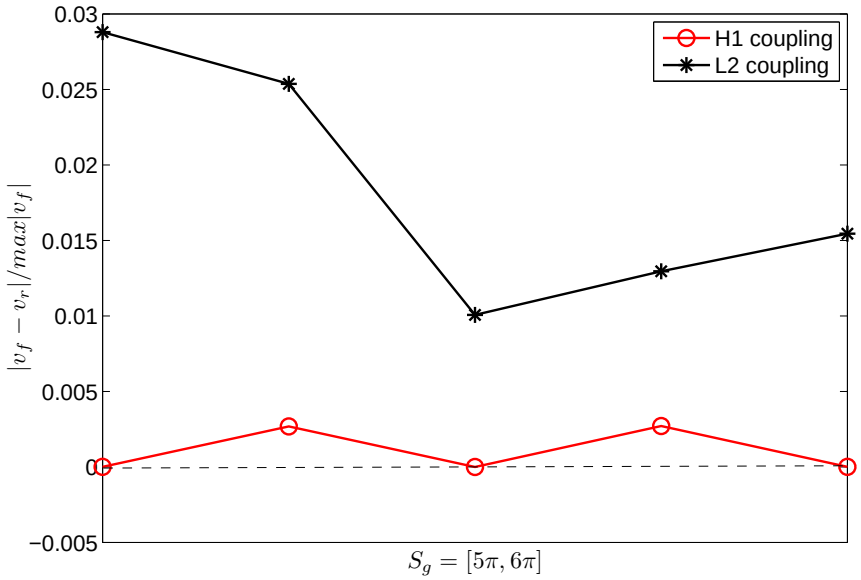

Figure 4.23: Effect of H^1 and L^2 couplings in the gluing zone. The relative difference of displacement is plotted.

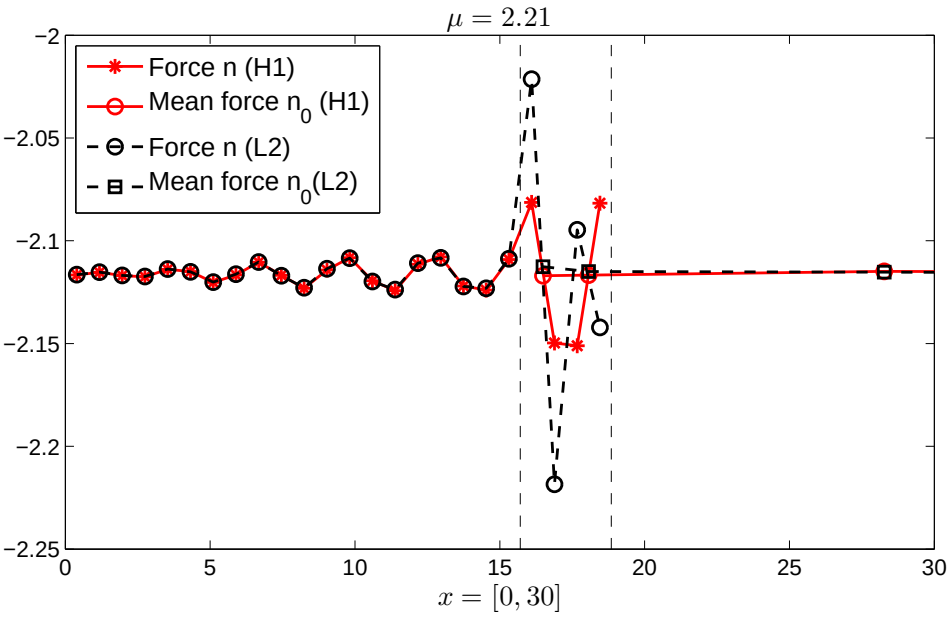

Figure 4.24: Effect of H^1 and L^2 couplings on normal forces.

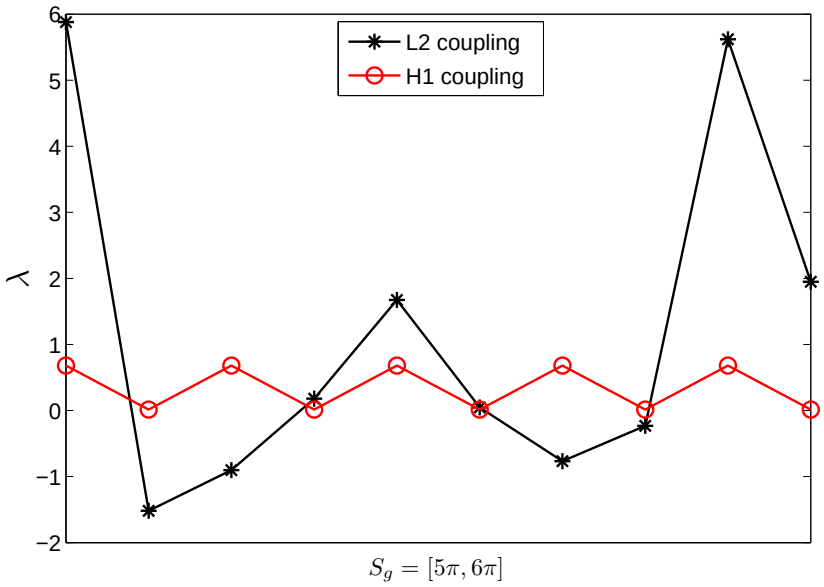

Figure 4.25: Lagrange multiplier within H^1 and L^2 couplings.

4.23.

4.6 Chapter conclusion

In this chapter, we have discussed how to connect a fine and a coarse model within the Arlequin framework. A typical cellular instability problem has been accurately analyzed, in which the coarse model is defined by envelope equations of Ginzburg−Landau type.

An Arlequin-problem involves a coupling operator and two models to be connected. The efficiency of the numerical technique depends on all three, but the coupling model has to be sufficiently robust and compatible with various choices of reduced models. In the case of envelope equations discussed here, the reduction operator leads to spurious oscillations in the Fourier coefficients that have been smoothed by the coupling operator. The presented reduction-based coupling has permitted us to accurately describe the response of the system near the boundary, even with a rather coarse reduced model.

The Arlequin method has been applied in a multi-scale framework, which has required to accurately define transition operators between the two levels, *i.e.* a prolongation operator from the coarse to the fine level and a reduction operator in the opposite sense. These two operators play a crucial role in the coupling technique, as well as the mediator bilinear form and its discretization. In the studied case, it is clearly better to use the reduction operator for a coupling at the coarse level rather than the prolongation operator for a coupling at the fine level. It will be interesting to discuss this question with other multi-scale models like those obtained in computational homogenization. It will be also interesting to apply a similar bridging technique for the coupling between full shell models and 2D envelope equations as introduced in [57]. Clearly, the bilinear form should be of H^1-type as in the nonlocal coupling introduced in [131] and the coupling has to be performed in the space of Fourier coefficients as established in the present chapter.

Chapter 5

Multi-scale modeling for instabilities in film/substrate by Fourier series

Contents

5.1 Introduction

Direct simulation of periodic wrinkles would spend considerable computation cost for simulating big sample with very refined meshes [121]. For example, the classical nonlinear 3D film/substrate model developed in Chapter 3, which couples 7-parameter shell elements and block elements, can describe moderately large displacements and rotations in the

film, while the computational cost would be rather high for simulating large samples with big wave number, which requires numerous finite elements. In this respect, one idea for simulating larger samples is to introduce reduced-order models, for example via the technique of slowly variable Fourier coefficients [54, 55, 56]. In this chapter, the macroscopic modeling methodology mentioned in Section 1.3 will be conducted both in 2D and 3D cases for film/substrate multi-scale modeling. A generalized macroscopic modeling framework will be deduced first, then it goes to specific 2D and 3D cases with simplifications and assumptions so as to be more efficient. Precisely, the 2D macroscopic film/substrate model will be based on the established classical model presented in Chapter 2, while all the mechanical fields are in the macroscopic perspective represented by Fourier coefficients. As for the 3D modeling of film/substrate, a nonlinear macroscopic membrane-wrinkling model that accounts for both membrane energy and bending energy will be deduced first. Then a linear macroscopic elastic model will be derived. Finally, following the same strategy as in Section 3.2.3, these two models will be coupled at the interface through Lagrange multipliers.

5.2 General macroscopic modeling framework

We will conduct a multi-scale approach based on the concept of Fourier series with slowly varying coefficients. Let us suppose that the instability wave number q is known. In this way, all the unknowns of model $U(x) = \{u_i(x), w_i(x)\}$ can be written in the form of Fourier series, whose coefficients vary more slowly than the harmonics:

$$U(x) = \sum_{j=-\infty}^{+\infty} U_j(x) e^{jiqx}, \tag{5.1}$$

where the Fourier coefficient $U_j(x)$ denotes the envelope for the j^{th} order harmonic, which is conjugated with $U_{-j}(x)$.

The macroscopic unknown fields $U_j(x)$ slowly vary over a period $\left[x, x + \frac{2\pi}{q}\right]$ of the oscillation. In practice, only a finite number of Fourier coefficients will be considered. As shown in Fig. 1.6, at least two functions $U_0(x)$ and $U_1(x)$ are necessary to describe nearly periodic patterns: $U_0(x)$ can be identified with the mean value while $U_1(x)$ represents the envelope or amplitude of the spatial oscillations. The mean value $U_0(x)$ is real valued, while the other envelopes are complex. Consequently, the envelope of the first harmonic $U_1(x)$ can be written as $U_1(x) = r(x)e^{i\varphi(x)}$, where $r(x)$ represents the amplitude modulation and $\varphi(x)$ is the phase modulation. If the phase varies linearly like $\varphi(x) = Qx + \varphi_0$, this type of approach is able to describe quasi-periodic responses whose wave number

$q+Q$ slightly differs from the *a priori* chosen q. Hence, the method makes it possible to account for a change in wave number.

The main idea of macroscopic modeling is to deduce differential equations satisfied by the amplitude $U_j(x)$. In what follows, we will develop a generalized macroscopic modeling framework for film/substrate system. Some calculation rules have been introduced in [54, 56] to manage these Fourier series with slowly varying coefficients. Derivative operators can be calculated exactly, according to the rules presented in Appendix B.

Let us apply the above methodology in general nonlinear elasticity problem. With the notations in [47], neglecting volume forces, the principle of virtual work can be expressed as

$$\int_\Omega \langle \delta\gamma \rangle \{s\} \, \mathrm{d}\Omega = \lambda \int_{\partial\Omega} \langle \delta u \rangle \{f\} \, \mathrm{d}\Omega, \tag{5.2}$$

where $\{\delta u\}$ is the virtual displacement vector and $\{f\}$ is the external loading vector at the boundary with the incremental loading parameter λ. In the framework of linear constitutive laws, the second Piola−Kichhoff stress $\{s\}$ and the Green−Lagrange strain vector $\{\gamma\}$ are linked linearly, while the strain is related to the displacement gradient $\{\theta\}$ by a quadratic relationship:

$$\begin{cases} \{s\} = [D]\{\gamma\}, \\ \{\gamma\} = [H]\{\theta\} + \dfrac{1}{2}[A(\theta)]\{\theta\}, \end{cases} \tag{5.3}$$

where the matrices $[D]$, $[H]$ and $[A(\theta)]$ are defined in [47]. Note that the matrix $[A(\theta)]$ satisfies the following symmetry property:

$$[A(\theta)]\{\varphi\} = [A(\varphi)]\{\theta\}. \tag{5.4}$$

We seek nearly periodic responses that vary rapidly in one direction. This characteristic direction and the period are described by a wave vector $\mathbf{q} \in \mathbb{R}^3$ that is assumed as a given parameter. In practice, this vector comes from a linear stability analysis. Hence, the vector $\{\Lambda(\mathbf{x})\}$, which includes displacement vector, its gradient, strain and stress tensors, is sought in the form of Fourier series, whose coefficients $\{\Lambda_j(\mathbf{x})\}$ vary slowly. For simplicity, we keep harmonics up to level 2 but it may achieve to high level for complex wave oscillation:

$$\Lambda(\mathbf{x}) = \sum_{j=-2}^{+2} \Lambda_j(\mathbf{x}) e^{jiqx}. \tag{5.5}$$

After applying it to the constitutive law (5.3), one can obtain a macroscopic constitutive law for harmonic 0 (real value) and two constitutive laws for harmonics 1 and 2 (complex

values), all these equations being coupled:

$$\begin{cases} \{\gamma_0\} = [D]^{-1}\{s_0\} = [H]\{\theta_0\} + \dfrac{1}{2}[A(\theta_0)]\{\theta_0\} + [A(\theta_{-1})]\{\theta_1\} + [A(\theta_{-2})]\{\theta_2\}, \\ \{\gamma_1\} = [D]^{-1}\{s_1\} = [H]\{\theta_1\} + [A(\theta_0)]\{\theta_1\} + [A(\theta_{-1})]\{\theta_2\}, \\ \{\gamma_2\} = [D]^{-1}\{s_2\} = [H]\{\theta_2\} + [A(\theta_0)]\{\theta_2\} + \dfrac{1}{2}[A(\theta_1)]\{\theta_1\}. \end{cases} \tag{5.6}$$

Therefore, a generalized continuum model has been defined, which is a sort of superposition of several continua. Like each field in the model, the displacement is replaced by a generalized displacement that includes five Fourier coefficients for $j \in [-2, 2]$. To facilitate the understanding and implementation, the macroscopic constitutive law (5.6) can be unified in the same generic form as the starting law (5.3):

$$\begin{cases} \{S\} = [D^{gen}]\{\Gamma\}, \\ \{\Gamma\} = [H^{gen}]\{\Theta\} + \dfrac{1}{2}[A^{gen}(\Theta)]\{\Theta\}, \end{cases} \tag{5.7}$$

where the generalized stress $\{S\}$, the generalized strain $\{\Gamma\}$ and the generalized displacement gradient $\{\Theta\}$ also include five Fourier coefficients for $j \in [-2, 2]$. The matrices that represent linear relationships are diagonal since the couplings between harmonics appear only for nonlinear terms, which leads to

$$[D^{gen}] = \begin{bmatrix} D & 0 & 0 & 0 & 0 \\ 0 & D/2 & 0 & 0 & 0 \\ 0 & 0 & D/2 & 0 & 0 \\ 0 & 0 & 0 & D/2 & 0 \\ 0 & 0 & 0 & 0 & D/2 \end{bmatrix}, \tag{5.8}$$

$$[H^{gen}] = \begin{bmatrix} H & 0 & 0 & 0 & 0 \\ 0 & 2H & 0 & 0 & 0 \\ 0 & 0 & 2H & 0 & 0 \\ 0 & 0 & 0 & 2H & 0 \\ 0 & 0 & 0 & 0 & 2H \end{bmatrix}. \tag{5.9}$$

The nonlinear aspects are taken into account by a single matrix:

$$[A^{gen}(\Theta)] = 2\begin{bmatrix} A(\theta_0)/2 & A(\theta_1^R) & A(\theta_1^I) & A(\theta_2^R) & A(\theta_2^I) \\ 0 & A(\theta_0) & 0 & A(\theta_1^R) & A(\theta_1^I) \\ 0 & 0 & A(\theta_0) & -A(\theta_1^I) & A(\theta_1^R) \\ 0 & A(\theta_1^R)/2 & -A(\theta_1^I)/2 & A(\theta_0) & 0 \\ 0 & A(\theta_1^I)/2 & A(\theta_1^R)/2 & 0 & A(\theta_0) \end{bmatrix}. \tag{5.10}$$

The size of this matrix is 30×45 in 3D cases and 15×20 in 2D cases.

Note that the j^{th} component of the displacement gradient is not the gradient of the j^{th} component of the displacement. The rule defining the Fourier components of a gradient vector reads

$$\{\nabla \mathbf{u}\}_j = \{\nabla(u_j)\} + ji[Q]\{u_j\}, \tag{5.11}$$

where

$$[Q] = \begin{bmatrix} \{q\} & 0 & 0 \\ 0 & \{q\} & 0 \\ 0 & 0 & \{q\} \end{bmatrix}. \tag{5.12}$$

In the same way, we will define the principle of virtual work for the extended macroscopic continuum. The previously defined technique with slowly variable Fourier coefficients can be applied to the balance equations. The weak form of those equations is then the extended principle of virtual work. Besides, this weak form can be deduced directly from the principle of virtual work of the initial problem (5.2) by using Parseval identity (B.3) (see Appendix B). The deduced principle of virtual work involves the Fourier coefficients of stress and strain:

$$\int_\Omega \sum_{j=-2}^{+2} \left\langle \delta\gamma_{-j} \right\rangle \{s_j\} \, \mathrm{d}\Omega = \lambda \int_{\partial\Omega} \sum_{j=-2}^{+2} \left\langle \delta u_j \right\rangle \{f_j\} \, \mathrm{d}\Omega, \tag{5.13}$$

where the left hand side involves Fourier coefficients of stress and strain, *i.e.* macroscopic stress and strain. One can find that the extended principle of virtual work takes the same form as the initial model (5.2):

$$\int_\Omega \langle \delta\Gamma \rangle \{S\} \, \mathrm{d}\Omega = \lambda \int_{\partial\Omega} \langle \delta U \rangle \{F\} \, \mathrm{d}\Omega. \tag{5.14}$$

It can be established that Eqs. (5.7) and (5.14) are derived from the stationarity of the following macroscopic potential energy:

$$\mathcal{P}^{gen}(U) = \frac{1}{2} \int_\Omega \langle \Gamma(U) \rangle [D^{gen}] \{\Gamma(U)\} \, \mathrm{d}\Omega - \lambda \int_{\partial\Omega} \langle U \rangle \{F\} \, \mathrm{d}\Omega. \tag{5.15}$$

Since the generalized macroscopic model has the same form as the initial microscopic model, its solution can be approximated by the same shape functions. In the microscopic model, the displacement and its gradient can be related to nodal variables via two interpolation matrices $[N]$ and $[G]$:

$$\begin{cases} \{u(\mathbf{x})\}^e = [N]\{v\}^e, \\ \{\nabla u(\mathbf{x})\}^e = [G]\{v\}^e. \end{cases} \tag{5.16}$$

After applying this discretization principle to the generalized displacement and the generalized displacement gradient, one can obtain interpolation formulae similar to (5.16). The generalized displacement will be expressed with respect to the generalized nodal displacement via a block diagonal matrix:

$$\{U(\mathbf{x})\}^e = [N^{gen}]\{V^{gen}\}^e, \tag{5.17}$$

where

$$[N^{gen}] = \begin{bmatrix} [N] & [0] & [0] \\ [0] & [N] & [0] \\ [0] & [0] & [N] \end{bmatrix}. \tag{5.18}$$

The other matrix interpolates the displacement gradient and it is a little complicated due to the derivative rule (5.11). The coupling between micro and macro scales appears at this level via the wave number matrix $[Q]$. First, let us separate the complex variables to real and imaginary parts from (5.11) by considering the matrix $[Q]$ is real:

$$\begin{aligned} \{\theta\}_j &= \{\theta_j^R\} + i\{\theta_j^I\} = \{\nabla(u_j)\} + ji[Q]\{u_j\} \\ &= \{\nabla(u_j^R)\} - j[Q]\{u_j^I\} + i\left(\{\nabla(u_j^I)\} + j[Q]\{u_j^R\}\right). \end{aligned} \tag{5.19}$$

The relation between the generalized displacement and the generalized displacement gradient vector $\{\Theta\}$ reads

$$\{\Theta(\mathbf{x})\}^e = \begin{Bmatrix} \{\theta_0\} \\ \{\theta_1^R\} \\ \{\theta_1^I\} \\ \{\theta_2^R\} \\ \{\theta_2^I\} \end{Bmatrix} = [G^{gen}]\{V^{gen}\}^e, \tag{5.20}$$

where

$$[G^{gen}] = \begin{bmatrix} [G] & [0] & [0] & [0 & [0]] \\ [0] & [G] & -[Q][N] & [0] & [0] \\ [0] & [Q][N] & [G] & [0] & [0] \\ [0] & [0] & [0] & [G] & -2[Q][N] \\ [0] & [0] & [0] & 2[Q][G] & [G] \end{bmatrix}. \tag{5.21}$$

Consequently, the discretization of the generalized strain tensor in Eq. (5.7) can be written as

$$\{\Gamma\} = \left([H^{gen}] + \frac{1}{2} [A^{gen}(\Theta)] \right) [G^{gen}] \{V^{gen}\}^e. \tag{5.22}$$

The above general macroscopic model can be directly applied to the 2D or 3D discretization of film/substrate systems. While considering the intrinsic property of the thin film that has been discussed in the previous chapters, the more efficient way is to take into account some kinematics simplifications for the film or to incorporate beam/shell/plate elements that are competitive for thin-walled structure modeling. This leads to the energy separation of the film/substrate system into two parts, *i.e.* film part and substrate part:

$$\mathbf{\Pi} = \mathbf{\Pi}_f + \mathbf{\Pi}_s. \tag{5.23}$$

Thus, in what follows, we will incorporate the general macroscopic modeling framework with nonlinear beam formulation for 2D case and nonlinear Föppl-von Kármán plate theory for 3D case, while the substrate is considered to be a linear elastic foundation.

5.3 A 2D macroscopic film/substrate model

The general macroscopic modeling framework established in the last section can be used directly for 2D film/substrate modeling, with the discretization of domain using 2D finite elements. However, some simplifications can be introduced as conducted in Chapter 2 to reduce the computational cost. One straight way is to develop a specific 2D Fourier-related film/substrate model based on the microscopic film/substrate model (2.8)−(2.14) established in Chapter 2, where the microscopic model has shown its validated effectiveness for post-buckling analyses. Thus, considering the identities presented in the last section, the kinematics in Eqs. (2.8)−(2.10) can be transformed to macroscopic

displacement fields as follows:

$$\text{Film}\begin{cases}\mathscr{U}_j^f = u_j^f - \left(z - \dfrac{h_f}{2} - h_s\right)\left(\dfrac{d}{dx} + ijq\right)\mathscr{W}_j^f, \\ \\ \mathscr{W}_j^f = w_j^f. \end{cases} \qquad h_s \le z \le h_t \tag{5.24}$$

$$1^{st}\text{ sublayer}\begin{cases}\mathscr{U}_j^{s1} = \dfrac{1-\eta}{2}(u_0)_j + \dfrac{1+\eta}{2}(u_1)_j, \\ \\ \mathscr{W}_j^{s1} = \dfrac{1-\eta}{2}(w_0)_j + \dfrac{1+\eta}{2}(w_1)_j. \end{cases} \qquad -1 \le \eta \le 1,\ (h_s - h_1) \le z \le h_s \tag{5.25}$$

$$n^{th}\text{ sublayer}\begin{cases}\mathscr{U}_j^{sn} = \dfrac{1-\eta}{2}(u_{n-1})_j + \dfrac{1+\eta}{2}(u_n)_j, \\ \\ \mathscr{W}_j^{sn} = \dfrac{1-\eta}{2}(w_{n-1})_j + \dfrac{1+\eta}{2}(w_n)_j. \end{cases} \qquad -1 \le \eta \le 1,\ 0 \le z \le h_n \tag{5.26}$$

In the same way, the constitutive and geometric equations in (2.11) and (2.12) can also be converted to macroscopic fields:

$$\begin{cases}(\sigma_{xx}^f)_j = E_f(\epsilon_{xx}^f)_j, \\ (\sigma_{xx}^{sn})_j = (\lambda_s + 2G_s)\,(\epsilon_{xx}^{sn})_j + \lambda_s(\epsilon_{zz}^{sn})_j, \\ (\sigma_{zz}^{sn})_j = (\lambda_s + 2G_s)\,(\epsilon_{zz}^{sn})_j + \lambda_s(\epsilon_{xx}^{sn})_j, \\ (\sigma_{xz}^{sn})_j = G_s(\gamma_{xz}^{sn})_j, \end{cases} \tag{5.27}$$

$$\begin{cases}(\epsilon_{xx}^f)_j = \left(\dfrac{d}{dx} + ijq\right)\mathscr{U}_j^f + \dfrac{1}{2}\displaystyle\sum_{j_1=-\infty}^{\infty}\left(\dfrac{d}{dx} + ij_1q\right)\left(\dfrac{d}{dx} + i\,(j-j_1)\,q\right)\mathscr{W}_{j_1}^f\mathscr{W}_{j-j_1}^f, \\ (\epsilon_{xx}^{sn})_j = \left(\dfrac{d}{dx} + ijq\right)\mathscr{U}_j^{sn}, \\ (\epsilon_{zz}^{sn})_j = \mathscr{W}_{j,z}^{sn}, \\ (\gamma_{xz}^{sn})_j = \mathscr{U}_{j,z}^{sn} + \left(\dfrac{d}{dx} + ijq\right)\mathscr{W}_j^{sn}, \end{cases} \tag{5.28}$$

Consequently, the internal virtual work (2.14) can be rewritten in the macroscopic

form:

$$\begin{aligned}\mathcal{P}_{int}\left(\delta\mathbf{u}\right) = &-\int_{\Omega^f}\sum_{j=-\infty}^{+\infty}(\sigma_{xx}^f)_j\delta(\epsilon_{xx}^f)_j\mathrm{d}\Omega \\ &-\sum_{sn}\int_{\Omega^{sn}}\sum_{j=-\infty}^{+\infty}\left[(\sigma_{xx}^{sn})_j\delta(\epsilon_{xx}^{sn})_j+(\sigma_{zz}^{sn})_j\delta(\epsilon_{zz}^{sn})_j+(\sigma_{xz}^{sn})_j\delta(\gamma_{xz}^{sn})_j\right]\mathrm{d}\Omega.\end{aligned} \tag{5.29}$$

Therefore, the microscopic model (2.8)−(2.14) has been transformed into its equivalent macroscopic form (5.24)−(5.29), with the unknowns $\{u_0,\, w_0,\, u_1,\, w_1,\, \ldots,\, u_n,\, w_n\}$ of the microscopic level being converted to the Fourier coefficients $\{(u_0)_j,\, (w_0)_j,\, (u_1)_j,\, (w_1)_j,\, \ldots,\, (u_n)_j,\, (w_n)_j\}$ of the macroscopic scale.

Since wrinkles usually appear on the top surface of the film/substrate system, which means local buckling plays a major role, three envelopes $U_0(x)$, $U_{-1}(x)$ and $U_1(x)$, respectively representing the mean field and amplitudes of fluctuation, are sufficient to describe such surface morphological instability (see Fig. 1.6). Hence, only three terms ($j=-1,0,1$) of Fourier coefficients will be considered in the transverse displacements. Besides, as relatively small oscillations appear in the longitudinal displacement field, only the zero order term ($j=0$) is reasonable to be taken into account. Similar approximations have been conducted and validated in previous works [119, 158].

5.3.1 Internal virtual work of the substrate

First, let us define the unknown variables in each sublayer

$$\langle\mathbf{q}^{sn}\rangle = \langle u_{n-1} \quad w_{n-1} \quad u_n \quad w_n\rangle\,, \tag{5.30}$$

$$\left\langle\mathbf{q}_{,x}^{sn}\right\rangle = \langle u_{n-1,x} \quad w_{n-1,x} \quad u_{n,x} \quad w_{n,x}\rangle\,. \tag{5.31}$$

According to the kinematics (2.10), the displacement field reads

$$\left\{\begin{array}{c}\mathscr{U}^{sn}\\ \mathscr{W}^{sn}\end{array}\right\} = [\mathbf{N}^z]\,\{\mathbf{q}^{sn}\}\,, \tag{5.32}$$

where

$$[\mathbf{N}^z] = \left[\begin{array}{cccc}\dfrac{1-\eta}{2} & 0 & \dfrac{1+\eta}{2} & 0\\ 0 & \dfrac{1-\eta}{2} & 0 & \dfrac{1+\eta}{2}\end{array}\right]. \tag{5.33}$$

The strain vector $\{\varepsilon^{sn}\}$ and stress vector $\{\mathbf{S}^{sn}\}$ can be respectively expressed as

$$\{\varepsilon^{sn}\} = \left\{ \begin{array}{c} \epsilon_{xx}^{sn} \\ \epsilon_{zz}^{sn} \\ \gamma_{xz}^{sn} \end{array} \right\} = [\mathbf{B}_1] \{\mathbf{q}^{sn}\} + [\mathbf{B}_2] \left\{\mathbf{q}_{,x}^{sn}\right\}, \tag{5.34}$$

$$\{\mathbf{S}^{sn}\} = [\mathbf{C}^{sn}] \{\varepsilon^{sn}\}, \tag{5.35}$$

in which

$$[\mathbf{B}_1] = \left[\begin{array}{cccc} \dfrac{1-\eta}{2} & 0 & \dfrac{1+\eta}{2} & 0 \\ 0 & -\dfrac{1}{h_n} & 0 & \dfrac{1}{h_n} \\ -\dfrac{1}{h_n} & 0 & \dfrac{1}{h_n} & 0 \end{array} \right], \tag{5.36}$$

$$[\mathbf{B}_2] = \left[\begin{array}{cccc} 0 & 0 & 0 & 0 \\ 0 & 0 & 0 & 0 \\ 0 & \dfrac{1-\eta}{2} & 0 & \dfrac{1+\eta}{2} \end{array} \right], \tag{5.37}$$

$$[\mathbf{C}^{sn}] = \left[\begin{array}{ccc} \lambda_s + 2G_s & \lambda_s & 0 \\ \lambda_s & \lambda_s + 2G_s & 0 \\ 0 & 0 & G_s \end{array} \right]. \tag{5.38}$$

The internal virtual work of the substrate can be represented as the sum of all the sublayers:

$$\begin{aligned} \mathcal{P}_{int}^{s}(\delta\mathbf{u}) &= -\int_0^L \int_0^{h_s} \langle \delta\varepsilon^s \rangle \{\mathbf{S}^s\} \, \mathrm{d}z\mathrm{d}x \\ &= -\int_0^L \left(\sum_{sn} \langle \delta\mathbf{q}^{sn} \rangle \underbrace{\int_0^{h_n} {}^T[\mathbf{B}_1] \{\mathbf{S}^{sn}\} \, \mathrm{d}z}_{\Phi} + \sum_{sn} \left\langle \delta\mathbf{q}_{,x}^{sn} \right\rangle \underbrace{\int_0^{h_n} {}^T[\mathbf{B}_2] \{\mathbf{S}^{sn}\} \, \mathrm{d}z}_{\Psi} \right) \mathrm{d}x. \end{aligned} \tag{5.39}$$

Through considering Eqs. (5.34) and (5.35), one can obtain

$$\Phi = \int_0^{h_n} {}^T[\mathbf{B}_1] [\mathbf{C}^{sn}] [\mathbf{B}_1] \, \mathrm{d}z \{\mathbf{q}^{sn}\} + \int_0^{h_n} {}^T[\mathbf{B}_1] [\mathbf{C}^{sn}] [\mathbf{B}_2] \, \mathrm{d}z \left\{\mathbf{q}_{,x}^{sn}\right\}, \tag{5.40}$$

$$\Psi = \int_0^{h_n} {}^T[\mathbf{B}_2] [\mathbf{C}^{sn}] [\mathbf{B}_1] \, \mathrm{d}z \{\mathbf{q}^{sn}\} + \int_0^{h_n} {}^T[\mathbf{B}_2] [\mathbf{C}^{sn}] [\mathbf{B}_2] \, \mathrm{d}z \left\{\mathbf{q}_{,x}^{sn}\right\}. \tag{5.41}$$

One can also combine the above two equations in the following form:

$$\left\{ \begin{array}{c} \Phi \\ \Psi \end{array} \right\} = [\mathbf{C}^s] \left\{ \begin{array}{c} \mathbf{q}^{sn} \\ \mathbf{q}^{sn}_{,x} \end{array} \right\}. \tag{5.42}$$

The macroscopic form of internal virtual work of the substrate involving three envelopes can be written as

$$\begin{aligned} \mathcal{P}^s_{int}(\delta\mathbf{u}) = -\sum_{sn} \int_0^L \Bigg(& \left\langle \delta\left(\mathbf{q}^{sn}\right)_0, \delta\left(\mathbf{q}^{sn}_{,x}\right)_0 \right\rangle [\mathbf{C}^s] \left\{ \begin{array}{c} \left(\mathbf{q}^{sn}\right)_0 \\ \left(\mathbf{q}^{sn}_{,x}\right)_0 \end{array} \right\} \\ & + 2 \left\langle \delta\left(\mathbf{q}^{sn}\right)_1, \delta\left(\mathbf{q}^{sn}_{,x}\right)_1 \right\rangle [\mathbf{C}^s] \left\{ \begin{array}{c} \left(\mathbf{q}^{sn}\right)_1 \\ \left(\mathbf{q}^{sn}_{,x}\right)_1 \end{array} \right\} \Bigg) \mathrm{d}x. \end{aligned} \tag{5.43}$$

Now we consider the discretization of substrate along the x direction. The unknown vectors can be given as

$$\{\mathbf{q}^{sn}\} = [\mathbf{N}^s]\{\mathbf{v}^s\}, \tag{5.44}$$

$$\left\{\mathbf{q}^{sn}_{,x}\right\} = \left[\mathbf{N}^s_{,x}\right]\{\mathbf{v}^s\}, \tag{5.45}$$

where $\{\mathbf{v}^s\}$ is the elementary unknown vector of the substrate and $[\mathbf{N}^s]$ is the shape function. Note that the longitudinal displacement u is discretized by linear Lagrange functions, while the transverse displacement w is discretized by Hermite functions. Consequently, the internal virtual work of the substrate can be written as

$$\begin{aligned} \mathcal{P}^s_{int}(\delta\mathbf{u}) &= -\sum_e \langle \delta\mathbf{v}^s \rangle \int_0^{l_e} \left({}^T[\mathbf{N}^s]\Phi + {}^T[\mathbf{N}^s_{,x}]\Psi \right) \mathrm{d}x \\ &= -\sum_e \langle \delta\mathbf{v}^s \rangle \int_0^{l_e} \left(\left[{}^T\mathbf{N}^s, {}^T\mathbf{N}^s_{,x} \right] [\mathbf{C}^s] \left[\begin{array}{c} \mathbf{N}^s \\ \mathbf{N}^s_{,x} \end{array} \right] \right) \mathrm{d}x \{\mathbf{v}^s\}, \end{aligned} \tag{5.46}$$

where l_e is the length of 1D element.

5.3.2 Internal virtual work of the film

As for the thin film, the strain energy is mainly generated by normal strain ϵ^f_{xx}, the other two terms ϵ^f_{zz} and γ^f_{xz} being neglected. By considering three envelopes, the macroscopic form of the internal virtual work for the film is expressed as

$$\mathcal{P}^f_{int}(\delta\mathbf{u}) = -\int_{\Omega^f} \sigma^f_{xx} \delta\epsilon^f_{xx} \mathrm{d}\Omega = -\delta \left(\frac{1}{2} \int_{\Omega^f} E_f \left[(\epsilon^f_{xx})_0^2 + 2 \left| (\epsilon^f_{xx})_1 \right|^2 \right] \mathrm{d}\Omega \right), \tag{5.47}$$

in which

$$\left(\epsilon_{xx}^{f}\right)_0 = u_{0,x}^{f} - \left(z - \frac{h_f}{2} - h_s\right) w_{0,xx}^{f} + \frac{1}{2}(w_{0,x}^{f})^2 + (w_{1,x}^{f})^2 + q^2(w_1^f)^2, \tag{5.48}$$

$$\begin{aligned}\left(\epsilon_{xx}^{f}\right)_1 = &\left[-\left(z - \frac{h_f}{2} - h_s\right)\left(w_{1,xx}^{f} - q^2 w_1^f\right) + w_{0,x}^{f} w_{1,x}^{f}\right] \\ &+ i\left[-2\left(z - \frac{h_f}{2} - h_s\right) q w_{1,x}^{f} + q w_{0,x}^{f} w_1^f\right],\end{aligned} \tag{5.49}$$

where $\left(\epsilon_{xx}^{f}\right)_0$ and $\left(\epsilon_{xx}^{f}\right)_1$ are respectively the zero order and the first order of the strain ϵ_{xx}^{f}.

Consequently, Eq. (5.47) can be rewritten in the following expanded form:

$$\begin{aligned}\mathcal{P}_{int}^{f}(\delta\mathbf{u}) = &-\int_0^L \left[S_a^f\left(\delta u_{0,x}^{f} + w_{0,x}^{f}\delta w_{0,x}^{f} + 2w_{1,x}^{f}\delta w_{1,x}^{f} + 2q^2 w_1^f \delta w_1^f\right) + S_b^f \delta\left(w_{0,x}^{f} w_{1,x}^{f}\right)\right. \\ &\left. + S_c^f \delta w_{0,xx}^{f} + S_d^f \delta\left(w_{0,x}^{f} w_1^f\right) + S_e^f \delta w_{1,x}^{f} + S_f^f \delta\left(w_{1,xx}^{f} - q^2 w_1^f\right)\right] \mathrm{d}x \\ = &-\int_0^L \left\langle \delta\varepsilon^f \right\rangle \left\{\mathbf{S}^f\right\} \mathrm{d}x,\end{aligned} \tag{5.50}$$

where

$$\begin{cases} S_a^f = E_f h_f\left(u_{0,x}^{f} + \frac{1}{2}(w_{0,x}^{f})^2 + (w_{1,x}^{f})^2 + q^2(w_1^f)^2\right), \\ S_b^f = 2E h_f w_{0,x}^{f} w_{1,x}^{f}, \\ S_c^f = \frac{1}{12} E_f h_f^3 w_{0,xx}^{f}, \\ S_d^f = 2E_f h_f q^2 w_{0,x}^{f} w_1^f, \\ S_e^f = \frac{2}{3} E_f h_f^3 q^2 w_{1,x}^{f}, \\ S_f^f = \frac{1}{6} E_f h_f^3\left(w_{1,xx}^{f} - q^2 w_1^f\right). \end{cases} \tag{5.51}$$

The generalized strain vector $\{\varepsilon^f\}$ of the film is defined as

$$\left\{\varepsilon^f\right\} = \left([\mathbf{H}] + \frac{1}{2}[\mathbf{A}(\mathbf{q}^f)]\right)\left\{\mathbf{q}^f\right\}, \tag{5.52}$$

in which

$$[\mathbf{H}] = \begin{bmatrix} 1 & & & & & 0 \\ & 0 & & & & \\ & & 1 & & & \\ & & & 0 & & \\ & & & & 1 & \\ 0 & & & & & 1 \end{bmatrix}, \tag{5.53}$$

$$[\mathbf{A}(\mathbf{q}^f)] = \begin{bmatrix} 0 & w^f_{0,x} & 0 & 2q^2 w^f_1 & 2w^f_{1,x} & 0 \\ 0 & w^f_{1,x} & 0 & 0 & w^f_{0,x} & 0 \\ 0 & 0 & 0 & 0 & 0 & 0 \\ 0 & w^f_1 & 0 & w^f_{0,x} & 0 & 0 \\ 0 & 0 & 0 & 0 & 0 & 0 \\ 0 & 0 & 0 & 0 & 0 & 0 \end{bmatrix}, \tag{5.54}$$

$$\left\langle \mathbf{q}^f \right\rangle = \left\langle u^f_{0,x} \quad w^f_{0,x} \quad w^f_{0,xx} \quad w^f_1 \quad w^f_{1,x} \quad \left(w^f_{1,xx} - q^2 w^f_1 \right) \right\rangle. \tag{5.55}$$

Since $[\mathbf{A}(\mathbf{q}^f)]$ and $\left\{\mathbf{q}^f\right\}$ are linear functions of u^f and w^f, the internal virtual work of the film (5.50) is in a quadratic form with respect to the displacement and the generalized stress:

$$\mathcal{P}^f_{int}\left(\delta\mathbf{u}\right) = -\int_0^L \left\langle \delta\mathbf{q}^f \right\rangle \left({}^T[\mathbf{H}] + {}^T[\mathbf{A}(\mathbf{q}^f)] \right) \left\{\mathbf{S}^f\right\} \mathrm{d}x, \tag{5.56}$$

where the generalized stress of the film reads

$$\left\{\mathbf{S}^f\right\} = [\mathbf{D}] \left([\mathbf{H}] + \frac{1}{2}[\mathbf{A}(\mathbf{q}^f)] \right) \left\{\mathbf{q}^f\right\}, \tag{5.57}$$

in which

$$[\mathbf{D}] = \mathtt{diag} \left(E_f h_f \quad 2E_f h_f \quad \frac{1}{12} E_f h_f^3 \quad 2q^2 E_f h_f \quad \frac{2}{3} q^2 E_f h_f^3 \quad \frac{1}{6} E_f h_f^3 \right). \tag{5.58}$$

Note that the discretization of unknown variables $\left\{\mathbf{q}^f\right\}$ takes the same shape function as for the substrate, *i.e.* Lagrange functions for the longitudinal displacement and Hermite functions for the transverse displacement.

5.3.3 Connection between the film and the substrate

As the film is bonded to the substrate, the displacement should be continuous at the interface. Therefore, the connection between the film and the substrate reads

$$\begin{cases} \mathscr{U}^f(x,h_s) = \mathscr{U}^{s1}(x,-1), \\ \mathscr{W}^f(x,h_s) = \mathscr{W}^{s1}(x,-1). \end{cases} \tag{5.59}$$

From Eqs. (2.8)−(2.9) and (5.59), the following relations can be obtained:

$$\begin{cases} u^f = u_0 - \dfrac{h_f}{2} w_{0,x}, \\ w^f = w_0. \end{cases} \tag{5.60}$$

Consequently, the corresponding macroscopic relation reads

$$\begin{cases} u_0^f = (u_0)_0 - \dfrac{h_f}{2}(w_0)_{0,x}, \\ w_0^f = (w_0)_0, \\ w_1^f = (w_0)_1. \end{cases} \tag{5.61}$$

5.4 A 3D macroscopic film/substate model

The general macroscopic modeling framework established in Section 5.2 can be used directly for 3D film/substrate modeling, by discretizing the domain using 3D finite elements. Nevertheless, it is cumbersome and especially not efficient for very thin film, since the huge difference ratio of thickness between the film and the substrate requires extremely refined meshes to keep the acceptable element aspect ratio. Some more flexible modeling schemes should be developed for 3D cases. One simple way is to develop a 3D macroscopic film/substrate model based on the same modeling strategy introduced in Chapter 3, where the 3D classical model has shown its competitive efficiency for post-bifurcation response of morphological instability. Thus, we consider the same film/substrate system as in Section 3.2, which includes the geometric and material properties as well as Hookean elasticity framework (see Fig. 3.2). However, the 3D macroscopic model will be totally different from the previous one. Precisely, this 3D macroscopic one couples a nonlinear macroscopic membrane-wrinkling model [57, 58] to represent the film and a linear macroscopic elasticity to describe the substrate, and these two models are coupled by introducing Lagrange multipliers. In what follows, this modeling scheme will lead to derive the integrated macroscopic film/substrate model.

5.4.1 Nonlinear macroscopic membrane-wrinkling model for the film

The technique of slowly variable Fourier coefficients will be applied to deduce the macroscopic membrane-wrinkling model based on the well-known Föppl-von Kármán equations for elastic isotropic plates that is considered as the reference model in this section:

$$\begin{cases} D\Delta^2 w - \operatorname{div}\left(\mathbf{N}\cdot\nabla w\right) = 0, \\ \mathbf{N} = \mathbf{L}^m \cdot \gamma, \\ \gamma = \dfrac{1}{2}\left(\nabla\mathbf{u} + {}^t\nabla\mathbf{u}\right) + \dfrac{1}{2}\left(\nabla w \otimes \nabla w\right), \\ \operatorname{div}\mathbf{N} = 0, \end{cases} \tag{5.62}$$

where $\mathbf{u} = (u, v) \in \mathbb{R}^2$ represents the in-plane displacement, while w is the deflection. The membrane stress and strain are denoted by $\mathbf{N}$ and γ, respectively. With the vectorial notations $\mathbf{N} = {}^t\{N_X, N_Y, N_{XY}\}$ and $\gamma = {}^t\{\gamma_X, \gamma_Y, \gamma_{XY}\}$, the membrane elastic matrix can be written as

$$\mathbf{L}^m = \frac{Eh}{1-\nu^2}\begin{bmatrix} 1 & \nu & 0 \\ \nu & 1 & 0 \\ 0 & 0 & \dfrac{1-\nu}{2} \end{bmatrix}. \tag{5.63}$$

The potential energy of the film, $\mathbf{\Pi}_f$, can be divided into a membrane part $\mathbf{\Pi}_{mem}$ and a bending part $\mathbf{\Pi}_{ben}$:

$$\begin{cases} \mathbf{\Pi}_f(\mathbf{u}, w) = \mathbf{\Pi}_{mem}(\mathbf{u}, w) + \mathbf{\Pi}_{ben}(w), \\ \mathbf{\Pi}_{mem}(\mathbf{u}, w) = \dfrac{1}{2}\displaystyle\iint_\Omega {}^t\gamma \cdot \mathbf{L}^m \cdot \gamma \mathrm{d}\Omega = \frac{Eh}{2(1-\nu^2)}\iint_\Omega \left(\gamma_X^2 + \gamma_Y^2 + 2(1-\nu)\gamma_{XY}^2 + 2\nu\gamma_X\gamma_Y\right)\mathrm{d}\Omega, \\ \mathbf{\Pi}_{ben}(w) = \dfrac{D}{2}\displaystyle\iint_\Omega \left(\left(\triangle w\right)^2 - 2(1-\nu)\left(\frac{\partial^2 w}{\partial X^2}\frac{\partial^2 w}{\partial Y^2} - \left(\frac{\partial^2 w}{\partial X \partial Y}\right)^2\right)\right)\mathrm{d}\Omega. \end{cases} \tag{5.64}$$

Macroscopic modeling of membrane energy

We adapt the technique of Fourier series with slowly variable coefficients in 2D framework [56]. For simplicity, we suppose that the instability wave number Q is known and the considered wrinkles spread only in the O_x direction. The unknown field $\mathbf{U}(X, Y) = \{\mathbf{u}(X, Y), w(X, Y), \mathbf{N}(X, Y), \gamma(X, Y)\}$, whose components are in-plane displacement, transverse displacement, membrane stress and strain, is written in the following form:

$$\mathbf{U}(X, Y) = \sum_{j=-\infty}^{+\infty} \mathbf{U}_j(X, Y) e^{jiQX}, \tag{5.65}$$

where the macroscopic unknown fields $\mathbf{U}_j(X,Y)$ vary slowly on the period $\left[X, X+\frac{2\pi}{Q}\right]$ of oscillations. It is not necessary to choose an infinite number of Fourier coefficients, so the unknown fields $\mathbf{U}(X,Y)$ are expressed in terms of two harmonics: the mean field $\mathbf{U}_0(X,Y)$ and the first order harmonics $\mathbf{U}_1(X,Y)e^{iQX}$ and $\overline{\mathbf{U}}_1(X,Y)e^{-iQX}$. The second harmonic should be taken into account to recover the results of the asymptotic Ginzburg−Landau double-scale approach [56]. Nevertheless, the second harmonic does not contribute to the membrane energy in the present case, since the rapid one-dimensional oscillations e^{iQX} are not extensional so that $\mathbf{N}_2 = 0, w_2 = 0$. Hence the second harmonic does not influence the simplest macroscopic models. A unique direction O_x for wave propagation is chosen in the whole domain. This assumption is a bit restrictive so that the current model can only describe sinusoidal pattern, which should be improved in the future. In principle, the mean field $\mathbf{U}_0(X,Y)$ is real and the envelope $\mathbf{U}_1(X,Y)$ is complex-valued. However, spatial evolutions of patterns can be reasonably accounted for with only two real coefficients in practice, even if a complex envelope can improve the treatment of boundary conditions [122].

After extending derivation rules in two-dimensional framework, the first Fourier coefficient of the gradient and the zero order coefficient of strain (*i.e.* mean value on a period) can be respectively expressed as

$$\{(\nabla w)_1\} = \left\{ \begin{array}{c} \dfrac{\partial w_1}{\partial X} + iQw_1 \\ \dfrac{\partial w_1}{\partial Y} \end{array} \right\}, \tag{5.66}$$

$$\{\gamma_0\} = \left\{ \begin{array}{c} \gamma_{X0} \\ \gamma_{Y0} \\ 2\gamma_{XY0} \end{array} \right\} = \left\{\gamma^{FK}\right\} + \left\{\gamma^{wr}\right\}, \tag{5.67}$$

in which

$$\left\{\gamma^{FK}\right\} = \left\{ \begin{array}{c} \dfrac{\partial u_0}{\partial X} + \dfrac{1}{2}\left(\dfrac{\partial w_0}{\partial X}\right)^2 \\ \dfrac{\partial v_0}{\partial Y} + \dfrac{1}{2}\left(\dfrac{\partial w_0}{\partial Y}\right)^2 \\ \dfrac{\partial u_0}{\partial Y} + \dfrac{\partial v_0}{\partial X} + \dfrac{\partial w_0}{\partial X}\dfrac{\partial w_0}{\partial Y} \end{array} \right\}, \tag{5.68}$$

$$\{\gamma^{wr}\} = \left\{ \begin{array}{c} \left|\dfrac{\partial w_1}{\partial X} + iQw_1\right|^2 \\ \left|\dfrac{\partial w_1}{\partial Y}\right|^2 \\ \left(\dfrac{\partial w_1}{\partial X} + iQw_1\right)\dfrac{\partial \overline{w}_1}{\partial Y} + \left(\dfrac{\partial \overline{w}_1}{\partial X} - iQ\overline{w}_1\right)\dfrac{\partial w_1}{\partial Y} \end{array} \right\}, \tag{5.69}$$

where the strain is divided into a classical part γ^{FK} that takes the same form as the initial Föppl-von Kármán model (5.62), and a wrinkling part γ^{wr} that depends only on the envelope of deflection w_1.

The strain-displacement law (5.67) can be simplified. First, the displacement field is reduced to a membrane mean displacement and to a bending wrinkling, *i.e.* $\mathbf{u}_1 = 0, w_0 = 0$, which only considers the influence of wrinkling on a flat membrane state. Second, the deflection envelope $w_1(X, Y)$ is assumed to be real, which disregards the phase modulation of the wrinkling pattern. Therefore, the envelope of the displacement has only three components $\mathbf{u}_0 = (u_0, v_0)$ and w_1 that will be rewritten for simplicity as $(u, v, w) = (u_0, v_0, w_1)$. Consequently, the simplified version of the strain field becomes

$$\{\gamma\} = \{\gamma_0\} = \{\varepsilon(\mathbf{u})\} + \{\gamma^{wr}\}\,, \tag{5.70}$$

in which

$$\{\varepsilon(\mathbf{u})\} = \left\{ \begin{array}{c} \dfrac{\partial u}{\partial X} \\ \dfrac{\partial v}{\partial Y} \\ \dfrac{\partial u}{\partial Y} + \dfrac{\partial v}{\partial X} \end{array} \right\}, \tag{5.71}$$

$$\{\gamma^{wr}\} = \left\{ \begin{array}{c} \left(\dfrac{\partial w}{\partial X}\right)^2 + Q^2 w^2 \\ \left(\dfrac{\partial w}{\partial Y}\right)^2 \\ 2\dfrac{\partial w}{\partial X}\dfrac{\partial w}{\partial Y} \end{array} \right\}. \tag{5.72}$$

The simplified membrane strain (5.70) is quite similar to that of the initial Föppl-von Kármán model. It is split, first in a linear part $\varepsilon(\mathbf{u})$ that is the symmetric part of the mean displacement gradient corresponding to the pure membrane linear strain, second in a nonlinear part γ^{wr} more or less equivalent to wrinkling strain. The main difference with the initial Föppl-von Kármán strain (5.62) is the extension $Q^2 w^2$ in the wave direction of wrinkles. This wrinkling strain is a stretching and is always positive. In the case of a compressive membrane strain, this wrinkling term leads to a decrease of the true strain.

By only considering the zero order harmonic, the reduced membrane energy becomes

$$\begin{aligned}\boldsymbol{\Pi}_{mem}(\mathbf{u},w) =& \frac{Eh}{2(1-\nu^2)}\iint_\Omega \left\{ \left(\frac{\partial u}{\partial X} + \left(\frac{\partial w}{\partial X}\right)^2 + Q^2 w^2 \right)^2 + \left(\frac{\partial v}{\partial Y} + \left(\frac{\partial w}{\partial Y}\right)^2 \right)^2 \right. \\ &+ 2(1-\nu)\left(\frac{1}{2}\left(\frac{\partial u}{\partial X} + \frac{\partial v}{\partial Y} \right) + \frac{\partial w}{\partial X}\frac{\partial w}{\partial Y} \right)^2 \\ &\left. + 2\nu \left(\frac{\partial u}{\partial X} + \left(\frac{\partial w}{\partial X}\right)^2 + Q^2 w^2 \right)\left(\frac{\partial v}{\partial Y} + \left(\frac{\partial w}{\partial Y}\right)^2 \right) \right\} \mathrm{d}\Omega.\end{aligned} \tag{5.73}$$

Macroscopic modeling of bending energy

Through simplifying the energy by keeping only the zero order term, it provides a formulation easier to be managed for the numerical discretization. The computation of the energy is based on the fact that only the zero order harmonic φ_0 of a function φ has a non-zero mean value:

$$\iint_\Omega \varphi \mathrm{d}\Omega = \iint_\Omega \varphi_0 \mathrm{d}\Omega. \tag{5.74}$$

This identity is applied to the bending energy in the framework $\mathbf{u}_1 = (u_1, v_1) = (0,0), w_0 = 0, w_1 \in \mathbb{R}$:

$$\varphi = (\Delta w)^2 - 2(1-\nu)\left(\frac{\partial^2 w}{\partial X^2}\frac{\partial^2 w}{\partial Y^2} - \left(\frac{\partial^2 w}{\partial X \partial Y} \right)^2 \right) = \varphi^A - 2(1-\nu)\varphi^B. \tag{5.75}$$

The first terms of bending energy reads

$$\begin{aligned}\varphi_0^A = (\Delta w)^2 &= \sum_{j=-\infty}^{+\infty} (\Delta w)_j (\Delta w)_{-j} = 2(\Delta w)_1 (\Delta w)_{-1} \\ &= 2\left|(\Delta w)_1\right|^2 = 2\left| \Delta w_1 - Q^2 w_1 + 2iQ\frac{\partial w_1}{\partial X} \right|^2.\end{aligned} \tag{5.76}$$

Due to the assumption of a real envelope $w = w_1$, the first term of the bending energy can be expressed as

$$\varphi_0^A = 2\left(\Delta w - Q^2 w\right)^2 + 8Q^2\left(\frac{\partial w}{\partial X}\right)^2. \tag{5.77}$$

In the same way, the second term of the bending energy φ_0^B reads

$$\varphi_0^B = 2\left(\frac{\partial^2 w}{\partial X^2} - Q^2 w \right)\frac{\partial^2 w}{\partial Y^2} - 2\left(\frac{\partial^2 w}{\partial X \partial Y} \right)^2 - 2Q^2\left(\frac{\partial w}{\partial Y} \right)^2. \tag{5.78}$$

As in [56], the derivatives of order three and order four in above differential equations can be neglected, since theses high order derivatives may lead to spurious oscillations and the derivatives of order two are sufficient to recover the Ginzburg−Landu asymptotic approach. Consequently, this leads to the simplified macroscopic bending energy:

$$\begin{aligned}\mathbf{\Pi}_{ben}(w) =& \frac{D}{2}\iint_{\Omega}\left\{Q^4w^2 - 2Q^2w\Delta w + 4Q^2\left(\frac{\partial w}{\partial X}\right)^2\right.\\ &\left. + 2(1-\nu^2)Q^2\left[w\frac{\partial^2 w}{\partial Y^2} + \left(\frac{\partial w}{\partial Y}\right)^2\right]\right\}\mathrm{d}\Omega.\end{aligned} \tag{5.79}$$

Full membrane-wrinkling model

The macroscopic model is deduced from the minimum of total energy that is the sum of membrane energy (5.73) and bending energy (5.79), which associates zero order harmonic for membrane quantities and real-valued first order harmonics for the deflection. In this way, the total energy is stationary at equilibrium:

$$\delta\mathbf{\Pi}_{mem} + \delta\mathbf{\Pi}_{ben} = 0. \tag{5.80}$$

The condition that any virtual displacement is zero at the boundary gives

$$\iint_{\Omega}\mathbf{N} : \delta\varepsilon\mathrm{d}\Omega = 0, \tag{5.81}$$

$$\iint_{\Omega}\mathbf{N} : \delta\gamma^{wr}\mathrm{d}\Omega + \delta\mathbf{\Pi}_{ben} = 0. \tag{5.82}$$

After straightforward calculations, one obtains the partial differential equations of the macroscopic problems:

$$\begin{cases} -6DQ^2\dfrac{\partial^2 w}{\partial X^2} - 2DQ^2\dfrac{\partial^2 w}{\partial Y^2} + \left(DQ^4 + N_X Q^2\right)w - \mathrm{div}\left(\mathbf{N}\cdot\nabla w\right) = 0,\\ \mathbf{N} = \mathbf{L}^m : \left[\varepsilon(\mathbf{u}) + \gamma^{wr}(w)\right],\\ \mathrm{div}\mathbf{N} = 0. \end{cases} \tag{5.83}$$

The above model (5.83) couples nonlinear membrane equations with a bifurcation equation satisfied by the envelope of wrinkling pattern. More discussion on the model can be found in [57, 58]. Since this model is a second order partial differential system, any classical C^0 finite element is acceptable for its discretization. In the application, 8-node quadratic quadrilateral elements (2D-Q8) with three degrees of freedom (u, v, w) per node will be used. Details on the discretization will be omitted here, since it is quite straightforward.

5.4.2 Linear macroscopic elasticity for the substrate

As explained in Section 3.2.2, linear isotropic elasticity theory is sufficient to represent the substrate, while the potential energy of the substrate (3.9) should be reformulated in the macroscopic framework. We apply the technique of slowly variable Fourier coefficients in 3D case [56]. To be consistent with the macroscopic membrane-wrinkling model, we also assume that the instability wave number vector $\{q\}$ is known and the wave spreads along the O_x direction. In other words, the vector $\{q\}$ is parallel to the unit vector $\{1,0,0\}$, *i.e.* $\{q\} = q\{1,0,0\}$. The unknown field $\mathbf{U}(X,Y,Z) = \{\mathbf{u}(X,Y,Z), \sigma(X,Y,Z), \varepsilon(X,Y,Z)\}$, whose components are displacement, stress and strain, is written in the following form:

$$\mathbf{U}(X,Y,Z) = \sum_{j=-\infty}^{+\infty} \mathbf{U}_j(X,Y,Z) e^{ji\{q\}X}, \tag{5.84}$$

where the macroscopic unknown fields $\mathbf{U}_j(X,Y,Z)$ vary slowly on the period $\left[X, X+\frac{2\pi}{q}\right]$ of oscillations. As discussed before, it is not necessary to choose an infinite number of Fourier coefficients and thus the unknown fields $\mathbf{U}(X,Y,Z)$ are expressed in terms of two harmonics: the mean field $\mathbf{U}_0(X,Y,Z)$ and the first order harmonics $\mathbf{U}_1(X,Y,Z)e^{i\{q\}X}$ and $\overline{\mathbf{U}}_1(X,Y,Z)e^{-i\{q\}X}$. Hence, the macroscopic potential energy of the substrate can be expressed as

$$\mathbf{\Pi}_s(\mathbf{u}_s) = \frac{1}{2}\int_\Omega \sum_{j=-1}^{+1} {}^t\varepsilon_{-j} : \mathbf{L}_s : \varepsilon_j \mathrm{d}\Omega - \lambda \mathbf{P}_e(\mathbf{u}_s), \tag{5.85}$$

where $\mathbf{L}_s$ is the elastic matrix of the substrate. It can be seen that the macroscopic potential energy (5.85) takes the same form as the classical one (3.9). Note that each unknown of the classical model is replaced by a vector of three times larger size, since it takes into account the zero order harmonic and the first order harmonic represented by a complex vector or by two real vectors. These generalized vectors, *i.e.* the generalized displacement $\{\mathbf{u}_s\}$, the generalized stress $\{\sigma\}$, the generalized strain $\{\varepsilon\}$ and the generalized displacement gradient $\{\theta\}$, are defined as

$$\begin{cases} \{\mathbf{u}_s\} = \left\{\{\mathbf{u}_0\}, \{\mathbf{u}_1^R\}, \{\mathbf{u}_1^I\}\right\}, \\ \{\sigma\} = \left\{\{\sigma_0\}, \{\sigma_1^R\}, \{\sigma_1^I\}\right\}, \\ \{\varepsilon\} = \left\{\{\varepsilon_0\}, \{\varepsilon_1^R\}, \{\varepsilon_1^I\}\right\}, \\ \{\theta\} = \left\{\{\theta_0\}, \{\theta_1^R\}, \{\theta_1^I\}\right\}. \end{cases} \tag{5.86}$$

For linear elasticity, one can get a constitutive law for the zero order harmonic (real number) and two constitutive laws for the first order harmonic (complex number), with

all the equations being coupled:

$$\begin{cases} \{\varepsilon_0\} = [L_s]^{-1}\{\sigma_0\} = [H]\{\theta_0\}, \\ \{\varepsilon_1\} = [L_s]^{-1}\{\sigma_1\} = [H]\{\theta_1\}, \end{cases} \tag{5.87}$$

where the matrix $[H]$ is detailed in [47]. Finally, the macroscopic behavior can be formulated in a general form:

$$\begin{cases} \{\sigma\} = [L_s^{gen}]\{\varepsilon\}, \\ \{\varepsilon\} = [H^{gen}]\{\theta\}, \end{cases} \tag{5.88}$$

where

$$[L_s^{gen}] = \begin{bmatrix} L_s & 0 & 0 \\ 0 & L_s/2 & 0 \\ 0 & 0 & L_s/2 \end{bmatrix}, \tag{5.89}$$

$$[H^{gen}] = \begin{bmatrix} H & 0 & 0 \\ 0 & 2H & 0 \\ 0 & 0 & 2H \end{bmatrix}. \tag{5.90}$$

Discretization of the 3D macroscopic model (5.85) takes the same shape functions as the 3D classical model (3.9), since they are quite similar, where the details are omitted. Thus, 8-node solid elements with reduced integration can be applied as well, but with totally 72 ($3 \times 3 \times 8$) degrees of freedom on each element.

5.4.3 Connection between the film and the substrate

As in Section 3.2.3, displacement continuity is satisfied at the interface. However, the macroscopic membrane-wrinkling elements for the film and 3D macroscopic block elements for the substrate cannot be simply joined directly since they belong to dissimilar elements. Therefore, additional incorporating constraint equations have to be employed. Hereby, Lagrange multipliers are applied to couple the corresponding node displacements of the same order harmonics in compatible meshes between the film and the substrate (see Fig. 3.4). Note that using 8-node linear block element here is only for coupling convenience, 20-node quadratic block element would be another good candidate, while both of them follow the same coupling strategy. Consequently, the stationary function of film/substrate system is given in a Lagrangian form:

$$\mathscr{L}(\mathbf{u}_f, \mathbf{u}_s, \ell) = \mathbf{\Pi}_f + \mathbf{\Pi}_s + \sum_{node\ i} \ell_i \left[\mathbf{u}_f(i) - \mathbf{u}_s(i)\right], \tag{5.91}$$

where the displacements of the film and the substrate are respectively denoted as $\mathbf{u}_f$ and $\mathbf{u}_s$, while the Lagrange multipliers are represented by ℓ. At the interface, the displacement continuity is satisfied at the same nodes and connects the middle surface of the film and the top surface of the substrate. From Eq. (5.91), three equations are obtained according to $\delta\mathbf{u}_f$, $\delta\mathbf{u}_s$ and $\delta\ell$:

$$\begin{cases} \delta\mathbf{\Pi}_f + \sum\limits_{node\ i} \ell_i \delta\mathbf{u}_f(i) = 0, \\ \delta\mathbf{\Pi}_s - \sum\limits_{node\ i} \ell_i \delta\mathbf{u}_s(i) = 0, \\ \sum\limits_{node\ i} \delta\ell_i \mathbf{u}_f(i) - \sum\limits_{node\ i} \delta\ell_i \mathbf{u}_s(i) = 0. \end{cases} \tag{5.92}$$

5.5 Resolution technique and bifurcation analysis

The same generic resolution techniques and bifurcation schemes established in Section 2.4 and 3.3 will be adapted to both 2D and 3D macroscopic film/substrate model, which includes using the ANM as a continuation technique to solve nonlinear differential equations and calculating bifurcation indicators to predict secondary bifurcations as well as the associated wrinkling modes on the post-buckling path. Since this general framework is also suitable for the current multi-scale problem and the procedure remains unchanged, the details will be omitted here.

5.6 Chapter conclusion

In this chapter, we revisit the film/substrate system from a multi-scale standpoint with respect to Fourier series. Firstly, a generic macroscopic modeling scheme is established, which is suitable for both 2D and 3D problems but not so efficient for very thin film in terms of computational cost. Thus, secondly, a simplified 2D macroscopic film/substrate model with three envelopes is derived based on the established microscopic model presented in Chapter 2. Development of the computer codes have been completed. It is expected to predict the primary sinusoidal wrinkles and entailing aperiodic modes observed in Chapter 2 with much fewer elements, which can save an enormous amount of computation time. Validation of the macroscopic model by comparison with 2D classical film/substrate model established in Chapter 2, should be included as part of short-term perspective. Lastly, following the same modeling scheme proposed in Chapter 3, a 3D nonlinear macroscopic film/substrate model has been developed. Precisely, this 3D model couples a macroscopic membrane-wrinkling model based on the well-known Föppl-von Kármán nonlinear plate theory and a linear macroscopic elasticity. Through introducing Lagrange multipliers at the interface, displacement continuity is satisfied in

a weak form. Self-developed computer codes for both macroscopic models and coupling procedures have been accomplished. It is expected to predict at least sinusoidal patterns observed in Chapter 3 with much fewer elements, which is competitive from computational standpoint. In the following, validation of the macroscopic model by comparison with 3D classical film/substrate model established in Chapter 3, will be included as part of short-term perspective.

Conclusion and perspectives

In this thesis, we proposed a whole framework to study surface wrinkling of thin films bound to soft substrates in a numerical way: from 2D to 3D modeling, from classical to multi-scale perspective. Both 2D and 3D models incorporated Asymptotic Numerical Method (ANM) as a robust path-following technique and bifurcation indicators well adapted to the ANM, so as to predict a sequence of multiple bifurcations and the associated instability modes on their post-buckling evolution path as the load is increased. The tracing of post-bifurcation evolution is an important numerical problem and it is definitely non-trivial. The ANM gives interactive access to semi-analytical equilibrium branches, which offers considerable advantage of reliability compared with classical iterative algorithms. Probably, it would be rather difficult to detect all the bifurcations found in this thesis by using conventional numerical methods. To our best knowledge, it appears to be the first work that addresses the post-bifurcation instability problems of film/substrate from the quantitative standpoint, through applying these advanced numerical approaches (path-following techniques, bifurcation indicators, bridging techniques, multi-scale approaches, Lagrange multipliers, *etc.*), which is viewed as a valuable contribution to the field of film/substrate post-buckling analyses.

In 2D cases of film/substrate system, a classical finite element model was used associating geometrically nonlinear beam for the film and linear elasticity for the substrate. The effect of boundary conditions and material properties of the substrate (homogeneous, graded material and orthotropic) on the bifurcation portrait is carefully studied, which was rarely explored in the literature. The evolution of wrinkling patterns and post-bifurcation modes including period-doubling has been detected beyond the onset of the primary sinusoidal wrinkling mode on the post-buckling evolution path (see Fig. 1).

In 3D cases, spatial pattern formation of film/substrate was investigated based on a nonlinear 3D finite element model associating geometrically nonlinear shell formulation for the film and linear elasticity for the substrate. Typical post-bifurcation patterns include sinusoidal, checkerboard and herringbone shapes, with possible spatial modulations, boundary effects and localizations. The post-buckling behavior often leads to intricate response curves with several secondary bifurcations that were rarely studied and only in

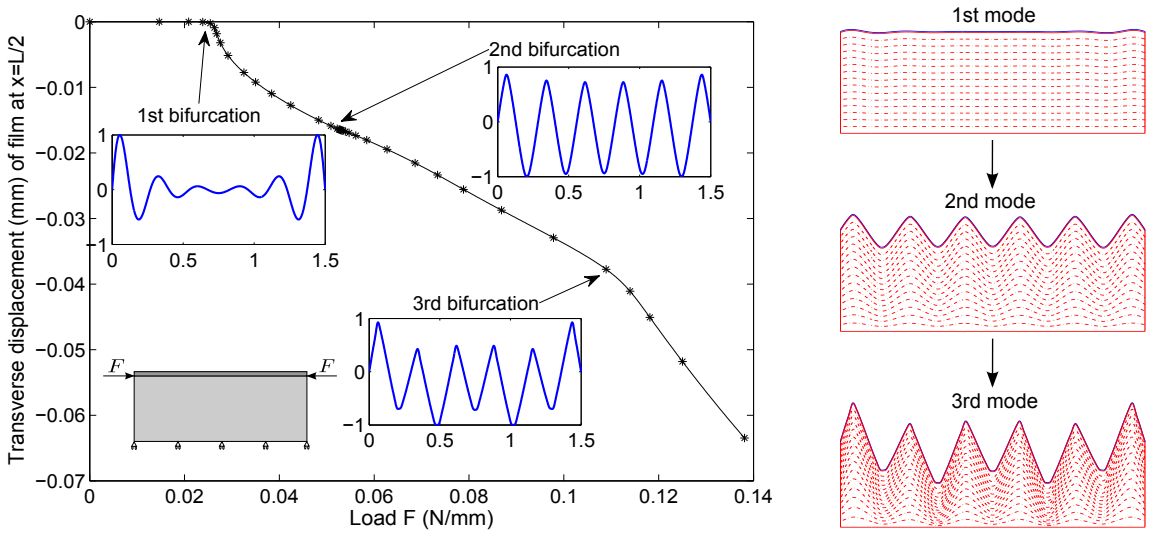

Figure 1: Bifurcation curve and the associated wrinkling modes with respect to the incremental compression. Period-doubling mode appears at the third bifurcation point.

the case of periodic cells [35]. In conventional finite element analysis, the post-buckling simulation may suffer from the convergence issue if the film is much stiffer than the substrate. Nevertheless, the proposed finite element procedure in this thesis allows accurately describing these bifurcation portraits by taking into account the effect of boundary conditions, without any convergent problem. The occurrence and evolution of sinusoidal, checkerboard and herringbone patterns were highlighted in Chapter 3. This work has been viewed as a valuable contribution to film/substrate buckling problems, where the model incorporating the ANM as a path-following technique to detect multiple bifurcations in the post-buckling analysis is interesting and meaningful.

A very original nonlocal coupling strategy is developed in this thesis, which is able to bridge classical models and multi-scale models concurrently, where the strengths of each model are fully exploited while their shortcomings are accordingly overcome. More precisely, we considered a partitioned-domain multi-scale model for a 1D nonlinear elastic wrinkling model. The coarse model, obtained from a suitable Fourier-reduction technique [56], is inaccurate near the boundary of the domain. Therefore, near the boundary, the full model is employed, which is then coupled to the coarse model in the remainder of the domain using the Arlequin method [20, 24] as a bridging-domain technique. Numerical results explicitly illustrate the effectiveness of this methodology. Besides, discussion on the transition between a fine and a coarse model was provided in a general way. The present method can also be seen as a guide for coupling techniques involving other reduced-order models. This work has been considered as an original, logical and relevant application of multi-scale modeling with good motivations, explanations and interesting numerical

results. The proposed bridging techniques are not merely limited to 1D case, but can also be flexibly extended to 2D or 3D cases. Thus, one direct potential perspective of application is to use the proposed bridging techniques to study 2D or 3D film/substrate buckling problems, which can be viewed as one of our future works.

A macroscopic modeling framework was provided based on the technique of slowly variable Fourier coefficients [54, 55, 56], which is in 3D situation and can be extended to any film/substrate modeling application. In particular, a 2D and a 3D macroscopic film/substrate model were derived from the classical models established in Chapter 2 and Chapter 3, respectively. Development of the computer codes for both 2D and 3D envelope models has been completed, while validation of the macroscopic models by comparison with classical film/substrate models should be included in the short-term perspective.

Some parts of the works presented in this thesis have been published in *International Journal of Solids and Structures* [159, 158] or in *International Journal of Non-Linear Mechanics* [160], while the ideas and schemes generated from the present thesis are expected to lead to more works in the future.

As for the short term perspective, validation of both 2D and 3D multi-scale models should be done by comparing with the results obtained in the established classical models. It can predict the patterns found in classical models with much fewer elements so as to significantly reduce the computational cost. As shown in Fig. 2, preliminary results demonstrate the evolution of sinusoidal wrinkles by using only 2 elements along the wave spreading direction, while 50 elements are required in this direction for the 3D classical model established in Chapter 3. However, due to the intrinsic limitation of any reduced-order model that clear and real boundary conditions are difficult to be taken into account, bridging techniques are really needed, which provides a flexible and efficient way to overcome this drawback. The considerable advantage of the proposed nonlocal reduction-based coupling strategy has been explicitly demonstrated in Chapter 4.

Application range of the above mentioned models is constrained by a large stiffness ratio E_f/E_s in the range $\mathcal{O}(10^4)$, which means the substrate is much softer than the film. In this range, critical strains are relatively small and thus the linear elastic framework is sufficient [43]. Some recent studies consider much softer films made of polymeric materials [31, 39, 161], typically with a stiffness ratio E_f/E_s in the range $\mathcal{O}(10)$, where the critical strain is relatively large and the small strain framework is no more appropriate. Therefore, finite strain models such as neo-Hookean hyperelasticity should be considered at least for the substrate [92]. By considering the large deformation of the substrate, some extremely localized instability modes like folding [146], creasing [38] or ridging [163] that require the nonlinearity of the substrate can be explored. It is not complicated to introduce nonlinear material laws in our framework (see Appendixes E and F) and development of

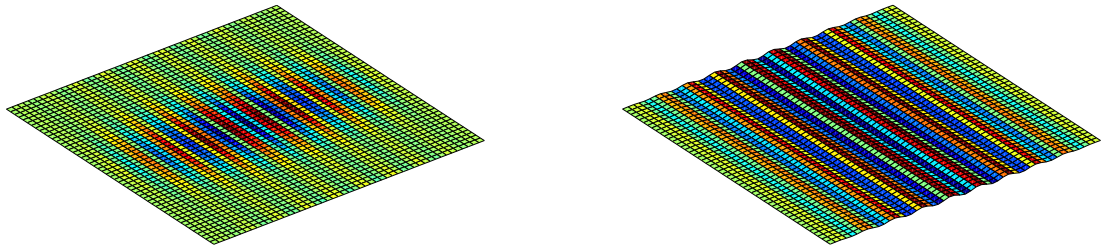

(a) (b)

Figure 2: 3D macroscopic film/substrate model under uniaxial compression: (a) the 1st wrinkling mode, (b) the 2nd wrinkling mode. Only two elements are used along the wave direction.

computer codes has been accomplished. Preliminary results illustrate a localized surface valley in the film center (see Fig. 3), namely folding, during the post-buckling evolution of the film/substrate with a stiffness ratio E_f/E_s in the range $\mathcal{O}(10)$, where neo-Hookean law is employed in the substrate within the ANM framework. Further investigations and discussions in this direction should be included in the perspectives.

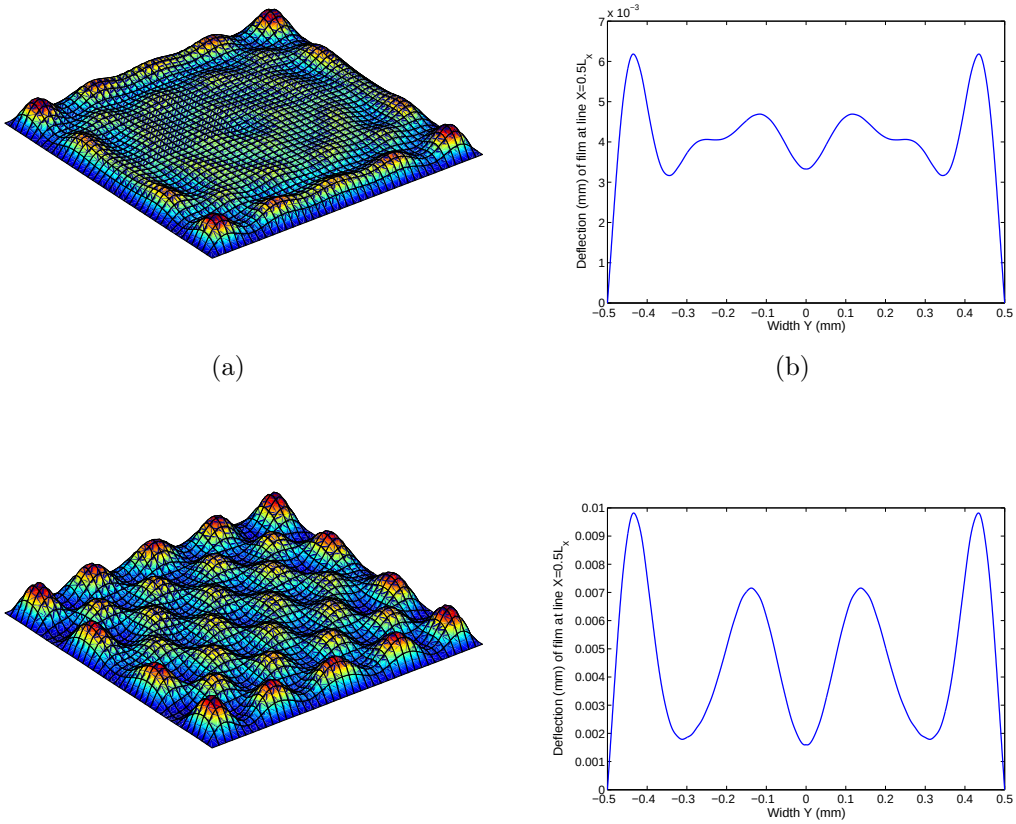

(a) (b)

(c) (d)

Figure 3: Thin films on hyperelastic substrates under equi-biaxial compression. The left column shows a sequence of wrinkling patterns, while the right column presents the associated instability shapes at the line $X = 0.5L_x$. Localized folding mode and checkerboard mode appear in the bulk.

Appendix A

Justification for exponential distribution of transverse displacement along the z direction

Let us recall Lamé−Navier equation

$$(\lambda + \mu)\,\mathbf{grad}\,(\text{div}\ \mathbf{u}) + \mu\Delta\mathbf{u} = 0, \tag{A.1}$$

where λ and μ are Lamé's first parameter and shear modulus, respectively. In two-dimensional case, Eq. (A.1) can be written as

$$\begin{cases} (\lambda + \mu)\,\dfrac{\partial^2 u}{\partial x^2} + (\lambda + \mu)\,\dfrac{\partial^2 w}{\partial x \partial z} + \mu\Delta u = 0, \\ \\ (\lambda + \mu)\,\dfrac{\partial^2 u}{\partial x \partial z} + (\lambda + \mu)\,\dfrac{\partial^2 w}{\partial z^2} + \mu\Delta w = 0. \end{cases} \tag{A.2}$$

As for sinusoidal wrinkles [89], the displacement field can be assumed as

$$\begin{cases} w\,(x, z) = f_1(z)\cos(kx), \\ u\,(x, z) = f_2(z)\sin(kx), \end{cases} \tag{A.3}$$

where f_1 and f_2 are the unknown functions, while k is the wave number. By introducing Eq. (A.3) into Eq. (A.2), one can obtain two ordinary differential equations

$$\begin{cases} -(\lambda+\mu)\,k^2 f_2 - (\lambda+\mu)\,k\dfrac{\partial f_1}{\partial z} + \mu\left(\dfrac{\partial^2 f_2}{\partial z^2} - k^2 f_2\right) = 0, \\ \\ (\lambda+\mu)\,k\dfrac{\partial f_2}{\partial z} + (\lambda+\mu)\,\dfrac{\partial^2 f_1}{\partial z^2} + \mu\left(\dfrac{\partial^2 f_1}{\partial z^2} - k^2 f_1\right) = 0. \end{cases} \tag{A.4}$$

These two coupled equations can be solved after introducing the boundary conditions, while the boundary conditions are not clear at the interface and bottom [9]. Nevertheless, it can be solved with unknown constants as

$$\begin{cases} f_1 = -\dfrac{1}{k^2}\left(c_1 e^{kz} + c_3 e^{-kz} - c_2 k e^{kz} + c_4 k e^{-kz} - c_1 kz e^{kz} + c_3 kz e^{-kz}\right), \\ f_2 = -\big(c_4\lambda k - 2c_3\mu + c_4\mu k + 2c_1\mu e^{2kz} + c_2\lambda k e^{2kz} + c_2\mu k e^{2kz} \\ \qquad +c_3\lambda kz + c_3\mu kz + c_1\lambda kz e^{2kz} + c_1\mu kz e^{2kz}\big)\left(\lambda k^2 e^{kz} + \mu k^2 e^{kz}\right)^{-1}, \end{cases} \tag{A.5}$$

where c_1, c_2, c_3 and c_4 are four unknown constants depending on the boundary conditions. Obviously, f_1 is an exponential type function. Therefore, the transverse displacement w should follow the exponential distribution along the thickness direction, which can be observed in Fig. 2.6. The most remarkable feature of the solution (A.5) is the length $1/k$ characterizing the exponential decay, which coincides with the wrinkling wavelength. This proves the property $\alpha = \lambda_x/\lambda_z = \mathcal{O}(1)$ in Section 2.2.

Appendix B

General methodology to obtain the macroscopic models

Within the Fourier approach, the differential equations satisfied by the amplitudes $U_j = (u_j, v_j, n_j)$ are deduced from the microscopic model simply by identifying the Fourier coefficients in each equation. The amplitudes $U_j(x)$ are assumed to be constant over a period $\left[x, x + \frac{2\pi}{q}\right]$ (see [54, 55, 56]). However, the derivative operators are calculated exactly, according to the following rules:

$$\left(\frac{da}{dx}\right)_j = (a')_j = \left(\frac{d}{dx} + jiq\right) a_j = (a_j)' + jiqa_j, \tag{B.1}$$

$$\left(\frac{d^2a}{dx^2}\right)_j = (a'')_j = \left(\frac{d}{dx} + jiq\right)^2 a_j = (a_j)'' + 2jiq(a_j)' - j^2q^2a_j, \tag{B.2}$$

where $a(x)$ is a Fourier series with slowly varying coefficients as in Eq. (4.4).

The other rules follow from Parseval identity and from the assumption of slowly varying coefficients:

$$\int_0^L a(x)b(x)\mathrm{d}x = \int_0^L \sum_{j=-\infty}^{+\infty} a_j(x)b_{-j}(x)\mathrm{d}x, \tag{B.3}$$

$$(ab)_j = \sum_{j_1=-\infty}^{+\infty} a_{j_1}b_{j-j_1}, \tag{B.4}$$

where $b(x)$ is also a Fourier series with slowly varying coefficients.

The membrane constitutive law (4.1−b) leads to the following macroscopic constitutive

law:

$$\frac{n_j}{ES} = \gamma_j = \left(\frac{d}{dx} + jiq\right) u_j + \frac{1}{2} \sum_{j_1=-\infty}^{+\infty} \left(\frac{d}{dx} + j_1 iq\right) v_{j_1} \left(\frac{d}{dx} + (j - j_1)\, iq\right) v_{j-j_1}. \quad \text{(B.5)}$$

Hence, in the case of two real envelopes, $U_0 = (u_0, v_0, n_0) \in \mathbb{R}$ and $U_1 = (u_1, v_1, n_1) \in \mathbb{R}$, the macroscopic constitutive law for the membrane stress n_0 becomes

$$\frac{n_0}{ES} = \gamma_0 = \frac{du_0}{dx} + \frac{1}{2}\left(\frac{dv_0}{dx}\right)^2 + \left(\frac{dv_1}{dx}\right)^2 + q^2 v_1^2. \quad \text{(B.6)}$$

Remark that the two last terms are always positive and correspond to an increase of tensile strain or to a decrease of the compressive strain. Therefore, this macroscopic law is able to account for the membrane stress decrease due to local wrinkling, particularly via the last term of Eq. (B.6).

The procedure to deduce a finite number of envelope equations is straightforward in the case of a simple nonlinear system as Eq. (4.1) (see [54, 55, 56]). Theoretically, the number of terms in the Fourier series can be very large (see Eq. (B.5)), but in practice, it is convenient to limit the number of harmonics. For instance, in [56], a macroscopic model involving five harmonics has been presented corresponding to wave numbers $0, \pm q, \pm 2q$. The corresponding potential energy has the following form:

$$\begin{aligned}
\mathcal{P}(u_0, u_1, u_2, v_0, v_1, v_2) = &\int_0^L \left(\frac{ES}{2}\left(\gamma_0^2 + 2|\gamma_1|^2 + 2|\gamma_2|^2\right) + \frac{EI}{2}\left(k_0^2 + 2|k_1|^2 + 2|k_2|^2\right)\right) \mathrm{d}x \\
&- \int_0^L f_0 u_0 \mathrm{d}x + \int_0^L \frac{c}{2}\left(v_0^2 + 2|v_1|^2 + 2|v_2|^2\right) \mathrm{d}x \\
&+ \int_0^L \frac{c_3}{4}\left(v_0^2 + 2|v_1|^2 + 2|v_2|^2\right)^2 \mathrm{d}x \\
&+ \int_0^L \frac{c_3}{4}\left(8|v_1|^2|v_2|^2 + 2|v_2|^4 + 8|v_0 v_1 + \overline{v_1} v_2|^2 + 2|v_1^2 + 2v_0 v_2|^2\right) \mathrm{d}x,
\end{aligned} \quad \text{(B.7)}$$

in which

$$\begin{cases} \gamma_0 = \dfrac{du_0}{dx} + \dfrac{1}{2}\left(\dfrac{dv_0}{dx}\right)^2 + \left|\left(\dfrac{d}{dx} + iq\right) v_1\right|^2 + \left|\left(\dfrac{d}{dx} + 2iq\right) v_2\right|^2, \\ \gamma_1 = \left(\dfrac{d}{dx} + iq\right) u_1 + \left(\dfrac{d}{dx} - iq\right) v_{-1} \left(\dfrac{d}{dx} + 2iq\right) v_2 + \dfrac{dv_0}{dx}\left(\dfrac{d}{dx} + iq\right) v_1, \\ \gamma_2 = \left(\dfrac{d}{dx} + 2iq\right) u_2 + \dfrac{dv_0}{dx}\left(\dfrac{d}{dx} + 2iq\right) v_2 + \dfrac{1}{2}\left(\left(\dfrac{d}{dx} + iq\right) v_1\right)^2, \\ k_0 = \dfrac{d^2 v_0}{dx^2}, \quad k_1 = \left(\dfrac{d}{dx} + iq\right)^2 v_1, \quad k_2 = \left(\dfrac{d}{dx} + 2iq\right)^2 v_2. \end{cases} \tag{B.8}$$

The model (B.7) includes five envelopes, but it may be unnecessarily intricate. In this context, further simplifications are introduced in the potential energy (B.7).

Appendix C

A macroscopic model with one real and one complex envelope

Additional simplifications would be introduced in the potential energy (B.7). Firstly, we consider only three harmonics $0, \pm q$, with one real envelope $U_0(x) = (u_0, v_0, n_0)$ and one complex envelope $U_1(x) = (u_1, v_1, n_1)$, or equivalently three real envelopes $U_0(x)$, $U_1^R(x)$, $U_1^I(x)$. The second restriction concerns the body axial force that does not fluctuate on the basic cell: $f(x) = f_0(x)$, which implies that the normal force does not fluctuate ($n_1 = 0$). This makes it possible to drop the unknown $u_1(x)$. In this case, the potential energy depends on the mean field $(u_0(x), v_0(x))$ and the envelope of the deflexion $v_1(x)$:

$$\begin{aligned}\mathcal{P}(u_0, v_0, v_1) = &\int_0^L \left(\frac{ES}{2}\gamma_0^2 + \frac{EI}{2}\left(k_0^2 + 2|k_1|^2\right)\right) \mathrm{d}x - \int_0^L f_0 u_0 \mathrm{d}x \\ &+ \int_0^L \frac{c}{2}\left(v_0^2 + 2|v_1|^2\right) \mathrm{d}x + \int_0^L \frac{c_3}{4}\left(v_0^4 + 12 v_0^2 |v_1|^2 + 6|v_1|^4\right) \mathrm{d}x,\end{aligned} \tag{C.1}$$

where

$$\gamma_0 = \frac{du_0}{dx} + \frac{1}{2}\left(\frac{dv_0}{dx}\right)^2 + \left|\left(\frac{d}{dx} + iq\right) v_1\right|^2. \tag{C.2}$$

Since v_1 is a complex valued function, the model (C.1) makes it possible to predict slow phase modulations. It is more accurate than the macroscopic model used in this thesis. In [122], it was proven that the account of a complex v_1 improves the solution near the boundary.

Appendix D

The residuals of the microscopic and macroscopic model

Through variation of potential energy in Eq. (4.17), one obtains

$$\mathcal{P}_f(\delta \boldsymbol{u}_f) = \int_{\Omega_f} \langle \delta u \;\; \delta u' \;\; \delta v \;\; \delta v' \;\; \delta v'' \rangle \left(\alpha_f \left\{ \begin{array}{c} 0 \\ ES(u' + v'^2/2) \\ cv + c_3 v^3 \\ ESv'(u' + v'^2/2) \\ EIv'' \end{array} \right\} - \beta_f \left\{ \begin{array}{c} f \\ 0 \\ 0 \\ 0 \\ 0 \end{array} \right\} \right) \mathrm{d}\Omega. \tag{D.1}$$

With Eq. (4.31), we define

$$\left\{ \begin{array}{c} \delta u \\ \delta u' \\ \delta v \\ \delta v' \\ \delta v'' \end{array} \right\}^e = [\boldsymbol{G}_f] \left\{ \delta \boldsymbol{Q}_f \right\}, \quad [\boldsymbol{G}_f] = \left[\begin{array}{c} \boldsymbol{N}_u^f \\ \boldsymbol{N}_u^{f'} \\ \boldsymbol{N}_v^f \\ \boldsymbol{N}_v^{f'} \\ \boldsymbol{N}_v^{f''} \end{array} \right]. \tag{D.2}$$

Therefore, the elementary residual $\left[\mathcal{R}_f(\boldsymbol{Q}_f)\right]^e$ can be written as

$$\left[\mathcal{R}_f(\boldsymbol{Q}_f)\right]^e = \int_{\Omega_e} [\boldsymbol{G}_f]^t \left(\alpha_f \left\{ \begin{array}{c} 0 \\ ES(u' + v'^2/2) \\ cv + c_3 v^3 \\ ESv'(u' + v'^2/2) \\ EIv'' \end{array} \right\} - \beta_f \left\{ \begin{array}{c} f \\ 0 \\ 0 \\ 0 \\ 0 \end{array} \right\} \right) \mathrm{d}\Omega. \tag{D.3}$$

In the same way, one can also obtain $[\mathcal{R}_r(\boldsymbol{Q}_r)]^e$ as follows:

$$[\mathcal{R}_r(\boldsymbol{Q}_r)]^e = \int_{\Omega_e} [\boldsymbol{G}_r]^t \left(\alpha_r \begin{Bmatrix} 0 \\ ES(u_0' + v_1'^2 + q^2 v_1^2) \\ 2ESq^2 v_1(u_0' + v_1'^2 + q^2 v_1^2) + 2EIq^4 v_1 + 2cv_1 + 6c_3 v_1^3 \\ 2ESv_1'(u_0' + v_1'^2 + q^2 v_1^2) + 12EIq^2 v_1' \end{Bmatrix} - \beta_r \begin{Bmatrix} f_0 \\ 0 \\ 0 \\ 0 \end{Bmatrix} \right) \mathrm{d}\Omega, \tag{D.4}$$

where

$$[\boldsymbol{G}_r] = \begin{bmatrix} \boldsymbol{N}_u^r \\ \boldsymbol{N}_u^{r\prime} \\ \boldsymbol{N}_v^r \\ \boldsymbol{N}_v^{r\prime} \end{bmatrix}. \tag{D.5}$$

By assembling $\left[\mathcal{R}_f(\boldsymbol{Q}_f)\right]^e$ and $[\mathcal{R}_r(\boldsymbol{Q}_r)]^e$, one achieves the residuals $\mathcal{R}_f(\boldsymbol{Q}_f)$ and $\mathcal{R}_r(\boldsymbol{Q}_r)$.

Appendix E

Finite strain hyperelasticity

Generally, the mechanical response of hyperelastic materials is described by strain energy potential function, Ψ, to fit the particular material. This function is a continuous scalar-valued function and is given in terms of the deformation gradient tensor, $\mathbf{F} = \nabla\mathbf{u}+\mathbf{I}$ ($\mathbf{u}$ being the displacement field and $\mathbf{I}$ being the second-order identity tensor), or some strain tensors, $\Psi = \Psi(\mathbf{F})$. In this paper, we limit the strain energy function to isotropic behavior throughout the deformation history. Isotropic hyperelastic materials can be expressed as a function of strain invariants of the right symmetric Cauchy−Green tensor, $\mathbf{C} = {}^t\mathbf{F} \cdot \mathbf{F}$. Therefore, the strain energy potential can be formulated as

$$\Psi = \Psi(\mathbf{C}) = \Psi\left(I_1, I_2, I_3\right), \tag{E.1}$$

in which

$$I_1 = \mathrm{tr}(\mathbf{C}), \tag{E.2}$$

$$I_2 = \frac{1}{2}\left[\left(\mathrm{tr}(\mathbf{C})\right)^2 - \mathrm{tr}(\mathbf{C}^2)\right], \tag{E.3}$$

$$I_3 = \det(\mathbf{C}) = \left[\det(\mathbf{F})\right]^2 = J^2. \tag{E.4}$$

One can obtain the derivatives of invariants with respect to $\mathbf{C}$ as follows:

$$\frac{\partial I_1}{\partial \mathbf{C}} = \frac{\partial[\mathrm{tr}(\mathbf{C})]}{\partial \mathbf{C}} = \mathbf{I}, \tag{E.5}$$

$$\frac{\partial I_2}{\partial \mathbf{C}} = \frac{1}{2}\left[2\mathrm{tr}(\mathbf{C})\mathbf{I} - \frac{\partial[\mathrm{tr}(\mathbf{C}^2)]}{\partial \mathbf{C}}\right] = I_1\mathbf{I} - \mathbf{C}, \tag{E.6}$$

$$\frac{\partial I_3}{\partial \mathbf{C}} = \frac{\partial J^2}{\partial \mathbf{C}} = I_3\mathbf{C}^{-1}. \tag{E.7}$$

Thus, the second Piola−Kirchhoff stress tensor can be expressed as

$$\begin{aligned}\mathbf{S} &= 2\frac{\partial \Psi}{\partial \mathbf{C}} = 2\left(\frac{\partial \Psi}{\partial I_1}\frac{\partial I_1}{\partial \mathbf{C}} + \frac{\partial \Psi}{\partial I_2}\frac{\partial I_2}{\partial \mathbf{C}} + \frac{\partial \Psi}{\partial I_3}\frac{\partial I_3}{\partial \mathbf{C}}\right) \\ &= 2\left[\left(\frac{\partial \Psi}{\partial I_1} + I_1\frac{\partial \Psi}{\partial I_2}\right)\mathbf{I} - \frac{\partial \Psi}{\partial I_2}\mathbf{C} + I_3\frac{\partial \Psi}{\partial I_3}\mathbf{C}^{-1}\right].\end{aligned} \tag{E.8}$$

Several forms of the strain energy function have been proposed in the literature to represent the isotropic hyperelastic material behavior. The most popular one used in the literature is the Ogden model for modeling rubberlike materials. The compressible Ogden constitutive law [127] is described in function of the eigenvalues $\lambda_i (i = 1, 2, 3)$ of the right Cauchy−Green tensor, $\mathbf{C}$, as follows:

$$\Psi = \sum_{i=1}^{N} \frac{\mu_i}{\alpha_i}\left(\lambda_1^{\alpha_i/2} + \lambda_2^{\alpha_i/2} + \lambda_3^{\alpha_i/2} - 3\right) + \sum_{i=1}^{N} \frac{\mu_i}{\alpha_i \beta_i}\left(J^{-\alpha_i \beta_i} - 1\right), \tag{E.9}$$

where N is a material constant, and μ_i, α_i and β_i are temperature-dependent material parameters.

The Mooney−Rivlin model and neo-Hookean form can be obtained as a particular case of the Ogden model (see [78]). Setting $N = 2$, $\alpha_1 = \alpha_2 = -2$, the strain energy potential of Mooney−Rivlin for the incompressible materials reads

$$\begin{aligned}\Psi &= c_1\left(\lambda_1^2 + \lambda_2^2 + \lambda_3^2 - 3\right) + c_2\left(\lambda_1^{-2} + \lambda_2^{-2} + \lambda_3^{-2} - 3\right) \\ &= c_1\left(I_1 - 3\right) + c_2\left(I_2 - 3\right).\end{aligned} \tag{E.10}$$

where the material constants $c_1 = \mu_1/2$ and $c_2 = -\mu_2/2$. The compressible form of the Mooney−Rivlin reads

$$\Psi = c\left(J - 1\right)^2 - d\log(J) + c_1\left(I_1 - 3\right) + c_2\left(I_2 - 3\right), \tag{E.11}$$

where c and d are temperature-dependent material constants. By prescribing that the reference configuration is stress-free, we can obtain $d = 2(c_1 + 2c_2)$. One can deduce the second Piola−Kirchhoff stress tensor from Eqs. (E.8) and (E.11):

$$\mathbf{S} = 2\left(c_1 + c_2 I_1\right)\mathbf{I} - 2c_2\mathbf{C} + \left[2cJ(J-1) - d\right]\mathbf{C}^{-1}. \tag{E.12}$$

The neo-Hookean model can be deduced from the strain energy of Mooney−Rivlin (E.11) by taking $c_2 = 0$. Another version of the neo-Hookean model, which is an extension

of linear isotropic constitutive law to large deformation, can be written as

$$\Psi = \frac{1}{2}\lambda_0 \left(\ln J\right)^2 - \mu_0 \ln J + \frac{1}{2}\mu_0 \left(I_1 - 3\right), \tag{E.13}$$

where λ_0 and μ_0 are Lamé's material constants. The second Piola−Kirchhoff stress tensor then reads

$$\mathbf{S} = \left(\lambda_0 \ln J - \mu_0\right) \mathbf{C}^{-1} + \mu_0 \mathbf{I}. \tag{E.14}$$

Appendix F

Automatic differentiation with the ANM

The implementation of the recurrence formulae as (2.47) is relatively simple for Föppl-von Kármán nonlinear plate or Navier−Stokes equations [160, 159], but it can be tedious in a more general constitutive framework. For example, there are several forms of strain energy potentials to describe hyperelastic behavior of rubberlike materials: Ogden, Mooney−Rivlin, neo-Hookean, Gent, Arruda−Boyce, *etc.* Each constitutive law should be set in the adapted ANM form. This requires different adaptations or even regularization techniques, which appears to be cumbersome and not straightforward sometimes. That is why some tools based on Automatic Differentiation (AD) techniques [72] have been proposed to compute high order derivatives of constitutive laws [102, 42, 111, 112], which allows one to introduce various potential energy functions of hyperelastic laws in a rather simple and automatic way.

This work applies the Matlab AD toolbox presented in [102] to compute Taylor series involved the ANM algorithm, see [47, 160, 159] and references cited therein. The AD has been first introduced in the ANM algorithm by Charpentier and Potier-Ferry [42] to make the algorithm more generic and easier to be implemented. The theoretical developments based on the generic Faá di Bruno formula for the higher order differentiation of compound functions have been presented in [102]. The main result reported in [102] is that from a proper initialization of the p-th Taylor coefficients of the independent unknown variables $(\mathbf{U}_p, \lambda_p)$ (see Eqs. (3.15) and (3.16)), the p-th Taylor coefficients $\mathbf{R}_p$ of the residual vector $\mathbf{R}(\mathbf{U}, \lambda)$, are equal to the p-th second hand side term involved in the ANM algorithm. This generic ANM algorithm has been implemented in a Matlab AD toolbox named Diamant. The Diamant series computation algorithm presented in Table F.1 organizes the propagation of Taylor coefficients $(\mathbf{U}_p, \lambda_p)$ of solution $(\mathbf{U}, \lambda)$: (i) evaluating Taylor coefficients $\mathbf{R}_p$ of the residual function $\mathbf{R}$, (ii) solving a linear system, (iii) computing

$(\mathbf{U}_p, \lambda_p)$ and (iv) updating intermediate variables.

Table F.1: Diamant series computations for the residual equation $\mathbf{R}\left(\mathbf{U}(a), \lambda(a)\right)$ with path parameter a satisfying Eq. (3.17).

Series computation
Construction of $\mathbf{L}_t^0(\mathbf{U}_0)$ using AD on $\mathbf{R}$
Decomposition of $\mathbf{L}_t^0$
Order 1:
(0) Initialization: $\mathbf{U}_1 = 0$ and $\lambda_1 = 1$
(i) Computation of the first Taylor coefficient $\mathbf{R}_1$ of $\mathbf{R}(\mathbf{U}, \lambda)$
(ii) Solution of $\mathbf{L}_t^0 \widehat{\mathbf{U}} = \mathbf{R}_1 (= \mathbf{F})$
(iii) Computation of $\lambda_1 = \pm 1/\sqrt{1 + \|\widehat{\mathbf{U}}\|^2}$ and $\mathbf{U}_1 = \lambda_1 \widehat{\mathbf{U}}$
(iv) Update of intermediate variables
Order $p = 2, \cdots, n$:
(0) Initialization: $\mathbf{U}_p = 0$ and $\lambda_p = 0$
(i) Computation of Taylor coefficient $\mathbf{R}_p$
(ii) Solution of $\mathbf{L}_t^0 \widehat{\mathbf{U}} = \mathbf{R}_p$
(iii) Computation of λ_p, $\mathbf{U}_p = \lambda_p / \lambda_1 \mathbf{U}_1 + \widehat{\mathbf{U}}$
(iv) Update of intermediate variables
End of the series computation

Bibliography

[1] ABAQUS: ABAQUS Analysis User's Manual, version 6.8 (2008)

[2] Abdelkhalek, S., Montmitonnet, P., Potier-Ferry, M., Zahrouni, H., Legrand, N., Buessler, P.: Strip flatness modelling including buckling phenomena during thin strip cold rolling. Ironmaking & Steelmaking **37**(4), 290–297 (2010)

[3] Abdelmoula, R., Damil, N., Potier-Ferry, M.: Influence of distributed and localized imperfections on the buckling of cylindrical shells. International Journal of Solids and Structures **29**, 1–25 (1992)

[4] Abichou, H., Zahrouni, H., Potier-Ferry, M.: Asymptotic numerical method for problems coupling several nonlinearities. Computer Methods in Applied Mechanics and Engineering **191**, 5795–5810 (2002)

[5] Aggoune, W., Zahrouni, H., Potier-Ferry, M.: High-order prediction-correction algorithms for unilateral contact problems. Journal of Computational and Applied Mathematics **168**, 1–9 (2004)

[6] Allgower, E., Georg, K.: Numerical continuation methods. Springer–Verlag, Berlin (1990)

[7] Aranson, I., Kramer, L.: The world of the complex Ginzburg-Landau equation. Reviews of Modern Physics **74**, 99–143 (2002)

[8] Assidi, M., Zahrouni, H., Damil, N., Potier-Ferry, M.: Regularization and perturbation technique to solve plasticity problems. International Journal of Material Forming **2**, 1–14 (2009)

[9] Audoly, B., Boudaoud, A.: Buckling of a stiff film bound to a compliant substrate–Part I: Formulation, linear stability of cylindrical patterns, secondary bifurcations. Journal of the Mechanics and Physics of Solids **56**(7), 2401–2421 (2008)

[10] Audoly, B., Boudaoud, A.: Buckling of a stiff film bound to a compliant substrate–Part II: A global scenario for the formation of herringbone pattern. Journal of the Mechanics and Physics of Solids **56**(7), 2422–2443 (2008)

[11] Audoly, B., Boudaoud, A.: Buckling of a stiff film bound to a compliant substrate–Part III: Herringbone solutions at large buckling parameter. Journal of the Mechanics and Physics of Solids **56**(7), 2444–2458 (2008)

[12] Babuška, I., Melenk, J.: The partition of unity method. International Journal for Numerical Methods in Engineering **40**, 727–758 (1997)

[13] Baguet, S., Cochelin, B.: On the behaviour of the ANM continuation in the presence of bifurcations. Communications in Numerical Methods in Engineering **19**(6), 459–471 (2003)

[14] Batoz, J., Dhatt, G.: Incremental displacement algorithms for nonlinear problems. International Journal for Numerical Methods in Engineering **7**, 883–900 (1971)

[15] Bauman, P., Ben Dhia, H., Elkhodja, N., Oden, J.: On the application of the Arlequin method to the coupling of particle and continuum models. Computational Mechanics **42**, 511–530 (2008)

[16] Bauman, P., Oden, J., Prudhomme, S.: Adaptive multiscale modeling of polymeric materials with Arlequin coupling and Goals algorithms. Computer Methods in Applied Mechanics and Engineering **198**, 799–818 (2009)

[17] Belytschko, T., Black, T.: Elastic crack growth in finite-elements with minimal remeshing. International Journal for Numerical Methods in Engineering **745**, 601–620 (1999)

[18] Belytschko, T., Lu, Y., Gu, L.: Element-free Galerkin methods. International Journal for Numerical Methods in Engineering **37**, 229–256 (1994)

[19] Ben Amar, M., Ciarletta, P.: Swelling instability of surface-attached gels as a model of soft tissue growth under geometric constraints. Journal of the Mechanics and Physics of Solids **58**(7), 935–954 (2010)

[20] Ben Dhia, H.: Multiscale mechanical problems: the Arlequin method. Comptes Rendus de l'Académie des Sciences Paris **IIb**(326), 899–904 (1998)

[21] Ben Dhia, H.: Global local approaches: the Arlequin framework. European Journal of Computational Mechanics **15**, 67–80 (2006)

[22] Ben Dhia, H.: Further insights by theoretical investigations of the multiscale Arlequin method. International Journal for Multiscale Computational Engineering **6**, 215–232 (2008)

[23] Ben Dhia, H., Jamond, O.: On the use of XFEM within the Arlequin framework for the simulation of crack propagation. Computer Methods in Applied Mechanics and Engineering **199**(21-22), 1403–1414 (2010)

[24] Ben Dhia, H., Rateau, G.: The Arlequin method as a flexible engineering design tool. International Journal for Numerical Methods in Engineering **62**, 1442–1462 (2005)

[25] Biscani, F., Giunta, G., Belouettar, S., Carrera, E., Hu, H.: Variable kinematic plate elements coupled via Arlequin method. International Journal for Numerical Methods in Engineering **91**(12), 1264–1290 (2012)

[26] Boucif, M., Wesfreid, J.E., Guyon, E.: Experimental study of wavelength selection in the elastic buckling instability of thin plates. European Journal of Mechanics A–Solids **10**, 641–661 (1991)

[27] Boutyour, E.: Méthode asymptotique-numérique pour le calcul des bifurcations: application aux structures élastiques. Ph.D. thesis, Université de Metz, France (1994)

[28] Boutyour, E., Zahrouni, H., Potier-Ferry, M., Boudi, M.: Bifurcation points and bifurcated branches by an asymptotic numerical method and Padé approximants. International Journal for Numerical Methods in Engineering **60**(12), 1987–2012 (2004)

[29] Bowden, N., Brittain, S., Evans, A., Hutchinson, J., Whitesides, G.: Spontaneous formation of ordered structures in thin films of metals supported on an elastomeric polymer. Nature **393**, 146–149 (1998)

[30] Bowden, N., Huck, W., Paul, K., Whitesides, G.: The controlled formation of ordered, sinusoidal structures by plasma oxidation of an elastomeric polymer. Applied Physics Letters **75**(17), 2557–2559 (1999)

[31] Brau, F., Vandeparre, H., Sabbah, A., Poulard, C., Boudaoud, A., Damman, P.: Multiple-length-scale elastic instability mimics parametric resonance of nonlinear oscillators. Nature Physics **7**, 56–60 (2011)

[32] Brezillon, A., Girault, G., Cadou, J.: A numerical algorithm coupling a bifurcating indicator and a direct method for the computation of Hopf bifurcation points in fluid mechanics. Computers and Fluids **39**, 1226–1240 (2010)

[33] Büchter, N., Ramm, E., Roehl, D.: Three-dimensional extension of non-linear shell formulation based on the enchanced assumed strain concept. International Journal for Numerical Methods in Engineering **37**, 2551–2568 (1994)

[34] Cadou, J., Cochelin, B., Damil, N., Potier-Ferry, M.: ANM for stationary navier-stokes equations ans with petrov-galerkin formulation. International Journal for Numerical Methods in Engineering **50**, 825–845 (2001)

[35] Cai, S., Breid, D., Crosby, A., Suo, Z., Hutchinson, J.: Periodic patterns and energy states of buckled films on compliant substrates. Journal of the Mechanics and Physics of Solids **59**(5), 1094–1114 (2011)

[36] Cai, Z., Fu, Y.: On the imperfection sensitivity of a coated elastic half-space. Proceedings of the Royal Society A: Mathematical, Physical and Engineering Sciences **455**, 3285–3309 (1999)

[37] Cai, Z., Fu, Y.: Exact and asymptotic stability analyses of a coated elastic half-space. International Journal of Solids and Structures **37**(22), 3101–3119 (2000)

[38] Cao, Y., Hutchinson, J.: From wrinkles to creases in elastomers: the instability and imperfection-sensitivity of wrinkling. Proceedings of the Royal Society A: Mathematical, Physical and Engineering Sciences **468**(2137), 94–115 (2012)

[39] Cao, Y., Hutchinson, J.: Wrinkling phenomena in neo-Hookean film/substrate bilayers. Journal of Applied Mechanics **79**(031019) (2012)

[40] Cao, Y., Jia, F., Zhao, Y., Feng, X., Yu, S.: Buckling and post-buckling of a stiff film resting on an elastic graded substrate. International Journal of Solids and Structures **49**(13), 1656–1664 (2012)

[41] Chamoin, L., Prudhomme, S., Ben Dhia, H., Oden, J.: Ghost forces and spurious effects in atomic-to-continuum coupling methods by the Arlequin approach. International Journal for Numerical Methods in Engineering **83**, 1081–1113 (2010)

[42] Charpentier, I., Potier-Ferry, M.: Automatic differentiation of the asymptotic numerical method: the Diamant approach. Comptes Rendus Mécanique **336**(3), 336–340 (2008)

[43] Chen, X., Hutchinson, J.: Herringbone buckling patterns of compressed thin films on compliant substrates. Journal of Applied Mechanics **71**, 597–603 (2004)

[44] Ciarlet, P.: A justification of the von Kármán equations. Archive for Rational Mechanics and Analysis **73**, 349–389 (1980)

[45] Cochelin, B.: A path-following technique via an asymptotic-numerical method. Computers and Structures **53**(5), 1181–1192 (1994)

[46] Cochelin, B., Damil, N., Potier-Ferry, M.: Asymptotic-numerical methods and Padé approximants for non-linear elastic structures. International Journal for Numerical Methods in Engineering **37**(7), 1187–1213 (1994)

[47] Cochelin, B., Damil, N., Potier-Ferry, M.: Méthode asymptotique numérique. Hermès Science Publications (2007)

[48] Cochelin, B., Medale, M.: Power series analysis as a major breakthrough to improve the efficiency of Asymptotic Numerical Method in the vicinity of bifurcations. Journal of Computational Physics **236**, 594–607 (2013)

[49] Cong, Y., Yvonnet, J., Zahrouni, H.: Simulation of instabilities in thin nanostructures by a perturbation approach. Computational Mechanics **53**, 739–750 (2014)

[50] Cross, M., Hohenberg, P.: Pattern formation out of equilibrium. Reviews of Modern Physics **65**, 851–1112 (1993)

[51] Damil, N., Potier-Ferry, M.: Wavelength selection in the postbuckling of a long rectangular plate. International Journal of Solids and Structures **22**, 511–526 (1986)

[52] Damil, N., Potier-Ferry, M.: A new method to compute perturbed bifurcation: Application to the buckling of imperfect elastic structures. International Journal of Engineering Science **26**(9), 943–957 (1990)

[53] Damil, N., Potier-Ferry, M.: Amplitude equations for cellular instabilities. Dynamics and Stability of Systems **7**, 1–34 (1992)

[54] Damil, N., Potier-Ferry, M.: A generalized continuum approach to describe instability pattern formation by a multiple scale analysis. Comptes Rendus Mécanique **334**(11), 674–678 (2006)

[55] Damil, N., Potier-Ferry, M.: A generalized continuum approach to predict local buckling patterns of thin structures. European Journal of Computational Mechanics **17**(5-7), 945–956 (2008)

[56] Damil, N., Potier-Ferry, M.: Influence of local wrinkling on membrane behaviour: A new approach by the technique of slowly variable Fourier coefficients. Journal of the Mechanics and Physics of Solids **58**(8), 1139–1153 (2010)

[57] Damil, N., Potier-Ferry, M., Hu, H.: New nonlinear multi-scale models for wrinkled membranes. Comptes Rendus Mécanique **341**(8), 616–624 (2013)

[58] Damil, N., Potier-Ferry, M., Hu, H.: Membrane wrinkling revisited from a multi-scale point of view. Advanced Modeling and Simulation in Engineering Sciences **1**(6), 1–35 (2014)

[59] Dervaux, J., Ben Amar, M.: Morphogenesis of growing soft tissues. Physical Review Letters **101**(068101), 1–4 (2008)

[60] Dervaux, J., Ben Amar, M.: Buckling condensation in constrained growth. Journal of the Mechanics and Physics of Solids **59**(3), 538–560 (2011)

[61] Doedel, E.: AUTO: A program for the automatic bifurcation analysis of autonomous systems. Congressus Numerantium **30**, 265–284 (1981)

[62] Dowaikh, M., Ogden, R.: On surface waves and deformations in a pre-stressed incompressible elastic solid. IMA Journal of Applied Mathematics **44**, 261–284 (1990)

[63] Drapier, S., Grandidier, J., Potier-Ferry, M.: A structural approach of plastic microbuckling in long fibre composites: comparison with theoretical and experimental results. International Journal of Solids and Structures **38**, 3877–3904 (2001)

[64] Efimenko, K., Rackaitis, M., Manias, E., Vaziri, A., Mahadevan, L., Genzer, J.: Nested self-similar wrinkling patterns in skins. Nature Materials **4**, 293–297 (2005)

[65] Feyel, F.: A multilevel finite element method (FE^2) to describe the response of highly non-linear structures using generalized continua. Computer Methods in Applied Mechanics and Engineering **192**, 3233–3244 (2003)

[66] Fischer, F., Rammerstorfer, F., Friedl, N., Wieser, W.: Buckling phenomena related to rolling and levelling of sheet metal. International Journal of Mechanical Sciences **42**, 1887–1910 (2000)

[67] Fish, J.: The s-version of finite element method. Computers and Structures **43**(3), 539–547 (1992)

[68] Fish, J., Aditya, N.: Adaptive and hierarchical modelling of fatigue crack propagation. International Journal for Numerical Methods in Engineering **36**, 2825–2836 (1993)

[69] Fish, J., Markolefas, S.: Adaptive s-method for linear elastostatics. Computer Methods in Applied Mechanics and Engineering **104**, 363–396 (1993)

[70] Genzer, J., Groenewold, J.: Soft matter with hard skin: From skin wrinkles to templating and material characterization. Soft Matter **2**(4), 310–323 (2006)

[71] Girault, G., Guevel, Y., Cadou, J.: An algorithm for the computation of multiple Hopf bifurcation points based on Padé approximants. International Journal for Numerical Methods in Engineering **68**, 1189–1206 (2012)

[72] Griewank, A.: Evaluating derivatives: Principles and techniques of algorithmic differentiation. Frontiers in Applied Mathematics, vol. 19, SIAM, Philadelphia (2000)

[73] Guevel, Y., Boutyour, E., Cadou, J.: Automatic detection and branch switching methods for steady bifurcation in fluid mechanics. Journal of Computational Physics **230**, 3614–3629 (2011)

[74] Guevel, Y., Girault, G., Cadou, J.: Parametric analysis of steady bifurcations in 2D incompressible viscous flow with high order algorithm. Computers and Fluids **100**, 185–195 (2014)

[75] Guidault, P., Belytschko, T.: On the L^2 coupling and the H^1 couplings for an overlapping domain decomposition method using Lagrange multipliers. International Journal for Numerical Methods in Engineering **70**, 322–350 (2007)

[76] Hayes, M., Rivlin, R.: Surface waves in deformed elastic materials. Archive for Rational Mechanics and Analysis **8**, 358–380 (1961)

[77] He, X., Kitipornchai, S., Liew, K.: Buckling analysis of multi-walled carbon nanotubes: a continuum model accounting for van der Waals interaction. Journal of the Mechanics and Physics of Solids **53**, 303–326 (2005)

[78] Holzapfel, G.: Nonlinear solid mechanics: A continuum approach for engineering. Wiley, Chichester, England (2000)

[79] Howarter, J., Stafford, C.: Instabilities as a measurement tool for soft materials. Soft Matter **6**(22), 5661–5666 (2010)

[80] Hoyle, R.: Pattern formation, an introduction to methods. Cambridge University Press (2006)

[81] Hu, H., Belouettar, S., Potier-Ferry, M., Daya, E.: Multi-scale modeling of sandwich structure using the Arlequin method, Part I: linear modelling. Finite Element in Analysis and Design **45**(1), 37–51 (2009)

[82] Hu, H., Belouettar, S., Potier-Ferry, M., Daya, E., Makradi, A.: Multi-scale nonlinear modelling of sandwich structures using the Arlequin method. Composite Structures **92**(2), 515–522 (2010)

[83] Hu, H., Belouettar, S., Potier-Ferry, M., Makradi, A.: A novel finite element for global and local buckling analysis of sandwich beams. Composite Structures **90**(3), 270–278 (2009)

[84] Hu, H., Damil, N., Potier-Ferry, M.: A bridging technique to analyze the influence of boundary conditions on instability patterns. Journal of Computational Physics **230**(10), 3753–3764 (2011)

[85] Huang, R.: Kinetic wrinkling of an elastic film on a viscoelastic substrate. Journal of the Mechanics and Physics of Solids **53**(1), 63–89 (2005)

[86] Huang, R., Im, S.: Dynamics of wrinkle growth and coarsening in stressed thin films. Physical Review E **74**(026214) (2006)

[87] Huang, R., Suo, Z.: Instability of a compressed elastic film on a viscous layer. International Journal of Solids and Structures **39**(7), 1791–1802 (2002)

[88] Huang, Z., Hong, W., Suo, Z.: Evolution of wrinkles in hard films on soft substrates. Physical Review E **70**(030601) (2004)

[89] Huang, Z., Hong, W., Suo, Z.: Nonlinear analyses of wrinkles in a film bonded to a compliant substrate. Journal of the Mechanics and Physics of Solids **53**(9), 2101–2118 (2005)

[90] Hunt, G., Bolt, H., Thompson, J.: Structural localization phenomena and the dynamical phase-space analogy. Proceedings of the Royal Society A: Mathematical, Physical and Engineering Sciences **425**, 245–267 (1989)

[91] Hunt, G., Peletier, M., Champneys, A., Woods, P., Wadee, M., Budd, C., Lord, G.: Cellular buckling in long structures. Nonlinear Dynamics **21**, 3–29 (2000)

[92] Hutchinson, J.: The role of nonlinear substrate elasticity in the wrinkling of thin films. Philosophical Transactions of the Royal Society A **371**(20120422) (2013)

[93] Im, S., Huang, R.: Wrinkle patterns of anisotropic crystal films on viscoelastic substrates. Journal of the Mechanics and Physics of Solids **56**(12), 3315–3330 (2008)

[94] Iooss, G., Mielke, A., Demay, Y.: Theory of steady Ginzburg-Landau equation in hydrodynamic stability problems. European Journal of Mechanics B–Fluids **8**, 229–268 (1989)

[95] Jacques, N., Elias, A., Potier-Ferry, M., Zahrouni, H.: Buckling and wrinkling during strip conveying in processing lines. Journal of Materials Processing Technology **190**, 33–40 (2007)

[96] Jamal, M., Elasmar, H., Braikat, B., Boutyour, E., Cochelin, B., Damil, N., Potier-Ferry, M.: Bifurcation indicators. Acta Mechanica **139**, 129–142 (2000)

[97] Jawadi, A., Boutyour, E., Cadou, J.: Asymptotic numerical method for steady flow of power-law fluids. Journal of Non-Newtonian Fluid Mechanics **202**, 22–31 (2013)

[98] Jepson, A.: Numerical Hopf bifurcation. Ph.D. thesis, California Institute of Technology, USA (1981)

[99] Karkar, S., Arquier, R., Lazarus, A., Thomas, O., Vergez, C., Cochelin, B.: Manlab: an interactive path-following and bifurcation analysis software. http://manlab.lma.cnrs-mrs.fr/ (2010)

[100] Kim, P., Abkarian, M., Stone, H.: Hierarchical folding of elastic membranes under biaxial compressive stress. Nature Materials **10**, 952–957 (2011)

[101] Koiter, W.: On the stability of elastic equilibrium (in Dutch with English summary). Ph.D. thesis, Delft University of Technology, Netherlands (1945)

[102] Koutsawa, Y., Charpentier, I., Daya, E., Cherkaoui, M.: A generic approach for the solution of nonlinear residual equations. Part I: The Diamant toolbox. Computer Methods in Applied Mechanics and Engineering **198**, 572–577 (2008)

[103] Kyriakides, S., Arseculeratne, R., Perry, E., Liechti, K.: On the compressive failure of fiber reinforced composites. International Journal of Solids and Structures **32**, 689–738 (1995)

[104] Lahman, H., Cadou, J., Zahrouni, H., Damil, N., Potier-Ferry, M.: High-order predictor-corrector algorithms. International Journal for Numerical Methods in Engineering **55**, 685–704 (2002)

[105] Landau, L., Lifshitz, E.: Theory of Elasticity. Pergamon, London (1959)

[106] Lazarus, A., Miller, J., Reis, P.: Continuation of equilibria and stability of slender elastic rods using an asymptotic numerical method. Journal of the Mechanics and Physics of Solids **61**(8), 1712–1736 (2013)

[107] Lecieux, Y., Bouzidi, R.: Experimental analysis on membrane wrinkling under biaxial load–Comparison with bifurcation analysis. International Journal of Solids and Structures **47**, 2459–2475 (2010)

[108] Lecieux, Y., Bouzidi, R.: Numerical wrinkling prediction of thin hyperelastic structures by direct energy minimization. Advances in Engineering Software **50**, 57–68 (2012)

[109] Lee, D., Triantafyllidis, N., Barber, J., Thouless, M.: Surface instability of an elastic half space with material properties varying with depth. Journal of the Mechanics and Physics of Solids **56**(3), 858–868 (2008)

[110] Lehoucq, R., Sorensen, D., Yang, C.: ARPACK User's Guide: Solution of large-scale eigenvalue problems with implicitly restarted Arnoldi methods. SIAM, Philadelphia (1998)

[111] Lejeune, A., Béchet, F., Boudaoud, H., Mathieu, N., Potier-Ferry, M.: Object-oriented design to automate a high order non-linear solver based on asymptotic numerical method. Advances in Engineering Software **48**, 70–88 (2012)

[112] Lejeune, A., Boudaoud, H., Potier-Ferry, M., Charpentier, I., Zahrouni, H.: Automatic solver for non-linear partial differential equations with implicit local laws: Application to unilateral contact. International Journal for Numerical Methods in Engineering **94**, 850–867 (2013)

[113] Léotoing, L., Drapier, S., Vautrin, A.: First applications of a novel unified model for global and local buckling of sandwich columns. European Journal of Mechanics A–Solids **21**(4), 683–701 (2002)

[114] Léotoing, L., Drapier, S., Vautrin, A.: Nonlinear interaction of geometrical and material properties in sandwich beam instabilities. International Journal of Solids and Structures **39**(13-14), 3717–3739 (2002)

[115] Li, B., Cao, Y., Feng, X., Gao, H.: Surface wrinkling of mucosa induced by volumetric growth: Theory, simulation and experiment. Journal of the Mechanics and Physics of Solids **59**(4), 758–774 (2011)

[116] Li, B., Cao, Y., Feng, X., Gao, H.: Mechanics of morphological instabilities and surface wrinkling in soft materials: a review. Soft Matter **8**(21), 5728–5745 (2012)

[117] Liang, K., Abdalla, M., Gürdal, Z.: A Koiter−Newton approach for nonlinear structural analysis. International Journal for Numerical Methods in Engineering **96**, 763–786 (2013)

[118] Liapounoff, A.: Problème général de la stabilité du mouvement. Annales de la Faculté des Sciences de Toulouse **9**, 203–474 (1907)

[119] Liu, Y., Yu, K., Hu, H., Belouettar, S., Potier-Ferry, M., Damil, N.: A new Fourier-related double scale analysis for instability phenomena in sandwich structures. International Journal of Solids and Structures **49**(22), 3077–3088 (2012)

[120] Mahadevan, L., Rica, S.: Self-organized origami. Science **307**, 1740 (2005)

[121] Medale, M., Cochelin, B.: A parallel computer implementation of the Asymptotic Numerical Method to study thermal convection instabilities. Journal of Computational Physics **228**, 8249–8262 (2009)

[122] Mhada, K., Braikat, B., Hu, H., Damil, N., Potier-Ferry, M.: About macroscopic models of instability pattern formation. International Journal of Solids and Structures **49**, 2978–2989 (2012)

[123] Moës, N., Dolbow, J., Belytschko, T.: A finite element method for crack growth without remeshing. International Journal for Numerical Methods in Engineering **746**(1), 131–150 (1999)

[124] Newell, A., Whitehead, J.: Finite band width, finite amplitude convection. Journal of Fluid Mechanics **38**, 279–303 (1969)

[125] Nezamabadi, S., Yvonnet, J., Zahrouni, H., Potier-Ferry, M.: A multilevel computational strategy for handling microscopic and macroscopic instabilities. Computer Methods in Applied Mechanics and Engineering **198**, 2099–2110 (2009)

[126] Nezamabadi, S., Zahrouni, H., Yvonnet, J.: Solving hyperelastic material problems by asymptotic numerical method. Computational Mechanics **47**, 77–92 (2011)

[127] Ogden, R.: Non-linear elastic deformations. Ellis Horwood, Chichester, England (1984)

[128] Pocivavsek, L., Dellsy, R., Kern, A., Johnson, S., Lin, B., Lee, K., Cerda, E.: Stress and fold localization in thin elastic membranes. Science **320**, 912–916 (2008)

[129] Pocivavsek, L., Leahy, B., Holten-Andersen, N., Lin, B., Lee, K., Cerda, E.: Geometric tools for complex interfaces: from lung surfactant to the mussel byssus. Soft Matter **5**(10), 1963–1968 (2009)

[130] Prudhomme, S., Ben Dhia, H., Bauman, P., Elkhodja, N., Oden, J.: Computational analysis of modelling error for the coupling of particle and continuum models by the Arlequin method. Computer Methods in Applied Mechanics and Engineering **197**, 3399–3409 (2008)

[131] Prudhomme, S., Bouclier, R., Chamoin, L., Ben Dhia, H., Oden, J.: Analysis of an averaging operator for atomic-to-continuum coupling methods by the Arlequin approach. Lecture Notes in Computational Science and Engineering, vol. 82, Springer–Verlag, Heidelberg (2012)

[132] Rodriguez, J., Rio, G., Cadou, J., Troufflard, J.: Numerical study of dynamic relaxation with kinetic damping applied to inflatable fabric structures with extensions for 3D solid element and non-linear behavior. Thin-Walled Structures **49**(11), 1468–1474 (2011)

[133] Rogers, J., Someya, T., Huang, Y.: Materials and mechanics for stretchable electronics. Science **327**, 1603–1607 (2010)

[134] Rossi, R., Lazzari, M., Vitaliani, R., Onate, E.: Simulation of light-weight membrane structures by wrinkling model. International Journal for Numerical Methods in Engineering **62**, 2127–2153 (2005)

[135] Ru, C.: Axially compressed buckling of a double-walled carbon nanotube embedded in an elastic medium. Journal of the Mechanics and Physics of Solids **49**, 1265–1279 (2001)

[136] Sanchez-Palencia, E.: Non-homogeneous media and vibration theory. Lecture Notes in Physics, vol. 127, Springer–Verlag, Berlin (1980)

[137] Sansour, C.: A theory and finite element formulation of shells at finite deformations involving thickness change: Circumventing the use of a rotation tensor. Archive of Applied Mechanics **65**, 194–216 (1995)

[138] Schmidt, E.: Uber die auflösung der nichtlinearen integralgleichungen und die verzweigung ihrer lösungen. Mathematische Annalen **65**, 370–399 (1908)

[139] Segel, L.: Distant side walls cause slow amplitude modulation of cellular convection. Journal of Fluid Mechanics **38**, 203–224 (1969)

[140] Seydel, R.: Numerical computation of branch points in nonlinear equations. Numerische Mathematik **33**, 339–352 (1979)

[141] Shield, T., Kim, K., Shield, R.: The buckling of an elastic layer bonded to an elastic substrate in plane strain. Journal of Applied Mechanics **61**, 231–235 (1994)

[142] Simo, J., Rifai, M.: A class of mixed assumed strain methods and method of incompatible modes. International Journal for Numerical Methods in Engineering **37**, 1595–1636 (1990)

[143] Song, J., Jiang, H., Liu, Z., Khang, D., Huang, Y., Rogers, J., Lu, C., Koh, C.: Buckling of a stiff thin film on a compliant substrate in large deformation. International Journal of Solids and Structures **45**(10), 3107–3121 (2008)

[144] Steigmann, D., Ogden, R.: Plane deformations of elastic solids with intrinsic boundary elasticity. Proceedings of the Royal Society A: Mathematical, Physical and Engineering Sciences **453**, 853–877 (1997)

[145] Strouboulis, T., Babuška, I., Copps, K.: The design and analysis of the Generalized Finite Element Method. Computer Methods in Applied Mechanics and Engineering **181**, 43–69 (2000)

[146] Sun, J., Xia, S., Moon, M., Oh, K., Kim, K.: Folding wrinkles of a thin stiff layer on a soft substrate. Proceedings of the Royal Society A: Mathematical, Physical and Engineering Sciences **468**(2140), 932–953 (2012)

[147] Swift, J., hohenberg, P.: Hydrodynamic fluctuations at the convective instability. Physical Review A **15**(1), 319–328 (1977)

[148] Vannucci, P., Cochelin, B., Damil, N., Potier-Ferry, M.: An asymptotic-numerical method to compute bifurcating branches. International Journal for Numerical Methods in Engineering **41**(8), 1365–1389 (1998)

[149] Waas, A., Schultheisz, C.: Compressive failure of composites, part II: Experimental studies. Progress in Aerospace Sciences **32**(1), 43–78 (1996)

[150] Wagner, W., Wriggers, P.: A simple method for the calculation of postcritical branches. International Journal for Numerical Methods in Engineering **5**, 103–109 (1988)

[151] Wang, S., Song, J., Kim, D., Huang, Y., Rogers, J.: Local versus global buckling of thin films on elastomeric substrates. Applied Physics Letters **93**(023126) (2008)

[152] Weinitshke, H.: On the calculation of limit and bifurcation points in stability problems of elastic shells. International Journal of Solids and Structures **21**, 79–95 (1985)

[153] Wesfreid, J., Zaleski, S.: Cellular structures in instabilities. Lecture Notes in Physics, vol. 210, Springer-Verlag, Heidelberg (1984)

[154] Wong, Y., Pellegrino, S.: Wrinkled membranes, Part I: experiments. Journal of Mechanics of Materials and Structures **1**(1), 3–25 (2006)

[155] Wriggers, P., Simo, J.: A general procedure for the direct computation of turning and bifurcation point. International Journal for Numerical Methods in Engineering **30**, 155–176 (1990)

[156] Wriggers, P., Wagner, W., Miehe, C.: A quadratically convergent procedure for the calculation of stability point in finite element analysis. Computer Methods in Applied Mechanics and Engineering **70**, 329–347 (1988)

[157] Xiao, S., Belytschko, T.: A bridging domain method for coupling continua with molecular dynamics. Computer Methods in Applied Mechanics and Engineering **193**, 1645–1669 (2004)

[158] Xu, F., Hu, H., Potier-Ferry, M., Belouettar, S.: Bridging techniques in a multiscale modeling of pattern formation. International Journal of Solids and Structures **51**(18), 3119–3134 (2014)

[159] Xu, F., Potier-Ferry, M., Belouettar, S., Cong, Y.: 3D finite element modeling for instabilities in thin films on soft substrates. International Journal of Solids and Structures **51**(21-22), 3619–3632 (2014)

[160] Xu, F., Potier-Ferry, M., Belouettar, S., Hu, H.: Multiple bifurcations in wrinkling analysis of thin films on compliant substrates. International Journal of Non-Linear Mechanics (2015). DOI 10.1016/j.ijnonlinmec.2014.12.006

[161] Yin, J., Yagüe, J., Eggenspieler, D., Gleason, K., Boyce, M.: Deterministic order in surface micro-topologies through sequential wrinkling. Advanced Materials **24**(40), 5441–5446 (2012)

[162] Zahrouni, H., Cochelin, B., Potier-Ferry, M.: Computing finite rotations of shells by an asymptotic-numerical method. Computer Methods in Applied Mechanics and Engineering **175**(1), 71–85 (1999)

[163] Zang, J., Zhao, X., Cao, Y., Hutchinson, J.: Localized ridge wrinkling of stiff films on compliant substrates. Journal of the Mechanics and Physics of Solids **60**(7), 1265–1279 (2012)

Abstract

Surface wrinkles of stiff thin layers attached on soft materials have been widely observed in nature and these phenomena have raised considerable interests over the last decade. The post-buckling evolution of surface morphological instability often involves strong effects of geometrical nonlinearity, large rotation, large displacement, large deformation, loading path dependence and multiple symmetry-breakings. Due to its notorious difficulty, most nonlinear buckling analyses have resorted to numerical approaches since only a limited number of exact analytical solutions can be obtained. This thesis proposes a whole framework to study the film/substrate buckling problem in a numerical way: from 2D to 3D modeling, from classical to multi-scale perspective. The main aim is to apply advanced numerical methods for multiple-bifurcation analyses to various film/substrate models, especially focusing on post-buckling evolution and surface mode transition. The models incorporate Asymptotic Numerical Method (ANM) as a robust path-following technique and bifurcation indicators well adapted to the ANM to detect a sequence of multiple bifurcations and the associated instability modes on their post-buckling evolution path. The ANM gives interactive access to semi-analytical equilibrium branches, which offers considerable advantage of reliability compared with classical iterative algorithms. Besides, an original nonlocal coupling strategy is developed to bridge classical models and multi-scale models concurrently, where the strengths of each model are fully exploited while their shortcomings are accordingly overcome. Discussion on the transition between different scales is provided in a general way, which can also be seen as a guide for coupling techniques involving other reduced-order models. Lastly, a general macroscopic modeling framework is developed and two specific Fourier-related models are derived from the well-established classical models, which can predict the pattern formation with much fewer elements so as to significantly reduce the computational cost.

Keywords: Wrinkling; Post-buckling; Bifurcation; Thin film; Multi-scale; Path-following technique; Bridging technique; Arlequin method; Finite element method.

Résumé

Le plissement dans les films minces sur un substrat plus mou a été largement observé dans la nature. Ces phénomènes ont suscité un intérêt considérable au cours de la dernière décennie. L'évolution en post-flambage d'instabilités morphologiques implique souvent de forts effets de non-linéarité géométrique, de grandes rotations, de grands déplacements, de grandes déformations, une dépendance par rapport au chemin de chargement et de multiples brisures de symétrie. En raison de ces difficultés notoires, la plupart des analyses non-linéaires de flambement ont recouru à des approches numériques parce qu'on ne peut obtenir qu'un nombre limité de solutions exactes de manière analytique. Cette thèse propose un cadre général pour étudier le problème de flambage de systèmes film/substrat de manière numérique : de la modélisation 2D ou 3D, d'un point de vue classique ou multi-échelle. L'objectif principal est d'appliquer des méthodes numériques avancées pour des analyses de bifurcations multiples aux divers modèles de film/substrat, en particulier en se concentrant sur l'évolution en post-flambement et la transition du mode à la surface. Les modèles intègrent la Méthode Asymptotique Numérique (MAN) comme une technique robuste de pilotage et des indicateurs de bifurcation qui sont bien adaptés à la MAN pour détecter une séquence de bifurcations multiples ainsi que les modes d'instabilité associés sur leur chemin d'évolution de post-flambement. La MAN donne un accès interactif aux branches d'équilibre semi-analytique, qui offre un avantage considérable en termes de la fiabilité par rapport aux algorithmes itératifs classiques. En outre, une stratégie originale de couplage non-local est développée pour coupler les modèles classiques et les modèles multi-échelles concurremment, où les forces de chaque modèle sont pleinement exploitées, et leurs lacunes surmontées. Une discussion sur la transition entre les différentes échelles est fournie d'une manière générale, qui peut également être considéré comme un guide pour les techniques de couplage impliquant d'autres modèles réduits. A la fin, un cadre général de modélisation macroscopique est développé et deux modèles spécifiques de type Fourier sont dérivés de modèles classiques bien établis, qui permettent de prédire la formation des modes d'instabilités avec beaucoup moins d'éléments et donc de réduire le coût de calcul de manière significative.

Mots-clés: Plissement; Post-flambement; Bifurcation; Film mince; Multi-échelle; Technique de cheminement; Méthode de couplage; Méthode Arlequin; Méthode des éléments finis.